ABSTRACT

Title of dissertation: PIEZOELECTRIC PHASED ARRAY ACOUSTO-ULTRASONIC INTERROGATION OF DAMAGE IN THIN PLATES

Ashish S. Purekar, Doctor of Philosophy, 2006

Dissertation directed by: Professor Darryll Pines
Department of Aerospace Engineering

Structural Health Monitoring (SHM) and Condition Based Maintenance (CBM) systems can provide substantial benefits for aging aerospace systems as well as newer systems still in the design process. In aging aerospace systems, a retrofitted SHM system would alert users of incipient damage preventing catastrophic failure. For newer systems, incorporating a SHM approach and using CBM techniques can reduce life-cycle costs. Central to such SHM and CBM systems is the ability to detect damage in a structure.

Traditional approaches to damage detection in structures involve one of two methods. In the modal dynamics approach, the natural frequencies and modeshapes of a structure shift when damage occurs. The location, type, and amount of damage is determined by the shifts in the modal properties due to damage. Alternately, in an Ultrasonics approach, the structure is scanned with a specialized transducer which induces high frequency vibrations in the structure. Damage in the structure is inferred when these vibrations are altered. In the same vein as Ultrasonics,

Acoustic Emission based methods listen for energy release in the structure upon defect growth. All of these techniques have limitations which hinder their usage in a practical system. This thesis attempts to develop a methodology with the benefits of the modal approach as well as the Ultrasonics/Acoustic Emission approach. The methodology is commonly referred to as an Acousto-Ultrasonic technique for damage detection.

The structural dynamics of plate structures is described as wavelike in nature where the plate is a medium for wave propagation. For thin plates, bulk wave propagation is described using Lamb wave modes. The two fundamental modes of wave propagation are the in-plane acoustic mode and the transverse bending mode. The interaction of these waves with a discontinuity or damaged region changes the way the waves propagate. Part of the incident wavefront is reflected back while the rest is transmitted through the damaged region. The presence of the reflected waves and the attenuation of the incident wave in the transmission case indicates that damage is present in the structure.

A reflected wave can be used to infer the location of damage on a structure. A phased array technique is used which isolates the source of these reflections in an effort to identify the damage location. Phased arrays are shown to act as directional filters which sense the structural vibrations of the plate and selectively look in a certain direction on the plate relative to the array orientation. Reflections from damage can then be extracted from sensor signals in an effort to locate a damage region. Damage in the form of a hole in an isotropic plate is examined and the phased array technique is used to show that the location of the hole can be determined as

well as trends indicating that the size can be determined.

For anisotropic materials, such as fiber reinforced composite laminates, the dynamics associated with wave propagation are more complicated. This is shown in composite laminates where wave propagation is dependent on the direction of travel. A more fundamental concern is developing an understanding of the wave propagation properties of a composite laminate. A model is developed to determine the dispersion relations for a laminate made of an arbitrary layup of orthotropic plies. The predicted results from the model are compared with experimental results showing that the dispersion relations can be accurately determined.

The phased array technique is then applied to wave propagation in a composite laminate to determine the presence of delamination damage. It is shown that delaminations do produce reflections from incident waves. Though the reflections are weak, they can be extracted from the structural dynamics by use of the phased array technique.

Traditional modal methods are then compared with a wave propagation approach. Modal methods are shown to have difficulty ascertaining low damage levels when using a small number of modes. As the amount of information increases, such as a larger set of modes and larger number of sensors, the modal methods become more sensitive. A wave propagation approach is shown to be sensitive to small damage amounts and the location and approximate extent of damage can be determined using less information.

PIEZOELECTRIC PHASED ARRAY ACOUSTO-ULTRASONIC INTERROGATION OF DAMAGE IN THIN PLATES

by

Ashish S. Purekar

Dissertation submitted to the Faculty of the Graduate School of the
University of Maryland, College Park in partial fulfillment
of the requirements for the degree of
Doctor of Philosophy
2006

Advisory Commmittee:

Professor Darryll Pines, Chair/Advisor
Professor Amr Baz
Professor Inderjit Chopra
Professor Sung Lee
Professor Norman Wereley

श्रीः

ACKNOWLEDGMENTS

I would like to thank my advisor, Professor Darryll J. Pines, for giving me the opportunity to explore a challenging and interesting topic. I would also like to thank the other committee members: Professor Amr Baz, Professor Inderjit Chopra, Professor Sung Lee, and Professor Norman Wereley. A bit of each of their teachings is in this thesis.

I owe a heartfelt thank you to my immediate and extended family. Their encouragement and unwavering support pulled me through difficult times. Hopefully, I will be able to reciprocate.

I would like to express my appreciation to my fellow students in the Aerospace Engineering Department, both old and new. There are too many to list and I would be remiss if I were to unintentionally exclude anyone. I have learned quite a lot from all of them, on both academic and noncollegiate topics.

Lastly and most importantly, an acknowledgement to the higher power that helps us along our paths.

अवधूत चिंतन

TABLE OF CONTENTS

LIST OF TABLES

LIST OF FIGURES

Chapter 1

Introduction

1.1 Motivation

Structural Health Monitoring (SHM) is a topic applicable to a variety of fields. In aerospace systems, where the factors of safety are low in order to maintain an efficient system, SHM is a necessity. Many aerospace systems, from aircraft to rotorcraft to the space shuttle program, are aging and approaching their design lifetimes. Rather than retiring a whole fleet of aircraft, another option is to extend the life of the aircraft using a SHM system. New designs of aerospace systems call for tighter structural tolerances as well as the use of non-traditional materials. A SHM system is beneficial for proper operation in both of these cases.

A commonly cited example for the need of a SHM system the case of the Aloha Airlines Flight 243 incident in April 1998 where a large section of the fuselage detached mid-flight. The aftermath is shown in Figure 1.1. A pre-flight visual inspection indicated that there were no obvious warning signs. Though only one life was lost during the incident, the possibility of other similar incidents brought the attention of SHM systems to the forefront for civilian aircraft. This is especially true for fleets of aging military and civilian aircraft. In the rotorcraft field, there has been collaboration between the U.S. and U.K. for a monitoring system since the early 1980s and was accelerated after a maritime accident with a CH-47 [1]. An example which illustrates the need for a reliable health monitoring system is the case of the Space Shuttle Columbia. The shuttle experienced catastrophic failure upon reentry into the atmosphere due to damage to the thermal protection system experienced after launch [2]. Figure 1.2 shows the damage to the leading edge of the wing produced by controlled experiments in the post-accident investigation.

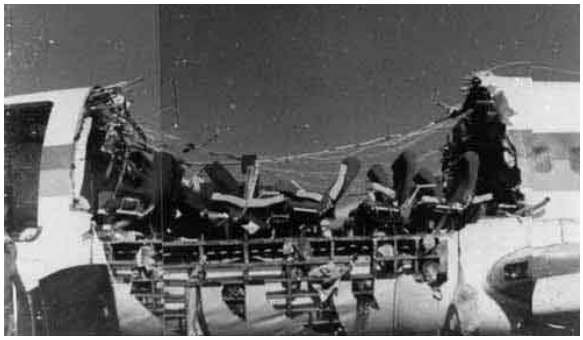

Figure 1.1: Aloha Airlines damage

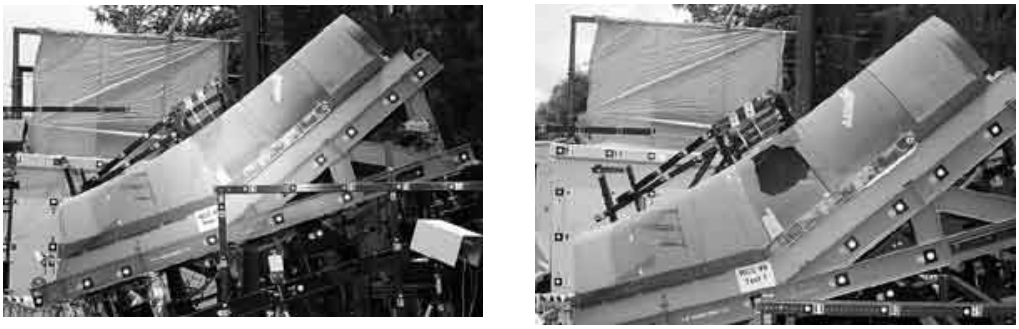

(a) Before impact (b) After impact

Figure 1.2: Damage due to foam impact on leading edge of shuttle wing

SHM systems are technologies which enable aircraft maintenance and operation personnel to : (1) ascertain the status of the vehicle, (2) maintain operating efficiency of the vehicle, and (3) reduce costs associated with operating and owning the vehicle. A SHM system could be retrofitted to an aging vehicle or integrated into the design process for newer programs.

Along the same lines as a SHM program, a Condition Based Maintenance (CBM) program represents a shift in how aircraft maintenance is conducted. Traditionally, maintenance schedules for an aerospace system were based on a "safe life" approach. A part is replaced at a prescribed time based on an estimation of the loads and conditions of use. Unfortunately, parts are removed and discarded even though they still may be structural viable [3]. As the understanding of fracture mechanics increases, a shift in the maintenance approach developed toward a damage

tolerant scheme. Though a part has small amounts of damage upon inspection it is still capable of carrying loads.

The promise that Condition Based Monitoring represents is an approach that retires components based on accumulated life [4]. A structural component with insignificant amounts of damage would be monitored continuously and only replaced when the damage amount approaches a critical level. The diagnostic and prognostic information is provided by a CBM program coupled with a SHM system. Thus, maintenance schedules can be simplified based on the on-board data collection of the flight environment and status of the part. The useful lifetime of a component increases as a result.

On-board SHM and CBM technologies are topics of interest in the aerospace industry for several reasons. The most obvious reason for a SHM system is the prevention of catastrophic failure of a vehicle and saving the lives of the crew as well as passengers. There are more subtle benefits that accompany a successful SHM and CBM program.

Maintenance typically adds up to $\sim$11% of the total life cycle costs of aircraft [5]. In the civilian airline arena, this becomes a significant amount of expenditure for a single aircraft. For the military, $\sim$\$1.6m/year is spent on maintaining each individual aircraft. A SHM/CBM system which reduces these figures would improve the efficiency of a fleet of aircraft. In a study performed by the Canadian military, a SHM scheme was projected to extend the life of a fleet of CF-188 aircraft approximately twelve years at a savings of close to \$400M. Besides the benefits to life cycle costs of an aircraft, current maintenance practices also lead to wasteful spending. A Federal Aviation Administration (FAA) sponsored study found that experienced inspectors only located about half of defects in a controlled inspection test [6]. Even the parts which are removed may have been incorrectly removed based on faulty inspection practices. In a survey of airline parts from British aircraft which were removed based on manual inspections, 18% of the parts were found to be free of defects [7]. Other studies have shown up to 40% of the parts which were removed have been found to be fault free.

While newer aircraft come into service as passenger aircraft, older aircraft are relegated to the role of transports. Structural changes are required for conversion from passenger aircraft to transport aircraft [8]. These structural changes alter the load paths and design criteria that are used in predicting the safe life of components. Furthermore, military aircraft operating conditions change based on the requirements by the military. A safe life approach to maintenance schedules is ineffective when the operating environment changes. A system that continuously monitors the structural components would alleviate the concerns associated with a change in operating conditions.

Besides the obvious benefit of providing advanced warning of possible dangerous situations, a SHM and CBM program also provides economic benefits. This enables the vehicle, whether it is a fixed wing aircraft, rotorcraft, or spacecraft, to reach a higher level of efficiency and longevity and is applicable to newer programs as well as retrofits for an aging fleet. Various initiatives are present in the different areas of the aerospace field to realize these potential benefits.

1.2 Sample of Current Practices in Aerospace Systems

1.2.1 Aircraft

The need for a SHM/CBM program is needed in the civilian and military programs to extend the life of aging aircraft. There are a variety of programs to bring SHM/CBM capabilities to current aircraft.

Northrup Grumman is exploring the use of Acoustic Emission based damage detection [9]. The USAF T-38 and F/A-18 aircraft are considered as a test beds for proposed damage detection schemes. Laboratory tests were conducted on structures simulating the wing spar of the T-38 aircraft and a bulkhead of the F/A-18 aircraft using an acoustic emission based technique.

The wing box structure of the C-130 transport aircraft has also been investigated for damage detection studies [10]. Manual inspection would require the wing structure to be dismantled in order to inspect damage critical areas. Ultrasonic

techniques were shown to be effective in examining components of the wing box structure which were susceptible to fatigue related damage.

The integration of SHM activities on the Eurofighter Typhoon aircraft has been examined on a systems level [11] by British Aerospace (BAE). Information from the aircraft is fed into a central processor which examines the status of the vehicle and compares it to reference states that have been simulated. The goal is to develop an efficient management system for a fleet of aircraft.

Future aircraft still in the development stages, such as the Joint Strike Fighter [12], will have integrated SHM capabilities. From the previous attempts at SHM programs for older aircraft, newer programs have the benefit of hindsight. The SHM/CBM system is integrated into the design process rather than added on as an after thought. The precise load history and flight conditions of a particular aircraft can be tracked, resulting in a greater understanding of the critical areas.

1.2.2 Rotorcraft

SHM activities in rotorcraft have been active since the the early 1980s and initiated due to the harsh vibratory environment that helicopters endure. Faults and improper maintenance to the helicopter engine, rotor components, and transmission are the causes of a significant portion of fatal helicopter accidents [13].

Boeing's interest in damage detection studies for rotorcraft is apparent in the introduction of Active Damage Interrogation program [14, 15]. Tests were conducted on a composite flexbeam article of a MD Explorer helicopter for edge delaminations. Transfer functions were used to evaluate the condition of the article and a damage index developed to quantify the status of the part.

Bell Helicopter Textron has shown interest in prevention and detection of faults in flexbeams. The composite flexure used in the Bell 406 developed delaminations due to the loads experienced during flight [16]. A combination of experimental and analytical methods are employed to identify the expected fatigue life of flexbeams based on fracture mechanics and expected loads [17].

1.2.3 Spacecraft

The Shuttle Modal Inspection System was developed to identify changes in the tail body flap which controls the pitch of the aircraft [18]. Frequency response functions were useful in determining changes in the flap whereas X-ray, ultrasonic, and visual techniques were inconclusive due to the large amount of thermal protection. Each of the orbiters that were tested (OV-101, OV-102, and OV-103) had different modal parameters which needed to be found before application of the modal methods of damage detection.

Damage detection techniques have also been examined for use with cryogenic fuel tanks of the space shuttle program as well as future space access vehicles. Health monitoring of fuel tanks is especially important for reusable launch vehicles that need to be certified prior to each launch [19]. An acoustic emission monitoring method was examined for the DC-XA fuel tank with limited success [20]. A variety of techniques are proposed for use with wide area damage detection in fuel tanks [21] made of composite materials.

Modal methods were useful in evaluating large space truss structures for damage [22, 23]. An experimental truss structure based on a proposed model of a space station was used as a testbed to examine various practical modal methods such as actuator and sensor placement, modal expansion, model reduction, and damage sensitivity.

Due to the difficulties experienced with previous space access platforms, newer designs are calling for increased reliability in future vehicles. Thus, there is a desire for an integrated health monitoring system for next generation space vehicles [24].

1.3 Existing Technology for Damage Detection

A key component to a SHM/CBM program is the ability to determine the status of a component of the system. Detecting damage in a structural component may be accomplished using a variety of methods. Many of the current techniques used in the aerospace field are adapted from the field of Non-Destructive Testing & Evaluation

(NDT&E) which has applications in manufacturing, construction, and maintenance industries.

Current research in SHM is focused toward developing technologies to accurately interrogate a structure for damage as well being adaptable to candidate vehicles. There are a variety of methods which may be borrowed from current NDT&E practices. They can be coarsely separated into techniques based on non-vibratory and vibratory information.

1.4 Non-Vibration Based Non Destructive Evaluation

There are various methods of non-vibration based inspection methods that have been used[25]. These are methods which do not rely on the dynamic mechanical properties of the structure to determine the presence of damage. Typically, these methods arise in the specific field or are adapted from other applications.

Visual inspection is the most basic inspection method and is used extensively in most current maintenance programs. Based on a maintenance schedule, an operator inspects critical areas of the aircraft looking for macroscopic scale damage. Thus, the part needs to be accessible and the damage needs to be viewable in order for visual inspection to be effective.

A dye penetrant is used along with visual inspection when the defect size is very small. This technique works particularly well for cracks as the dye is pulled into voids by capillary action. After excess penetrant is removed, a developing agent is used to coat the surface. The dye penetrant, which is accumulated in the void, then stains the developer and can be seen under normal lighting conditions or through the use of ultraviolet light. Subsurface defects are more difficult to ascertain. Additionally, the surface of the structure to be tested should be relatively smooth and non-porous.

In radiographic techniques, a radiation source is used to illuminate the structure with X-rays or gamma rays and the corresponding image of the structure is captured. In this case, subsurface voids are obvious in the image. Many techniques exist which use some form of radiographic techniques, such as:

1. Microfocus Radiography - A focused beam is used to examine a small area on the part for defects.

2. Real-Time Radiography - Instead of a photographic type film on which the image is exposed, a fluorescent film is used which is illuminated temporarily. This technique is adaptable to dynamic tests.

3. Flash Radiography - A short burst of X-rays are used to illuminate the object which gives a snapshot of dynamic motion.

4. Radiation Gaging - A collimated beam of X-rays or gamma rays are used to inspect the part for very small changes in the density-thickness product of the structure. This technique is useful for measuring small changes in the density of the part.

The equipment required for such a system makes it infeasible for an on-board system. Additionally, the part needs to be isolated from the rest of the structure for ideal testing conditions which makes this technique impractical for an on-board system.

Eddy current sensing techniques are used to inspect metallic parts with specialized transducers. These transducers impart AC magnetic fields on the structure. Damage in the material produces eddy currents in the structure and this affects the electrical impedance of the transduction device. For this technique to work reliably, the structure needs to be conductive. This requirement cannot be guaranteed with composite materials that are integrated in newer aerospace systems.

There are a few drawbacks associated with the previous methods. Visual inspection techniques are inadequate for on-board SHM applications. Dye penetrants, besides relying heavily on operator training to produce reliable results, are also not appropriate for on-board damage detection. Radiographic techniques rely on expensive and bulky equipment to inspect parts and is more appropriate for examining a component after removal from the system. Eddy current techniques are only useful for components made of conductive material. Additionally, only surface or near surface defects may be noticed.

1.5 Vibration Based Non Destructive Evaluation

An on-board SHM which provides real-time status of various components will need to be a stand alone system capable of inspecting critical components using in-situ transduction mechanisms in a near real-time sense. This is difficult to accomplish using traditional non-vibration based NDE methods. If the dynamic characteristics of the structure are used along with appropriate transduction mechanisms, the problem becomes much easier to handle. There has been extensive work on various vibration based techniques for damage detection. Some these approaches are discussed below.

1.5.1 Modal Dynamics

The classical view of the dynamics of an arbitrary structure is in terms of natural frequencies and mode shapes. Natural frequencies are the frequencies at which the kinetic and potential energies in the system are transferred back and forth. A modeshape is the characteristic form that the structure takes at a given natural frequency.

The basic properties of a structure are described in terms of mass and stiffness matrices, $\mathbf{M}$ and $\mathbf{K}$, respectively. For damage detection purposes, the damaged structure would have a different mass and stiffness distribution than the nominal (or updated) model of the structure. When a structure is damaged, the natural frequencies and mode shapes undergo a shift. The basic premise of damage detection using modal methods is to determine the location and extent of damage based on an updated model of the structure and an experimentally measured set of natural frequencies and mode shapes of the damaged structure.

A modal approach for damage detection has been examined for many aerospace systems. A comprehensive review of research for damage detection based on modal dynamics is presented in Doebling, et. al. [26] and Sohn, et. al. [27]. A variety of steps are necessary in order to use modal methods in a damage detection scheme. A baseline model is necessary in order to examine the modal properties of the damage

system. The baseline model may be constructed from an analytical representation of the system which is modified based on experimentally identified modal parameters of the actual system. The modal parameters tend to shift as the structure is progressively damaged. This shift is used with a damage detection technique to determine the location and amount of damage. When updating the baseline model and applying a damage detection technique, typically, only a limited set of sensors are available. Either model reduction or modal expansion is used to match the degrees of freedom in the model with the experimentally determined modal parameters. The damage detection algorithms which are commonly used rely on the modal residual to determine the location and amount of damage in the structure. Three common modal damage detection schemes based on system matrix updating are the Optimal Matrix Updating [28, 29], Sensitivity-Based Element-By-Element Method [30], and Eigenstructure Assignment - Damage Location Method [13].

While there is a variety of work regarding modal based damage detection studies for aerospace components, all fundamentally hinge on the change in natural frequencies and mode shapes of the structure. A shift in the set of modal parameters is an important criteria for damage detection. These techniques have been shown to be effective in damage detection of structures that may be modeled as discrete systems, such as truss structures, buildings, bridges, and oil platforms [31, 32, 33, 34]. The Kabe model [35] is generally used as the benchmark test case for a modal based damage detection scheme. For aerospace structures, where the components are typically treated as continuous structures, the efficacy of modal damage detection schemes becomes more subjective. Research done simulating typical aerospace components, such as beams and plates, where incipient damage detection is important, has produced conflicting results. Kessler [36] conducted a series of modal tests of composite laminates with delamination as well as through hole damage at various locations. The first six experimental modes of the laminate exhibited negligible changes in frequency. Tracy and Pardoen [37] use the change in natural frequency of a composite laminate as a way of locating damage. They observe that the first few modes of a delaminated beam are not much different from the corresponding

nominal case unless the delamination size reaches a critical level. Kulkarni and Frederick [38] examine a composite shell and the effect of delamination on the natural frequencies. A model of a shell is used to find simulated results. It is noted that the effect of the delamination on the natural frequency of the structure is dependent on a variety of factors which may prohibit its use in a damage detection application.

Under ideal circumstances, modal methods are able to locate damage over the entire structure as well have sensitivity to small amounts of damage. There are, however, practical issues which degrade the performance of modal techniques.

1. A significant concern in modal damage detection techniques is obtaining a model of the nominal structure with which to compare the natural frequencies and mode shapes of the damaged structure. In actual structures, the boundary conditions play a very prominent role in the properties of the lower modes. Even if the structure is uniform, good agreement between the actual structure and the nominal structural model may be difficult to achieve because of poor boundary conditions.

2. A method is needed to excite the structure such that all of the natural frequencies and mode shapes are present. Due to this requirement, the actuator cannot be placed at a nodal location of a mode shape. For large structures, excitation becomes an important issue as the power needed to move the structure may become substantial.

3. Damping becomes an important factor as the poles in the frequency response of the structure spread out due to damping. This causes an uncertainty in determining the natural frequencies as peaks in the frequency responses are rounded off. Damping is more significant at higher frequencies, where the modal techniques tend to show the greatest sensitivity.

4. If the higher modes are used for damage detection purposes, the model of the structure needs to be able to predict these higher modes. As a result, the model of the structure would be large and the algorithms which are used to

detect damage pose a significant computational barrier to a fast and efficient damage detection scheme.

5. A set of sensors are required to be distributed over the structure to capture the characteristic mode shapes. As the mode of interest grows, the number of sensors needed to capture the mode shape increases. For higher modes, a large number of sensors are needed which could pose a problem for instrumentation and data acquisition.

1.5.2 Impedance Based Methods

In an impedance based approach, the transduction mechanism plays an important role in the damage detection scheme. When bonded to a structure, the electro-mechanical properties of the transducer is a function of the active material as well as the mechanical properties of the substructure on which it is bonded. By exciting the transducer and monitoring the current drawn, the impedance of the of the transducer is determined. This impedance would change depending if the structure is damaged, as the stiffness of the structure would change. A simple model of the impedance based damage detection scheme is shown in Figure 1.3 where the active material and substructure are coupled. If either the mass, m, or the stiffness, k, change, the impedance of the bonded transducer changes also. A commonly used active material for this approach is a piezoelectric ceramic which can be readily bonded and shaped to fit the desired application. Piezoelectric materials feature coupling between the mechanical properties (stress and strain) and electrical properties (charge and electric field).

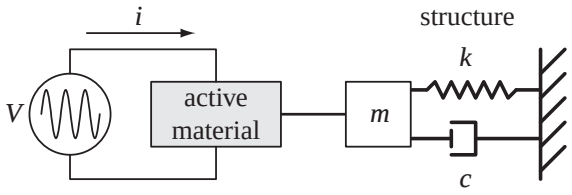

Figure 1.3: Impedance based method diagram

Much of the current work in impedance based damage detection is based off of work by Liang, et. al. [39] where the simplified expression for the electromechanical impedance of a coupled active material and substructure are derived. Applications mentioned in the work extend to modal analysis, actuator placement, co-located sensor/actuators, and acoustic resonance are discussed, though damage detection was not a direct application mentioned. An impedance based damage detection technique was demonstrated on an experimental bolted bridge joint by Ayres, et. al. [40]. A piezoceramic patch used as the transduction device and was shown to be sensitive to a loss of bolt strength near the patch. The sensitivity was reduced as the affected bolt was moved further away. In work by Chaudhry, et. al. [41], the impedance based method was used to monitor the tail section of a model airplane. A damage metric indicated that local alterations to the plane were readily apparent; however, alterations further away were not apparent. Park, et. al. [42] conducted simulations and experimental tests of a damaged beam with the impedance based method and showed sensitivity to small amounts of damage. It was noted that at the higher frequency region, damping of the modes plays an important role in the response and adversely affects the ability of impedance based methods. Giurgiutiu [43] used the impedance method for damage detection on an Aluminum plate using piezoceramic patches. As damage was moved further away from the interrogating sensor, the sensitivity decreased.

Impedance based methods are sensitive to small amounts of damage, though this sensitivity drops off dramatically with increasing distance between the damaged location and the transducer. A network of impedance based transducers would be necessary to examine an entire structure for damage. A relatively large structure would need to be instrumented with many impedance based devices in order to provide an effective damage detection tool.

1.5.3 Ultrasonics

Ultrasonics is another classical NDT&E method for damage assessment of a structure. In this method, specialized transducers are used to excite the structure with

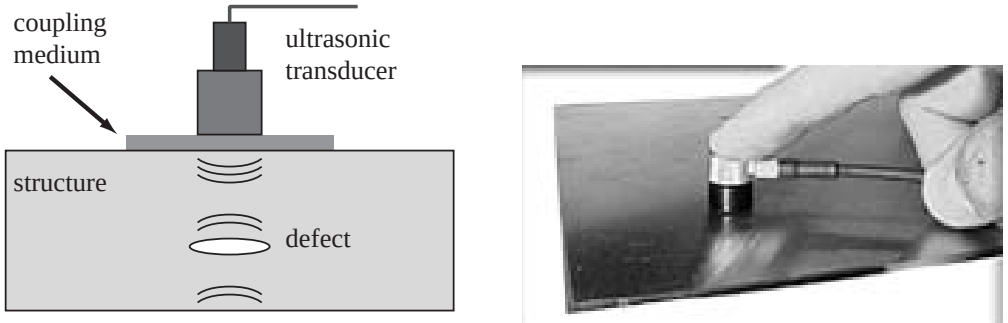

(a) Ultrasonic transducer schematic (b) Inspection (Courtesy of Krautkramer)

Figure 1.4: Ultrasonic testing

high frequency acoustic waves, shown in Figure 1.4. It is essentially a transient technique where waves travel through the structure and reflect off of the back end toward the transducer, which also senses the vibrations or has alternate sensing elements. In the presence of damage or discontinuity, a reflection from the damaged region is present and damage size and location can be inferred from this information. Typically, the transducers use piezoelectric elements for both excitation and sensing.

Ultrasonic techniques have reached a level of maturity such that transduction devices and the associated signal processing may be bought from commercial vendors. When integrated with image processing, a view of the internal damage may be seen, known as C-scans.

While commonly used ultrasonic techniques are capable of locating small defects in structures, there are several factors which prohibit their use in an actual SHM system. Much like the local impedance method, the transducer must be local to the damaged location in order to detect its presence. Coupling between the transducer and structure plays an important role in ultrasonic techniques. The coupling medium is the material between the transducer and the structure of interest. This coupling medium could be air or a liquid, such as water or oil. In the dry coupling case, where transfer of energy is through the surrounding air, there is significant acoustic impedance mismatch between the air and the driver of the transducers as well as between the air and structure. The signal levels of the dry coupling cases are

very low. Signals generated in such a case have poor signal quality as much of the energy is not transferred to the structure. A coupling medium is required between the ultrasonic transducer and the structure to be examined. In liquid coupling cases, the acoustic impedance mismatch improves and the quality of the signals are better; however, there needs to be a layer of water or oil on the structure. This is not a practical situation for an on-board SHM/CBM scheme.

1.5.4 Acoustic Emission

Along with Non-Vibration based methods discussed earlier, acoustic emission, as part of NDT&E techniques has been used in other fields. When a structure is loaded, any defects present in the structure are stressed. As the load increases, the stresses around the defect increase the defect may grow in size. When the defect size grows rapidly, the sudden change in the stress field around the defect releases energy in the form of an acoustic emission into the structure and propagates through the structure, shown in Figure 1.5. The bandwidth of acoustic emissions encompasses a broad frequency range (50 kHz to 2 MHZ). A set of sensors placed over the structure may locate the propagating defect based on triangulating the source of the acoustic emission. A wide area of the structure may be surveyed by relatively few sensors. Acoustic emission based applications have been proposed for various aerospace systems [44].

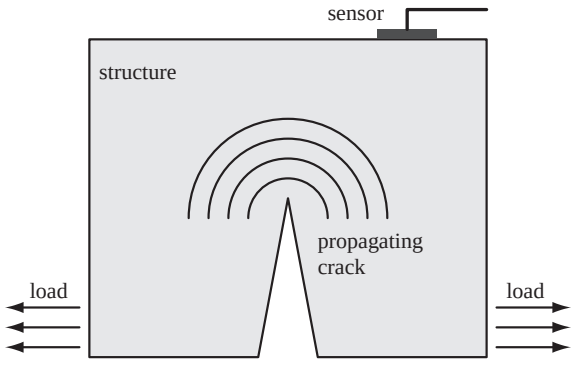

Figure 1.5: Acoustic Emission in a structure

The basic premise behind the acoustic emission method requires the growth of the damage in order to produce useful information. An implicit assumption is that the damage is stable and will not expand critically. An internal defect in an structural component would remain dormant until the appropriate loads are placed to produce an acoustic emission event. A SHM/CBM programs typically requires continuous assessment of the component. There are more fundamental concerns with acoustic emission as damage detection methodology.

The singular nature of acoustic emissions in structures is a hindrance to its effectiveness. Since the release of energy into the structure is essentially unpredictable and non-repeatable, signal discrimination and noise are key issues that need to be resolved [45]. The electronics and signal processing for each sensor signals needs to be able to differentiate between an acoustic emission event and other surrounding noise. This was shown in experimental work by Wilkerson [20] where a cryogenic fuel tank was pressurized during a fill with liquid nitrogen and monitored for acoustic emissions due to fatigue in the tank structure. It was concluded that the acoustic activity in the tank was largely due to the interaction of the fluid with internal insulation and this adversely affected any damage detection goals. For structures operating in a dynamic environment, the transient and non-repeatable phenomenon of acoustic emission will be mixed in with noise from other sources. For composites structures, acoustic emission events are considerably more "noisy" since the wave propagation properties are more complex [46]. The signals from different damage types in composites produce widely varying acoustic emission event magnitudes and proper calibration of sensors becomes an issue. The algorithm used to identify acoustic emissions must be able to distinguish between useful information and noise which is present in the system.

1.5.5 Acousto-Ultrasonics

A topic of research which has received much interest for health monitoring applications is the Acousto-Ultrasonics (AU) method. The basic principle is to gather acoustic emission type of information without producing stress fields that cause the

damage to grow. AU is a wide area damage detection scheme which has shown the capability to locate small damage. In the previous damage detection schemes mentioned, with the exception of acoustic emission based methods, there was a trade-off between the sensitivity to small damage and the ability to interrogate the whole structure. There are difficulties with acoustic emission based techniques which hinder its applicability. An AU approach attempts to locate small defects over a large area. An excitation transducer is used to send interrogating waves through a structure which is monitored using sensing transducers, shown in Figure 1.6.

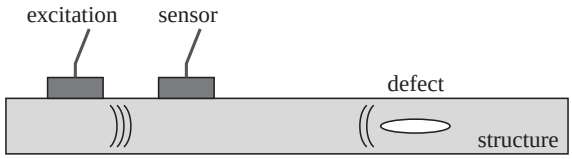

Figure 1.6: Acoustic-Ultrasonics in a structure

The transmission of information in AU is based on the wave propagation properties of the structure. For solid bodies, wave propagation is a well known phenomenon with an extensive history [47]. Normal aerospace applications focus on wave propagation in thin plates which are described in terms of Lamb wave dynamics [48, 49]. Worlton [50] is commonly cited as one of the first references to propose an AU type approach for damage detection in structures and Rose [51] has presented a literature review of the most salient work with regard to AU research. Dalton [52, 53] conducted studies of Lamb wave propagation through aircraft structures and noted that long range inspection is possible. Cawley and Alleyne [54] discussed the different Lamb modes present in thin plates and their applicability toward damage detection. It is mentioned that dispersion, the change in the shape of the waveform as the wave propagates through the structure, is an important factor in choosing a wave mode for AU damage detection. Wilcox, et. al. [55] extends Cawley's thoughts about factors critical for AU inspection of structures. The more important factors include:

1. Dispersion of a wave packet

2. Attenuation of the wave mode

3. Sensitivity of a mode to damage

4. Ability of a transducer to excite a certain wave mode

5. Ability of a transducer to detect a certain wave mode

6. Ability of a transducer to isolate a particular wave mode from others

These factors are separated into two categories, the first three items deal with the internal wave propagation mechanics in the structure and the second three items deal with transduction issues. Much of the current research in AU attempts to generate a better understanding of these factors or improve upon current practices.

Wave Interaction with Defects in Isotropic Structures

Understanding the interaction of a wave with a defect in an isotropic structure is important for damage detection applications. Kraut [56] presented a review of the basic ideas behind wave scattering after a wave packet approaches a defect in a structure. Gubernatis, et. al. [57] attempts to present an exact formulation based on continuum mechanics for a wave scattering due to a void in a solid body in an attempt to solve for the scattered displacement field. In their second paper [58], an approximation is used to simplify the solution approach. Agrawal [59] developed a model of the scattered field based on a boundary integral formulation. Boström [60] presents a review of work based on developing a numerically efficient scheme of predicting the wave scattering field for a crack in a solid using continuum mechanics and a description of the behavior around a crack region. Alleyne and Cawley [61] used a finite element formulation to produce a time domain simulation of the interaction of different Lamb modes with a notch in the plate. Reflected and transmitted magnitudes of the scattered waves were found and shown to be frequency dependent. A comparison between finite element and experiments for the scattering of symmetric mode with a notch in a plate was conducted by Lowe and Diligent [62]. Diligent [63] performed numerical simulations of different mode interactions with various damage

types. Weak mode conversion is shown to exist when a mode of one type is incident on a damaged area and different mode is produced. Lee and Staszewski [64, 65] constructed a finite difference model to predict wave propagation through a thin plate. The wave field for the whole plate showed the scattering of the incident wave from the crack. Experiments were used to corroborate the results of the simulation. Giurgiutiu, et. al. [66] conducted numerical and experimental studies of reflections of Lamb modes from cracks in an Aluminum plate. Kehlenbach, et. al. [67] used a laser vibrometer system to scan a plate as a wave approached a damage and was scattered. The scattered wave field was shown to spread throughout the plate. Ihn and Chang [68] experimentally examined the interaction of Lamb waves with a crack and developed a damage index based on the scattering information.

Wave Propagation in Laminates

While wave propagation in isotropic materials is a well established phenomenon, wave propagation in non-isotropic materials is not as straightforward. Since current aerospace structures are incorporating composite materials in their design, AU inspection of these structures requires a basic understanding of wave propagation applied to these materials. Dong and Nelson [69] introduced a finite element scheme that used a quadratic displacement distribution through the thickness. The mass and stiffness matrices which are dependent on the frequency and wavenumber are used to determine the wavenumber-frequency relationship for a laminate constructed of orthotropic laminae. Yamada and Nemat-Nasser [70] modeled wave propagation in a thick laminate where waves could propagate through the thickness. Karunasena, et. al. [71] generalized Dong and Nelson's method for wave propagation in all three directions, including the thickness direction. Murakami [72, 73] attempted to develop a mixture theory approach for a laminate. The concepts were to extend toward composites of various types, such as fiber reinforced composites and particulate composites. Galán and Abascal [74] presents a more rigorous finite element formulation, similar to Dong and Nelson, to predict the dispersion relations for an arbitrary laminate which resulted in an easily implementable formulation. Sun and Tan [75]

compared numerically derived transient response of an orthotropic plate to impact with experimental results and showed good agreement. It was shown that the wave-fronts propagate at different speeds through the laminate. Clark and Thwaites [76] showed experimentally that the wave speed depends on the direction of wave propagation for different layups. There were significant differences when comparing to predictions based on classical laminated plate theory. Jaleel, et. al. [77] used a finite difference scheme to simulate the transient response of a composite plate. Lih and Mal [78] compared the exact solutions with shear deformable plate theory models for composite laminates. Banarjee, et. al. [79] extends Lih and Mal's results and compares the shear deformable plate theory results with experiment.

Wave Interaction with Defects in Composite Laminates

Mode interaction with composite materials mainly deals with delamination damage. Fällström [80] conducts tests using an optical interferometry technique and shows the wave field for a laminate at different points after impact. The same type of wave field is shown as with Clark and Thwaites [76]. Delaminations in the laminate cause the wave field to be altered and this shows up in the resulting wave field image. Taillade, et. al. [81] used an different interferometry technique to visualize wave propagation on composite laminate. The interaction with a delamination in the laminate is shown and the corresponding altered wave field image. The position of the delamination relative to the thickness is altered and an AU approach is used to capture reflections. The in-plane mode is shown to be sensitive to delamination in the laminate. Guo and Cawley [82] set up a finite element model to show that delaminations do produce reflection from incident waves. They provide experimental results [83] to show that AU is feasible for damage detection in composite laminates. Tan, et. al. [84] conducted a series of experiments where the magnitude of the in-plane mode was monitored as it propagated through a laminate. There is a decrease in amplitude as the wave modes travels through the delamination, suggesting that energy is extracted from the wave mode. Birt [85] conducts an experimental study of an in-plane wave mode and its interaction with various delamination types and

laminate layups. Valdés, et. al. [86] showed experimentally that the bending mode is also sensitive to delaminations. A finite element simulation was set up to predict the same transient results. Most of the effort toward understanding the interaction of wave modes with delamination is empirically based.

Mechanisms for Transduction

Early work on transduction mechanisms for AU adapted ultrasonic transducers. Though effective in exciting and sensing of Lamb waves, their applicability for a damage detection scheme is limited due to their large size. Transducers using patches of active materials, and piezoelectrics in particular, have a considerably lower profile and are able to produce the same type of results. Much of the modeling associated with transduction using piezoelectric patches is based off of work by Crawley and de Luis [87] where a bond layer is introduced between the active element and substructure and loads are transferred through shear stresses. Sonti, et. al. [88] examined the distribution of loads on a two dimensional structure and determined the ability of a patch of a given shape to excite wave modes. Grondel, et. al. [89] explored the ability of a piezoceramic patch to selectively excite one mode over another in a thin plate. Giurgiutiu [90] examined the ability of a single patch to excite the different modes in an Aluminum plate and compared the analytical results with experimental results. Giurgiutiu also discusses the possibility of selectively exciting a given mode. Veidt, et. al. [91] develops closed form expressions for the response of a plate to excitation using a piezoelectric patch and the transient response is compared to experimental results. Raghavan and Cesnik [92] developed expressions based on Lamb wave theory for a piezoceramic actuator on a structure and compared the ability of the patch to excite the asymmetric and symmetric modes of a plate. Moetakef, et. al. [93] showed a comparison between experimental and finite element simulations of the transient response of a beam with actuation piezoceramic patches. Further work showed that a set of these patches working together could produce desirable waveforms in the structure. A subset of the work on developing transduction mechanisms focus on using sets of actuators, known as Interdigitated

Transducers, to selectively excite wave modes in a plate. Joshi [94] introduced the idea of interdigital transducers for selectively exciting waves in beams in structures for health monitoring purposes. Wilcox [95] goes into more depth on the design and issues of interdigital transducers for wave excitation in structures.

Signal Processing

Since AU signals generally produce transient signals, a way of interpreting the results needs to be devised. Traditionally techniques such as the Fourier Transform and Short Time Fourier Transform have been used to analyze time domain signals. More recent techniques, such as the wavelet transform and the empirical mode decomposition, have been explored. Wavelet analysis was developed earlier than the empirical mode decomposition and much effort has been placed into using wavelets as a damage detection tool [96]. Abbate, et. al. [97] used wavelet analysis as a way of removing noise in transient ultrasonic signals. Features of the transient data corresponding to flaws in the structure are brought out by the wavelet denoising. Prosser, et. al. [98] used a wavelet transform technique to extract the dispersion relations for a Aluminum plate. Quek, et. al. [99] examined transient data from a beam with a crack with wavelet analysis and found promising results. Silva, et. al. [100] used the wavelet transform in enhance ultrasonic signals taken from an Aluminum panel to detection corrosion on the surface. Wavelet analysis was used to determine the wave speed which is affected by corrosion in the material. Su and Ye [101, 102] used characteristics of the wavelet transform of the transient response of a composite plate in a neural network algorithm to determine the location of a hole in a composite plate. The neural network was trained based on a set of transient data and the neural network approach was applied to experimental cases. The empirical mode decomposition [103] is a transient technique which attempts to alleviate some of the limitations that a wavelet analysis has. A major limitation of wavelet signal processing is the isolation of specific frequency components at each point in time. The empirical mode decomposition method, by providing a precise definition of frequency, is able to overcome this hurdle. Quek, et. al. [104] compares

the results obtained from the wavelet analysis in a previous paper with results from an empirical mode decomposition. The empirical mode decomposition was shown to provide a more direct method of extracting information needed for damage detection purposes. Salvino and Pines [105] showed the ability of the empirical mode decomposition to extract phase information from transient signals and use the results to infer damage in a structure.

AU Motivated Damage Detection for Simple Structures

Though not strictly labeled as Acousto-Ultrasonic, damage detection activities which focus on wave propagation methods fit under the same heading. Much work in damage detection for simple structures has been explored using wave propagation methods. Discrete structures exhibit wave propagation properties which have been used for damage detection. Pines [106] showed sensitivity of the wave propagation parameters of a discrete structure to changes in the properties of a unit cell. The response of the discrete structure when boundary conditions are eliminated show a greater sensitivity to damage [107]. Ma [108] extended Pines' work on extracting the dereverberant response of a discrete structure for damage detection purposes. The methodology was shown to work experimentally for a model of a three story building structure. Damage detection in beams and rods using wave propagation methods at lower frequencies include work by Doyle [109, 110, 111] and Lakshmanan [112, 113, 114], amongst others.

1.6 Present Study

An Acousto-Ultrasonic approach with in-situ transduction has shown promise as a component of SHM/CBM programs for aerospace structures. This thesis intends to improve on the current state of the art for purposes of wide area damage detection of plate structures.

For isotropic structures, the AU approach is based on well known wave propagation properties of plates and has shown a sensitivity to incipient damage. Various

approaches have been taken to tackle the problem of damage location and sizing at arbitrary locations. Most of these approaches use transducers which are distributed over the structure [115, 116, 101, 102]. An optimization type of algorithm is used to locate a defect on the structure from the captured transient data. The main difficulty with this type of approach is the necessity for a wide distribution of transducers on the plate.

This work shows the the use of a sensor array and the associated signal processing as an effective tool for locating damage in a two dimensional structure without instrumenting the whole plate with transducers. The responses from the each element of the sensor array can be summed such that the array senses in a particular direction for damage. The size of damage which may be detected depends on the mode and frequency region of the interrogating signal on the plate. A sizing study is presented to examine the ability of a interrogating signal to sense different damage sizes on an Aluminum plate.

For composite structures, knowledge of the wave propagation properties is important for any wave propagation type of approach, whether it is ultrasonics or acoustic emission or Acousto-Ultrasonics. A finite element model designed specifically to find the wave propagation properties for a composite laminates is developed. These results are compared with experimental results for composite laminates. This information is used for processing of sensor array data for detecting delamination damage in composite laminate. Experimental results show the presence of a delamination using sensor array signal processing.

A comparison between the AU approach and a modal approach is shown for damage detection in a beam. The modal response as well as transient simulation is found using a FE model of the structure. The modal information is used in the various modal damage detection schemes and the transient response is used in the AU approach.

1.7 Organization of Dissertation

This dissertation shows the development of a damage detection scheme using Lamb waves along with sensor arrays to locate damage in a plate structure. A discussion of wave propagation mechanics is presented in Chapter 2 followed by a development of wave propagation models of plate structures. Excitation and sensing of structural waves in using piezoelectric materials is explored at the end of Chapter 2. The introduction of sensor arrays and the signal processing associated is presented in Chapter 3. Various limiting issues in the signal processing using sensor arrays are discussed. The combination of the two areas, wave propagation and sensor arrays, for damage detection purposes in an isotropic plate is shown in Chapter 4. Experimental results show the ability of wide array damage detection using a sensor array to located small damage in plate structures. A sizing study is shown where the properties of the interrogating signal plays an important role in determining sensitivity to the size of damage. The extension of the sensor array toward composites plates is shown in Chapter 5. The wave propagation properties of a composite laminate is modeled and compared to experimental results provided by the sensor array. The filtering capabilities of the sensor array is used in a damage detection application for a composite laminate with an embedded delamination. A sample comparison between common established modal methods for damage detection and wave propagation damage detection is shown in Chapter 6. The different schemes aim to locate and quantify small damage on a beam with transverse vibration. Concluding thoughts, including contributions and limitations of the current work and possible future directions for research are highlighted in Chapter 7.

Chapter 2

Wave Propagation in Thin Plates

2.1 Introduction

Typically, structural dynamics of thin plates is expressed in terms of modal dynamics. Natural frequencies and corresponding modeshapes make up the dynamic response of the structure. The most widely used formulation to determine natural frequencies and modeshapes is the finite element method where the structure is discretized into elements in which the potential and kinetic energies are formulated. Using variational mechanics, the variation of the difference between the kinetic and potential energies give rise to a second order differential equation which describes the structure's dynamics, $\mathbf{M}\ddot{\mathbf{x}} + \mathbf{K}\mathbf{x} = \mathbf{0}$. Where $\mathbf{M}$ and $\mathbf{K}$ are the mass and stiffness matrices and $\mathbf{x}$ is the vector of nodal degrees of freedom. When the structure is assumed to vibrate harmonically, the governing equation becomes an eigenvalue problem, $\left(-\mathbf{M}\omega_n^2 + \mathbf{K}\right)\mathbf{x}_n = \mathbf{0}$, where ω_n is the nth natural frequency of vibration and the corresponding eigenvector, $\mathbf{x}_n$, is the modeshape associated with the nth natural frequency.

For the lower order modes, few elements are needed to accurately model the behavior of the structure. As the number of modes increase, more elements are required to predict the dynamic behavior of the plate. For plate structures, the modeshapes of the plate appear wavelike at higher frequencies. A more appropriate method for understanding the dynamics of the plate at higher frequencies needs to be investigated. This is accomplished by examining wave mechanics and its application to structural vibrations in plates.

2.2 Wave Mechanics

Wave propagation in a medium involves oscillations in time as well as in space. The relationship between wavenumber, k, and the temporal frequency, ω, plays a critical role in wave propagation studies. The wavenumber is the spatial frequency of a wave in a medium. There is a direct analogy between frequency/time quantities and wavenumber/space quantities:

$$\omega \Longleftrightarrow t$$

$$k \Longleftrightarrow x$$

The wavelength of a given wave is found from the corresponding wavenumber:

$$\lambda = \frac{2\pi}{k} \tag{2.1}$$

Dynamics in a medium can be described in terms of wave propagation whether the vibrations are transient or steady state. There is generally a one-to-one correspondence between the temporal frequency, ω, which a wave vibrates and the corresponding spatial frequency, k. An example is shown in Figure 2.1.

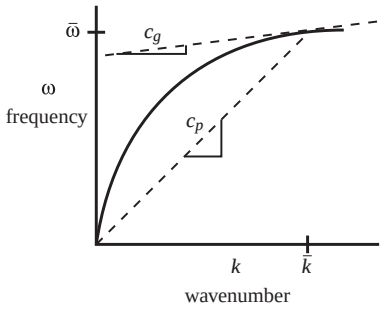

Figure 2.1: Wavenumber-frequency relationship and related parameters

The general form of wave propagation in one direction can be described by a complex exponential, $e^{i(-kx+\omega t)}$, where the phase angle is found from the complex term:

$$\alpha = \angle e^{i(-kx+\omega t)} = -kx + \omega t \tag{2.2}$$

The phase velocity of a wave is found by determining the condition such that the phase angle remains constant:

$$\alpha = -kx_1 + \omega t = -k\left(x + \Delta x\right) + \omega\left(t + \Delta t\right) \tag{2.3}$$

which results in the relation $c_p = \Delta x/\Delta t = \omega/k$. As the wave propagates through the x and t domains, the points on the waveform which correspond to a specific phase angle propagate with velocity, c_p. Alternately, if the propagating wave were described by $e^{i(kx+\omega t)}$, the phase velocity would be $c_p = -\omega/k$. The phase speed is independent of the sign of the wavenumber:

$$c_p = \frac{\omega}{k} \tag{2.4}$$

This is the ratio of the frequency to the wavenumber, seen in Figure 2.1. A negative wavenumber corresponds to a wave traveling in the positive x direction and a positive wavenumber corresponds to wave traveling in the negative x direction. The magnitude of the wavenumber describes the physical characteristics of the wave while the sign of the wavenumber indicates the direction of travel.

Transient dynamics in a medium are initiated using a a transient excitation signal. Take, for example, the sample transient signal in Figure 2.2(a) where the time series is constructed of 5 cycles at 10 kHz. The corresponding frequency components of the transient is presented in Figure 2.2(b). The frequency domain function can be found using a Fourier transform:

$$F\left(\omega\right) = \int f(t)e^{-i\omega t}dt \tag{2.5}$$

The frequency components of the signal includes frequencies other than 10 kHz. This is generally true for any transient signal. As the number of cycles are increased, the width of the peak in Figure 2.2(b) gets narrower. Any transient signal can be decomposed into its frequency components and when the structure is excited using the transient, these frequency components are individually present in the structure. The magnitude of phase angle of these frequency components may vary. The general expression for a transient based on its frequency content is found through the inverse

Fourier transform:

$$f(t) = \frac{1}{2\pi} \int F(\omega) e^{i\omega t} d\omega \tag{2.6}$$

where $f(t)$ is the excitation waveform and $F(\omega)$ the frequency spectrum that makes up the transient. The response at any point in the medium then is constructed by adding each of the frequency components and introducing the wavenumber corresponding to the frequency of excitation:

$$w(x,t) = \int B(\omega) e^{i(k(\omega)x + \omega t)} d\omega \tag{2.7}$$

where $B(\omega)$ depends on $F(\omega)$ and the mechanics of the system. For every frequency component, ω_n, that is used to construct the excitation, the corresponding wavenumber, $k(\omega_n)$, is present to propagate the excitation through the structure.

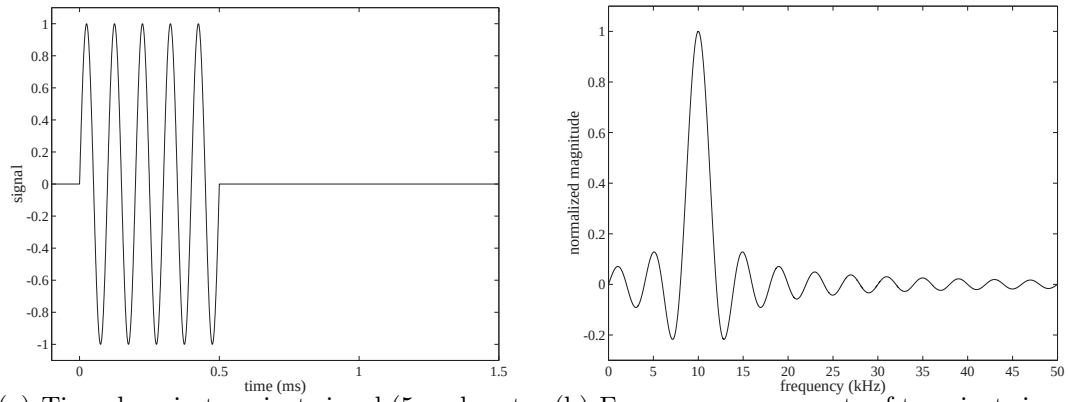

(a) Time domain transient signal (5 cycles at 10 kHz)

(b) Frequency components of transient signal

Figure 2.2: Transient signal and frequency makeup

If the wavenumber-frequency relationship is linear, then the phase speed of a wave in the medium is constant. Regardless of x in Equation (2.7), the overall shape of the transient does not change as it propagates through the structure. The shape of the transient in Figure 2.2(a) would be the same as the pulse moves through the structure. This is seen in mediums where the governing partial differential equation of the dynamics is described using only second order derivatives in space and time. This phenomenon is observed in acoustics where a pulse is the same regardless of

the distance from the source that was traveled. These types of waves are called non-dispersive waves.

There are instances when the wavenumber-frequency relationship is not linear. This type of behavior occurs in systems where the governing partial differential equation contains higher order spatial derivatives than the second order derivatives seen for non-dispersive systems. In this case, the phase speed of a wave depends on the frequency of excitation. A transient signal made up of a group of frequencies will not maintain its shape because each of the frequency components in the signal travel at differing speeds. The phase angle of each component in Equation (2.7) shift relative to each other as the transient moves along x. Waves of this type are described as dispersive because the transient wave form does not maintain its shape. Plate dynamics exhibit dispersive behavior and is further illustrated in the following sections.

For the tone burst signal in Figure 2.2, only a narrow band of frequencies are present. The group of waves corresponding to this narrow band of frequencies will propagate through the structure with an overall group speed which may be different than the phase speed mentioned earlier. For the simple case where a small band of frequencies are present, the integral in Equation (2.7) has limits:

$$w(x,t) = \int_{\bar{\omega}-\Delta\omega/2}^{\bar{\omega}+\Delta\omega/2} e^{i(-k(\omega)x+\omega t)} d\omega \tag{2.8}$$

$\bar{\omega}$ is the center frequency with a bandwidth of $\Delta\omega$. A Taylor series expansion of the wavenumber-frequency relationship around $\bar{\omega}$ is used as an approximation:

$$k(\omega) \approx k(\bar{\omega}) + \frac{\partial k}{\partial \omega}(\bar{\omega})(\omega - \bar{\omega}) \tag{2.9}$$

This approximation is used in the original integral:

$$w(x,t) = \int_{\bar{\omega}-\Delta\omega/2}^{\bar{\omega}+\Delta\omega/2} e^{i\left(-\left(k(\bar{\omega})+\frac{\partial k}{\partial \omega}(\bar{\omega})(\omega-\bar{\omega})\right)x+\omega t\right)} d\omega \tag{2.10}$$

By using a change of coordinates, $\omega_l = \omega - \bar{\omega}$, the integral can be centered around $\bar{\omega}$ to simplify the expression:

$$w(x,t) = e^{i(-k(\bar{\omega})x+\bar{\omega}t)} \int_{-\Delta\omega/2}^{\Delta\omega/2} e^{i\omega_l\left(-\frac{\partial k}{\partial \omega}(\bar{\omega})x+t\right)} d\omega_l \tag{2.11}$$

There is a closed form solution to the integral:

$$w(x,t) = e^{i(-k(\bar{\omega})x+\bar{\omega}t)}\Delta\omega\frac{\sin\left(\left(-\frac{\partial k}{\partial\omega}(\bar{\omega})\,x+t\right)\Delta\omega/2\right)}{\left(-\frac{\partial k}{\partial\omega}(\bar{\omega})\,x+t\right)\Delta\omega/2} \tag{2.12}$$

The above expression describes the wave propagation behavior of a group of waves composed of a narrow band of frequencies with a bandwidth of $\Delta\omega$ and a center frequency of $\bar{\omega}$. The first term is the carrier wave, $e^{i(-k(\bar{\omega})x+\bar{\omega}t)}$, which has a frequency of $\bar{\omega}$ and the corresponding wavenumber, $k(\bar{\omega})$. The second term describes the group wave and its modulation of the carrier wave. The details of this expression depends on the magnitude of each frequency present in the signal. In the development in Equation (2.12), a simplification was made where the frequency content was uniform throughout the bandwidth. The behavior of the group wave term is essentially the same regardless of the distribution over the bandwidth. A velocity of propagation of the group wave can be determined by examining the phase angle in the same way as the phase speed presented previously:

$$\left(-\frac{\partial k}{\partial\omega}(\bar{\omega})\,x+t\right)\frac{\Delta\omega}{2} = \left(-\frac{\partial k}{\partial\omega}(\bar{\omega})\,(x+\Delta x)+(t+\Delta t)\right)\frac{\Delta\omega}{2} \tag{2.13}$$

Defining $c_g = \Delta x/\Delta t$ yields a relationship between group speed and the wavenumber-frequency curve:

$$c_g = \frac{\partial\omega}{\partial k}(\bar{\omega}) \tag{2.14}$$

For a group wave composed of a packet of frequencies centered around $\bar{\omega}$. The group speed is the local slope of the frequency-wavenumber relationship, as is shown in Figure 2.1. Note that if the wavenumber-frequency relationship is linear, then the group speed is constant and is the same as the phase speed. If the wavenumber-frequency relation is non-linear, the dynamics are dispersive and the group speed is dependent on the frequency of interest.

Figure 2.3 shows an example of non-dispersive and dispersive behavior using Equation (2.12). In this case, $\bar{\omega}$=5 Hz, $\Delta\omega$=2.5 Hz and c_p = 1 m/s. For the non-dispersive case, the waveform propagates with the phase speed and the shape of the waveform does not change as the wave moves through the different x locations. For the dispersive case, the transient moves at the group speed (c_g) of 1.5 m/s and the

form of the wave changes shape as it propagates through the different x locations. The frequency content of both sets of waveforms are the same but dispersion causes the waveform to shift.

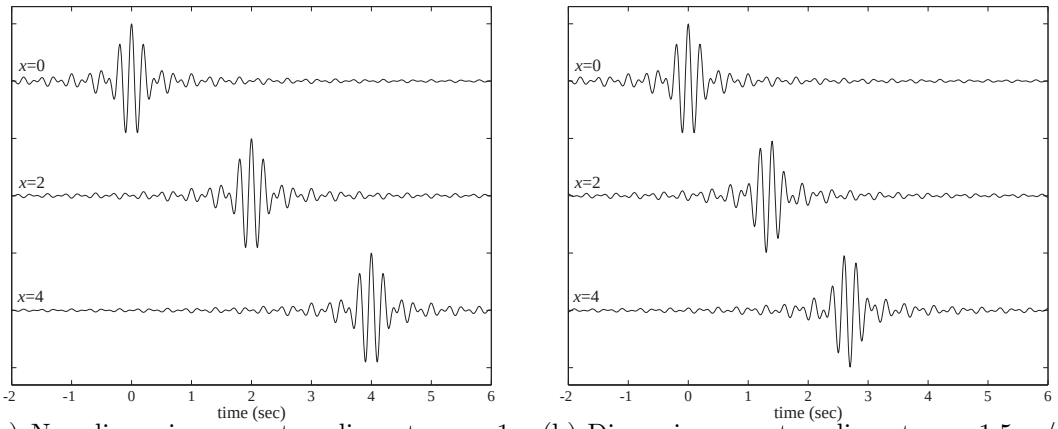

(a) Non-dispersive wave traveling at $c_p = 1$ m/s (b) Dispersive wave traveling at $c_g = 1.5$ m/s

Figure 2.3: Transient signal and frequency makeup

The properties of waves in a medium depend highly on the wavenumber frequency relations. Not only does the wavenumber describe the spatial distribution of the wave of a given frequency, but the speed of wave propagation is dependent on this relation as well. The speed of propagation of a single frequency (c_p) is ω/k and the group speed (c_g) of a packet of waves is $\partial\omega/\partial k$.

2.3 Plate Dynamics - 1st Order Theory

2.3.1 Transverse Vibrations

The governing dynamics for an isotropic thin plate is developed in Appendix C.1. For the plate shown in Figure 2.4, the governing differential equation for the transverse dynamics is used as a starting point:

$$\frac{Et_p^3}{12\left(1-\nu^2\right)}\left(\frac{\partial^2}{\partial x^2}+\frac{\partial^2}{\partial y^2}\right)^2 w+\rho t_p\frac{\partial^2 w}{\partial t^2}=0 \tag{2.15}$$

$D = \frac{Et_p^3}{12(1-\nu^2)}$ is the plate rigidity and ρt_p is the mass per area of the plate. An important assumption in the development of the governing equation of motion is

that there is no shear deformation in the $x-z$ and $y-z$ planes:

$$\gamma_{xz} = \frac{\partial u}{\partial z} + \frac{\partial w}{\partial x} = 0 \quad \text{and} \quad \gamma_{yz} = \frac{\partial v}{\partial z} + \frac{\partial w}{\partial y} = 0 \tag{2.16}$$

As a result, the displacement in the longitudinal directions are then coupled with the transverse displacements. The in-plane displacements, u and v, vary linearly with the thickness and are dependent on the transverse displacement:

$$u = -z\,\partial w/\partial x \quad \text{and} \quad v = -z\,\partial w/\partial y \tag{2.17}$$

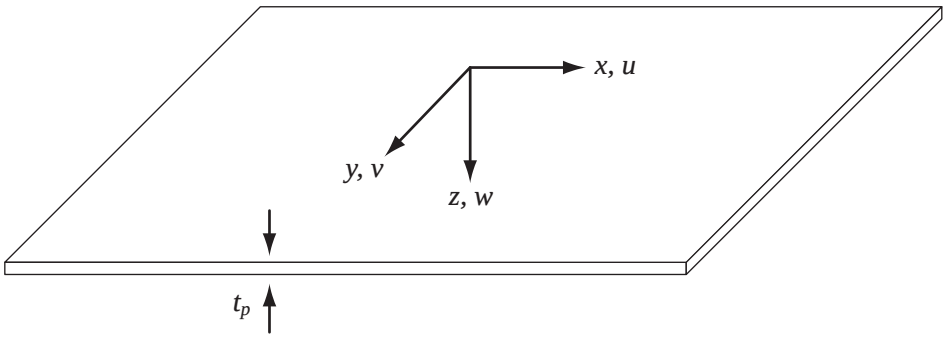

Figure 2.4: Plate coordinate system

A displacement field of the form $w(x,y,t) = w_0 e^{i(\omega t - kx)}$ describes a plane wave traveling in the x direction. The plane wave vibrates in time with frequency ω and wavenumber, or spatial frequency, k. The governing differential equation is written in a simplified form:

$$\left(k^4 D - \omega^2 \rho t_p\right) w_0 = 0 \tag{2.18}$$

Solving for the wavenumber results in four roots which describe the fundamental wave propagation properties of the plate:

$$k = \pm\sqrt{\omega}\sqrt[4]{\frac{\rho t_p}{D}} \text{ and } \pm i\sqrt{\omega}\sqrt[4]{\frac{\rho t_p}{D}} \tag{2.19}$$

The two real roots correspond to plane waves propagating in opposite directions along the x-axis while the imaginary roots correspond to evanescent, or near field,

terms which die out spatially. If the plane wave was assumed to propagate in the y direction, the same roots would appear as only a change in coordinates is involved. Since the plate is assumed to be isotropic, waves traveling in any direction would have the same wave propagation properties.

The wavenumber-frequency relationship describes the wavenumber of a propagating wave for a given temporal frequency:

$$k = \sqrt{\omega}\sqrt[4]{\frac{\rho t_p}{D}} \tag{2.20}$$

The wavelength of a wave of a given wavenumber is $\lambda = 2\pi/k$. The phase speed, c_p, of a wave in the thin plate is function of the plate rigidity and mass per unit area:

$$c_p = \frac{\omega}{k} = \sqrt{\omega}\sqrt[4]{\frac{D}{\rho t_p}} \tag{2.21}$$

The phase speed of a wave at a given frequency increases as the rigidity of the plate increases. The group speed for a packet of waves traveling in a thin plate is non-linear:

$$c_g = \frac{d\omega}{dk} = 2\sqrt{\omega}\sqrt[4]{\frac{D}{\rho t_p}} \tag{2.22}$$

In radial coordinates, the governing differential equation in Equation (2.15) is slightly altered:

$$D\left(\frac{\partial^2}{\partial r^2} + \frac{1}{r}\frac{\partial}{\partial r} + \frac{1}{r^2}\frac{\partial^2}{\partial \theta^2}\right)^2 w + \rho t_p \frac{\partial^2 w}{\partial t^2} = 0 \tag{2.23}$$

If the displacement field is assumed to be axisymmetric, the derivatives with respect to θ are eliminated. Assuming $w = w_0 e^{-i\omega t}$ yields set of differential equations:

$$\left(\frac{\partial^2}{\partial r^2} + \frac{1}{r}\frac{\partial}{\partial r} + \omega\sqrt{\frac{\rho t_p}{D}}\right)\left(\frac{\partial^2}{\partial r^2} + \frac{1}{r}\frac{\partial}{\partial r} - \omega\sqrt{\frac{\rho t_p}{D}}\right) w_0 = 0 \tag{2.24}$$

There are two sets of second order differential equations which are solved using Bessel functions:

$$\begin{aligned}
&\left(\frac{\partial^2}{\partial r^2} + \frac{1}{r}\frac{\partial}{\partial r} + \omega\sqrt{\frac{\rho t_p}{D}}\right) w_0 = 0 \quad \text{yields} \quad w_0 = c_1 H_0^{(1)}(\beta r) + c_2 H_0^{(2)}(\beta r) \\
&\left(\frac{\partial^2}{\partial r^2} + \frac{1}{r}\frac{\partial}{\partial r} - \omega\sqrt{\frac{\rho t_p}{D}}\right) w_0 = 0 \quad \text{yields} \quad w_0 = c_3 I_0(\beta r) + c_4 K_0(\beta r)
\end{aligned} \tag{2.25}$$

where $\beta = \sqrt{\omega}\sqrt[4]{\rho t_p / D}$. The $H_0^{(1)}$ and $H_0^{(2)}$ solutions are made up of Bessel functions of the first and second kind, J_0 and Y_0, and are oscillatory. The I_0 and K_0 solutions are modified Bessel functions of the first and second kind and act like exponentially decaying functions. The solutions act the same way as the solutions for the plane wave solution in rectangular coordinates. For large arguments, βr, the solutions take on limiting forms:

$$H_0^{(1)}(\beta r) = \sqrt{\frac{2}{\pi\beta r}} e^{i(\beta r - \pi/4)} \quad \text{and} \quad H_0^{(2)}(\beta r) = \sqrt{\frac{2}{\pi\beta r}} e^{-i(\beta r - \pi/4)}$$
$$I_0(\beta r) = \frac{1}{\sqrt{2\pi\beta r}} e^{(\beta r)} \quad \text{and} \quad K_0(\beta r) = \frac{\pi}{\sqrt{2\beta r}} e^{-(\beta r)} \tag{2.26}$$

The exponentially decaying terms, I_0 and K_0, are the evanescent terms from the plane wave solutions seen earlier. The wavelike terms, $H_0^{(1)}$ and $H_0^{(2)}$, are the propagating wave solutions except, in this case, the magnitude of the waves decrease as the waves move outward in radial direction. The wavenumber-frequency relationship is the same for the plane wave case and the radial case.

When a point source is used to excite the structure, the transient response of the plate is composed of these Bessel solutions. The behavior of the Bessel solutions is very similar to the exponentials that were observed to describe the behavior of a plane wave.

2.3.2 In-Plane Vibrations

The governing equations for in-plane vibration, derived in Appendix C.2, for a thin plate are coupled:

$$\frac{Et_p}{1-\nu^2}\left(\frac{\partial^2 u}{\partial x^2} + \nu\frac{\partial^2 v}{\partial x \partial y} + \frac{1-\nu}{2}\left(\frac{\partial^2 u}{\partial y^2} + \frac{\partial^2 v}{\partial x \partial y}\right)\right) - \rho t_p \frac{\partial^2 u}{\partial t^2} = 0$$
$$\frac{Et_p}{1-\nu^2}\left(\frac{\partial^2 v}{\partial y^2} + \nu\frac{\partial^2 u}{\partial x \partial y} + \frac{1-\nu}{2}\left(\frac{\partial^2 v}{\partial x^2} + \frac{\partial^2 u}{\partial x \partial y}\right)\right) - \rho t_p \frac{\partial^2 v}{\partial t^2} = 0 \tag{2.27}$$

In this case, the in-plane displacements, u and v, are assumed to be constant through the thickness. By assuming a plane wave in the x direction of the form, $u = u_0 e^{i(\omega t - kx)}$ and $v(x, y) = 0$, the second expression in Equation (2.27) is eliminated and the first expression is reduced:

$$-\frac{Et_p}{1-\nu^2}k^2 + \omega^2 \rho t_p = 0 \tag{2.28}$$

Since the in-plane dynamics is expressed with a second order differential equation, there are only two roots for the wavenumber-frequency equation. Only propagating waves exist for the in-plane dynamics, unlike the transverse dynamics where evanescent terms are present. The wavenumber-frequency relationship for the in-plane dynamics is linear with the frequency of interest:

$$k = \pm\omega\sqrt{\frac{\rho}{E}}\sqrt{1-\nu^2} \tag{2.29}$$

The phase and group speeds are then equal to each other:

$$c_p = \frac{\omega}{k} = \sqrt{\frac{E}{\rho}}\frac{1}{\sqrt{1-\nu^2}} \quad \text{and} \quad c_g = \frac{\partial\omega}{\partial k} = \sqrt{\frac{E}{\rho}}\frac{1}{\sqrt{1-\nu^2}} \tag{2.30}$$

The in-plane dynamics are associated with the propagation of acoustic waves in solids.

The wavenumber-frequency relationship is nonlinear in the case of transverse vibration of a thin plate and linear in the case of in-plane vibrations. As a result, both the phase and group speeds are frequency dependent for transverse vibrations and constant for in-plane vibrations. Due to the assumption of no shear deformation, the displacement field through the thickness of the plate is prescribed. This causes the model of the thin plate to be stiffer than necessary and produces inaccurate results at higher frequencies. Lamb wave theory provides a more thorough description of the wave propagation dynamics.

2.4 Waves in Solid Medium

The wave propagation properties for thin plates from the previous section holds for cases where the wavelength of the wave is much larger than the thickness of the plate. As the frequency of interest increases and the wavelength decreases, the assumptions made for the thin plate theory do not hold. The thin plate theory assumes no shear deformation which allows the in-plane and transverse components to be coupled. A more general description of the wave propagation properties would necessarily take into account shear deformation.

The force balance equations, derived in Appendix A, for a solid body are used as a starting point:

$$\begin{aligned} \sigma_{xx,x} + \sigma_{xy,x} + \sigma_{xz,x} + f_x &= \rho\ddot{u} \\ \sigma_{yy,y} + \sigma_{yx,y} + \sigma_{yz,y} + f_x &= \rho\ddot{v} \\ \sigma_{zz,z} + \sigma_{xz,z} + \sigma_{yz,z} + f_z &= \rho\ddot{w} \end{aligned} \tag{2.31}$$

The (,)s in the subscripts refer to differentiation. The stress-strain relations, terms of Lamé's constants, are used:

$$\sigma_{lj} = \lambda\varepsilon_{kk}\delta_{lj} + 2\mu\varepsilon_{lj} \tag{2.32}$$

The mathematical definition of the strain-displacement relations are used:

$$\varepsilon_{lj} = \frac{1}{2}\left(u_{l,j} + u_{j,l}\right) \tag{2.33}$$

The stress-strain and strain-displacement relations are substituted into the force balance equation:

$$\left(\lambda + \mu\right) u_{l,jl} + \mu u_{j,ll} + f_j = \rho\ddot{u}_j \tag{2.34}$$

$$\left(\lambda + \mu\right) \nabla\left(\nabla \cdot \boldsymbol{u}\right) + \mu\left(\nabla \cdot \nabla\right)\boldsymbol{u} + \mathbf{f} = \ddot{\mathbf{u}} \tag{2.35}$$

The displacement vector, $\boldsymbol{u}$, is assumed to be a composed of the gradient of a scalar field, φ, and the curl of a vector field, $\mathbf{H}$:

$$\boldsymbol{u} = \nabla\varphi + \nabla \times \mathbf{H} \quad \text{such that} \quad \nabla \cdot \mathbf{H} = 0 \tag{2.36}$$

The scalar field, φ, is the dilatational, or volumetric expansion, component while the vector field, $\mathbf{H}$, is the distortional component. There is no change in volume associated with $\mathbf{H}$ because of the condition, $\nabla \cdot \mathbf{H} = 0$, and this ensures uniqueness of the solution. Removing the external forcing term, $\mathbf{f}$, and substituting the assumed displacement field into the governing equations of motions leaves a set of equations in φ and $\mathbf{H}$:

$$\left(\lambda + \mu\right) \nabla\left(\nabla^2\varphi\right) + \mu\nabla^2\left(\nabla\varphi\right) = \rho\nabla\ddot{\varphi} \tag{2.37}$$

$$\left(\lambda + \mu\right) \nabla\left(\nabla \cdot \left(\nabla \times \mathbf{H}\right)\right) + \mu\nabla^2\left(\nabla \times \mathbf{H}\right) = \rho\left(\nabla \times \ddot{\mathbf{H}}\right) \tag{2.38}$$

The equations of motion can be simplified:

$$\underset{\text{dilatation}}{(\lambda+2\mu)\,\nabla^2\varphi-\rho\ddot{\varphi}=0} \qquad \underset{\text{distortion}}{\mu\nabla^2\mathbf{H}-\rho\ddot{\mathbf{H}}=0} \tag{2.39}$$

For plane waves, the dilatation field is assumed to be of the form $\varphi = e^{i(k_l x-\omega t)}$ and the components of the distortional vector field are assumed to be of the form $H_x = 0$, $H_y = 0$, and $H_z = e^{i(k_t x-\omega t)}$. The wave propagation characteristics for the both the dilatational as well as distortional dynamics can be determined:

$$(\lambda+2\mu)\,k_l^2=\omega^2\rho \quad \text{and} \quad \mu\,k_t^2=\omega^2\rho \tag{2.40}$$

The wavenumber-frequency relationships for dilatational and distortional waves in an unbounded solid can be determined:

$$\underset{\text{dilatation}}{k_l=\omega\sqrt{\frac{\rho}{\lambda+2\mu}}} \qquad \text{and} \qquad \underset{\text{distortion}}{k_t=\omega\sqrt{\frac{\rho}{\mu}}} \tag{2.41}$$

The corresponding phase speed for these waves are found from the above expressions:

$$\underset{\text{dilatation}}{c_l=\sqrt{\frac{\lambda+2\mu}{\rho}}} \qquad \text{and} \qquad \underset{\text{distortion}}{c_t=\sqrt{\frac{\mu}{\rho}}} \tag{2.42}$$

In both of these cases, the wavenumber-frequency relationship is linear and the phase and group speeds are the same. A waveform associated with these waves do not change as the wave travels through the solid. The phase velocities of in-plane acoustic waves, c_l, and the distortional waves, c_t, for various materials are presented in Table 2.1. The acoustic waves, c_l, are much faster than the distortional waves, c_k.

2.5 Lamb Waves

In the previous section, two types of waves were shown to propagate in an unbounded medium. The forms of these waves change when the geometry of the medium

Material	E (GPa)	ν	ρ (kg/m^3)	c_l (km/s)	c_t (km/s)
Aluminum	70	.3	2700	6.45	3.10
Steel	210	.29	7850	5.92	3.22
Copper	110	.3	8960	4.06	2.17
Titanium	117	.32	4510	6.09	3.13

Table 2.1: Wave speeds for various materials

changes. For thin plates and shells, the top and bottom surfaces are considered to be traction free. The solutions of the differential equations in Equation (2.39) with traction free boundary conditions are known as Lamb waves [48, 49, 47].

A plane wave traveling in the x direction in Figure 2.4 is assumed where the components of φ and $\mathbf{H}$ corresponding to displacements in the y direction are eliminated. The corresponding displacement vector, $\boldsymbol{u}$, is composed of two parts:

$$\boldsymbol{u} = \begin{bmatrix} u \\ v \\ w \end{bmatrix} = \begin{bmatrix} \varphi_{,x} \\ 0 \\ \varphi_{,z} \end{bmatrix} + \begin{bmatrix} -\vartheta_{,z} \\ 0 \\ \vartheta_{,x} \end{bmatrix} \tag{2.43}$$

$\vartheta = H_y$ is the rotation about the y axis. This reduction in the displacement vector precludes the possibility of a plane wave which travels in the x direction and has displacement components in the horizontal direction, y. These types of waves are found when a more generalized problem is examined. Using the given displacement vector, $\boldsymbol{u}$, the governing relations are second order differential equations:

$$\varphi_{,xx} + \varphi_{,zz} + k_l^2 \varphi = 0 \quad \text{and} \quad \vartheta_{,xx} + \vartheta_{,zz} + k_t^2 \vartheta = 0 \tag{2.44}$$

The displacements are assumed to be a plane wave in the x direction:

$$\varphi = \bar{\varphi}(z)\, e^{ikx} \quad \text{and} \quad \vartheta = \bar{\vartheta}(z)\, e^{ikx} \tag{2.45}$$

The differential equations can be reduced:

$$\bar{\varphi}_{,zz} - \left(k^2 - k_l^2\right) \bar{\varphi} = 0 \quad \text{and} \quad \bar{\vartheta}_{,zz} - \left(k^2 - k_t^2\right) \bar{\vartheta} = 0 \tag{2.46}$$

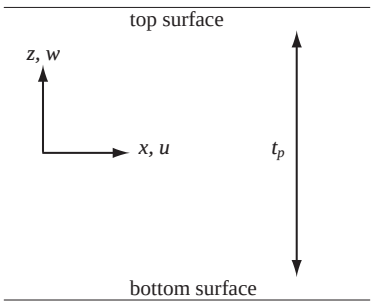

Figure 2.5: Lamb wave coordinate system

The assumption that the wave is traveling in the x direction may be generalized to a wave traveling in any direction on the x-y plane as long as the displacements lateral to that direction are eliminated. If that generalization is made, then the k^2 term in Equation (2.46) may be replaced by $k_x^2 + k_y^2$ where k_x and k_y are the components of the wavenumber vector projected on the x and y axes, respectively. The solutions to the differential equations in Equation (2.46) are hyperbolic cosine and hyperbolic sine functions:

$$\begin{aligned} \bar{\varphi} =& A_s \cosh\left(\left(\sqrt{k^2 - k_l^2}\right) z\right) + A_a \sinh\left(\left(\sqrt{k^2 - k_l^2}\right) z\right) \\ \bar{\vartheta} =& B_s \sinh\left(\left(\sqrt{k^2 - k_t^2}\right) z\right) + B_a \cosh\left(\left(\sqrt{k^2 - k_t^2}\right) z\right) \end{aligned} \tag{2.47}$$

The stresses on the top and bottom surfaces, $z = \pm t_p/2$, in Figure 2.5, provide boundary conditions to determine k, A_s, A_a, B_s, and B_a in Equation (2.47). The normal stress, σ_{zz}, and shear stress, σ_{xz}, are set to be nonexistent:

$$\sigma_{zz} = \lambda\left(\varepsilon_{xx} + \varepsilon_{yy} + \varepsilon_{zz}\right) + 2\mu\varepsilon_{zz} = 0 \quad \text{and} \quad \sigma_{xz} = 2\mu\varepsilon_{zx} = 0 \tag{2.48}$$

The boundary conditions can be expressed in terms of the φ and ϑ variables:

$$\begin{aligned} \lambda\left(\varphi_{,xx} + \varphi_{,zz}\right) + 2\mu\left(\varphi_{,zz} + \vartheta_{,xz}\right) &= 0 \\ \varphi_{,xz} - \vartheta_{,zz} + \varphi_{,xz} + \vartheta_{,xx} &= 0 \end{aligned} \tag{2.49}$$

By substituting the assumed solutions into the boundary conditions and evaluating at $z = t_p/2$ and $-t_p/2$, a set of four equations are generated with the four unknowns,

A_s, A_a, B_s, and B_a:

$$\begin{bmatrix} \left(2k^2-k_t^2\right)\cosh\left(\sqrt{k^2-k_l^2}\frac{t_p}{2}\right) & i2k\sqrt{k^2-k_t^2}\cosh\left(\sqrt{k^2-k_t^2}\frac{t_p}{2}\right) \\ i2k\sqrt{k^2-k_l^2}\sinh\left(\sqrt{k^2-k_l^2}\frac{t_p}{2}\right) & -\left(2k^2-k_t^2\right)\sinh\left(\sqrt{k^2-k_t^2}\frac{t_p}{2}\right) \\ \left(2k^2-k_t^2\right)\cosh\left(\sqrt{k^2-k_l^2}\frac{t_p}{2}\right) & i2k\sqrt{k^2-k_t^2}\cosh\left(\sqrt{k^2-k_t^2}\frac{t_p}{2}\right) \\ -i2k\sqrt{k^2-k_l^2}\sinh\left(\sqrt{k^2-k_l^2}\frac{t_p}{2}\right) & \left(2k^2-k_t^2\right)\sinh\left(\sqrt{k^2-k_t^2}\frac{t_p}{2}\right) \end{bmatrix}$$

$$\begin{bmatrix} \left(2k^2-k_t^2\right)\sinh\left(\sqrt{k^2-k_l^2}\frac{t_p}{2}\right) & i2k\sqrt{k^2-k_t^2}\sinh\left(\sqrt{k^2-k_t^2}\frac{t_p}{2}\right) \\ i2k\sqrt{k^2-k_l^2}\cosh\left(\sqrt{k^2-k_l^2}\frac{t_p}{2}\right) & -\left(2k^2-k_t^2\right)\cosh\left(\sqrt{k^2-k_t^2}\frac{t_p}{2}\right) \\ -\left(2k^2-k_t^2\right)\sinh\left(\sqrt{k^2-k_l^2}\frac{t_p}{2}\right) & -i2k\sqrt{k^2-k_t^2}\sinh\left(\sqrt{k^2-k_t^2}\frac{t_p}{2}\right) \\ i2k\sqrt{k^2-k_l^2}\cosh\left(\sqrt{k^2-k_l^2}\frac{t_p}{2}\right) & -\left(2k^2-k_t^2\right)\cosh\left(\sqrt{k^2-k_t^2}\frac{t_p}{2}\right) \end{bmatrix} \begin{bmatrix} A_s \\ B_s \\ A_a \\ B_a \end{bmatrix} = \begin{bmatrix} 0 \\ 0 \\ 0 \\ 0 \end{bmatrix} \quad (2.50)$$

The 4×4 matrix in Equation (2.50) can be rearranged into a block diagonal matrix which separates the symmetric components from the asymmetric components resulting in two reduced eigenvalue problems:

$$\begin{bmatrix} \left(2k^2-k_t^2\right)\cosh\left(\sqrt{k^2-k_l^2}\frac{t_p}{2}\right) & i2k\sqrt{k^2-k_t^2}\cosh\left(\sqrt{k^2-k_t^2}\frac{t_p}{2}\right) \\ i2k\sqrt{k^2-k_l^2}\sinh\left(\sqrt{k^2-k_l^2}\frac{t_p}{2}\right) & -\left(2k^2-k_t^2\right)\sinh\left(\sqrt{k^2-k_t^2}\frac{t_p}{2}\right) \end{bmatrix} \begin{bmatrix} A_s \\ B_s \end{bmatrix} = \begin{bmatrix} 0 \\ 0 \end{bmatrix}$$

$$\begin{bmatrix} \left(2k^2-k_t^2\right)\sinh\left(\sqrt{k^2-k_l^2}\frac{t_p}{2}\right) & i2k\sqrt{k^2-k_t^2}\sinh\left(\sqrt{k^2-k_t^2}\frac{t_p}{2}\right) \\ i2k\sqrt{k^2-k_l^2}\cosh\left(\sqrt{k^2-k_l^2}\frac{t_p}{2}\right) & -\left(2k^2-k_t^2\right)\cosh\left(\sqrt{k^2-k_t^2}\frac{t_p}{2}\right) \end{bmatrix} \begin{bmatrix} A_a \\ B_a \end{bmatrix} = \begin{bmatrix} 0 \\ 0 \end{bmatrix} \quad (2.51)$$

There is a characteristic equation for the symmetric mode case:

$$\left(2k^2-k_t^2\right)^2\cosh\left(\sqrt{k^2-k_l^2}\frac{t_p}{2}\right)\sinh\left(\sqrt{k^2-k_t^2}\frac{t_p}{2}\right) - 4k^2\sqrt{k^2-k_l^2}\sqrt{k^2-k_t^2}\cosh\left(\sqrt{k^2-k_t^2}\frac{t_p}{2}\right)\sinh\left(\sqrt{k^2-k_l^2}\frac{t_p}{2}\right) = 0 \quad (2.52)$$

There is a characteristic equation for the asymmetric mode case:

$$\left(2k^2-k_t^2\right)^2\cosh\left(\sqrt{k^2-k_t^2}\frac{t_p}{2}\right)\sinh\left(\sqrt{k^2-k_l^2}\frac{t_p}{2}\right) - 4k^2\sqrt{k^2-k_l^2}\sqrt{k^2-k_t^2}\cosh\left(\sqrt{k^2-k_l^2}\frac{t_p}{2}\right)\sinh\left(\sqrt{k^2-k_t^2}\frac{t_p}{2}\right) = 0 \quad (2.53)$$

Embedded in the k_l and k_t terms in Equations (2.52) and (2.53) is the frequency of interest, ω. For a given frequency, the two equations can be solved for k corresponding to the wavenumber for the symmetric and asymmetric modes. The symmetric modes are the in-plane modes and the asymmetric modes are the out-of-plane, or

transverse, modes. At low frequencies, only two real modes exist, the A0 and S0 modes. As the frequency of interest increases, additional modes of each type appear. From the matrix relations in Equation (2.51), the A and B terms for each type of mode can be found and from these terms, the displacement field is determined.

Figure 2.6 shows the wavenumber-frequency relationship for Aluminum. In general, isotropic materials will exhibit the same trends. The A0 and S0 modes are the fundamental modes and only ones present at low frequencies. The A1, S1, A2, and S2 modes are higher order modes that exist at higher frequencies. The solutions to the equations produce an infinite number of higher modes but only the first three for each symmetry case are shown. Figure 2.7 shows the phase velocity, c_p, for these different modes. The phase velocity of the S0 mode is constant at the lower wavenumbers/frequencies and is faster than the distortional wave speed, c_t. The phase velocity of A0 mode is dependent on wavenumber/frequency, increasing with wavenumber/frequency and asymptotically approaching c_t. Figure 2.8 shows the group velocity. The relationship between wavenumber and frequency and the corresponding phase and group speeds make up the dispersion relations for the thin plate.

The shape of the displacement field at low frequencies is shown in Figures 2.9 and 2.10 for the S0 and A0 mode, respectively. As wavenumber/frequency increases, the displacement fields change. Figures 2.11 and 2.12 shows the change in the displacement field of the fundamental modes as the wavenumber increases. Figure 2.13 shows the displacement field for the higher order modes for both the symmetric and asymmetric cases.

Lamb wave modes are the solutions to the governing equations for motion in a plate structure. There is a restriction on the shear deformation that was presented for the simple approximation. Figure 2.14 shows the wavenumber-frequency relationship for the two fundamental modes of the Lamb wave theory and the 1st order approximations shown previously. The simple approximations match the full solutions relatively well for the lower wavenumber/frequency region; however, as the frequency of interest increases, the wavenumber which is predicted by the sim-

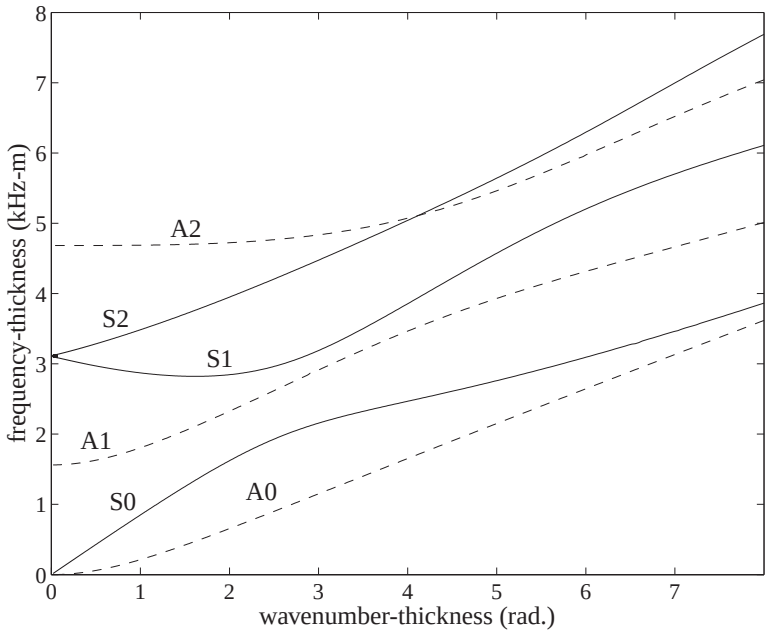

Figure 2.6: Wavenumber-frequency relationship for Aluminum

ple approximations veers from for the Lamb theory. The simple approximations under-predict the wavenumber because they do not allow shear deformations.

2.6 Finite Element Model for Wave Propagation

The solution for the Lamb modes can also be found using a finite element formulation. A common approach is to build a complex model of the plate with elements along all three directions. If plane strain assumptions are used, the model could be reduced to a discretization in two directions. Using a time domain numerical integration scheme, the transient response of a plate could be found through which the wave propagation properties could be ascertained. There is a more direct method of finding the wavenumber-frequency relationship using a specialized finite element scheme [74].

In this case, the assumed displacement is prescribed as a plane wave in the same way as previous sections. The plate is discretized through the thickness only which allows for a relatively few number of elements to be used. A form of the

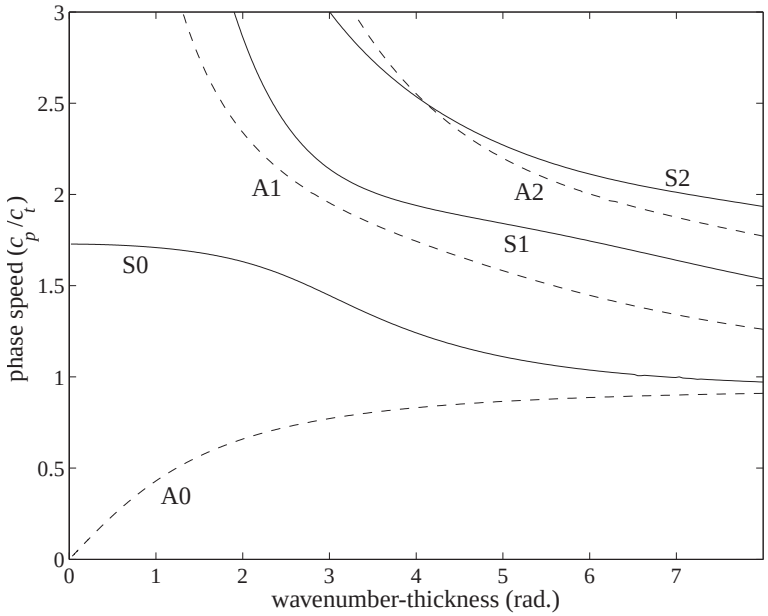

Figure 2.7: Normalized phase velocity (Aluminum)

kinetic and potential energies is found based on the assumed complex displacement field. The kinetic energy is a function of the temporal frequency and the potential energy is a function of the wavenumber of a plane wave. The final problem reduces to an eigenvalue relationship. Along with predicting the dispersion relations for an isotropic plate, the wavenumber-frequency relationship for the equivalent Lamb modes in a built-up structure, such as a composite laminate, can be found by using this finite element model.

The common expressions for strain and kinetic energies in a solid, U and T respectively, are used:

$$U = \int_V \frac{1}{2}\, \boldsymbol{\varepsilon}^T \mathbf{E}\, \boldsymbol{\varepsilon}\, dV \quad \text{and} \quad T = \int_V \frac{1}{2}\, \rho\, \dot{\boldsymbol{u}}^T \dot{\boldsymbol{u}}\, dV \tag{2.54}$$

where $\boldsymbol{\varepsilon}$ is the strain, $\mathbf{E}$ is the material elasticity, $\boldsymbol{u}$ is the displacement, and ρ is the material density. By assuming a plane wave propagating in the x direction, plane strain conditions are applied. A reduced set of strain and displacement components are used:

$$\boldsymbol{\varepsilon} = [\varepsilon_{xx} \quad \varepsilon_{zz} \quad \gamma_{xz}]^T \quad \text{and} \quad \boldsymbol{u} = [u \quad w]^T \tag{2.55}$$

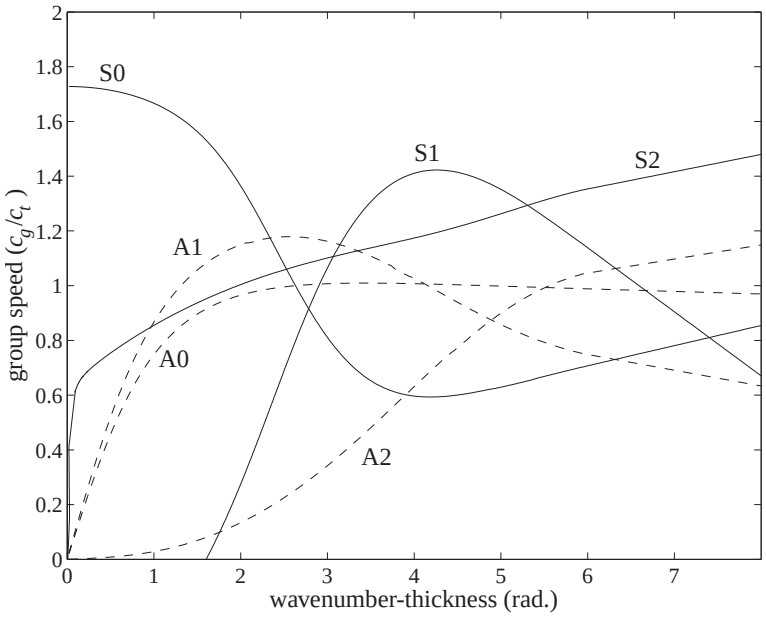

Figure 2.8: Normalized group velocity (Aluminum)

The common expressions strain-displacement relationship are used:

$$\begin{bmatrix} \varepsilon_{xx} \\ \varepsilon_{zz} \\ \gamma_{xz} \end{bmatrix} = \begin{bmatrix} \frac{\partial u}{\partial x} \\ \frac{\partial w}{\partial z} \\ \frac{\partial u}{\partial z} + \frac{\partial w}{\partial x} \end{bmatrix} \tag{2.56}$$

A complex displacement field in the material is assumed. This represents the same plane wave behavior, where k is the wavenumber and ω is the frequency. as used in previous sections:

$$\boldsymbol{u}\,(x,z,t) = \mathbf{u}e^{i(kx-\omega t)} \quad \text{where} \quad \mathbf{u} = \begin{bmatrix} \mathsf{u} \\ \mathsf{w} \end{bmatrix} \tag{2.57}$$

This assumption states that the material is vibrating both in time with a temporal frequency of ω and along the x-axis, with a wavenumber, or spatial frequency, of k. The components of the $\mathbf{u}$ vector are the in-plane and vertical displacements at a cross-section and are solely a function of z. Using this description for the

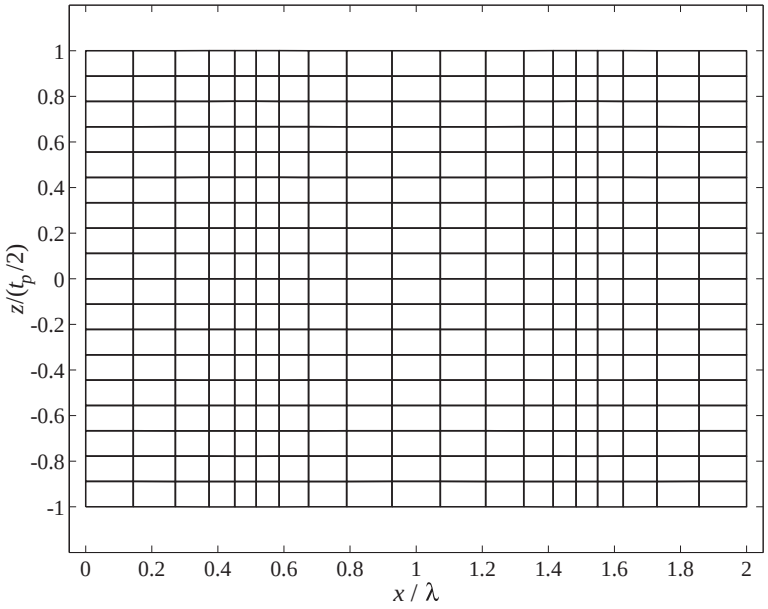

Figure 2.9: S0 mode (kt_p =.02 rad)

displacement of the solid, the strains in the material are complex as well:

$$\begin{bmatrix} \varepsilon_{xx} \\ \varepsilon_{zz} \\ \gamma_{xz} \end{bmatrix} = \mathbf{B}\mathbf{u}e^{i(kx-\omega t)} \quad \text{where} \quad \mathbf{B} = \begin{bmatrix} ik & 0 \\ 0 & \frac{\partial}{\partial z} \\ \frac{\partial}{\partial z} & ik \end{bmatrix} \tag{2.58}$$

The $\mathbf{B}$ matrix contains the derivative operator in the z direction as well the wavenumber, k. Additionally, the imaginary number, i, is present due to the assumption of a complex displacement field in Equation (2.57). When incorporated into the strain energy term, the complex conjugate of $\mathbf{B}$ will be used in order to ensure that total strain energy remains a real number.

The plate is then discretized through the thickness with n elements, as shown in Figure 2.15, and shape functions are used to approximate the displacement components in $\mathbf{u}$ for each element. In the current model, a linear distribution is used for the u and w variables. The nodes for the element are located at the top and bottom of the the element and the two degrees of freedom at each node are in-plane displacement, u_n, and transverse displacement, w_n. The in-plane and transverse

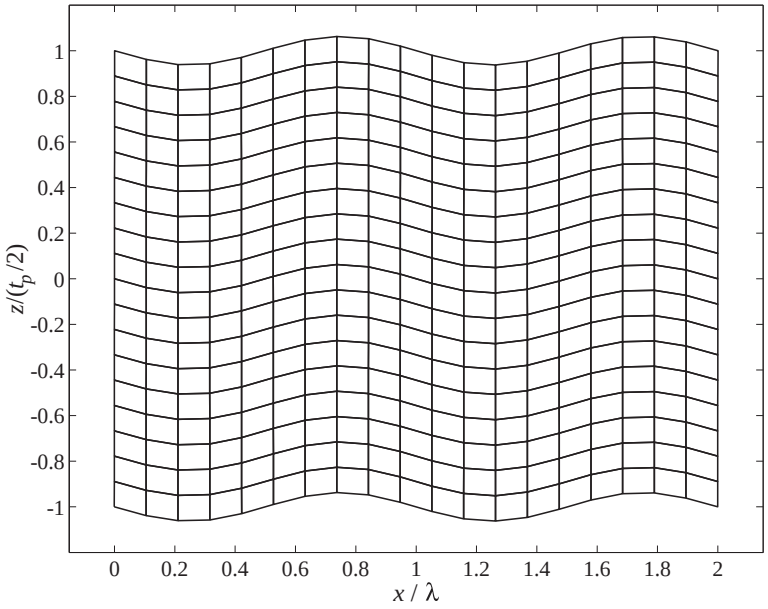

Figure 2.10: A0 mode (kt_p =.02 rad)

displacements for any point in the element can be determined:

$$\mathbf{u} = \mathbf{N}\mathbf{u}_e \quad \text{where} \quad \mathbf{u}_e = \begin{bmatrix} \mathsf{u}_1 \\ \mathsf{w}_1 \\ \mathsf{u}_2 \\ \mathsf{w}_2 \end{bmatrix} \tag{2.59}$$

$\mathbf{N}$ is the matrix of shape functions:

$$\mathbf{N} = \begin{bmatrix} \mathsf{N}_1 & 0 & \mathsf{N}_2 & 0 \\ 0 & \mathsf{N}_1 & 0 & \mathsf{N}_2 \end{bmatrix} \quad \text{where} \quad \begin{matrix} \mathsf{N}_1 = \frac{1-\xi}{2} \\ \mathsf{N}_2 = \frac{1+\xi}{2} \end{matrix} \quad , \xi = \frac{2z - (z_n + z_{n+1})}{z_{n+1} - z_n} \tag{2.60}$$

In the development of the shape functions, ξ is the local mapping variable, z is the position through the thickness, and z_n and z_{n+1} are the vertical positions of the node points for element n. The strain is related to the nodal degrees of freedom by $\boldsymbol{\varepsilon} = \mathbf{Y}\mathbf{u}_e$ where $\mathbf{Y} = \mathbf{B}\mathbf{N}$.

For each element, the strain and kinetic energies can then be constructed based on the nodal degrees of freedom. Because the energy terms are real numbers, the complex conjugate of the $\mathbf{Y}$ matrix is used:

$$U_e = \frac{1}{2}\int_{z_n}^{z_{n+1}} \mathbf{u}_e^H\, \mathbf{Y}^H \mathbf{E}_n\, \mathbf{Y}\, \mathbf{u}_e\, dz \qquad T_e = \frac{1}{2}\omega^2 \int_{z_n}^{z_{n+1}} \rho\, \mathbf{u}_e^H\, \mathbf{N}^T\, \mathbf{N}\, \mathbf{u}_e\, dz \tag{2.61}$$

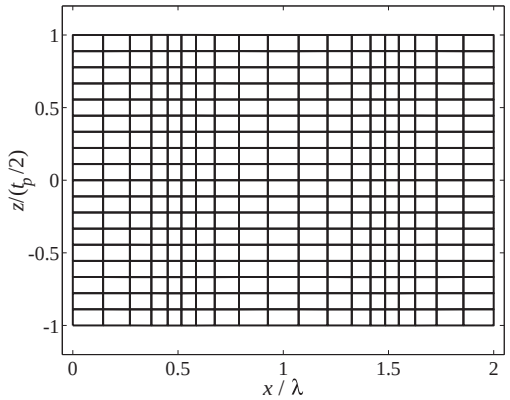

(a) S0 mode ($kt_p \rightarrow 0$)

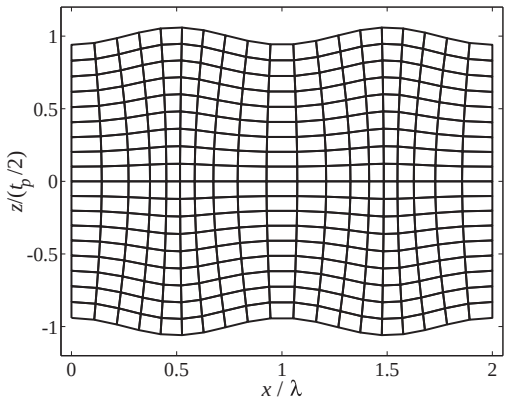

(b) S0 mode ($kt_p = 3$)

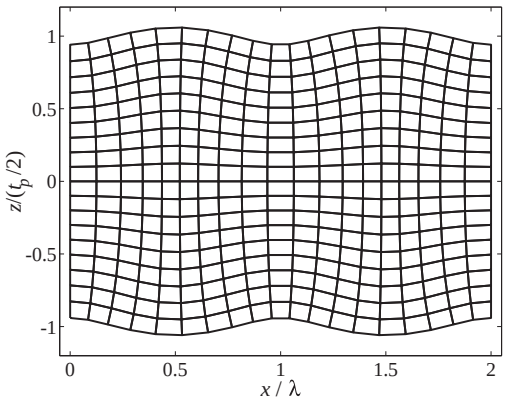

(c) S0 mode ($kt_p = 6$)

Figure 2.11: Fundamental Modes at different frequencies/wavenumbers

The superscript H represents the complex conjugate transpose of the respective matrix or vector. The integration only needs to be performed over the z direction. By pulling out the nodal degree of freedom vectors from the integration, the familiar forms of the stiffness and mass matrices are found:

$$\mathbf{K}_e = \int_{z_n}^{z_{n+1}} \mathbf{Y}^H \, \mathbf{E}_n \, \mathbf{Y} \, dz \qquad \mathbf{M}_e = \int_{z_n}^{z_{n+1}} \rho \, \mathbf{N}^H \, \mathbf{N} \, dz \tag{2.62}$$

The strain and kinetic energy terms are summed for all of the elements which producing global mass and stiffness matrices. Variational mechanics yields the eigenvalue problem that is to be solved:

$$\delta \left(U - T \right) = 0 \quad \rightarrow \quad \left(\mathbf{K}_g - \omega^2 \mathbf{M}_g \right) \mathbf{u}_g = \mathbf{0} \tag{2.63}$$

δ is the variational operator, $\mathbf{K}_g$ and $\mathbf{M}_g$ are the global mass and stiffness matrices, and $\mathbf{u}_g$ is the global nodal degree of freedom vector. In this case, $\mathbf{K}_g$ takes on a

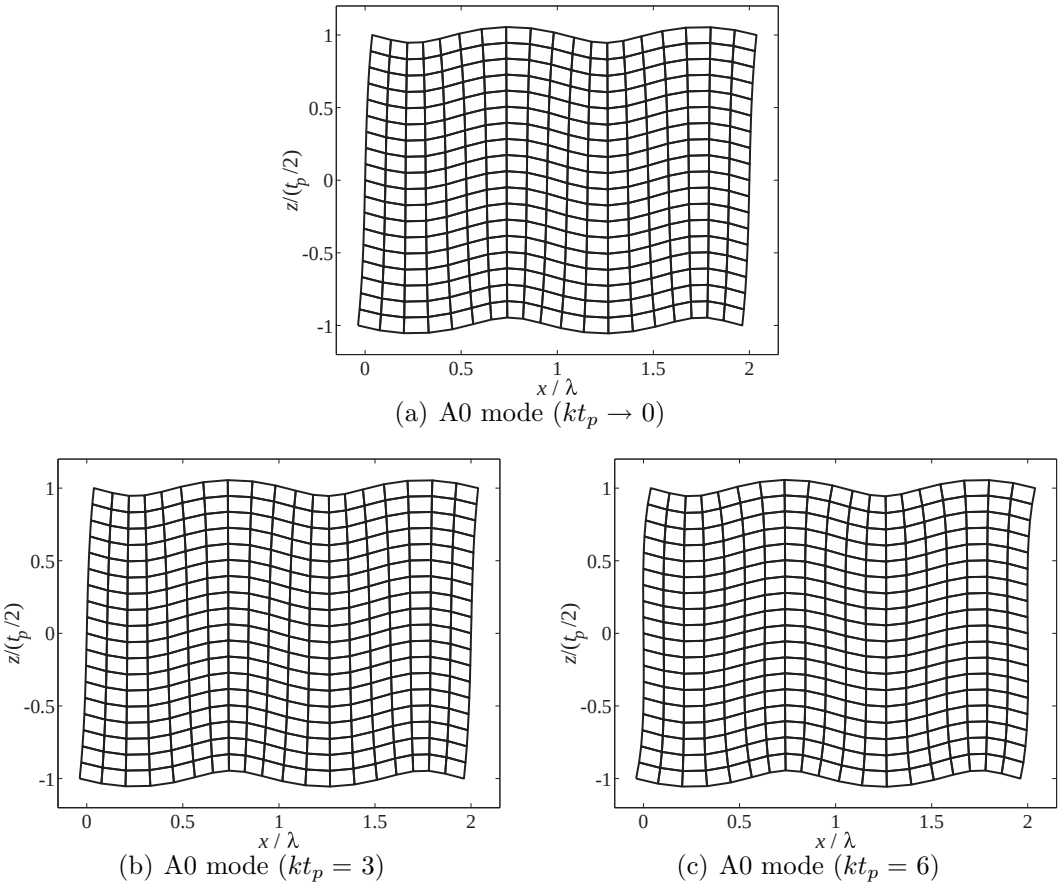

(a) A0 mode ($kt_p \to 0$)

(b) A0 mode ($kt_p = 3$)

(c) A0 mode ($kt_p = 6$)

Figure 2.12: Fundamental Modes at different frequencies/wavenumbers

more complicated form because the wavenumber, k, is embedded in its formulation. $\mathbf{K}_g$ is quadratic with respect to the wavenumber and can be factored such that the eigenvalue problem can be presented as quadratic equation:

$$\left(k^2\mathbf{K}_{g,2} + ik\mathbf{K}_{g,1} + \mathbf{K}_{g,0} - \omega^2\mathbf{M}_g\right)\mathbf{u}_g = \mathbf{0} \tag{2.64}$$

The matrix expressions are a function of both k and ω where k is part of the stiffness terms and ω corresponds to the inertial term. Both $\mathbf{K}_{g,2}$ and $\mathbf{K}_{g,0}$ are symmetric matrices whereas $\mathbf{K}_{g,1}$ is antisymmetric. The solution to the eigenvalue problem could be performed by either assuming a value for ω and solving for the corresponding k term or vice versa. By assuming a value for k, the problem reduces to a linear eigenvalue problem. If a frequency is assumed, the resulting quadratic eigenvalue problem can be reconstructed into a linear eigenvalue problem by introducing state

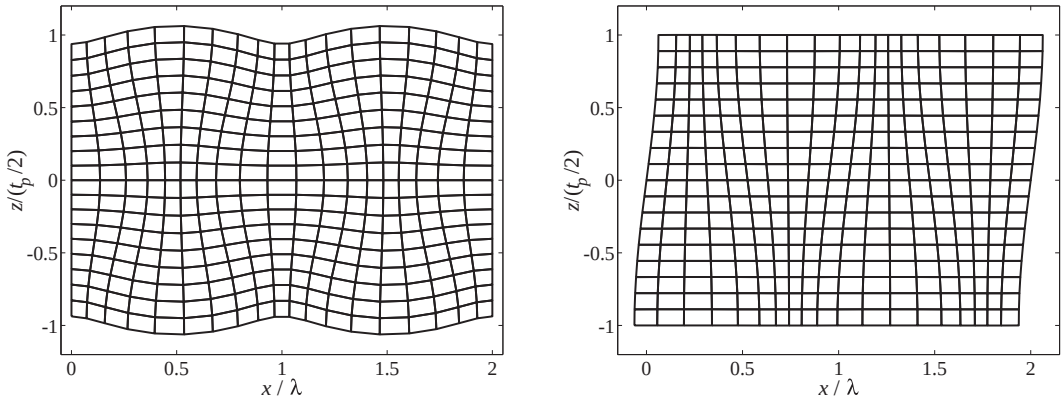

(a) S1 mode ($kt_p \to 0$)

(b) A1 mode ($kt_p \to 0$)

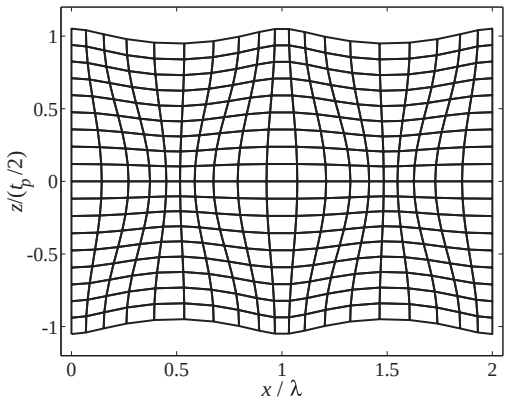

(c) S2 mode ($kt_p \to 0$)

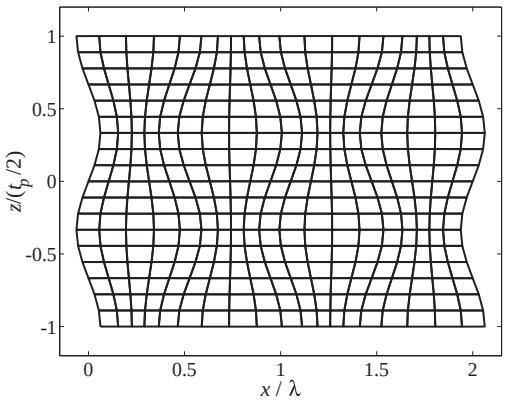

(d) A2 mode ($kt_p \to 0$)

Figure 2.13: Higher order modes

space formulation:

$$ik \begin{bmatrix} \mathbf{I} & \mathbf{0} \\ \mathbf{0} & -\mathbf{K}_{g,2} \end{bmatrix} \begin{bmatrix} \mathbf{u}_g \\ ik\mathbf{u}_g \end{bmatrix} = \begin{bmatrix} \mathbf{0} & \mathbf{I} \\ \mathbf{K}_{g,0} - \omega^2 \mathbf{M}_g & \mathbf{K}_{g,1} \end{bmatrix} \begin{bmatrix} \mathbf{u}_g \\ ik\mathbf{u}_g \end{bmatrix} \tag{2.65}$$

The wavenumber-frequency relationship for the Lamb modes in an isotropic plate can be determined by using this finite element formulation. The plots in Figure 2.16 shows a comparison of the wavenumber-frequency relationship found using the finite element formulation with the Lamb theory results shown earlier. The FE model can be used to predict the wavenumber-frequency curves for the higher order modes as well, as shown in Figure 2.17. There is some difficulty in predicting the higher order modes but a model with more elements would be able to predict the these modes with improved accuracy. The FE model tends to be stiffer than the exact solution because the assumed displacement function only approximates the actual

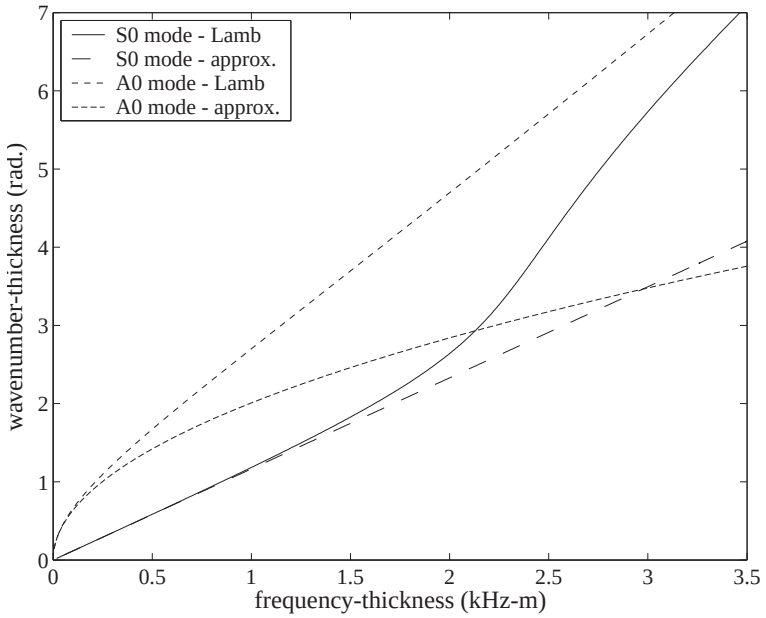

Figure 2.14: Comparison of Lamb theory with approximation (Aluminum)

displacement field using a polynomial fit. As the number of elements increases, the approximated displacement field approaches the actual field and the wavenumber-frequency relationship converges to the exact solution. Alternately, a higher order polynomial representing the displacement field may be assumed to achieve better convergence. Eigenvectors, $\mathbf{u}_g$, from the eigenvalue problem are used to predict the modeshape for the each individual mode and the shape functions in $\mathbf{N}$ are used to interpolate between the node points for each element.

Using a finite element formulation, the dispersion relations for Lamb modes in an Aluminum plate can be determined. An important extension of the finite element method presented here is that plates composed of individual layers with different material properties could be examined as well. A laminate constructed of individual plies has Lamb wave like behavior. An analytical type of approach developed earlier would be cumbersome because of displacement continuity and stress equilibrium between the individual plies which needs to be enforced. The finite element method is able to predict the Lamb wave behavior of a laminate by discretizing the laminate into the individual plies. This is particularly useful when predicting the

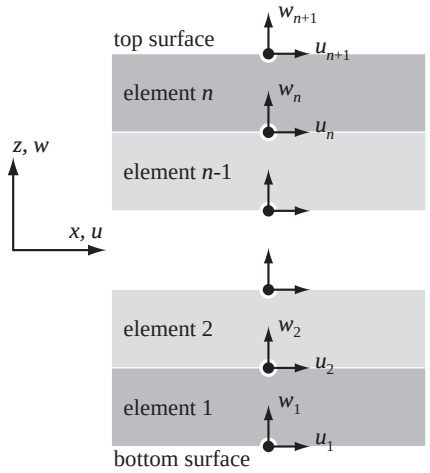

Figure 2.15: Discretization through plate thickness

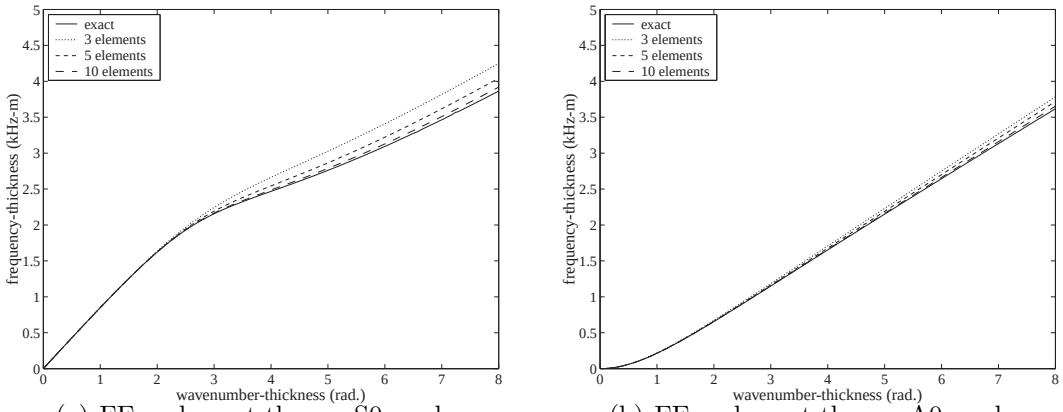

(a) FE and exact theory, S0 mode (b) FE and exact theory, A0 mode

Figure 2.16: Comparison of FE and exact theory

high frequency wavelike behavior of composite laminates which are constructed of plies with arbitrary orientation direction. The plane strain material properties, $\mathbf{E}_n$, of the nth ply is used to construct the stiffness matrices. Further description of the construction of the material elasticitiy matrix for composite laminates is discussed in Section 5.2.2. Solution of the the resulting eigenvalue problem to determine dispersion relations of the laminate proceeds as described in this section.

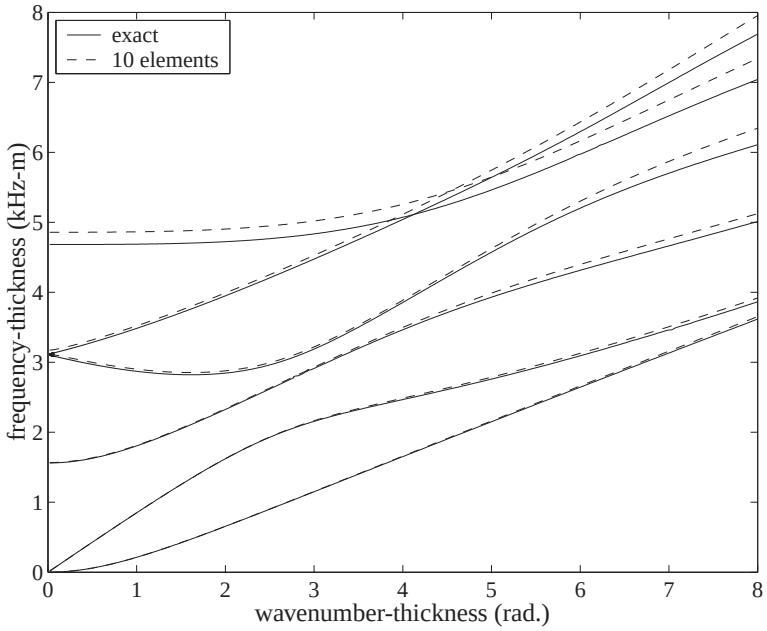

Figure 2.17: Wavenumber-Frequency for first 6 modes (FE and exact)

2.7 Excitation and Sensing of Lamb Waves using Piezoelectric Materials

One of the more common methods of transduction of high frequency dynamics in structures is the use of piezoelectric materials. In the traditional Non-Destructive Evaluation field, ultrasonic and angle-wedge transducers typically use piezoelectric materials as their active elements. Piezoelectric materials have significant coupling between the mechanical properties of stress and strain and electrical properties of charge and electric field and described in the constitutive piezoelectric equations:

$$\begin{aligned} \boldsymbol{\mathcal{D}} &= \mathbf{d}^T \boldsymbol{\sigma} + \boldsymbol{\epsilon}^{\boldsymbol{\sigma}} \boldsymbol{\mathcal{E}} \quad \text{Direct Effect} \\ \boldsymbol{\varepsilon} &= \mathbf{S}^{\boldsymbol{\mathcal{E}}} \boldsymbol{\sigma} + \mathbf{d} \boldsymbol{\mathcal{E}} \quad \text{Converse Effect} \end{aligned} \tag{2.66}$$

where $\boldsymbol{\sigma}$ and $\boldsymbol{\varepsilon}$ are mechanical stress and strain vectors respectively and $\boldsymbol{\mathcal{D}}$ and $\boldsymbol{\mathcal{E}}$ are electrical displacement and electrical field vectors. $\mathbf{S}^{\boldsymbol{\mathcal{E}}}$ is the compliance matrix for constant electric field and $\boldsymbol{\epsilon}^{\boldsymbol{\sigma}}$ is the matrix of dielectric properties for constant stress. The $\mathbf{d}$ matrix couples the mechanical and electrical properties and are referred to as the piezoelectric strain coefficients.

For a piezoelectric sheet bonded to a structure, as shown in Figure 2.18, an

applied voltage produces a mechanical deformation which also deforms the underlying structure. Similarly, a mechanical deformation of the structure would also deform the bonded piezoelectric element producing a change in the electrical degrees of freedom. This transduction mechanism allows a piezoelectric element to act as an actuator, a sensor, or both simultaneously. Typical properties of ceramic and polymer based piezoelectric materials are shown in Table 2.2.

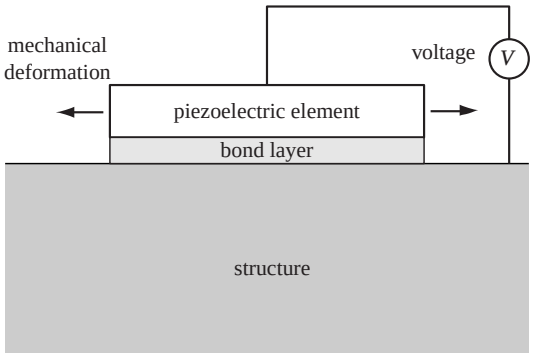

Figure 2.18: Diagram of piezoceramic on structure

	Ceramic (PZT-5H [117])	Polymer (PVDF [118])
ρ (kg/m^3)	7500	1780
S_{11}^E (10^{-12} m^2/N)	16.5	250
d_{31} (10^{-12} V/m)	-274	23
d_{33} (10^{-12} V/m)	593	-33
ϵ_{33}/ϵ_0 (ϵ_0=8.85$\times 10^{-12}$ F/m)	3400	12

Table 2.2: Typical Properties of Piezoelectric Materials

2.7.1 Actuators

Excitation of a plate structure using a sheet actuator is best modeled by induced strain actuation [87] and a brief description of the model follows. In this induced strain model a bond layer is introduced between the piezoelectric element and the

plate, shown in Figure 2.19. Load transfer occurs through the bond layer through the use of shear stresses. The force balance equation for the piezoelectric element is used as a starting point:

$$t_{pe}\frac{\partial \sigma_{xx}^{pe}}{\partial x} - \tau_{xz} = 0 \tag{2.67}$$

The superscript *pe* refers to the piezoelectric element. The loading on the structure depends on the type of actuation intended. For pure extensional loading, an actuation element on both the top and bottom surfaces are used in-phase while for pure bending, the actuation elements on the two surfaces are out of phase. The displacement profiles for the two cases are shown in Figure 2.20. The actuation moment or extensional force can be related to the stress in the top surface of the plate:

$$\begin{aligned} \text{Moment} \qquad & M = b\int_{-t_p/2}^{t_p/2} z\sigma_{xx}^{p}(z)dz = 2b\int_{0}^{t_p/2} z\sigma_{xx}^{ps}\frac{z}{t_p/2}dz = \frac{t_p^2}{6}\sigma_{xx}^{ps} \\ \text{Extensional Force} \qquad & F = b\int_{-t_p/2}^{t_p/2} \sigma_{xx}^{p}(z)dz = 2b\int_{0}^{t_p/2} \sigma_{xx}^{ps}dz = t_p\sigma_{xx}^{ps} \end{aligned} \tag{2.68}$$

b is the element width and the superscript *ps* refers to the plate surface. The incremental change in the moment and extensional force can be related to the shear stress on the top and bottom surfaces:

$$\begin{aligned} \frac{\partial M}{\partial x} = b\frac{t_p^2}{6}\frac{\partial \sigma_{xx}^{ps}}{\partial x} = -b\tau_{xz}t_p \qquad & \text{yields} \qquad \frac{\partial \sigma_{xx}^{ps}}{\partial x} + \frac{6}{t_p}\tau_{xz}^{ps} = 0 \\ \frac{\partial F}{\partial x} = bt_p\frac{\partial \sigma_{xx}^{ps}}{\partial x} = -2b\tau_{xz} \qquad & \text{yields} \qquad \frac{\partial \sigma_{xx}^{ps}}{\partial x} + \frac{2}{t_p}\tau_{xz}^{ps} = 0 \end{aligned} \tag{2.69}$$

Both the extension and bending case can be represented by a single equation:

$$\frac{\partial \sigma_{xx}^{ps}}{\partial x} + \frac{\alpha}{t_p}\tau_{xz}^{ps} = 0 \tag{2.70}$$

where the α term in the plate surface equation is based on a static analysis and depends on whether an extension (α=2) or bending (α=6) actuation is prescribed.

The shear stress and displacements in the piezoelectric element and surface of the plate are related by the shear stiffness of the bond layer, G:

$$\tau_{xz} = G\frac{u^{pe} - u^{ps}}{t_s} \tag{2.71}$$

The two expressions in Equations (2.67) and (2.70) can be rearranged using a stress-strain relationship, $\sigma = E\varepsilon$, and the given expression for the shear stress.

$$\underbrace{\frac{\partial \varepsilon_{xx}^{pe}}{\partial x} - \frac{G}{E_{pe} t_{pe} t_s}\left(u^{pe} - u^{ps}\right) = 0}_{\text{piezoelectric element}} \qquad \underbrace{\frac{\partial \varepsilon_{xx}^{ps}}{\partial x} + \frac{\alpha G}{E_p t_p t_s}\left(u^{pe} - u^{ps}\right) = 0}_{\text{plate surface}} \tag{2.72}$$

The coupled differential equations can be combined into a single differential equation by using the strain-displacement relationship, $\varepsilon_{xx} = \partial u / \partial x$:

$$\frac{\partial^2 \left(\varepsilon_{xx}^{pe} - \varepsilon_{xx}^{ps}\right)}{\partial x^2} - \frac{G}{t_s}\left(\frac{1}{E_{pe} t_{pe}} + \frac{\alpha}{E_p t_p}\right)\left(\varepsilon_{xx}^{pe} - \varepsilon_{xx}^{ps}\right) = 0 \tag{2.73}$$

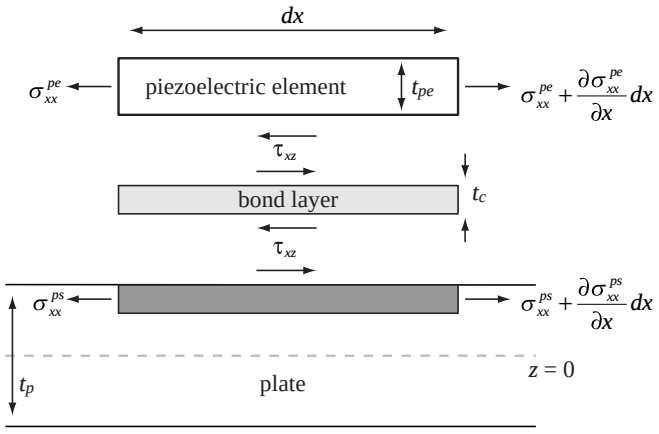

Figure 2.19: Loading diagram for pin force model

The solution to the differential equation is composed of hyperbolic sine and cosine functions:

$$\left(\varepsilon_{xx}^{pe} - \varepsilon_{xx}^{ps}\right) = C_1 \sinh\left(\Gamma x\right) + C_2 \cosh\left(\Gamma x\right)$$
$$\text{where } \Gamma = \sqrt{\frac{G}{t_s}\left(\frac{1}{E_{pe} t_{pe}} + \frac{\alpha}{E_p t_p}\right)} \tag{2.74}$$

The term, Γ, is known as the shear lag parameter and plays an important role in determining the properties of a given sized transducer. The boundary conditions

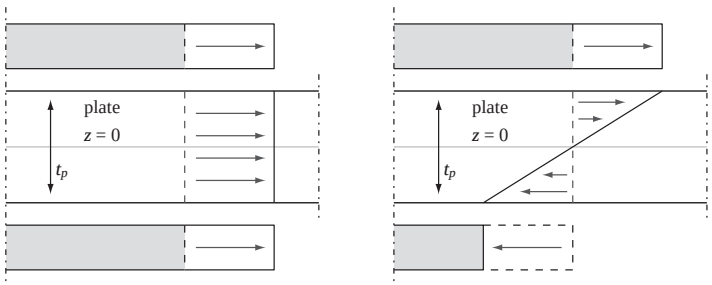

(a) Applied extension force (b) Applied moment

Figure 2.20: Displacement field due to applied loadings

are set such that the difference in the strains at the edges of the actuation element equals the free strain of the piezoelectric for an applied voltage:

$$(\varepsilon_{xx}^{pe} - \varepsilon_{xx}^{ps})|_{x=-L/2} = \Lambda \ , \ (\varepsilon_{xx}^{pe} - \varepsilon_{xx}^{ps})|_{x=L/2} = \Lambda \quad \text{where} \quad \Lambda = \frac{d_{31}V}{t_{pe}} \tag{2.75}$$

The solution to the differential equation is expressed in terms of the hyperbolic cosine:

$$(\varepsilon_{xx}^{pe} - \varepsilon_{xx}^{ps}) = \Lambda \frac{\cosh(\Gamma x)}{\cosh(\Gamma L/2)} \tag{2.76}$$

The shear stress distribution is found using previous expressions:

$$\tau_{xz} = \tau_0 \frac{\sinh(\Gamma x)}{\cosh(\Gamma L/2)} \quad \text{where} \quad \tau_0 = \frac{G}{t_s}\frac{\Lambda}{\Gamma} \tag{2.77}$$

The distribution of shear stress from Equation (2.77) indicates that the loading on the plate is concentrated at the edges of the actuation element, shown in Figure 2.21. When an ideal bond exists, the bond layer shear stiffness is infinite ($G \to \infty$) and the loading on the structure is modeled as concentrated shear stresses at the edges of the element.

Crawley and de Luis [87] observe that actuation by piezoelectric elements depends on two important factors, a strong bond between the element and substructure and a stiff actuator relative to the substructure. While the bond depends on the coupling method, there are different types of piezoelectric materials that may be used for actuation. Piezoceramic materials are appropriate for excitation of metallic or rigid composite substructures as their mechanical properties matches that of the structure more so than a softer piezoelectric material.

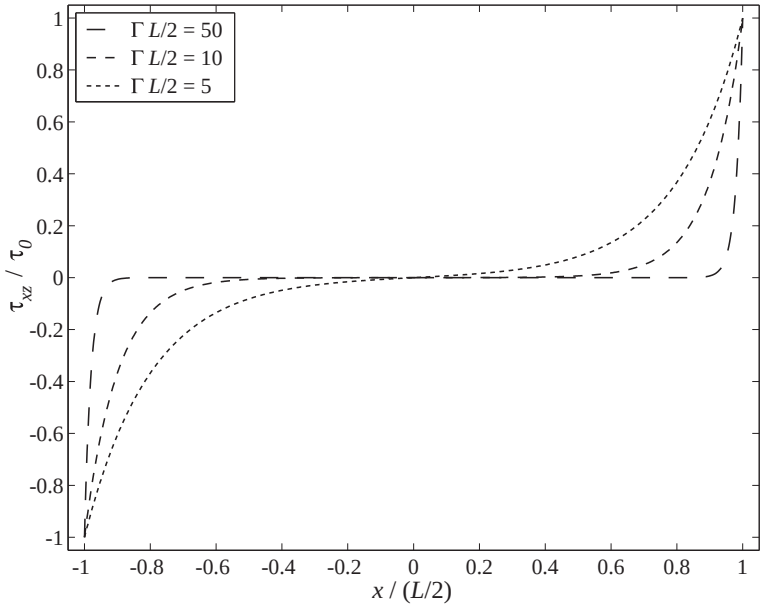

Figure 2.21: Shear stress distribution for various values of $\Gamma L/2$

The induced strain model is valid for excitation of Lamb wave modes [90, 92] despite its quasi-static assumptions. For the one dimensional case where the actuator element has length, L, the distribution of shear stresses on the top surface of the structure, assuming an ideal bond, can be expressed using Dirac delta functions:

$$\tau_{xz}(x) = \tau_0 \left(-\delta \left(x + \frac{L}{2} \right) + \delta \left(x - \frac{L}{2} \right) \right) \tag{2.78}$$

The ability of the actuation element to excite a wave mode depends on the spatial distribution of the loads [88]. The response of the structure with a distributed load is the superposition of the responses due to each elemental load individually. Properties of this superposition can be investigated more thoroughly by examining the wavenumber spectrum of the loading distribution:

$$\Theta(k) = \int \tau_{xz}(x) e^{-ikx} dx = -i2\tau_0 \sin \left(\frac{kL}{2} \right) \tag{2.79}$$

For the induced strain model, where the excitation shear stresses are assumed to be at the edges of the piezoceramic element, Θ describes the ability of the element to excite a wave of a given wavenumber. There is a zero of $|\Theta|$ at $kL/2 = n\pi$ where n is an integer. In this region of the wavenumber domain, the actuation element

does a poor job of excitation because the wave produced by one of the point loads is canceled out by the other. For the shear distribution given in Equation (2.77), the corresponding wavenumber response can be found also:

$$\Theta(k) = -i2\tau_0 \frac{L}{2} \left(\frac{(\Gamma L/2)\sin(kL/2)}{(\Gamma L/2)^2 + (kL/2)^2} - \frac{(kL/2)\cos(kL/2)}{(\Gamma L/2)^2 + (kL/2)^2} \frac{\sinh(\Gamma L/2)}{\cosh(\Gamma L/2)} \right) \quad (2.80)$$

The same expression as in Equation (2.79) is found when the shear modulus term, G, is assumed to be very large in the τ_0 and Γ terms. This is seen in Figure 2.22 where the wavenumber responses with increasing Γ approaches the ideal bond case. Additionally, a softer bond causes the actuation ability of the piezoelectric element to decrease. The peaks in the wavenumber response decrease as the bond becomes softer, despite the wider wavenumber response of the actuator.

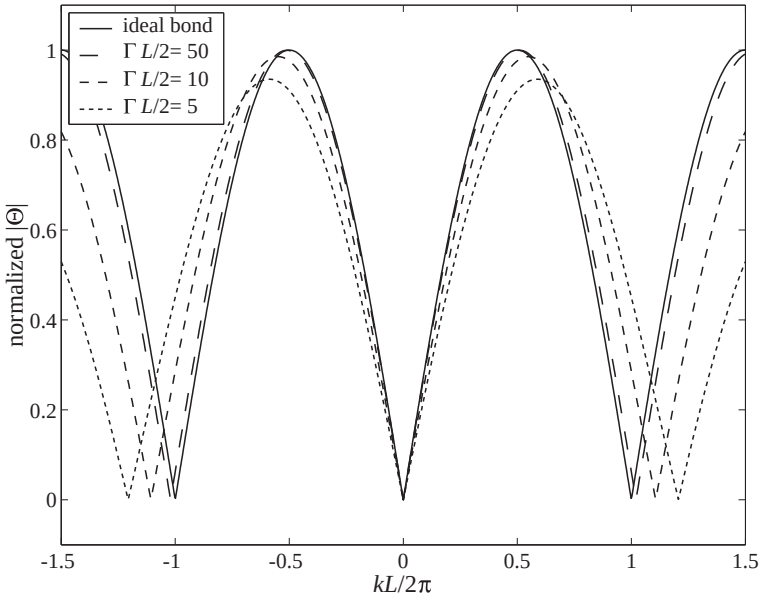

Figure 2.22: Wavenumber response (Θ) of actuator using induced strain model

The ability of a single sheet actuator of a given size to excite Lamb waves depends on the wavenumber of interest, regardless of the specific Lamb mode. Since the wavenumber-frequency relationships of the S0 and A0 behave differently, the capability of the actuator depends on the size of the actuator as well as the frequency of interest.

If an actuator sheet is bonded to both the top and bottom surfaces, the ability of the actuator to excite a given mode also depends on the relative phases of the top and bottom element displacements. The S0 mode can be preferentially excited by the appropriate combination of excitation voltages and piezoelectric polarity such that the displacements in the top and bottom elements are in phase with each other. Alternately, the A0 mode can be preferentially excited when the top and bottom elements displace out of phase with respect to each other. Regardless of the preferred mode, the size of the actuation element and the associated spatial distribution of loads governs the capabilities of the actuation element.

The same concepts introduced for the linear case can be applied to a planar actuation element. The shape of the actuator plays a role in the ability of the actuator to excite different modes [88, 92, 90]. More specifically, the distribution of stresses by the actuation element and its two dimensional Fourier transform describe the capabilities of a bonded piezoelectric actuation element in much the same as is presented for the one dimensional case.

2.7.2 Sensors

The same mechanical issues that affect a piezoelectric actuators performance also affect a piezoelectric sensor's performance, though the goals are different. The development of the actuator performance based on the induced strain model in the previous section can also be used to determine the response of a piezoelectric sensor based on a transfer of shear loads. For sensing applications, the transduction mechanism must not affect the underlying structure. Polymer piezoelectrics work well in this regard as their presence on the structure adds little overall stiffness.

The component of the electric displacement corresponding to an applied strain is using the piezoelectric coefficients:

$$\mathcal{D}_3 = \begin{bmatrix} d_{31} & d_{32} \end{bmatrix} \begin{bmatrix} C_{11}^{\mathcal{E}} & C_{12}^{\mathcal{E}} \\ C_{12}^{\mathcal{E}} & C_{22}^{\mathcal{E}} \end{bmatrix} \begin{bmatrix} \varepsilon_{xx}^{pe} \\ \varepsilon_{yy}^{pe} \end{bmatrix} \tag{2.81}$$

where $\mathbf{C}^{\boldsymbol{\mathcal{E}}}$ is the stiffness matrix of the material at constant field. The electric

displacement is integrated over the area of the sensor element to get a charge representing a measure of the strain in the material:

$$q = \int_A \mathcal{D}_3 \, dA \tag{2.82}$$

Unlike a traditional foil based strain sensors which requires a Wheatstone bridge and the associated bridge excitation, a piezoelectric material can act as a self-powered strain sensor. In this case, the Direct Effect in the piezoelectric constitutive relations are used in order to extract the amount of mechanical deformation based on a change in the electrical degrees of freedom [119].

The differences between the piezoelectric strain and plate surface strain in Equation (2.74) can be solved. Assuming equal plate surface strains on the edges of the piezoelectric element, $\varepsilon_{xx}^{ps} = \varepsilon_{xx,0}^{ps}$, and nonexistent piezoelectric strains at the edges of the element, the strain distribution in the piezoelectric element can be found:

$$\varepsilon_{xx}^{pe} = \varepsilon_{xx,0}^{ps} \left(1 - \frac{\cosh(\Gamma x)}{\cosh(\Gamma L/2)} \right) \tag{2.83}$$

The normalized piezoelectric strains for different values of the shear lag parameter, Γ, is shown in Figure 2.23. In the case of a single sensing element on the top of the plate, an adjustment is made to a component of Γ where α=2 for an in-plane sensor and α=3 for bending. As the shear stiffness of the bond layer increases, more of the strain is transferred to the piezoelectric element. Assuming an ideal bond, the strain in the piezoelectric element can be expressed in terms of the Heaviside step function, He:

$$\varepsilon_{xx}^{pe} = \varepsilon_{xx,0}^{ps} \left(He\left(x + \frac{L}{2}\right) - He\left(x - \frac{L}{2}\right) \right) \tag{2.84}$$

In this case, the piezoelectric strain is the same as the plate surface strain.

For a linear sensor, where the strains in the off directions are neglected, the charge per unit width can be expressed in terms of the surface strains. The total charge for a sensor element in the ideal bond case can be expressed as an integral of two Heaviside step functions:

$$q = b \int \frac{d_{31}}{E_{pe}} \varepsilon_{xx}^{pe} dx = b \int_{-L/2}^{L/2} \frac{d_{31}}{E_{pe}} \varepsilon_{xx,0}^{ps} \left(He\left(x + \frac{L}{2}\right) - He\left(x - \frac{L}{2}\right) \right) dx \tag{2.85}$$

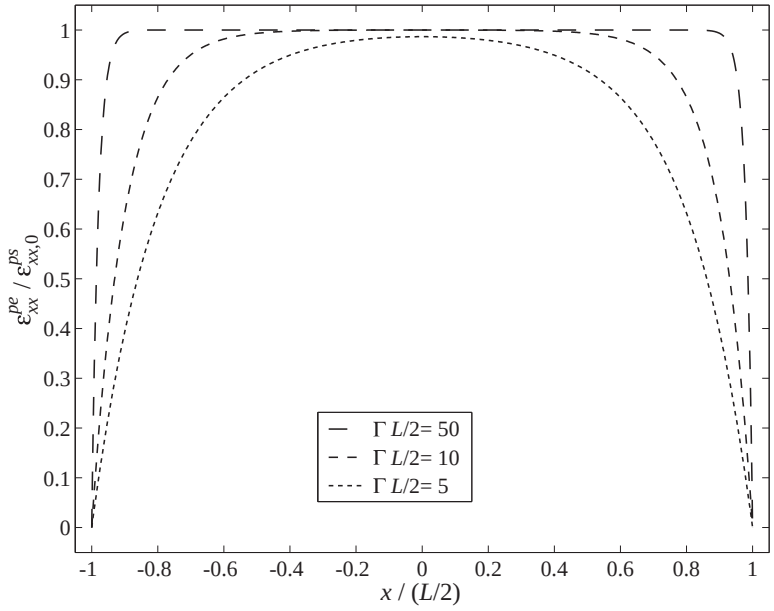

Figure 2.23: Strain distribution in sensor for various values of $\Gamma L/2$

where b is the width of the sensor element. For a wave propagation case, the strain as well as the displacement can be described in terms of a complex exponential. Assuming a wavelike strain distribution, $\varepsilon^{ps}_{xx,0} = \bar{\varepsilon}^{ps}_{xx,0} e^{-ikx}$, the integral takes on the familiar form of the Fourier transform:

$$q = b \int_{-L/2}^{L/2} \frac{d_{31}}{E_{pe}} \bar{\varepsilon}^{ps}_{xx,0} \left(He\left(x + \frac{L}{2}\right) - He\left(x - \frac{L}{2}\right) \right) e^{-ikx} dx \tag{2.86}$$

By summing the charge over the entire length of the sensor, the piezoelectric sensor effectively performs a Fourier transform function. For the ideal bond case where all of the strain is transferred to the piezoelectric, the wavenumber response of the sensor is a simple relationship:

$$Q(k) = b \frac{d_{31}}{E_{pe}} \bar{\varepsilon}^{ps}_{xx,0} L \frac{\sin(kL/2)}{kL/2} \tag{2.87}$$

The wavenumber response of the strain distribution reveals the sensitivity of a sensor element of length, L, to a given wavenumber, k. There is a zero of the wavenumber response at $kL/2 = n\pi$, which is the same as for the actuator case. At this wavenumber region, the sensor is not able to sense a structural wave. For the piezoelectric strain distribution in Equation (2.83), the wavenumber response becomes

more complicated:

$$Q(k) = b\frac{d_{31}}{E_{pe}}\bar{\varepsilon}^{ps}_{xx,0}L\left(\frac{\sin(kL/2)}{kL/2} - \frac{(kL/2)\sin(kL/2)}{(kL/2)^2+(\Gamma L/2)^2} - \frac{(\Gamma L/2)\cos(kL/2)}{(kL/2)^2+(\Gamma L/2)^2}\frac{\sinh(\Gamma L/2)}{\cosh(\Gamma L/2)}\right) \quad (2.88)$$

The wavenumber response for a linear sensor with given shear lag is shown in Figure 2.24. For the lower wavenumber region, the magnitude of the response decreases as the shear lag factor increases. The sensitivity of the sensor decreases; however, the bandwidth of the sensor increases, as seen by the zero of $|Q|$ moving further out in the wavenumber domain.

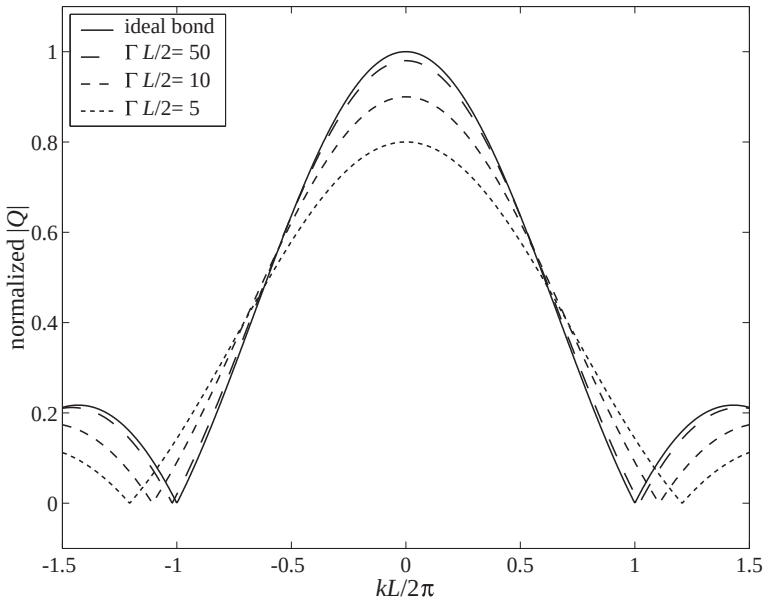

Figure 2.24: Wavenumber response (Q) of sensor using Induced Strain Model

2.7.3 Equipment

Unless otherwise noted, the set of experiments conducted in this thesis made use of a common set of laboratory equipment. For signal conditioning of the PVDF sensor signals before data acquisition, a charge amplifier circuit with additional gain stages was constructed. A simplified diagram of the charge amplifier circuit is shown in Figure 2.25 where a feedback capacitor, C_f, gathers the charge generated by the

deformation of the piezoelectric element. Each of the sensor signals passed through this signal conditioning circuitry to the Tektronix TDS420A digital oscilloscope, shown in Figure 2.26(a). The TDS420A stored the data on a disk which was then decompressed and read and manipulated as the set of sensor data. The actuation transducers used was a PZT-5H piezoceramic element which was bonded to the plate as a source for the interrogating signal. The excitation signal was constructed and transferred to the Agilent 33220A function generator, shown in Figure 2.26(b), which could read the digital signal and output the corresponding analog signal to the power amplifier. The power amplifier was necessary to provide the power necessary to excite the actuation element at the voltages and frequencies necessary. A schematic is shown in Figure 2.27. Since the piezoceramic actuation element acts as a capacitor, whose impedance drops with frequency, larger currents are needed when exciting at high frequency ranges. Typically, a function generator cannot provide the power necessary for such applications. The Piezo Systems, Inc. EPA-104 power amplifier, shown in Figure 2.26(c), could provide the power necessary to drive the piezoceramic element at the desired frequencies.

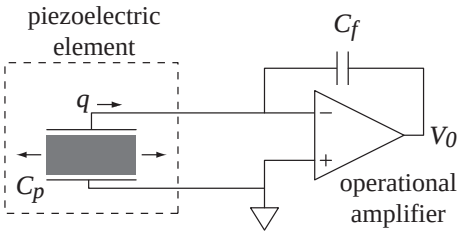

Figure 2.25: Circuit diagram of simplified charge amplifier

2.8 Summary

Wave propagation mechanics relies heavily on the wavenumber-frequency relationship for the structure. In the simple case where the wavenumber-frequency relationship is linear, the waves behave uniformly with constant phase and group speeds and exhibit a non-dispersive behavior. In the case where the wavenumber-frequency

(a) Tektronix TDS420A oscilloscope

(b) Agilent 33220A function generator

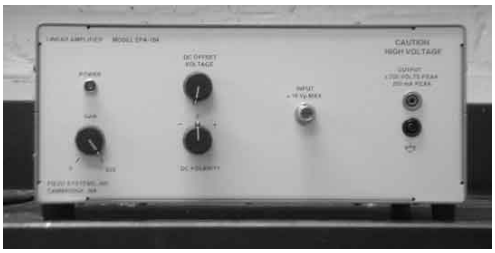

(c) Piezo Systems, Inc. EPA-104 power amplifier

Figure 2.26: Experimental equipment

relationship is nonlinear, the behavior becomes more complicated.

In the development of the wave propagation mechanics of the simplified plate dynamics, the behavior depends on the frequency/wavenumber range of interest. At lower frequency/wavenumber ranges, the in-plane dynamics are non-dispersive and well behaved. The out-of-plane, or transverse, dynamics are dispersive from the outset. Though the simplified plate dynamics present simple expressions for the dispersion relations, the assumption of no shear deformation that the model is based make the dispersion relations useful only at low frequencies.

A Lamb wave approach predicts these dispersion relations with a more complete description of the displacement of the material in the structure. Generating the dispersion relations becomes much more difficult than the expressions derived from the 1st order approximations; but, in doing so, both the in-plane and transverse fundamental modes are captured as well as higher order modes.

A finite element approach is used to simplify the approach to predicting the dispersion relations based on approximating the exact solution with a polynomial. As the number of elements in the finite element approach increases, the predicted

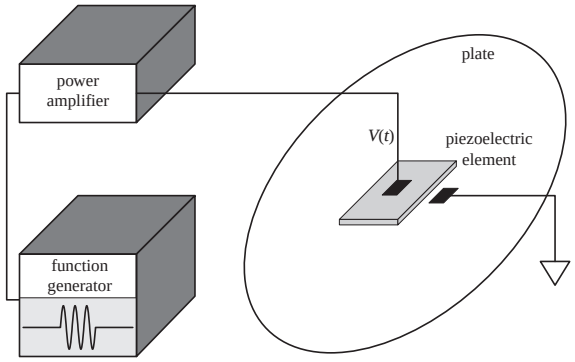

Figure 2.27: Excitation of piezoceramic element

dispersion relations converge to the exact solutions. The power in the finite element approach lies in its ability to predict the dispersion relations for a plate made up of layers of different materials and material properties. This is simply accomplished by discretizing the plate based on the number of layers and assigning differing material properties based on those layers. The extension to composite materials with laminae made up of plies of various orientation is easily modeled in this way.

Actuation and sensing of structural waves using piezoelectric elements is examined using a model which incorporates the shear layer between the element and plate surface. Actuation as well as sensing capabilities of an element is dependent on the stiffness of the bonding material as well as the thickness of the bond layer. It is shown that as the bonding material stiffness increases and bond layer decreases, the actuation magnitude as well as sensor response increase at the cost of reduced bandwidth.

Chapter 3

Wavenumber Filters

3.1 Introduction

A signal from a source may be degraded by noise and interference from other sources. An array of sensors may be used to improve the quality of the signal from the desired source. Though the signals from each sensor in the array are different from each other, there is an internal consistency in the content of the signals. For the simple case where the source is in-line with a linear array, there is a time shift between the individual sensors signals in the array, shown in Figure 3.1. The time shift is dependent on a few factors:

1. Wave propagation properties in the medium
2. Distance between the sensors in the array
3. Position of the source signal relative to the array

This last factor is important in distinguishing one signal source from another.

Figure 3.1: Array and source in-line

One approach to signal processing is to take the time domain signals and shift them back and forth in time with respect to a reference signal. The time shift is dependent on the velocity of the wave in the medium and the distance between the

sensors. The summation of the time shifted signals would then bring out the desired signal content in the sensor signals.

For a more robust approach, a Green's function can be used to describe the propagation of information from a point source through the medium. At a set of sensing locations, the signal propagation from the point source can be approximated. This approximation shows that the phase information can be described in terms linear and quadratic phase adjustments to a baseline phase term. The corrections can be used as a tool to break down the signal for directional sensing.

Following a simplification of the wave field from a point source, the response of an element in the array is expressed in terms of a plane wave propagating through the array. The summation of these individual inputs produces the array response. These concepts are widely used in the acoustic and electromagnetic mediums. In an acoustic medium, the sensors are groups of microphones, as shown in Figure 3.2, and in the electromagnetic medium, the sensor is the antenna. The transmission of information in both of these mediums is wavelike. High frequency dynamics of structures such as thin plates and shells is also best described in terms of wave propagation.

An array of sensors is naturally most sensitive to a signal arriving from a particular direction relative to the array orientation. For the array in Figure 3.2, a source located directly in front will produce the largest signal and sources located at other positions will have reduced magnitude signals. In order to enhance the information from a source at another location, the array is reoriented, or steered, to point at the new source. The quality of the desired signal is improved by realigning the array such that the time shift between the signals is eliminated.

For a static array which can not be realigned, a signal processing technique may be used to accomplish the same goal. This signal processing technique, known as phased array processing, consolidates the group of signals taken from an array of sensors[120]. In essence, an array of static sensors can be virtually steered such that it looks in a particular direction.

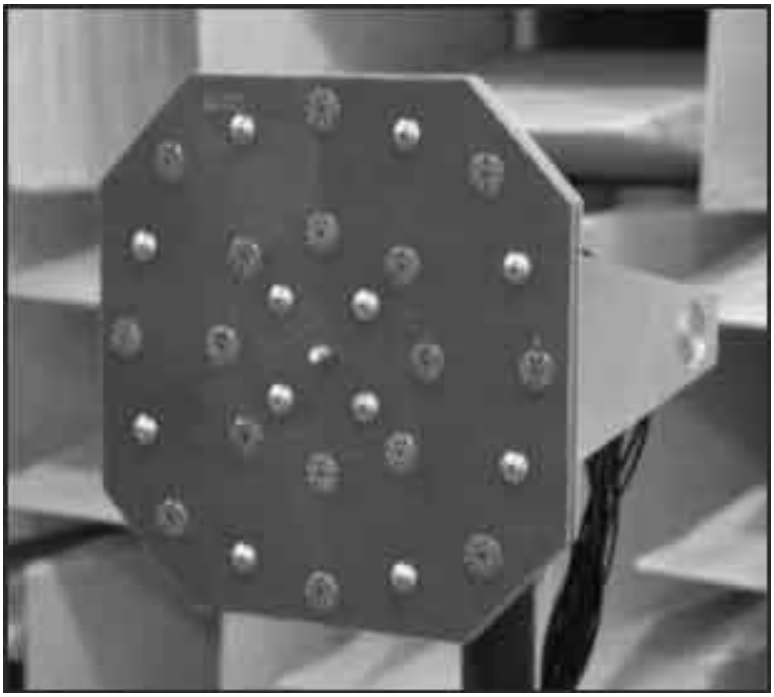

Figure 3.2: Acoustic array (Courtesy U. of Florida)

Along with the acoustic and electromagnetic media, phased array concepts can also be applied to high frequency dynamics of plate structures. This is particularly useful since sensors on plates are generally bonded and are not easily moved. The ability of sensor arrays to act like filters allows the vibrations of the thin plate to be decomposed and separated into a more manageable representation of the dynamics.

Besides time shifting of signals, another approach toward signal processing is to view the signals based on the spatial distribution of the sensors. The array of sensors enables signal processing to be performed in the wavenumber domain. This is analogous to the time-frequency processing that is more commonly used. A signal in the time domain can be broken down into its frequency components by taking a Fourier series or Fourier transform in time. Similarly, a sensor array produces a signal in the spatial domain which can be broken down into its wavenumber, or spatial frequency, components. Filtering in the spatial domain extracts information from signals which would not be possible with a single sensor. There are issues associated with a spatial filtering approach which are adaptations of time domain

signal processing concerns applied to the spatial domain. Nevertheless, useful spatial filtering can be accomplished while taking these issues into account.

Wavenumber filtering has been discussed before in the context of structural dynamics. Many applications deal with structural vibration control, where the vibrations of a structure can be reduced by eliminating the propagation of waves through the structure [121, 122, 123, 124, 125, 126, 127]. Alleyne and Cawley [61] used wavenumber information to interpret simulation results. Joshi [94] suggested the possibility of using arrays for damage detection. Various current research efforts explore the possibility of using phased array processing for damage detection purposes. Wooh and Shi [128, 129] conducted simulation studies of arrays in multiple dimensions. Purekar and Pines [130] showed experimental results of the capabilities of phased arrays for damage detection. The use of sensor arrays as tools for damage detection in structures has shown wide applicability [131, 132, 133]

3.2 Time Domain Signal Processing

For a group of sensors, the time it takes for a signal to pass from one sensor to another depends on the distance between the sensors and the speed of the wave, $\Delta t = \Delta x/c$. Knowing this, a group of sensor signals may be time shifted relative to a reference sensor in order to align each of the sensor signals [131]. When the sensor signals are summed up, the signal corresponding to the desired wave direction is enhanced:

$$v_{tot}(t) = \frac{1}{N}\sum_{n=1}^{N} v_n(t + \Delta t_n) \tag{3.1}$$

v is the sensor signal and Δt depends on the location of the nth sensor relative to the reference sensor and the velocity of the wave.

An example is shown in Figure 3.3(a) where two different waves are shown to pass at different times between the different x locations. The first wave is a rightward wave which travels from x_1 to x_3 and occurs at $\sim$-2 sec. The second wave is a leftward wave which travels from x_3 to x_1 and occurs at $\sim$2 sec. If the rightward wave is the source of interest, the leftward wave needs to removed. This

can be accomplished by time shifting the signals, $v_n(t)$, such that only the rightward wave is present when the shifted signals are summed together. Figure 3.3(b) shows the different time shifted signals where the rightward wave occurs at the same point in time. The signal at x_1 is shifted forward in time and the signal at x_3 is shifted backward in time. The information corresponding to the leftward wave is separated even more because of the time shifting. When the resulting shifted signals are summed and normalized, the rightward wave is dominant in the response, shown in Figure 3.3(c). Though only three signals are used, there is a significant difference in the rightward wave relative to the signal corresponding to the leftward wave. The addition of more signals improves the final result. The portion of the signal which is desired is enhanced while unwanted parts are reduced, though not completely eliminated.

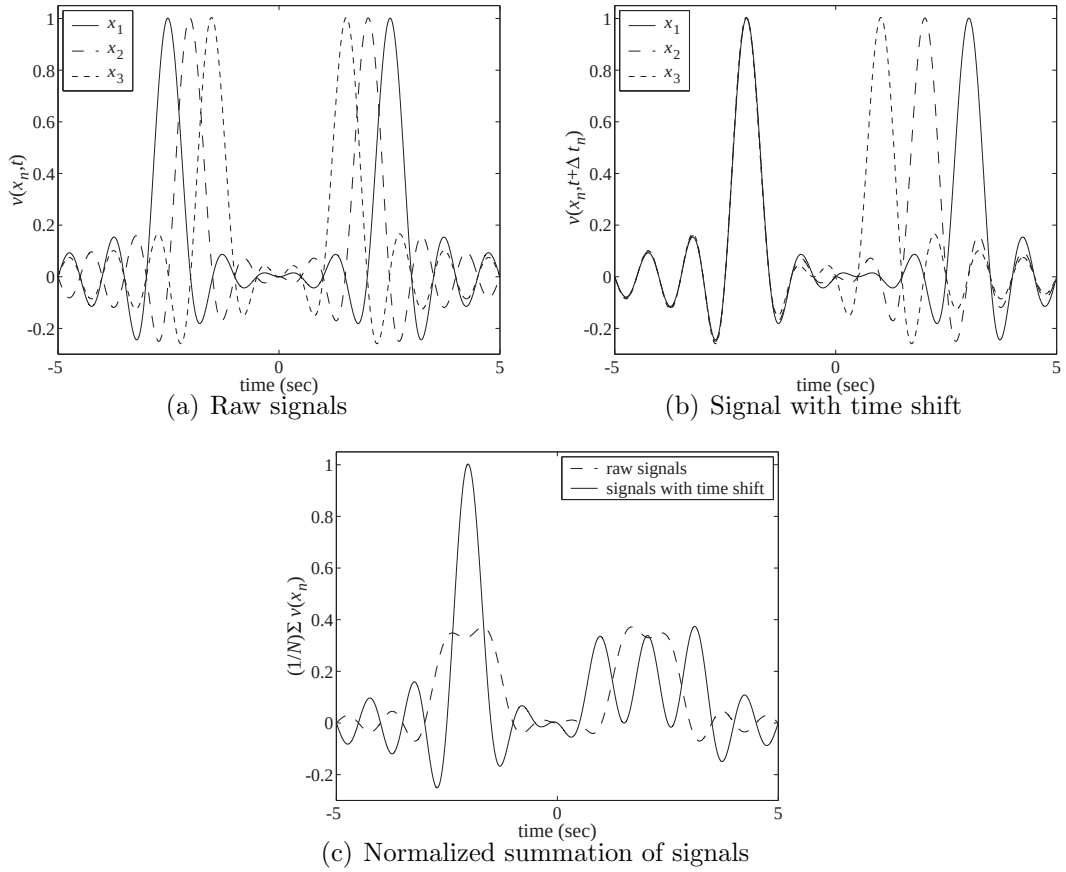

(a) Raw signals

(b) Signal with time shift

(c) Normalized summation of signals

Figure 3.3: Time shifting as a signal processing method

3.3 Green's Function and Approximation

The expression for the impulse response of a system to an impulse loading is used as a starting point:

$$w(\mathbf{r},\omega) = \frac{1}{2\pi}\int G(\mid \mathbf{r}-\mathbf{r}_0 \mid, t)e^{i\omega t}d\omega \tag{3.2}$$

G is the Green's function, $\mathbf{r}$ is the vector to the location of interest, and $\mathbf{r}_0$ is the vector to the source, shown in Figure 3.4. The general expression for the Green's function takes a complex form:

$$G(|\mathbf{r}-\mathbf{r}_0|,\omega) = \bar{G}(|\mathbf{r}-\mathbf{r}_0|)e^{-ik(\omega)|\mathbf{r}-\mathbf{r}_0|} \tag{3.3}$$

In the expression for the the Green's function, the $\bar{G}$ term corresponds to the magnitude term and the complex exponential, $e^{-ik(\omega)|\mathbf{r}-\mathbf{r}_0|}$ is the phase component which is dependent on the wavenumber in the medium as well as the distance, $|\mathbf{r}-\mathbf{r}_0|$. The phase component is important when using arrays to extract information about a source.

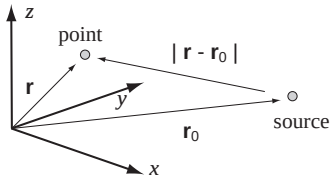

Figure 3.4: Vector diagram

Assuming the sensing element is located near the origin, such that $|\mathbf{r}| \ll |\ \mathbf{r}_0|$, an approximation can be made to the phase term in Equation (3.3):

$$\exp\left(-ik|\mathbf{r}-\mathbf{r}_0|\right) \approx \exp\left(-ik\mathsf{r}_0\right)\exp\left(ik\hat{\mathbf{r}}_0\cdot\mathbf{r}\right)\exp\left(-ik\left(\frac{\mathsf{r}^2-\left(\hat{\mathbf{r}}_0\cdot\mathbf{r}\right)^2}{2\mathsf{r}_0}\right)\right) \tag{3.4}$$

This expansion is known as the Fraunhofer approximation (as opposed to the Fresnel approximation which neglects the $\hat{\mathbf{r}}_0\cdot\mathbf{r}$ term in the third term of the approximation). The first term in Equation (3.4) is the bulk phase shift from the source location to the origin, $\exp\left(-ik\mathsf{r}_0\right)$. The second term, $\exp\left(ik\hat{\mathbf{r}}_0\cdot\mathbf{r}\right)$, is a first order correction of

the phase approximation based on the location of the sensor element, $\mathbf{r}$. This is a linear correction to the phase shift due its dependence on r. The third expression in Equation (3.4) is a correction based on the curvature of the wavefront from the source and is a quadratic correction because its dependence on r^2. For a set of sensors aligned along a vector, $\hat{\mathbf{r}}$, near the origin, the linear and quadratic phase corrections are used for array steering and focusing, respectively.

An array of sensors is steered such that the phase differences between the different elements in the array are eliminated. The linear phase shift, $\exp(ik\hat{\mathbf{r}}_0 \cdot \mathbf{r})$, is based on a plane wave with wavenumber, k, propagating along the vector pointing to the source. An array of sensors positioned along the $\mathbf{r}$ vector would have no relative phase differences if $\hat{\mathbf{r}_0} \cdot \mathbf{r} = 0$, or if the two vectors are normal to each other. This is shown graphically in Figure 3.5(a) where $\theta = 90°$. An array of sensors, such as the set of microphones shown earlier, work best together when facing the plane wave.

If the source is located near the sensors, the phase associated with the curvature of the wavefront becomes important. The curvature of the wavefront is shown in Figure 3.5(b). The quadratic term in Equation (3.4) is an adjustment based on this curvature. This is dependent on the distance to the source, r_0, where the closer the source, the larger the curvature. An array of sensors positioned along $\mathbf{r}$ would need to be shifted in the $\hat{\mathbf{r}}_0$ direction to match the curvature of the approaching wave. The effect of the wavefront curvature decreases as the travel distance increases. This is seen in Figure 3.6 where the phase adjustment needed to be made decreases as the distance to the source decreases. The adjustment needed to match the curvature of the wavefront is known as focusing of the array. Though this would improve the response of the array, the distance to the source needs to be known in order to make the adjustment. Additionally, adjusting for the phase curvature is a secondary effect in comparison to the steering of the array in normal applications.

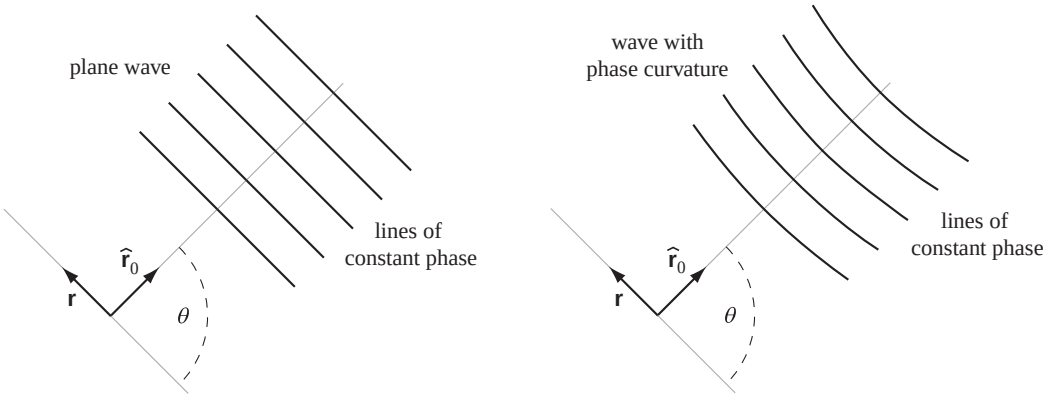

(a) Plane wave (b) Wave with phase curvature

Figure 3.5: Wavenumber vectors

3.4 Phased Array Signal Processing

A more robust method of signal processing of a group of sensor signals involves the use of wavenumber filters for directional sensing applications. The goal in the case of wavenumber filters is similar to time shifting in that unwanted information is removed while bringing out the desired signal source. This is known as virtually steering the array toward the source of interest, as shown in Figure 3.7. The abilities and limitations of wavenumber filters can be examined in a rigorous manner based on Fourier techniques.

The group of sensor signals is consolidated into one signal called the array response. The simplest method of consolidation is to add up the sensor signals:

$$\psi = \int v(x, y)\, dA \tag{3.5}$$

ψ is the array response and v is the sensor output at location (x, y). In mechanical systems, the sensor signals could represent commonly used quantities such as strain, displacement, or acceleration. If weights are applied to the sensors then the behavior of the array response will depend on the characteristics of these weights:

$$\psi = \int \phi(x, y)\, v(x, y)\, dA \tag{3.6}$$

$\phi(x, y)$ is the set of gains, or spatial weighting. The spatial weights applied to the group of sensors determines the content of the array response. For the simple

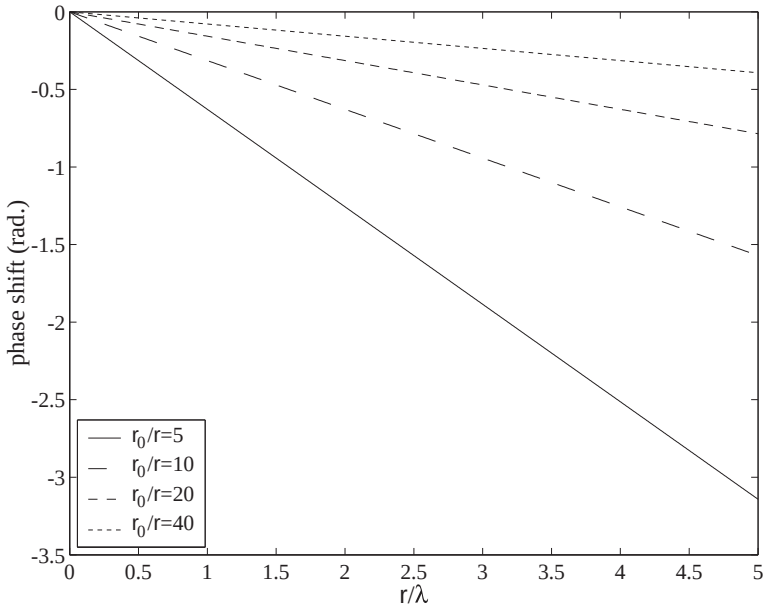

Figure 3.6: Phase shift from wavefront curvature

case where the array is distributed along the x axis, the array response becomes an integral in one dimension:

$$\psi = \int \phi(x)\, v(x)\, dx \tag{3.7}$$

For a transient case, both the sensor signals and and the array response become functions of time, t, as well. A Fourier identity describes the wavenumber response of the array:

$$\int \phi(x)\, v(x,t)\, dx = \int \Phi(-k_x)\, V(k_x,t)\, dk_x \tag{3.8}$$

Φ and V are the wavenumber domain counterparts to the spatial functions, ϕ and v, respectively. The spatial-wavenumber domain relationship is analogous to the time-frequency domain relationship which is more common in signal processing techniques. Unlike the time-frequency domain relationships, both the positive and negative portions of the wavenumber domain may be potentially used. The array response formulation in Equation (3.8) is restricted to the x-axis and the k_x term refers to the wavenumber along that axis.

From the Fourier identity, the spatial weighting function, $\phi(x)$, determines the properties of the array response given sensor signal $v(x,t)$. The application of

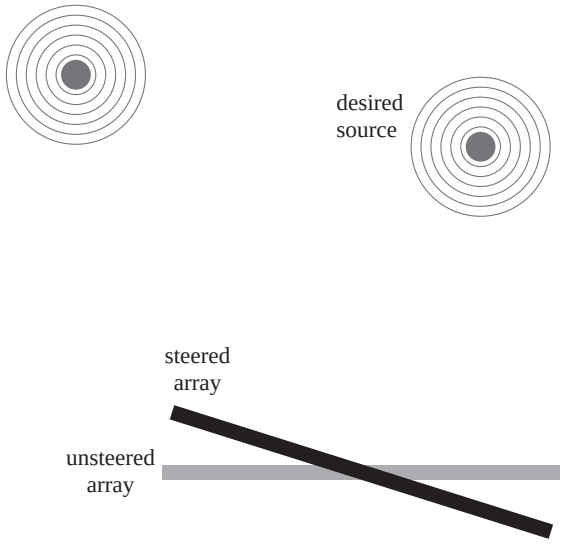

Figure 3.7: Array steering

a spatial weighting and the resulting integration effectively decomposes the signal in the same way that the Fourier transform decomposes a time domain signal into complex exponential components.

Assuming a wave propagating with a given frequency and wavenumber, the plane wave can be described in terms of a wavenumber vector, $\vec{k}$, which indicates the wave propagation properties as well as its direction of motion, shown in Figure 3.8. To virtually steer the array to look in the direction of the oncoming plane wave, the spatial weights, $\phi(x)$, applied to the array needs to be defined such that only information from the oncoming direction is passed through to the array response. The spatial weights collectively act as a filter which only allows part of the gathered information corresponding to the oncoming plane wave to pass through. Since the array is distributed along the x-axis, the spatial filter can only use the component of the wavenumber vector along the array axis, k_x, as a source of information.

The wavenumber spectrum of an ideal filter, $\Phi(k_x)$, is shown in Figure 3.9(a) where the δ function is placed at the desired wavenumber, $\bar{k}_x$. In this case, the only component of the wavenumber domain which is allowed to pass through to the array response is $\bar{k}_x$. The limits, $\pm k_{x,max}$, correspond to waves traveling in opposite

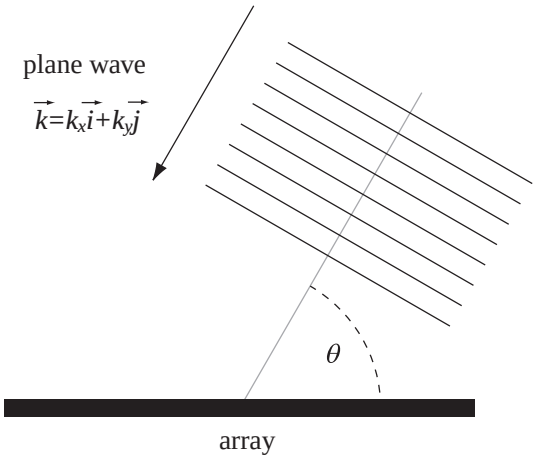

Figure 3.8: Plane wave approaching array

directions along the array axis while a wavenumber of $k_x = 0$ corresponds to a wave which is traveling normal to the array axis, shown in Figure 3.10. There is a one-to-one relationship between $\bar{k}_x$ and the direction of wave propagation as seen in Figure 3.9(b). A δ function placed between $-k_{x,max}$ and $k_{x,max}$ in the wavenumber domain corresponds to a spatial weighting functions which is sensitive to a specific angle. In this way, the array is virtually steered by the spatial weights so that it is only sensitive to a wave traveling in a particular direction.

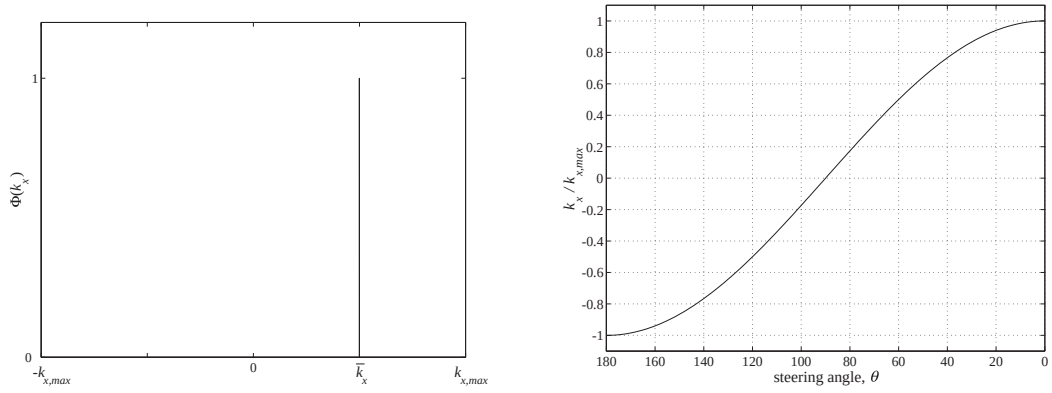

(a) Ideal spatial filter

(b) $\bar{k}_x$ versus steering angle, $\bar{\theta}$

Figure 3.9: Wavenumber filters

Virtual steering is analogous to rotating a physically orientable antenna so

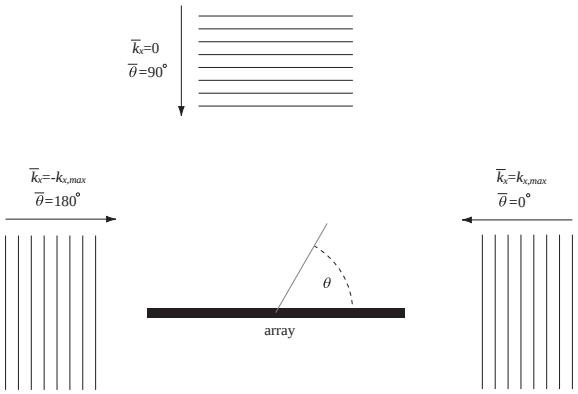

Figure 3.10: Plane waves relative to array

that it looks in a particular direction. In both these cases, the sensing mechanism is altered so that the phase angle of a plane wave traveling in a particular direction is the same at each sensing location. For waves coming from undesired directions, there are small phase angle shifts at each sensing location. By summing the sensor responses together, the in-phase components add constructively while the out-of-phase components add destructively. Since signals arriving from the off steering locations are out-of-phase with respect to each other, they add destructively and are not seen by the array, thus they are filtered out.

The spatial weighting function corresponding to the ideal filter in Figure 3.9(a) contains both imaginary and real parts:

$$\phi(x) = \cos\left(\bar{k}_x x\right) + i \sin\left(\bar{k}_x x\right) \tag{3.9}$$

The real part of the spatial weighting is an even function with respect to the center of the array while the imaginary part is an odd function. The array response can then be split into two parts:

$$\psi = \int \phi_R(x)\ v(x)\ dx + i \int \phi_I(x)\ v(x)\ dx \tag{3.10}$$

$\phi_R(x)$ and $\phi_I(x)$ refer to the real and imaginary components of the spatial weighting, respectively. It is important to note that if $\Phi(k_x)$ is not an even function in the wavenumber domain then the corresponding Fourier counterpart, $\phi(x)$, will have an imaginary component.

Since, in general, directional filtering involves a bandlimited section of the wavenumber domain which includes both the positive and negative regions, then the spatial weighting function will necessarily have real and imaginary components. The positive and negative regions of the wavenumber domain correspond to waves which propagate in different directions along the array. If the direction of the wave is of no consequence, then only the real component of the spatial weighting is of concern.

The imaginary component of the array response can be achieved by using a $\pi/2$ phase shift. A way of introducing a $\pi/2$ phase shift needed for directional filtering is to utilize time domain signal manipulation assuming the sensor signals is band limited around frequency ω_c. Differentiation introduces a $i\omega$ term into the frequency response of the signal while integration produces a $-i/\omega$ term into the frequency response. Integration is an appropriate choice to use with experimental signals because it is numerically more stable than differentiation. Assuming that the wave is propagating in time with frequency ω_c, then the array response in Equation (3.10) can be reformulated:

$$\psi(t) = \int \phi_R(x)\, v(x,t)\, dx - \omega_c \int \phi_I(x) \left(\int v(x,t)\, dt \right) dx \tag{3.11}$$

This formulation eliminates the imaginary term seen previously and is easily implementable as well.

The restriction that the sensor signals are narrow-band serves an important purpose for a two reasons. For a linear array, the array is sensitive to the projection of the wavenumber vector onto the array axis, k_x. If wide-band signals are used, a situation could arise where the same k_x corresponds to waves of different frequencies arrive from different directions:

$$\begin{aligned} k_x = k(\omega_1)\cos(\theta_1) &= k(\omega_2)\cos(\theta_2) \\ \frac{k(\omega_1)}{k(\omega_2)} &= \frac{\cos(\theta_2)}{\cos(\theta_1)} \end{aligned} \tag{3.12}$$

Additionally, the imaginary component distinguishes the direction of the wave as it passes through the array. Since the direction of wave propagation is determined

by the sign of the wavenumber, the imaginary component in Equation (3.9) distinguishes between the leftward and rightward waves, as it is an odd function with respect to x. The inclusion of the imaginary component in Equation (3.11) is due to the simplification that integrating the sensor signals allows. If, however, the source direction is known, then the direction of the propagating waves are known and the array response can expressed in terms of just the real part of the spatial weighting:

$$\psi(t) = \int \phi_R(x)\, v(x,t)\, dx \tag{3.13}$$

Since the spatial weighting effectively performs the spatial Fourier transform of the sensor signals, the array response may be used to examine the wavenumber content of the sensor signals at each instance in time. This is useful in determining the frequency/wavenumber content of the spatial distribution.

3.5 Finite Length Arrays

For the development of the array response in the previous section, the array was assumed to be continuous and of infinite length. In practical situations, the array will be of a finite length and an understanding of the capabilities of such an array size is important. The integrals in Equation (3.7) will have limits of $-L/2 \leq x \leq L/2$ for an array of length L. The corresponding wavenumber spectrum of the spatial weights will be altered because of the limitation imposed on the length of the array. Limiting the size of the array corresponds to a widening of the bandpass characteristics of the wavenumber filter. The δ function in the wavenumber domain in Figure 3.9(a) will expand into a lobe and encompass a range of wavenumbers. Due to the finite length of the array, the wavenumber filter allows for unwanted wavenumbers to pass through to the array response.

For example, consider the spatial weighting of $\phi(x) = 1$ where the array is sensitive to waves traveling in the 90° direction. The Fourier counterpart, $\Phi(k_x)$, is the delta function $\delta(k_x)$ which is the ideal spatial filter shown in 3.9(a) where $\bar{k}_x = 0$. By setting $\phi(x) = 1$ for $-L/2 \leq x \leq L/2$, the array has a length of L. The

new wavenumber spectrum of the spatial weighting function is a sinc function:

$$\Phi(k_x) = \int_{-L/2}^{L/2} e^{-ik_x x} dx = L \frac{\sin(k_x L/2)}{(k_x L/2)} \tag{3.14}$$

There appears to be a singularity when $k_x L/2$ approaches 0 as the denominator in the expression vanishes. When small angle assumptions are used for the numerator, $\sin(k_x L/2) \rightarrow k_x L/2$, and the numerator and denominator of Equation (3.14) cancel out.

A representative curve based on Equation (3.14) is shown in Figure 3.11(a). For the ideal filter steered at $\bar{k}_x = 0$, only waves traveling at $\theta = 90°$ are permitted in the array response; however, when the length of the array is finite, wavenumbers other than $k_x = 0$ are allowed through, corrupting the ideal filter characteristics. The destructive interference relied upon by the ideal filter to cancel out-of-phase components is not as complete for the finite length array causing extra information to pass through from off-steered directions. As the length of the finite array increases, the width of the main lobe in Figure 3.11(b) decreases.

The wavenumber beamwidth is a measure of the bandwidth, Δk_x, of the wavenumber filter and is a function of the size of the main lobe in the wavenumber spectrum of the spatial weights. The bandwidth of the filter is the length of the axis where $\Phi \geq \Phi_{max}/\sqrt{2}$ and for the finite array used in Equation (3.14), the bandwidth is determined by finding the k_x which satisfies $\sin(k_x L/2)/(k_x L/2) = 1/\sqrt{2}$. There are two points on the wavenumber spectrum which satisfy this criterion:

$$\frac{k_x L}{2} = 1.14 \quad \text{and} \quad \frac{k_x L}{2} = -1.14 \tag{3.15}$$

The wavenumber beamwidth is $\Delta k_x = 4.56/L$ and is only dependent on the length of the array. Since the beamwidth is a measure of the wavenumber sensitivity of the array, it is advantageous to have long array lengths.

While steering of an ideal array will shift the location of the delta function in Figure 3.9(a), steering of a finite array shifts the main lobe in Figure 3.11(a) so that it is centered at different locations, seen in Figure 3.12(a). This is accomplished by

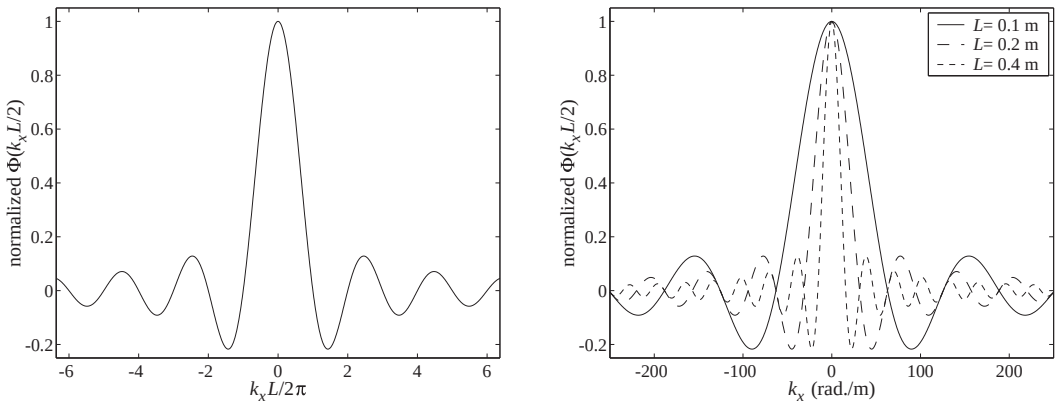

(a) Representative array response for finite array

(b) Array response for array of various lengths

Figure 3.11: Wavenumber response for finite array

introducing an offset term in Equation (3.14) such that the main lobe shifts:

$$\Phi(k_x) = L\frac{\left(\sin(\left(k_x - \bar{k}_x\right) L/2\right)}{\left(\left(k_x - \bar{k}_x\right) L/2\right)} \tag{3.16}$$

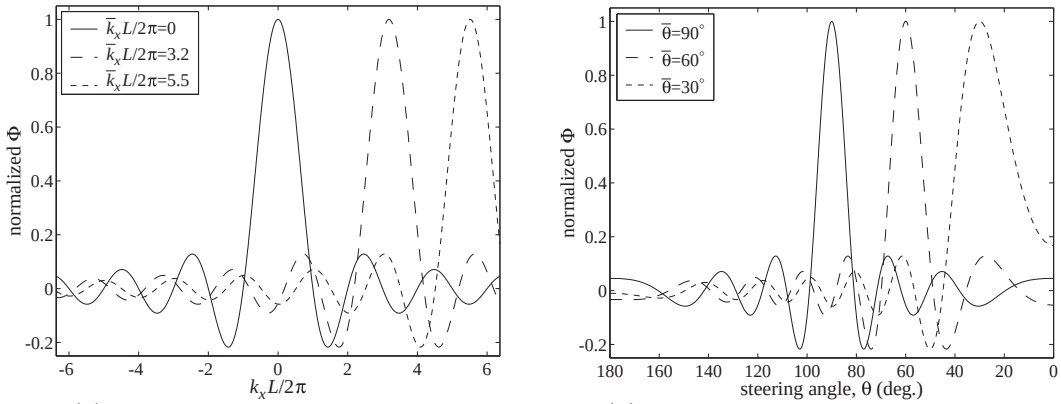

(a) As function of wavenumber

(b) As function of steering angle, θ

Figure 3.12: Array responses

Figure 3.12(b) shows the same responses as in Figure 3.12(a) except, in this case, as a function of angle, θ. The width of the main lobe in the filter response increases as the main lobe is steered off of $\theta = 90°$. This is due to the nonlinear relationship between steering angle and projected wavenumber, $k_x = k\cos(\theta)$. The ability of the array to distinguish between waves coming from different angles depends

on the direction the array is steered toward. This is seen in Figure 3.9(b) where, at steering angles of 0° and 180° the corresponding wavenumber does not change very much. The beamwidth of the spatial weights is then a function of the steering angle and is determined in the same way as for the wavenumber beamwidth. Figure 3.13 plots the angular beamwidth of the spatial filter. As expected, the beamwidth is smallest when the array is steered toward 90° and increases as the steering angle moves to the extremes. The beamwidth gets smaller at the very extreme steering angles because there is a maximum angle of 0° and 180°. The plot also shows that the beamwidth of the array drops as either the length of the array or the wavenumber of interest increases. For a given array size then, it is advantageous to use a larger wavenumber because the capabilities of the array improve.

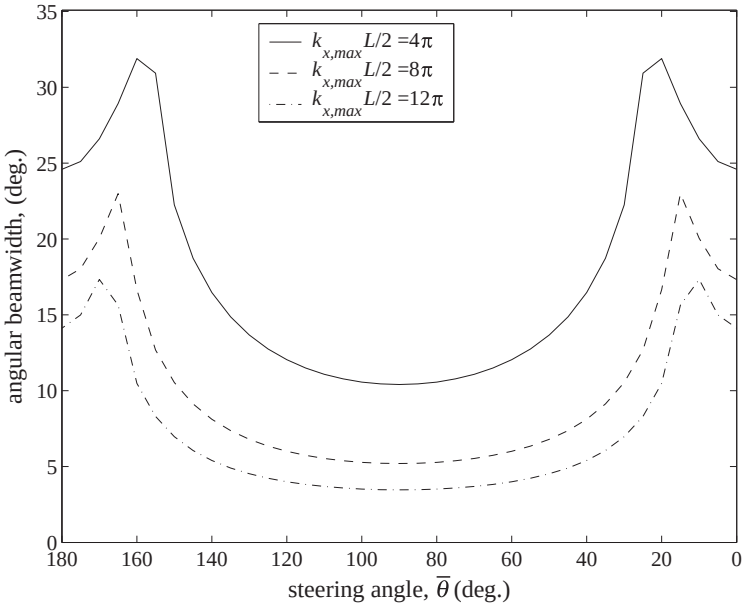

Figure 3.13: Angular beamwidth of spatial weights

For waves arriving perpendicular to the array, a steering angle of 90° or wavenumber of 0, the filter can distinguish between small changes in incoming angles because the main lobe's width is relatively small. For waves arriving parallel to the array, steering angles of 0° and 180° or a normalized wavenumber $k_x/k_{x,max} = \pm 1$, the main lobe becomes wider and the array has trouble in filtering out waves that

are close to the desired steering angle.

Restricting the size of an infinite array to a finite length is interpreted as modifying the array distribution by using a rectangular window function. Window functions are sets of weights that have prescribed wavenumber domain properties. This modifies the wavenumber response of the ideal filter but makes the filter a more manageable length. Other window functions can also be used to to produce a better wavenumber response than that produced by the rectangular window function. The main goals of window functions are two-fold:

1. Reduce the width of the main lobe in the wavenumber response in Figure 3.11(a). This lobe appears because the array is finite and is considered a degradation from the ideal wavenumber response.

2. Reduce the magnitude of the side lobes. These are the peaks which appear next to the main lobe in Figure 3.11(a). Though the side lobes are at a lower amplitude, information corresponding to these portions of the wavenumber domain will pass through the filter, corrupting the quality of the array response.

There is, however, a trade-off between the width of the main lobe and the magnitude of the side lobes.

The simplest window function is a rectangular window. A number of continuous window functions have been developed which have better qualities than the rectangular window. These window functions and their spatial distributions are shown in Table 3.1. All of the given window functions are defined for $-L/2 \leq x \leq L/2$ and vanish outside of that region.

Applying a window function to the spatial weighting creates a new wavenumber filter. The new wavenumber response of the combined spatial weights is the convolution of the wavenumber responses of both the original spatial weighting and the window function:

$$\phi_w(x) = \phi(x)\, h(x) \qquad \Phi_w\left(k_x\right) = \Phi\left(k_x\right) * H\left(k_x\right) \tag{3.17}$$

$\phi_w(x)$ is the windowed spatial weighting and $\Phi_w\left(k_x\right)$ its Fourier counterpart. Similarly, $h(x)$ is the window function and $H\left(k_x\right)$ its Fourier counterpart. Any combi-

Window Function	Analytical Form			
	a	b	c	
Rectangular	1	0	0	$h(x) = a + b\cos\left(\frac{2\pi x}{L}\right) + c\cos\left(\frac{4\pi x}{L}\right)$
Hanning	1/2	1/2	0	
Hamming	.54	.46	0	
Blackman	.42	.5	.08	
Cosine	$h(x) = \cos(\pi x/L)$			
Bartlett (Triangular)	$h(x) = 1 - \lvert x\rvert / (L/2)$			
Welch	$h(x) = 1 - (x/(L/2))^2$			
Kaiser	$h(x) = J_o\left(\alpha\sqrt{1-(x/(L/2))^2}\right)/I_o(\alpha)$			
Tukey	$h(x) = \begin{cases} 1 & \text{if } 0 \le \lvert x\rvert \le (1-r)L/2 \\ \frac{1}{2}\left(1+\cos\left(\pi\frac{x-(1-r)L/2}{rL/2}\right)\right) & \text{if } (1-r)L/2 \le \lvert x\rvert \le L/2 \end{cases}$			
Gauss	$h(x) = e^{-\frac{1}{2}\left(\alpha\frac{x}{L/2}\right)^2}$			
Modified Bartlett-Hanning	$h(x) = .24\,(1 - \lvert x\rvert/(L/2)) + .76\,(1/2 + 1/2\cos(\pi x/(L/2)))$			
Bohman	$h(x) = (1 - x/(L/2))\cos(\pi x/(L/2)) + (1/\pi)\sin(\pi x/(L/2))$			

Table 3.1: Common Window Functions, Defined Over $-L/2 \le x \le L/2$

nation of window functions could be used with the knowledge that the wavenumber spectrum of the resulting hybrid window would be a convolution of the individual wavenumber spectra.

The analytical form of the wavenumber spectra of the most common window functions are presented in Table 3.2. The wavenumber spectrum for the rectangular window (with a=1, $b = 0$, and $c = 0$) matches that in Equation (3.14). Since the window functions are even functions with respect to x, their corresponding wavenumber spectra are also even functions with k. The more common window functions as

	Window Function	Wavenumber Spectrum
Rectangular, Hanning, Hamming, and Blackman	$h(x) = a + b\cos(2\pi x/L) + c\cos(4\pi x/L)$	$H(k) = aL\frac{\sin(kL/2)}{kL/2} + b\frac{L}{2}\left(\frac{\sin(kL/2-\pi)}{kL/2-\pi} + \frac{\sin(kL/2+\pi)}{kL/2+\pi}\right) + c\frac{L}{2}\left(\frac{\sin(kL/2-2\pi)}{kL/2-2\pi} + \frac{\sin(kL/2+2\pi)}{kL/2+2\pi}\right)$
Cosine	$h(x) = \cos(\pi x/L)$	$H(k) = \frac{L}{2}\left(\frac{\sin\left(\frac{kL}{2}-\frac{\pi}{2}\right)}{\frac{kL}{2}-\frac{\pi}{2}} + \frac{\sin\left(\frac{kL}{2}+\frac{\pi}{2}\right)}{\frac{kL}{2}+\frac{\pi}{2}}\right)$
Bartlett (Triangular)	$h(x) = 1 - \lvert x\rvert/(L/2)$	$H(k) = \frac{L}{2}\frac{\sin^2\left(\frac{kL}{4}\right)}{\left(\frac{kL}{4}\right)^2}$
Welch	$h(x) = 1 - (x/(L/2))^2$	$H(k) = 2L\frac{1}{(kL/2)^2}\left(\frac{\sin(kL/2)}{kL/2} - \cos(kL/2)\right)$

Table 3.2: Wavenumber Spectra of Window Functions

well as their wavenumber spectra are also plotted in Figure 3.14. The wavenumber spectra associated with the different window functions exhibit the same properties as the rectangular window; there is a dominant main lobe and corresponding side lobes. All of the window functions have reduced sidelobe heights compared to the rectangular window function wavenumber spectrum. The trade-off occurs when the beamwidth of the different functions are examined as all of the newer window functions have wider beamwidths compared to the rectangular window.

Typically, the spatial weights corresponding to the ideal wavenumber filter is used along with a particular window function. The convolution of the two wavenumber responses causes the main lobe in the window function's wavenumber spectrum, $H(k_x)$, to be shifted to the position of the δ function of the ideal filter's wavenumber spectrum:

$$\Phi_w(k_x) = H\left(k_x - \bar{k}_x\right) \tag{3.18}$$

Thus the wavenumber response of a finite length filter is a function of the steering direction of the ideal filter as well as the wavenumber response of the window function. Because the ideal filter wavenumber spectrum is convoluted with the window

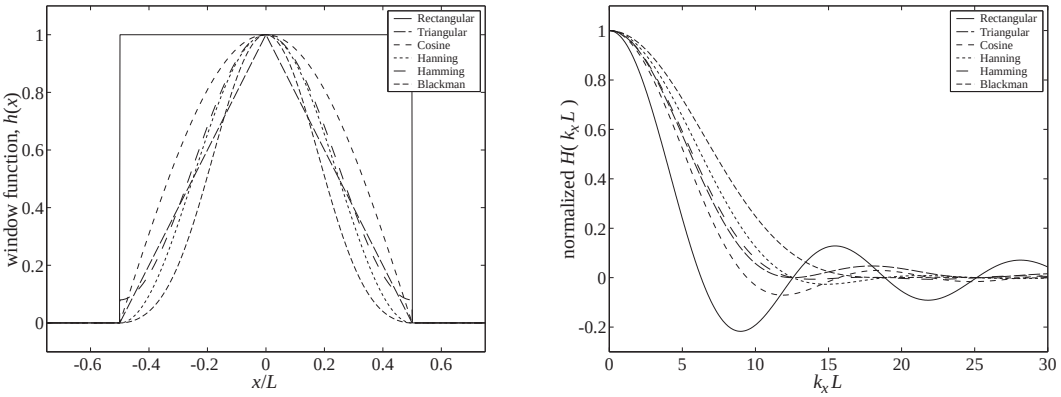

(a) Spatial distribution (b) Wavenumber spectra of window functions

Figure 3.14: Window functions

function's wavenumber spectrum, a finite array will not be able to provide an ideal filter's capability. The finite array will necessarily have a main lobe which will let undesired wavenumbers pass through.

3.6 Discrete Arrays

Though a continuous sensor array has been used before[125, 126], typically an array is composed of a series of discrete sensors, as shown in Figure 3.15. A discrete sensor array is more appropriate for directional sensing of wave propagation in a plate because the spatial weighting needs to be changed in order to manipulate the array sensing direction. Different sets of spatial weights are needed to steer the array. After all of the signals are gathered, a group of sensor signals could then be processed to look in a particular direction.

For the case of a discrete array, the integral in Equation (3.7) is replaced by a summation over the number of elements in the array:

$$\psi(t) = \frac{1}{N} \sum_{n=-(N-1)/2}^{(N-1)/2} \phi(x_n)\, v(x_n, t) \tag{3.19}$$

$x_n = n\Delta x$ and N is the number of sensors and assumed to be odd. Sensor spacing, Δx, becomes an important quantity in determining the array's capabilities.

For an array of N elements, the discrete array response can be expressed in a

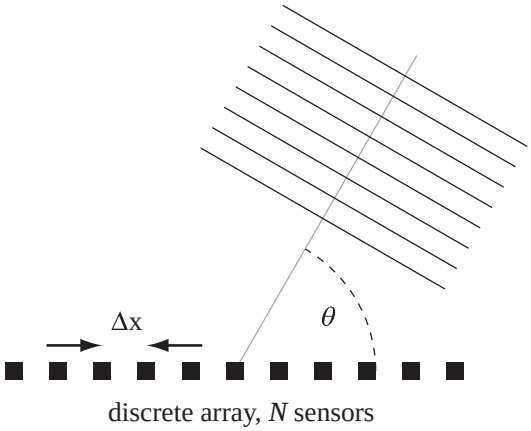

Figure 3.15: Plane wave with a discrete array

closed form expression:

$$\Phi\left(k_x N\Delta x\right) = \frac{\sin\left(k_x N\Delta x/2\right)}{\sin\left(k_x \Delta x/2\right)} \tag{3.20}$$

This expression is very similar to the expression for the finite continuous array in Equation (3.14). The array response for the discrete array is shown in Figure 3.16(a) for various N. The width of the main lobe of the array response decreases as the number of elements in the array increase. By using a larger number of elements in the array, the array appears to be longer, which improves its filtering characteristics. If the limits of $k\Delta x/2\pi$ are extended in Figure 3.16(a), other large lobes appear which have the same magnitude as the main lobe that appears at $k\Delta x/2\pi = 0$.

The additional large lobes, called grating lobes, in Figure 3.16(b) are found by examining the analytical form of the discrete array in Equation (3.20). Both the numerator and denominator in the expression are periodic functions. The zeros of the numerator occur at $k_x N\Delta x/2\pi = m$ and the zeros of the denominator occur at $k_x \Delta x/2\pi = p$ where m and p is any integer. Note that the zeros of the numerator are a function of the number of elements in the array, N, while the denominator has no such dependence. Just as in the finite length array case for Equation (3.14), there appears to be a singularity when $k_x\Delta x$ approaches 0. The numerator and denominator cancel when using small angle assumptions for the sine function. The period of the denominator is larger than the numerator. This is apparent when

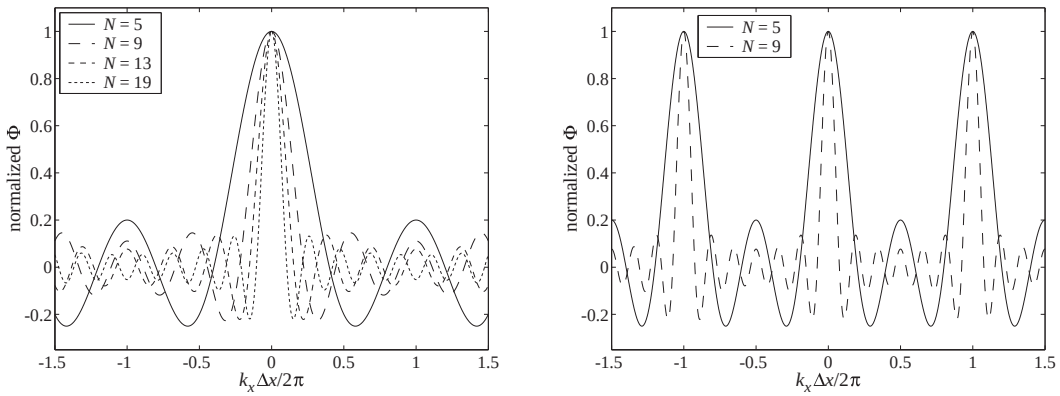

(a) Discrete array wavenumber response (b) Grating lobes

Figure 3.16: Discrete array

observing the plots in Figure 3.16 as the wavenumber spectrum crosses the x-axis multiple times before the grating lobes appear. The grating lobes appear when both the numerator and denominator vanish, $p = m/N$. When grating lobes are present in the wavenumber domain of interest, an undesirable situation arises where the the array becomes highly sensitive to multiple regions in the wavenumber domain. A limitation on the maximum allowable wavenumber is placed such that the denominator in Equation (3.20) is prevented from reaching a zero corresponding to these grating lobes, $|k_x \Delta x/\pi| < 2$ or $k_x < 2\pi/\Delta x$. This limitation prevents grating lobes from appearing in the wavenumber response of the unsteered array and is inversely proportional to the sensor spacing in the array.

This limitation assumes that the main lobe appears at $k_x = 0$. In practical applications, the array should be steerable from one direction to the other and there should be only one main lobe in the wavenumber range of interest. When the main lobe is shifted to steer the array, the grating lobes are also shifted. A situation can occur where the grating lobe enters the domain of interest, shown in Figure 3.17.

A tighter limitation is then placed such that grating lobes do not appear regardless of the position of the main lobe in the wavenumber range of interest. This limitation is equivalent to satisfying the Nyquist condition in the spatial domain.

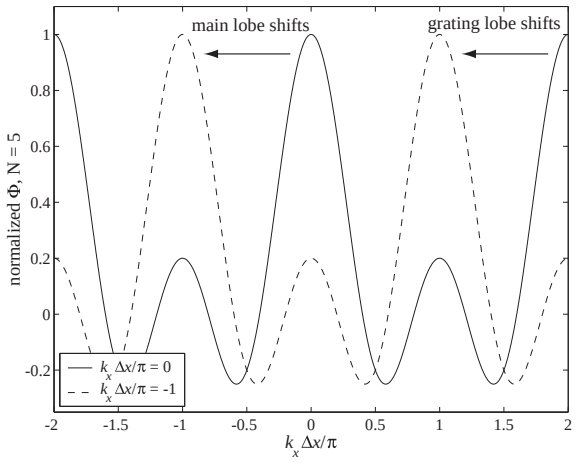

Figure 3.17: Wavenumber response of discrete array after steering

The maximum wavenumber that can be used is dependent on the array spacing:

$$k_x < \pi/\Delta x \tag{3.21}$$

From this relationship, the cutoff wavenumber is $k_{x,co} = \pi/\Delta x$. In time domain signal processing, the Nyquist condition is a commonly used limit where the frequency of interest must be less than half the sampling frequency. In order to eliminate the presence of any part of the grating lobe, a stricter limit is placed on the maximum wavenumber where $k_{x,co} = .4(2\pi/\Delta x)$. The same restriction holds in the time domain as the sensor spacing is equivalent to the time step which defines the sampling frequency. If k_{co} is exceeded then grating lobes appear in the spatial weights wavenumber response. This causes the array to be sensitive to two directions at once which corrupts its unique directional sensing ability.

Window functions are also used for a set of discrete points. The window functions mentioned previously in Table 3.1 are adapted for use for a discrete set of points by simply evaluating the window function at each sensor location on the x axis. The goals of these window functions are the same as those for the continuous windows with the underlying requirement of satisfying the spatial Nyquist condition.

A windowing technique designed specifically for discrete elements is the Dolph-Chebyshev window function. The spatial weighting function may be described by a

series of δ functions on the x axis:

$$h(x) = \sum_{-(N-1)/2}^{(N-1)/2} h_n \delta(x - n\Delta x) \tag{3.22}$$

The continuous Fourier transform used in Equation (3.14) in order to find the wavenumber response of the spatial weighting function can be discretized such that the integral becomes a summation:

$$H(k_x) = \int h(x) e^{-ik_x x} dx = h_0 + \sum_{n=1}^{(N-1)/2} h_n 2 \cos\left(2n \frac{k_x \Delta x}{2}\right) \tag{3.23}$$

The summation can be expressed in terms of a Chebyshev polynomial of order $(N-1)$ using the class of Chebyshev polynomials of the first kind, described in more detail in Appendix E. The coefficients, h_n, are determined based on an $N-1$ order Chebyshev polynomial and a prescribed ratio between the heights of the side lobes and the main lobe. The Dolph-Chebyshev technique ensures that the resulting beamwidth will be the smallest possible. The wavenumber responses for two different cases of side lobe levels of a discrete array is shown in Figure 3.18. As the number of sensors increase, the array is able to do a better job of wavenumber filtering. The trade off with the Dolph-Chebyshev method is also seen where the beamwidth grows as the side lobe levels are reduced.

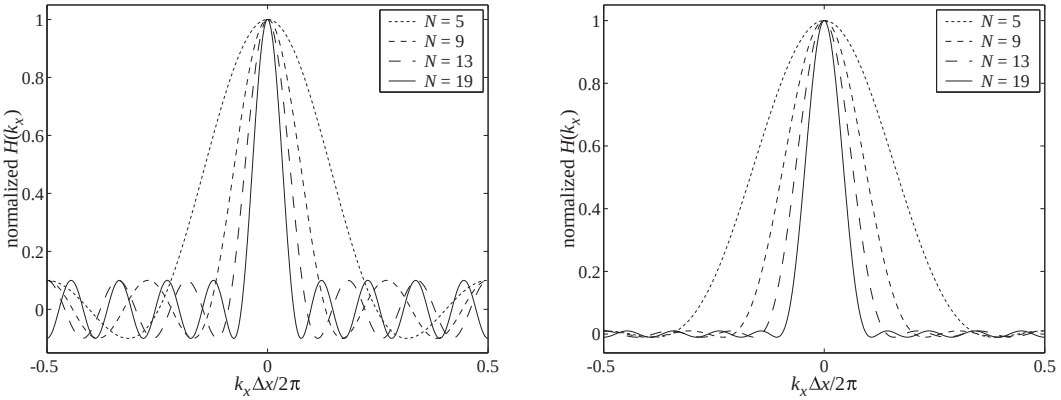

(a) Wavenumber response (r=.1) (b) Wavenumber response (r=.01)

Figure 3.18: Wavenumber responses using Dolph-Chebyshev window

The major benefit with the Dolph-Chebyshev weighting is the ability to effectively remove the side lobe levels with limited impact on the width of the main lobe.

This is shown in Figure 3.19 where the array response using the rectangular weights (all of weights are uniform) is compared to a Dolph-Chebyshev spatial weighting. For both the eleven and nineteen sensor case, the side lobe levels were effectively eliminated with a slight degradation to the width of the main lobe.

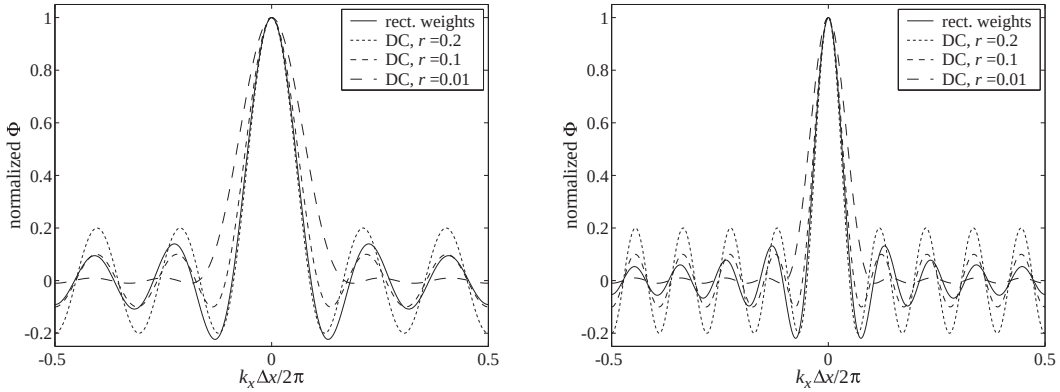

(a) Array response (N=11) (b) Wavenumber response (N=19)

Figure 3.19: Comparison between rectangular and Dolph-Chebyshev weighting

3.7 Implementation of Phased Array Signal Processing

An array bonded to a structure which is capable of steering in different directions will necessarily be finite and discrete. The components needed for data acquisition and processing of the sensor signals are shown in Figure 3.20. For a large number of sensor signals are expected, a multiplexer enables the sampling of multiple sensors using one channel of data. Filtering and amplification of the raw data can be performed using analog electronics as part of the signal conditioning. This may include the bandpass filter which is necessary for directional filtering. Temporal integration can be performed using either analog or discrete methods. An analog integration would require doubling the number of channels collecting data. To keep the number of input channels low in the experimental setup, temporal integration was performed using discrete approximations after the signals were gathered. Similarly, the spatial weights can be applied using analog amplifiers; however, since the array will need to be steered to different directions, the spatial weights were adjusted as a

post-processing step after the data acquisition.

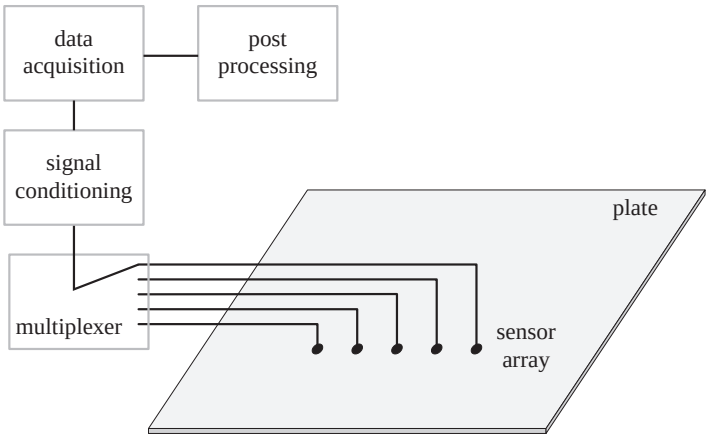

Figure 3.20: Components of data acquisition

The described construction of the array response from a set of sensor signals from an array is a discrete implementation of Equation (3.11). A discrete version is shown in Equation (3.24):

$$\psi(t) = \frac{1}{N} \sum_{n=-(N-1)/2}^{(N-1)/2} \phi_R(x_n)\, v(x_n, t) - \omega_c \frac{1}{N} \sum_{n=-(N-1)/2}^{(N-1)/2} \phi_I(x_n) \left(\int v(x_n, t)\, dt \right) \tag{3.24}$$

$\phi_R(x_n)$ and $\phi_I(x_n)$ are the spatial weights at location x_n. A diagram of the construction of the array response using individual sensor signals is shown in Figure 3.21.

3.8 Summary

Propagation of information from a source to a sensing location can be described in terms of a generic solution. The phase information of the solution is used by sensor arrays to listen selectively to a given source. An approximation is made to the phase of a signal from an arbitrary location. The approximation is shown to be composed of multiple parts, including linear and quadratic phase components. The linear phase component provides information necessary to steer an array while the quadratic correction term provides information necessary to focus an array.

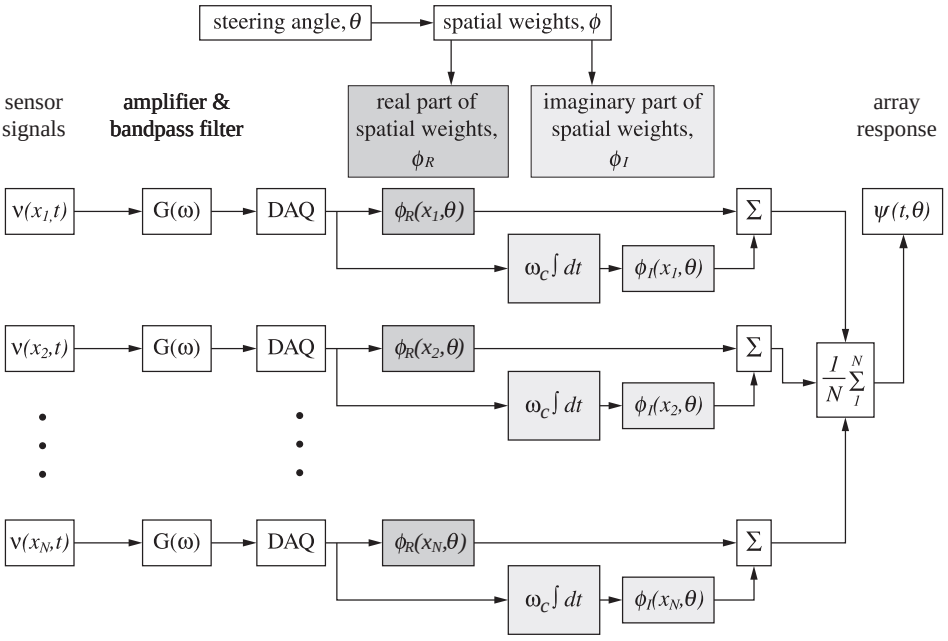

Figure 3.21: Signal flow diagram for creating array response

Sensor arrays and the associated signal processing enable signals to be filtered in the wavenumber domain. For plane waves propagating in a medium such that the wavenumber of the wave is independent of the direction of propagation, there is a unique relationship between steering angle and the projected wavenumber of the wave onto the array axis. The spatial weighting function applied to the sensor array directionally steers the array such that the array response only contains information propagating in a particular direction.

The development of the array response formulation is for a linear one dimensional array though the same techniques can be extended and applied to arrays with a sensor distribution in two or three dimensions. For practical purposes, a sensor array will have a finite number of discrete sensors. This degrades the ideal filtering characteristics of the array. Using appropriate signal processing on the time domain data, a group of transient signals can be analyzed to produce a consolidated signal which has directional filtering properties.

There are a number of issues with using a phased array technique for analyzing

data from a group of sensors on a plate. The main issues are summarized below:

1. The spatial weights that are used are based on the assumption that a plane wave is approaching the array. This assumption is valid if the source of the signal is far away from the sensor array. As the sensor array gets closer to the source signal, the wavefront which hits the array will have non-zero curvature. There are corrections that can be made to the spatial weighting function to take this curvature into account. This is known as "focusing" the array and the distance to the source needs to be known beforehand to determine these corrections. The plane wave assumption does provide a linear phase variation approximation to the wavefront of large curvature. Steering will still be able to determine the direction to the source provided the curvature of the wavefront is not too large.

2. When an array is constrained to be of finite length, there is a spreading out of the ideal delta function directional filtering characteristic into a lobe pattern. A main lobe is placed where the original delta function was located. This becomes a problem when looking at the "endfire" conditions of the array ($\theta = 0^\circ$ or 180°) where the array has reduced angular resolution.

3. Along with the spreading out of the ideal directional filtering characteristics, a finite array wavenumber response will also contain side lobes next to the main lobe. The simple rectangular window function has side lobes of large magnitude thereby affecting the directional filtering capability. This can be somewhat resolved by using window functions at the expense of widening the main lobe of the filter response.

4. Discretizing the array into individual elements raises a spatial sampling issue where the maximum wavenumber that can be seen is dependent on the distance between sensors. The spatial Nyquist condition must be satisfied in order to ensure the array is not equally sensitive to waves travelling in radically different directions.

5. Directional filtering is achieved by projecting the wavenumber vector onto the array distribution. Since the array distribution is along a line, this projection is the same if θ is negative or positive. Consequently, for a linear array, the phased array technique cannot distinguish between waves that approach from the front or back of the array distribution.

Chapter 4

Damage Detection In Isotropic Plates

4.1 Introduction

Damage detection in isotropic plates is accomplished using transient plate dynamics along with a sensor array to decompose the response of the plate. The sensor array is shown to be able to deconstruct a set of signals into component wavenumbers. To verify this, the wavenumber-frequency relationship for the Aluminum plate can be reproduced using experimental data for both the A0 and S0 modes.

For a damage detection application, an array is positioned at the bottom edge of a plate and the damage, in the form of a hole, is placed on the plate. From the array response, the location of the damaged region on the plate can be ascertained. This is done using both the A0 and S0 modes. The reflection from the damaged region is shown to grow as the size of the hole increases, indicating the size of the damage. In this manner, multiple damaged regions can be detected. A sizing study is shown next where the reflection of a Lamb mode from a damaged region is dependent on the size of the damage as well as the interrogating wave. This is shown for the A0 and S0 cases. The array is also shown to be able to determine loss of preload from a bolt.

4.2 PVDF Sensor Array

A sensor array made from a 52 μm (.002 in.) thick PolyVinyliDene Fluoride (PVDF) piezoelectric sheet from Measurement Specialities, Inc. is used in the experimental damage detection setup. The sensor array, shown in Figure 4.1, is composed of 19 elements with a spacing of 3.175 mm (1/8 in.) where each sensor element has a

diameter of 1.59 mm (1/16 in.). The corresponding maximum cutoff wavenumber for the array is $k_{x,co} \approx 791\text{rad/m}$. The wavenumber beamwidth of the array depends on the number of elements in the array.

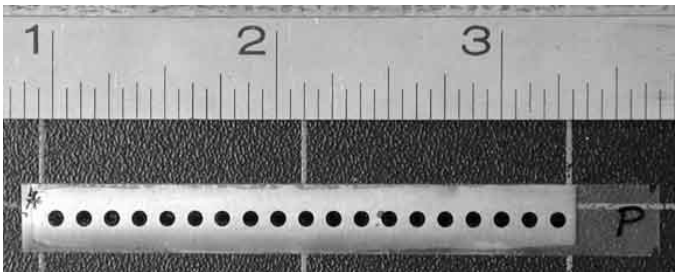

Figure 4.1: PVDF array

4.3 Reconstruction of Wavenumber Frequency Relation for Aluminum Plate

The sensor array and the ability to decompose the spatial signals into component wavenumber was validated by experiment on an Aluminum plate of 1.52 mm (.060 in.) thickness. A diagram of the setup is shown in Figure 4.2(a). A single 3.2 mm $\times$ 3.2 mm (1/8 in. $\times$ 1/8 in.) PZT-5H piezoceramic actuator was placed on the right edge of the top surface of the plate.

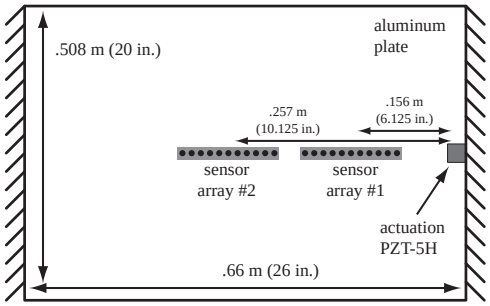

(a) Experimental setup

(b) Close-up of actuator and sensor arrays

Figure 4.2: Array validation on Aluminum plate

The actuator was excited with a transient signals at various frequencies and the sensor signals from each element of each array was gathered. The transient

signal made up of a windowed 3 cycle tone burst at 40 kHz is shown in Figure 4.3. The signals at each sensor location was gathered using a charge amplifier along with a gain stage at each sensor location. The signals were passed to a Textronix TDS420A oscilloscope which saved the signals to a disk. Each sensor signal was averaged 100 times before writing to the data file. A sample of the saved transient sensor signals is shown in Figure 4.4. The sensor for each array are numbered from 1 to 19 from right to left in Figure 4.2(a). The signals which are shown correspond to the A0 mode propagating in the plate. The transient hits the rightmost element first and travels to the left, as expected. Additionally, the groups of signals show that the transient passes through the first array before the second array. If the time period of the transient response is extended, reflections from the top and bottom edges also appear as well as a reflection from the left edge of the plate. Figure 4.5 shows the sensor signals at an excitation of 3 cycle burst of 100 kHz. In these cases, the transient is traveling faster than the 40 kHz case. A weak S0 signal appears in the 100 kHz case which arrives much earlier than the A0 mode. In this region of the frequency domain, the actuator is exciting both the A0 and S0 modes, though the S0 mode is much weaker.

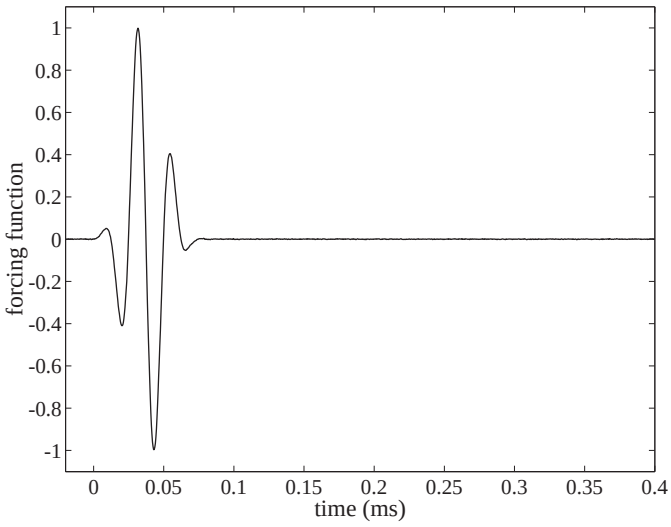

Figure 4.3: Excitation signal sent to actuation element

The signals gathered from each sensor array is gathered and processed to

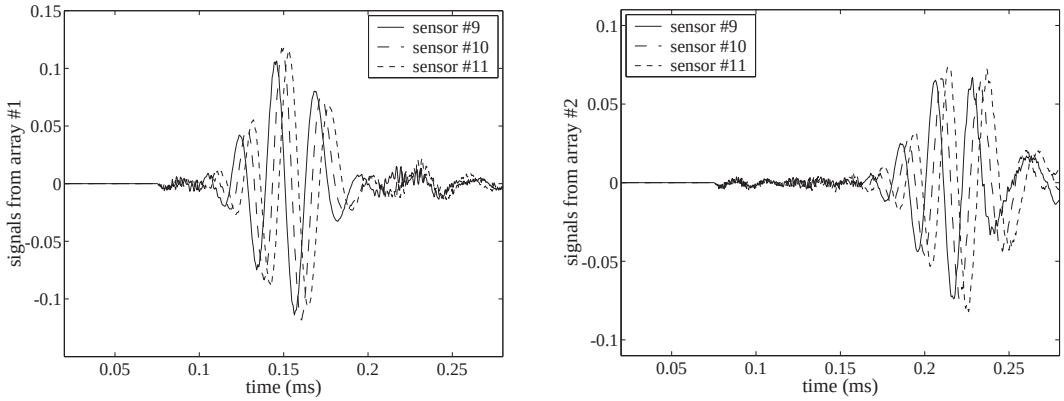

(a) Array #1 (b) Array #2

Figure 4.4: Transient signals at 40 kHz.

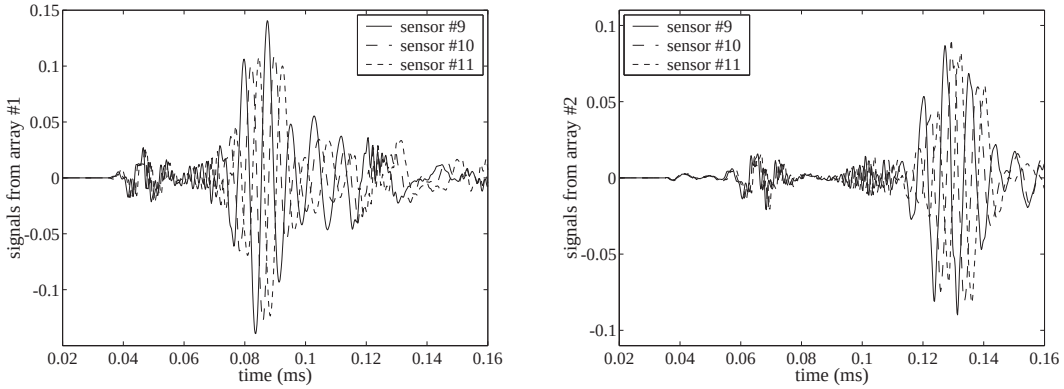

(a) Array #1 (b) Array #2

Figure 4.5: Transient signals at 100 kHz.

produce an array response. The array response is produced for each wavenumber using the algorithm provided in the previous chapter. Dolph-Chebyshev spatial windowing was used where the sidelobe levels where prescribed as 1% of the main lobe level. The array response for each array is shown in Figure 4.6. The contour plots show the magnitude of the array response as a function of wavenumber and time. For Array #1, the array response shows the initial wavefront arriving at $\sim$.17 ms with a wavenumber of $\sim$350 rad/m. Another wave arrives at $\sim$.47 ms with a much lower wavenumber. The second wave corresponds to the wave reflecting off of the top and bottom edges of the plate and approaching the array. The same type of characteristics are seen in the array response corresponding to Array #2. The

initial transient from the actuator arrives at ∼.25 ms with a wavenumber of ∼350 rad/m. The reflections from the top and bottom edges also appears at a much lower wavenumber later on in time. The same trends can be seen for the array responses corresponding to the 100 kHz case, shown in Figure 4.7. The initial transient from the actuator appears at ∼.09 ms for Array #1 and ∼.15 ms for Array #2 at a wavenumber of ∼600 rad/m. The reflections from the top and bottom edges show up later on in time, at a lower wavenumber.

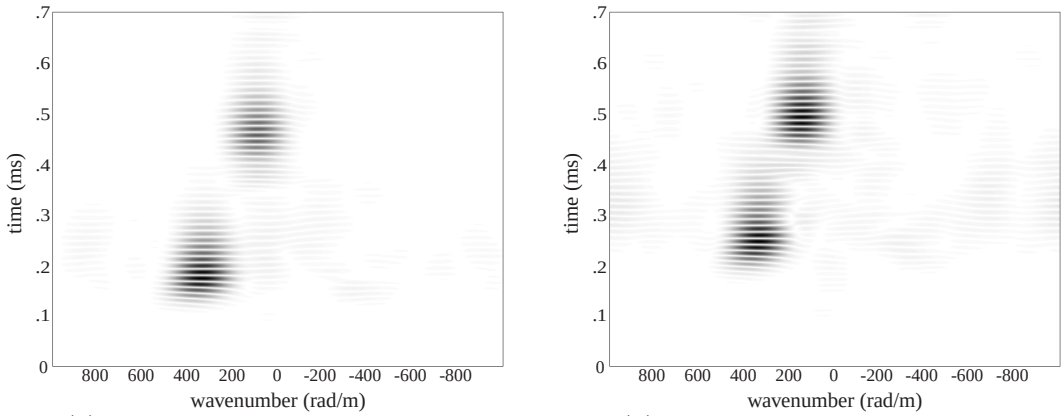

(a) Array response for Array #1 (b) Array response for Array #2

Figure 4.6: Array response for 40 kHz excitation

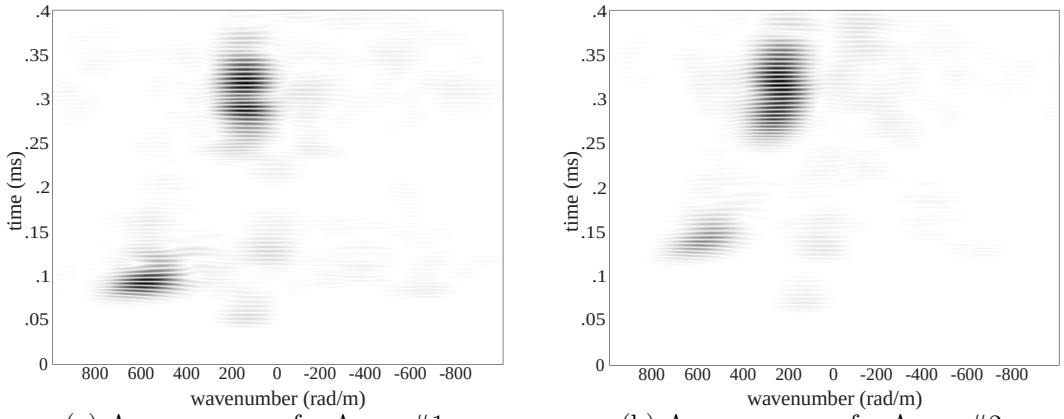

(a) Array response for Array #1 (b) Array response for Array #2

Figure 4.7: Array response for 100 kHz excitation

The array response for Array #1 using 40 kHz case in Figure 4.6(a) was reconstructed by varying two parameters, the number of sensors and the type of

spatial windowing. Figure 4.8 shows the case when only the middle 7 and middle 13 sensor elements are used with a Dolph-Chebyshev window. The width of the lobes increase as fewer sensors are used to create the array response. The wavenumber response of the array spreads out as the length of the array decreases. The array response using all 19 sensor signals but different windowing functions are shown in Figure 4.9. For the case where no windowing function is used, sidelobes may be seen next to the main lobes in the response. The case where the Blackman window is used shows a spreading out of the response while eliminating the sidelobes. The Dolph-Chebyshev windowing eliminates the sidelobes while keeping the width of the main lobe as small as possible.

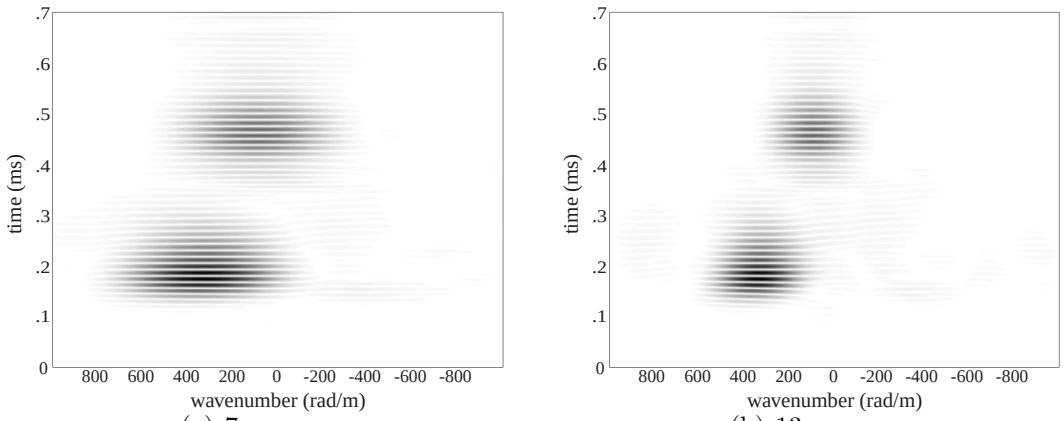

(a) 7 sensors (b) 13 sensors

Figure 4.8: Array response 40 kHz excitation

The array responses were found for a range of frequencies using all 19 elements with Dolph-Chebyshev windowing. The wavenumber corresponding to peak of the array response when the initial transient passed was kept and this information is used to reconstruct the wavenumber-frequency relationship for the Aluminum plate. The wavenumber-frequency curve for both the A0 and S0 modes can be reconstructed by this method. The results are shown in Figures 4.10(a) and 4.10(b) for the A0 and S0 modes respectively. For the A0 mode, there is a difference between the exact theory and the 1st order approximation in the Kirchoff theory. For the S0 mode, this difference is not as profound at the frequencies that were examined. In both

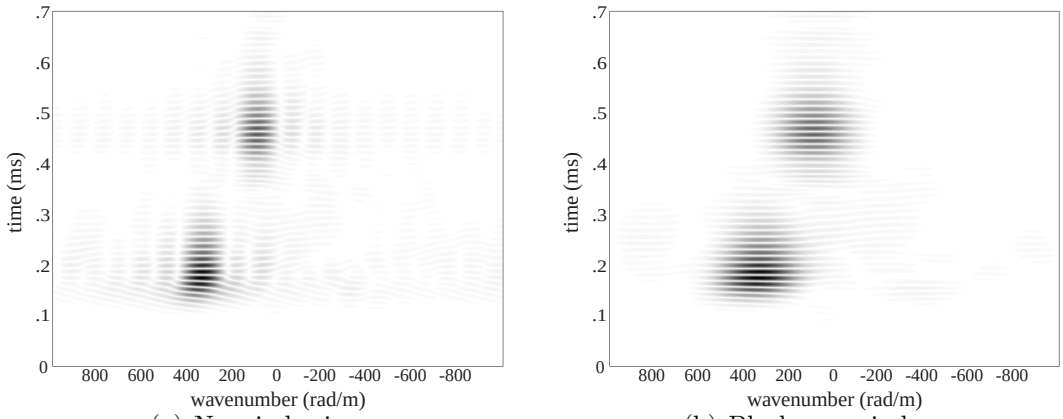

(a) No windowing (b) Blackman window

Figure 4.9: Array response 40 kHz excitation

cases, the experimental results followed the exact theory relatively well.

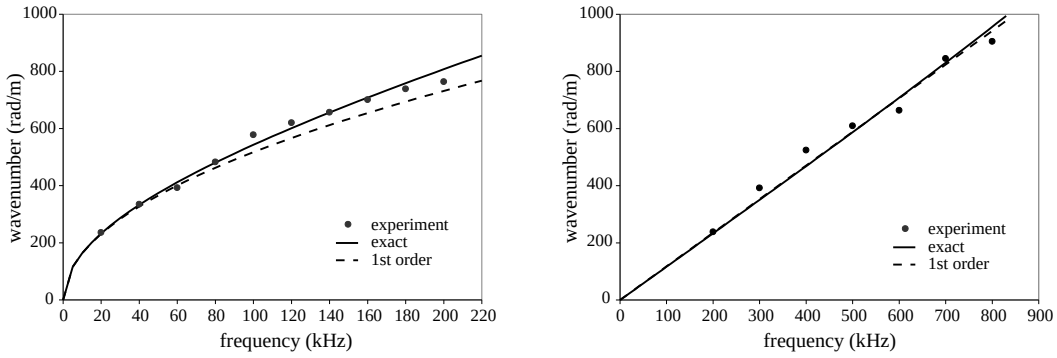

(a) A0 mode (b) S0 mode

Figure 4.10: Wavenumber-Frequency relationship for Aluminum plate

The array response for the 40 kHz case and the corresponding wavenumber of ∼350 rad/m is shown in the time domain plot in Figure 4.11(a). The reflection from the top and bottom edges are removed from the responses. The array has been used to filter out the waves arriving from an undesired direction. Figure 4.11(b) is the array response which is filtered at ∼600 rad/m for the 100 kHz case. The phase lag between any two sensor responses or the two array responses may be used to determine the group velocity of a wave. The experimental group velocity is shown in Figures 4.12(a) and 4.12(b) for the A0 and S0 mode, respectively. In

both cases, the experimental results match the exact theory relatively well. For the plots in the dispersion curves, the exact theory and first order approximations vary significantly. This is because the group velocity is related to the slope of the wavenumber-frequency relationship.

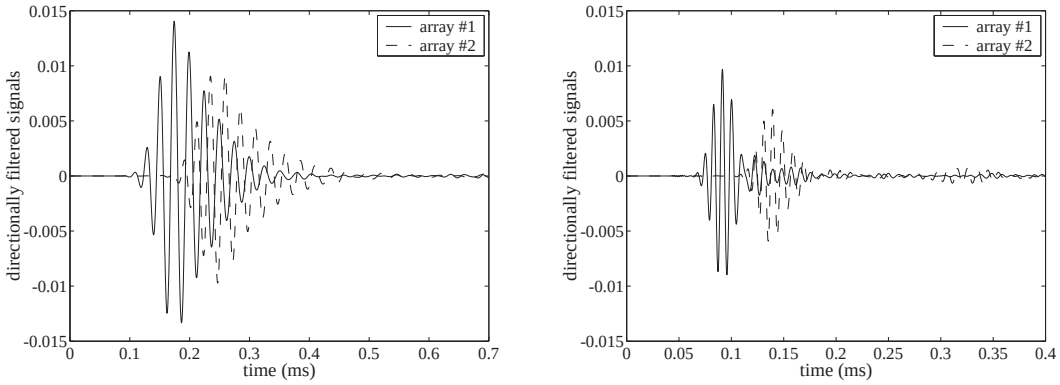

(a) 40 kHz (b) 100 kHz

Figure 4.11: Wavenumber filtered transient signals

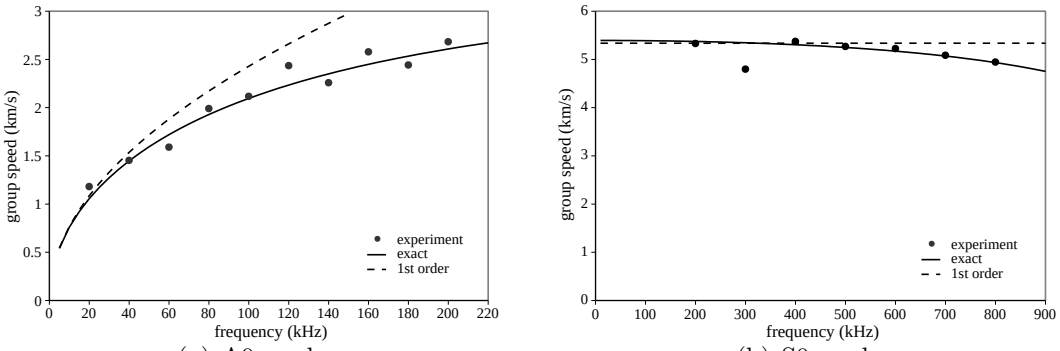

(a) A0 mode (b) S0 mode

Figure 4.12: Group velocity for Aluminum plate

The array response was shown to be able to deconstruct a set of signals from an array into its component wavenumbers. The fundamental dispersion relations for a thin plate may be reproduced using the sensor array and the associated signal processing.

4.4 Damage Detection Setup

The two common ways of damage detection are a pitch-catch arrangement and a pulse echo method, shown in Figure 4.13. In the pitch-catch method, a transducer is used to send out an interrogating signal and transducers located at different positions monitor the dynamics in order to determine the location of damage. In the pulse-echo method, a transducer (or actuator-sensor pair) is used to send out an interrogating signal and sense the reflection from the same location. In the present work, the pulse-echo method will be used where the actuation element and the sensing mechanism are colocated, shown in Figure 4.14(a). By using this method of damage detection, only a small section of the plate needs to be instrumented.

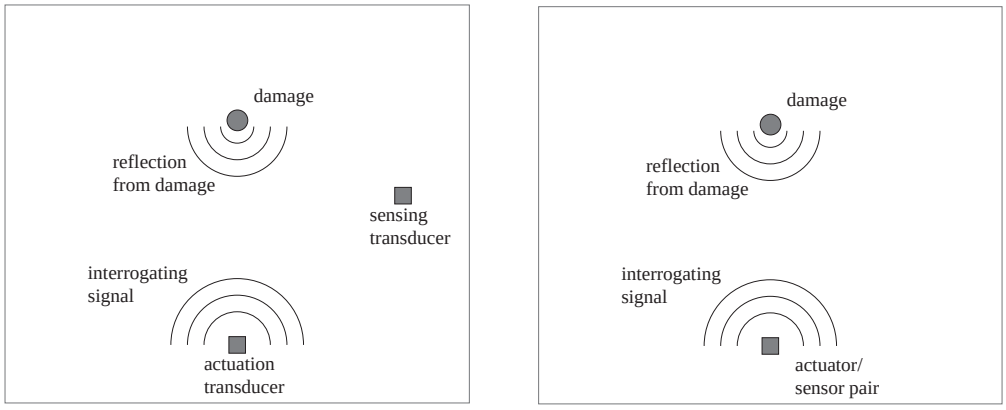

(a) Pitch catch method (b) Pulse echo method

Figure 4.13: Wave propagation damage detection methods

Both the A0 and S0 Lamb mode of the plate may be used for damage detection purposes since the actuation element was bonded to the top of the plate. The interrogating signals consisted of a windowed tone burst of a given frequency. The structural wave produced by this signal propagates through the plate and reflects off of a damaged area, if present, and off of boundaries. For the damage detection setup given, the interrogating signals and the corresponding excited wavenumber is summarized in Table 4.1. The frequency of the interrogating signal, and the corresponding wavenumber of the wave propagating through the structure, plays a role in the damage detection scenario for two reasons. Higher frequency waves

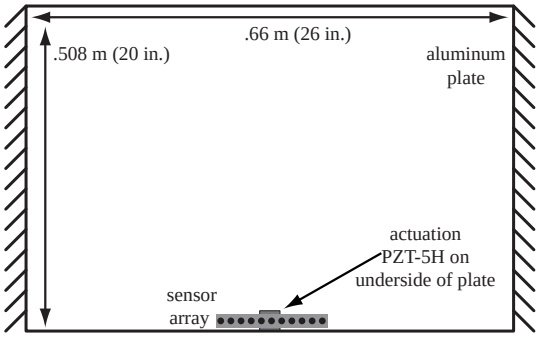

(a) Damage detection setup diagram

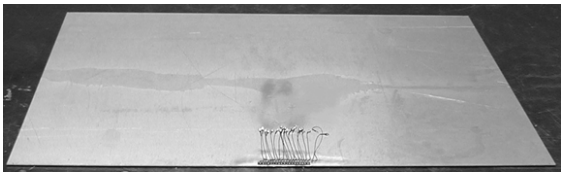

(b) Picture of plate

Figure 4.14: Wave propagation damage detection methods

are generally more appropriate for detecting small amounts of damage while lower frequency waves tend to pass through damaged regions unchanged. Secondly, the angular resolution of the sensor array is dependent on the wavenumber of interest. The angular resolution increases as the interrogating wavenumber increases up until the Nyquist wavenumber which is a limiting condition for the array. The sensor array gathered the transient signals in the same way as the previous section. The array response was used to look for a reflection from a hole drilled .3048 m (12 in.) from the bottom edge of the plate. The pulse-echo damage detection methodology is shown in Figure 4.15(a). The objective is to locate the damage position relative to the array by determining the polar pair, l and θ, in Figure 4.15(b).

Mode	# cycles	forcing frequency (kHz)	wavenumber (rad/m)
A0	3	180	760
S0	5	600	710

Table 4.1: Excitation Parameters for Damage Detection

The array response for a hole diameter of 9.52 mm (3/8 in.) is shown in Figure 4.16. For the A0 mode, the difference between the damaged signal and the undamaged signals are used to bring out the reflection from the hole. For the S0 mode, the raw signals are used in the array processing. Using either the A0 or S0

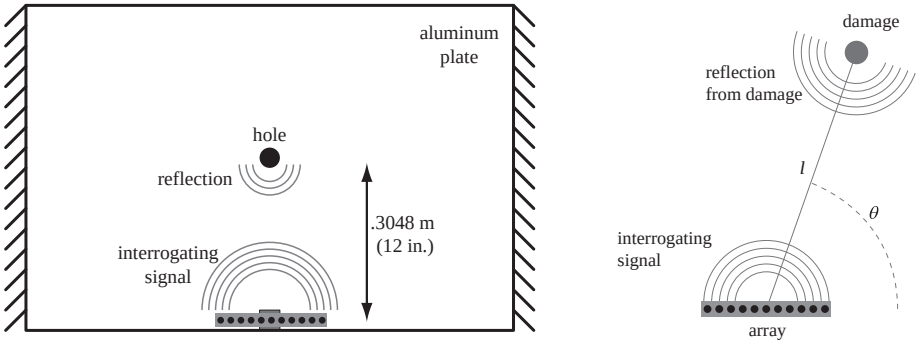

(a) Diagram of damage detection of hole at 90°

(b) Location of damage relative to array

Figure 4.15: Location of damage relative to array

mode of the plate, the reflection from the damaged region can be picked out by the array. The reflection arrives earlier for the S0 mode because of the faster group speed. The reflections from the top edge as well as the left and right edges occur later on in time. These reflections from the boundary conditions are not included in the array response plots because they tend to drown out the reflection from the hole. Thus, the dynamics associated with the reflection from the damaged region may be identified based on the reflection time and position relative to the array. The array responses for the other damaged cases are similar, though the magnitudes of the reflections vary. The time domain plots for the array steered toward θ =90° is shown in Figure 4.17. The phase lag between the input excitation signal and the the reflection from the damage indicate the distance along 90° that the damage is located. This position is determined using the group speed of the mode at the given frequency:

$$l = \frac{1}{2}\frac{\Delta t}{c_{gr}} \tag{4.1}$$

Additionally, for both the A0 and S0 modes, the reflections from the damaged region grow as the size of the damage grows. This information may be used to gain more information about the size of the damaged region.

The position of the damage relative to the array can be determined based on the position of the reflection in the array response and the power in the portion of the

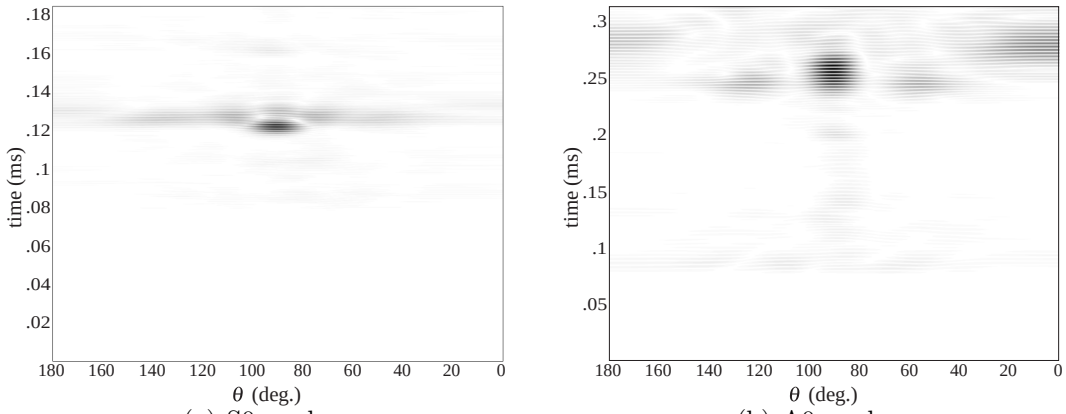

(a) S0 mode (b) A0 mode

Figure 4.16: Array response for 9.52 mm (3/8 in.) diameter hole

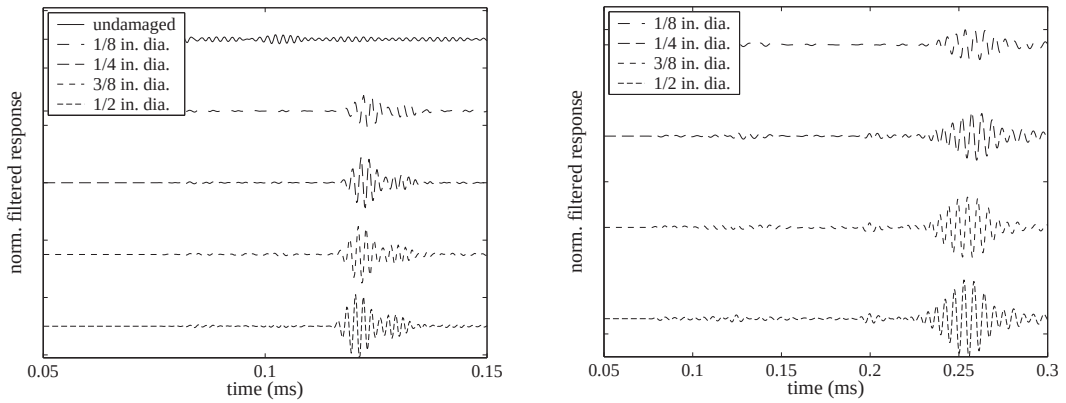

(a) S0 mode (b) A0 mode

Figure 4.17: Array response various hole diameters

waveform corresponding to the reflection is an indicator of the size of the damaged region. The portion of the transient corresponding to the reflection is isolated using a windowing function. A damage index can be constructed by normalizing the energy in the reflection relative to the energy in the input signal:

$$DI = \frac{\int \left|\psi_r\left(\bar{\theta},\omega\right)\right|^2 d\omega}{\int \left|F(\omega)\right|^2 d\omega} \tag{4.2}$$

where $\psi_r\left(\bar{\theta},\omega\right)$ is the time domain Fourier transform of the array steered toward $\bar{\theta}$ and windowed around the reflection. $F(\omega)$ is the Fourier transform of the input signal. The input signal and the windowed portion of the reflection are shown in

Figure 4.18 for the S0 mode and Figure 4.19 for the A0 mode. The magnitudes of the Fourier transforms are shown in Figure 4.20. The main peak of the frequency spectrum occurs at 180 kHz for the A0 mode and 600 kHz for the S0 mode, as expected. Only the portion around these frequencies need to be taken into consideration when determining the damage index, DI, since the signal consists of a narrow band of frequencies. This was done for all of the damage cases and the results are shown in Figure 4.21. As the size of the damage grows, the Damage Index increases. Ideally, the normalization quantity would be based on the component of the array response corresponding to the outward propagating wave. In the experiment, however, significant electrical interference corrupted the initial transient portion of the sensor signals.

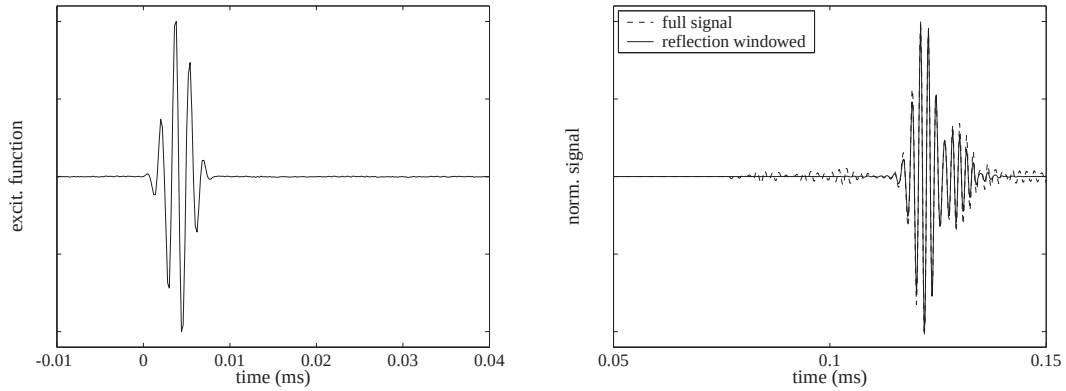

(a) Excitation

(b) Portion of signal corresponding to reflection

Figure 4.18: Excitation signal and windowed portion of reflection for S0 mode

Another Aluminum plate was set up in a similar fashion as the first plate. In this case, the hole location was placed at a different location, shown in Figure 4.22(a). The damaged region was placed at 120° relative to the array axis at a distance of .2845 m (11.2 in.). The actuation element was excited with the same forcing functions for both the A0 and S0 modes used in the previous experiment. The transient signals from the sensor arrays were gathered and processed in the same manner. The array responses for both the A0 and S0 cases are shown in Figure 4.23 for the 9.52 mm (3/8 in.) hole. The array responses show a maximum along 120°

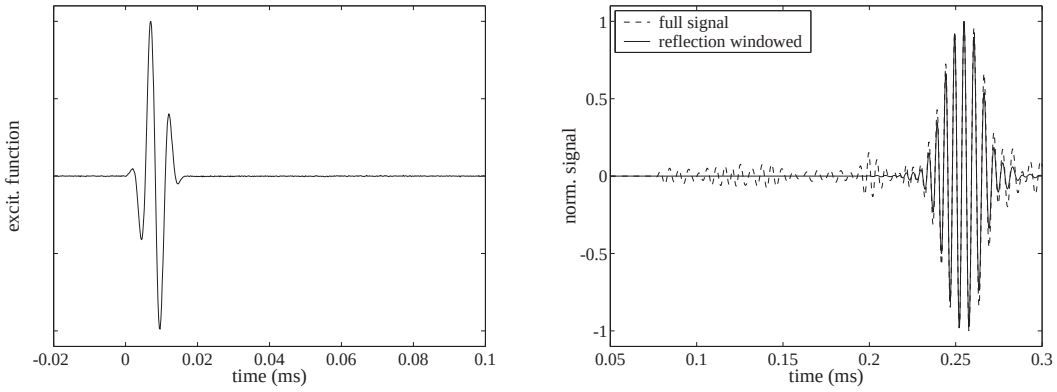

(a) Excitation (b) Portion of signal corresponding to reflection

Figure 4.19: Excitation signal and windowed portion of reflection for A0 mode

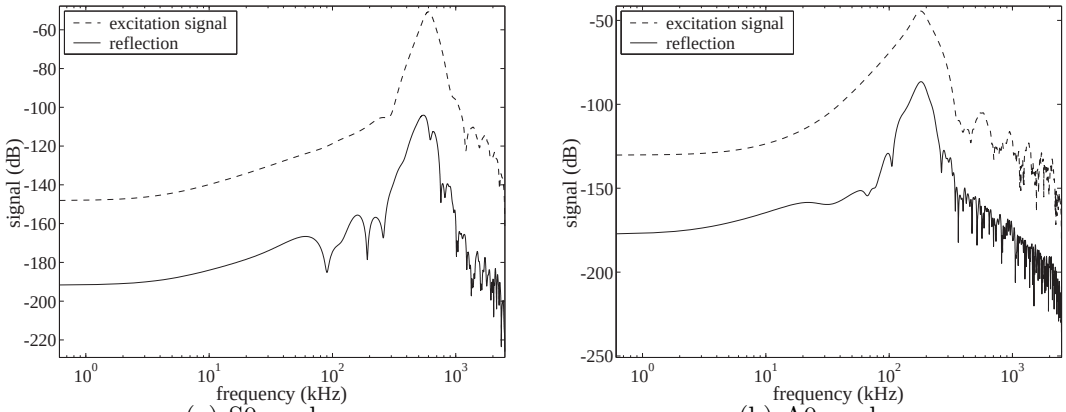

(a) S0 mode (b) A0 mode

Figure 4.20: Frequency spectrum of excitation and reflection signals

corresponding to the reflection from the damage. The reflection arrives earlier than the case where the damage was at 90° because of the shorter paths involved. As with the previous case, the array response constructed for the A0 mode used signals which were the difference between the damaged and undamaged cases whereas the raw transients are used for the S0 mode. There are regions in the array response using the A0 mode in Figure 4.23(b) where the array response is significant at $\theta =$ 0° and 180°. These are the reflections from the left and right edges of the plate and can be removed from consideration.

An additional hole was placed on the plate and the transient signals were

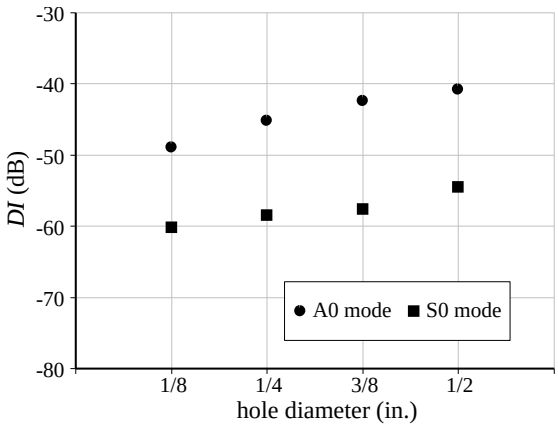

Figure 4.21: Damage Index (DI) for hole at 90°

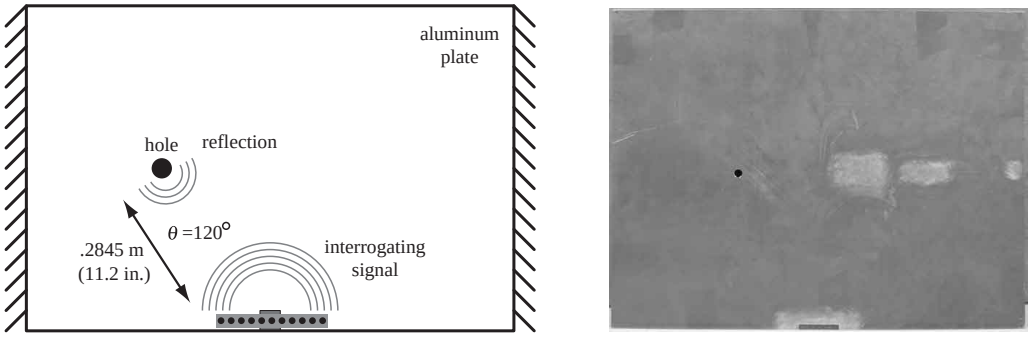

(a) Diagram of damage detection of hole at 120°

(b) Picture of plate

Figure 4.22: Hole at 120°

captured in order to determine the location of the second hole. The placement of the second hole is shown in Figure 4.24(a). The array response for the S0 mode is shown in Figure 4.24(b). Reflections from both holes are seen at the appropriate steering directions and the time of the reflections correspond to the distance from the array. The reflection from the first hole appears at ∼.12 ms in the 120° direction and the reflection from the second hole appears at ∼.09 ms in the 38° direction. The hole at 120° had a 12.7 mm (1/2 in.) dia. while the hole at 38° had a 9.52 mm (3/8 in.) dia. Thus the reflection from the smaller hole is lower in magnitude in comparison to the reflection from the larger hole. Multiple damage sites can be located based on the array response because of the ability to deconstruct the transient signals. The

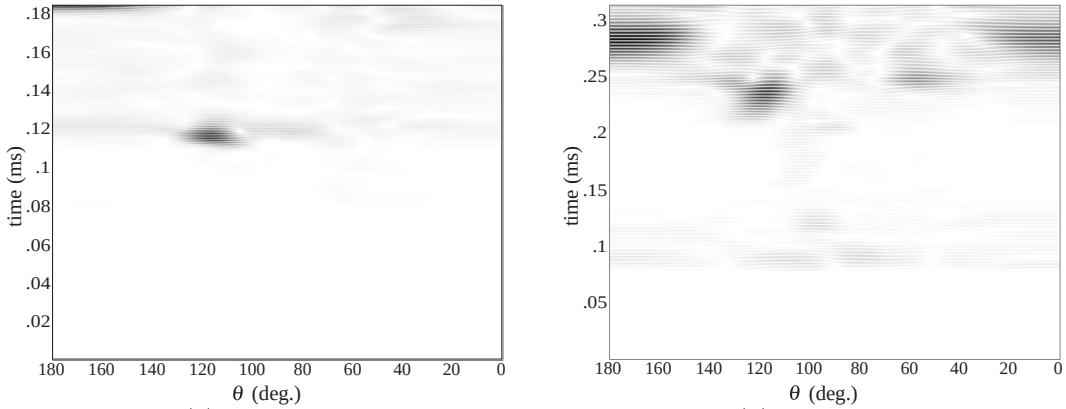

(a) S0 mode (b) A0 mode

Figure 4.23: Array response for 9.52 mm (3/8 in.) diameter hole

A0 mode did not capture the response from the second hole. The Damage Index was used to quantify the magnitude of the reflection. The trends shown in Figure 4.25 show the same trends as in the previous example. In the case of multiple holes, each may be examined independently. The magnitudes between Figures 4.25 and 4.21 do not match up due partially to different bonding methods used to attach the sensor array and actuation element to the plates. The input signals used for normalization were the same for both cases but the strength of the signal from the sensors and the ability of the actuation elements to excite the plate depended on the bonding method.

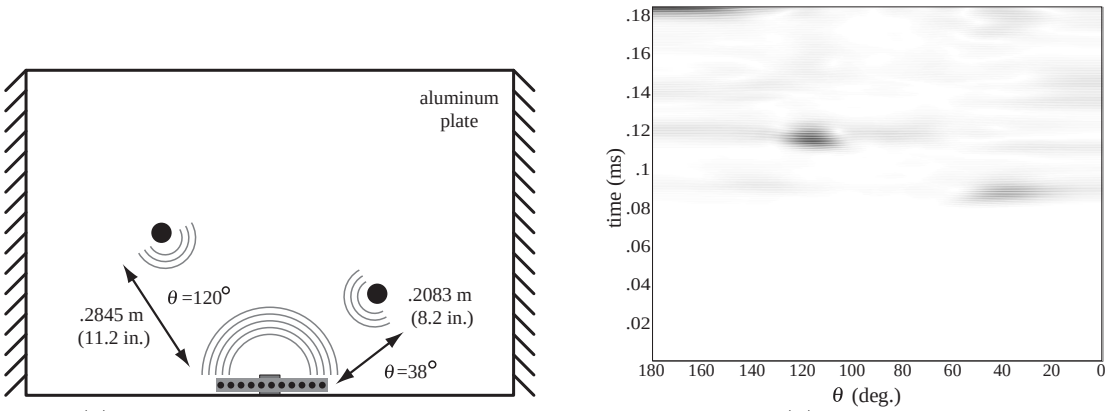

(a) Additional hole placed at 38° (b) S0 mode

Figure 4.24: Array response for plate with 2 damaged regions

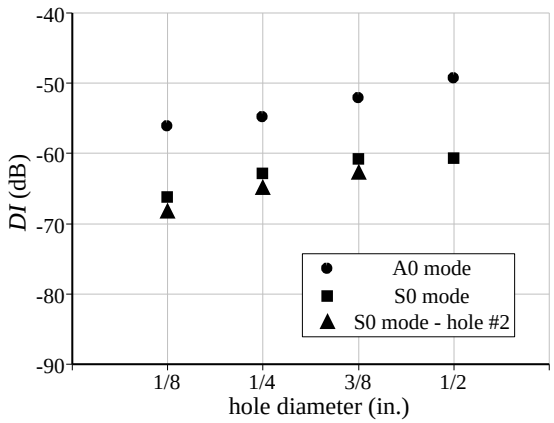

Figure 4.25: Damage Index (DI) for hole at second plate

4.5 Sensitivity Analysis

The content of the interrogating signal plays an important role in the sensitivity of a damage detection scheme. For a pulse-echo approach, the scattering relationship governs the effectiveness of a particular damage detection scheme. The scattering, S, is defined as the ratio of reflected wave from a discontinuity to the incident wave:

$$S = \frac{w_{ref}(\omega)}{w_{inc}(\omega)} \tag{4.3}$$

The subscripts ref and inc refer to reflected and incident components respectively. Typically, the scattering is complex where the magnitude determines the part of the incident wave which is reflected back and the phase angle indicates the phase lag between the incident and reflected waves. The ability of a particular Lamb mode to interrogate a plate depends on the scattering and needs to be explored further. In order to examine the this behavior empirically, a 1.52 mm (.060 in.) thick Aluminum plate was instrumented with a sensor array and actuator, shown in Figure 4.26(a).

The actuation piezoceramic element was used to excite the structure with Lamb waves. The waves propagated outward, through the array, and reflected off of the hole. The sensor array is used to gather the transient signals to capture both the incident waveform as well as the reflected waveform. The sensor array is able to isolate components at given wavenumbers and separate the incident waves

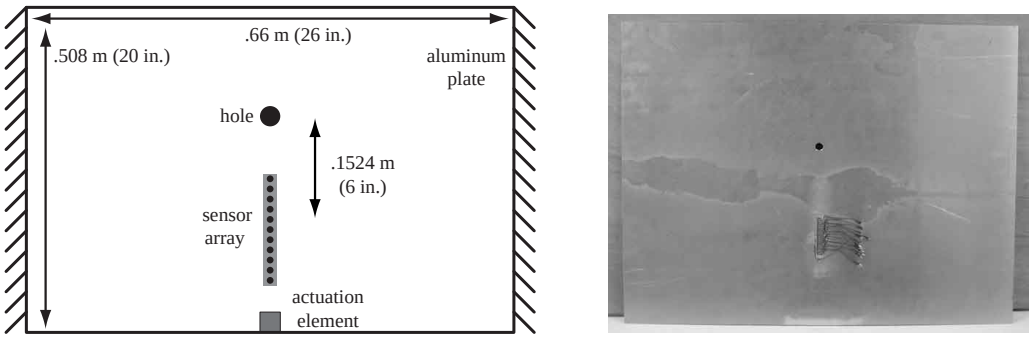

(a) Experimental setup for reflection from hole (b) Picture of plate

Figure 4.26: Setup to measure Reflection Coefficient

from the reflected waves. A set of signals were captured for various frequencies and various damage sizes. The array response for a forcing frequency of 140 kHz and a hole diameter of 9.52 mm (3/8 in.) is shown in Figure 4.27. The incident wave to the hole and the reflection from the hole are circled. The negative region of the wavenumber domain corresponds to waves traveling toward the damaged region and the positive region of the wavenumber domain corresponds to waves traveling in the opposite direction. The incident portion has significant magnitude but the reflection is much weaker and is not as apparent in the contour plot. Nevertheless, the reflection is present and can be seen in the time domain plots corresponding to a wavenumber of 650 rad/m which is the wavenumber of the A0 mode at 140 kHz for the plate. This can be observed in the plots in Figure 4.28 where the plots are the portions of the array response corresponding to ±650 rad/m. The incident waveform is the same regardless the presence of damage. The reflection waveforms show the reflection at the array at ∼.21 ms. and are shown to grow as the size of the damage increases.

Part of the scattering information may be found by using the signals corresponding to the incident and reflected waves:

$$RC = \frac{\int \left|\psi_{ref}\left(\bar{k},\omega\right)\right|^2 d\omega}{\int \left|\psi_{inc}\left(\bar{k},\omega\right)\right|^2 d\omega} \tag{4.4}$$

$\bar{k}$ is the wavenumber of interest and ψ_{inc} and ψ_{ref} correspond to the portions of the waveforms corresponding to the incident and reflected waves. Just as in the

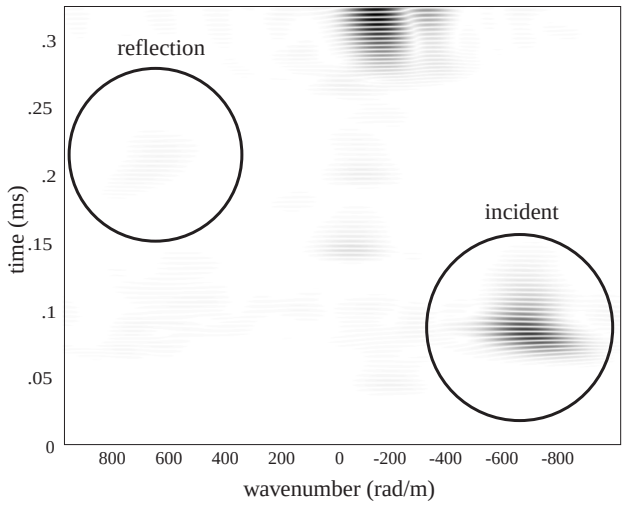

Figure 4.27: Array response for 140 kHz excitation and 9.52 mm (3/8 in.) diameter hole

previous section, the spectrum is a narrow band signal so only the components near the dominant portion of the spectrum need to be considered. The reflection coefficient found using this expression is a positive real number, unlike the scattering expression described previously. The frequency spectrum of the incident wave and reflections are presented in Figure 4.29(a) for the case of 140 kHz excitation. Overall, the reflections are weak compared to the incident wave and this is seen in the large difference in magnitudes between the incident and reflection components. Amongst the reflections, the strength of the reflections increase as the size of the damage increases, which is expected. The reflection coefficient for 140 kHz excitation is shown in Figure 4.29(b).

The reflection coefficient can be found for various frequencies for both the S0 and A0 modes. All of the results may be displayed by normalizing the hole diameter with respect to the wavelength corresponding to the the excitation frequency. The results are shown for both the A0 and S0 mode in Figure 4.30. The plots show the ability of a given mode to detect damage of a given size. When the wavelength of the interrogating signal is large (corresponding to a low frequency) compared to the damaged region, the reflection from the hole is relatively weak. As the

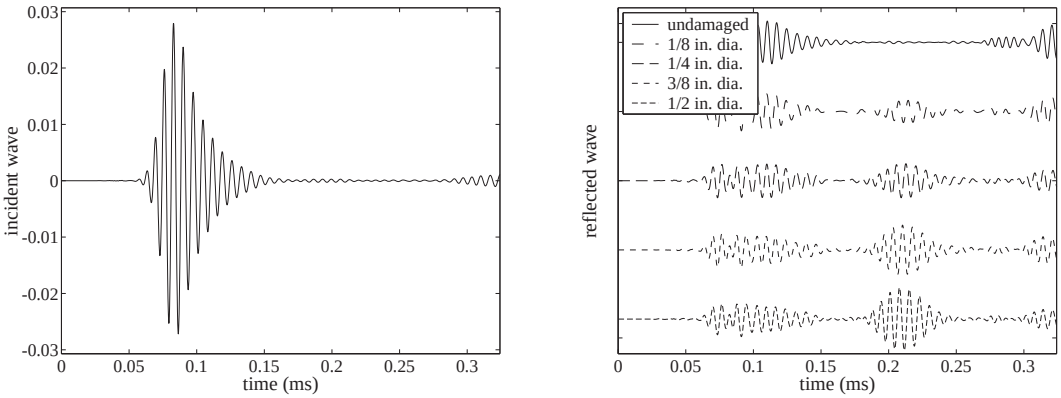

(a) Incident waveform (b) Reflection waveforms

Figure 4.28: Array response for 140 kHz with 9.52 mm (3/8 in.) dia. hole

interrogating frequency increases, and the wavelength starts to approach the size of the damage, the reflection increases. After a certain point, the magnitude of the reflection levels off. This occurs when the damage size is larger than the wavelength of interest. For damage detection applications where the size of the damage is of interest, the interrogation frequency should correspond to the range where the reflection coefficient has the highest slope. As the damage size increases, there is a significant increase in the reflection. Though both the A0 and S0 modes show the same trends, the S0 mode shows the greatest sensitivity because of the larger magnitude of RC.

4.6 Changes in Boundary Condition

Apart for interrogating the internal structure of a plate for damage, a sensor array coupled with Lamb wave dynamics may be used to look for changes in boundary conditions. This is particularly useful for boundaries made of bolted joints or rivets. In the case of bolted joints, a loss of torque load on a bolt alters the boundary conditions. This alteration in the boundary condition can be sensed by Lamb waves as they reflect off of the boundary. The scattering expression used earlier applies in this case also. An experimental setup, shown in Figure 4.31(a), was used to evaluate the sensor arrays ability to evaluate the condition of a bolted joint. The left and

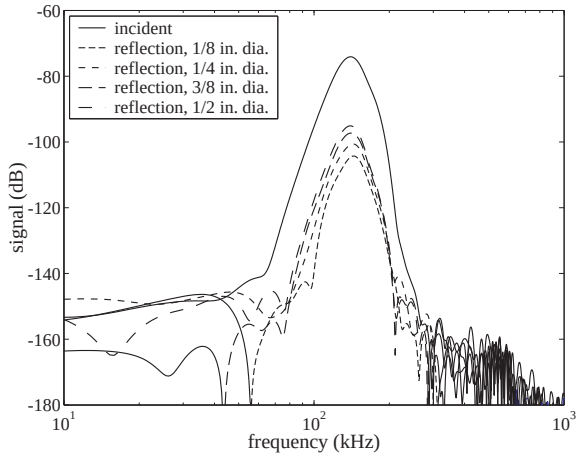

(a) Frequency spectrum of incident and reflections

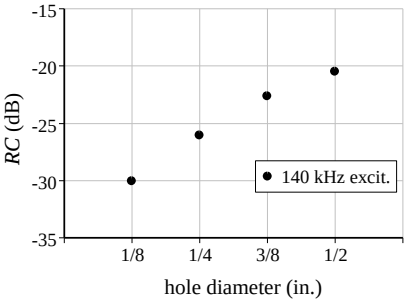

(b) Reflection Coefficient

Figure 4.29: 140 kHz excitation

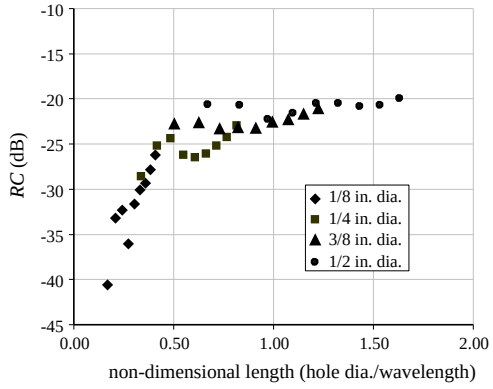

(a) A0 mode

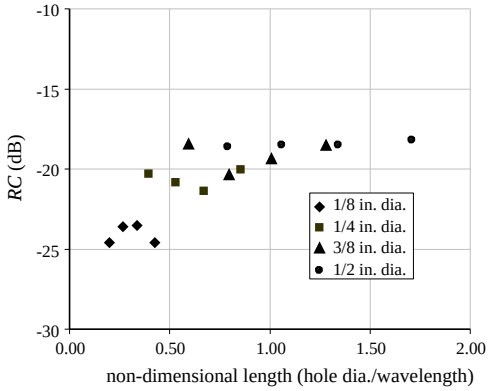

(b) S0 mode

Figure 4.30: Reflection Coefficient

right edges are bolted to Aluminum bars with a rectangular cross section of 1.25 cm $\times$ 2.5 cm (.5 in. $\times$ 1 in.). All of the bolts were set at a nominal 24 N-m torque.

The torque level of the middle bolt in the set of bolts on the right edge of the plate was varied. For each torque level, the actuation element was used to excite the plate with a transient signal and the signals from the sensor array was gathered. When the torque level on the bolt is changed, the boundary condition at that region changes slightly. As a wave mode approaches the right edge, the reflection is governed by the boundary condition. Figure 4.32 shows the response

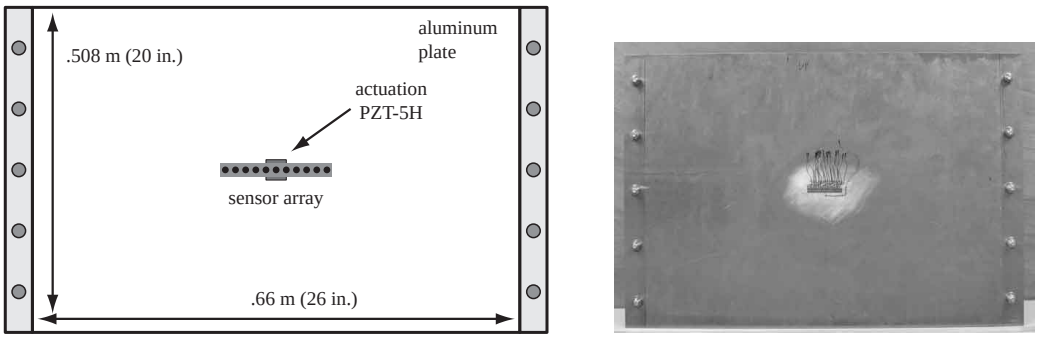

(a) Bolted joint setup diagram. (b) Picture of plate

Figure 4.31: Setup to evaluate bolted joint

of the middle sensor of the array for transient excitations of 20 kHz and 100 kHz where the torque level on the middle bolt of the right edge is varied. For the 20 kHz case, the reflection from the top and bottom edges of the plate arrive at ∼.6 ms and the reflections from the left and right edges arrive at ∼1.2 ms. For the 100 kHz excitation the reflection from the top and bottom edges arrive at ∼.3 ms and from the left and right edges at ∼.5 ms. For both excitation frequencies, the transient response does not change significantly when the torque level on the bolt changes.

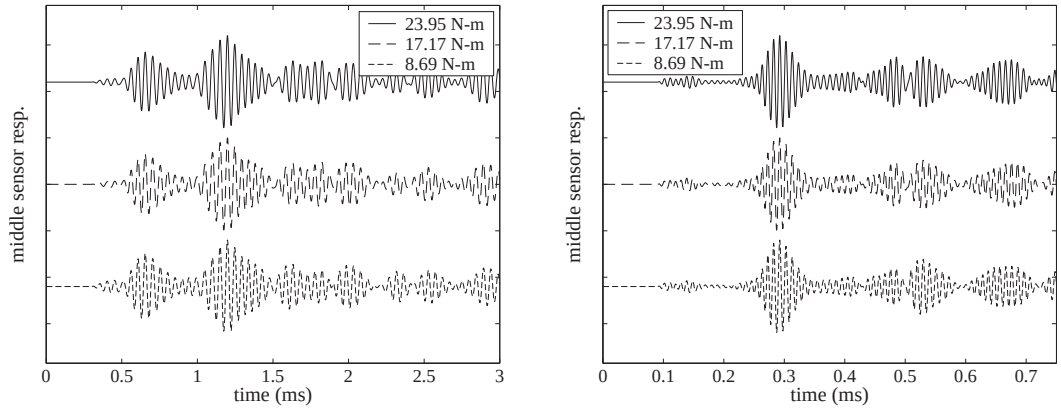

(a) 20 kHz excitation (b) 100 kHz excitation

Figure 4.32: Response of middle sensor of array

The sensor array was used to directionally filter the data from the right and left edges and eliminate the reflections from the top and bottom edges. The directionally filtered waveforms are shown in Figure 4.33 for the rightward propagating

component (from the left edge of the plate) and the leftward propagating component (from the right edge of the plate). Under ideal circumstances where the left and right edges are bolted exactly the same, the leftward and rightward propagating components would be the same. There are inconsistencies, such as slight differences between the distance from the array to the left and right edges and the nonuniform clamped areas at the edges, which cause the waveforms to be different. The rightward propagating component does not change between the different torque levels, as expected. The leftward propagating component shows a slight observable difference at ∼1.2 ms. The effect of an altered boundary variation is more apparent for the 100 kHz excitation frequency, shown in Figure 4.34. While the rightward propagating component shows no difference, the leftward propagating component at ∼.45 ms displays a significant change between the different torque levels. These differences are not evident using just a single sensor response because Lamb modes propagating through the structure and reflecting off of unchanged boundaries drown out any small changes to a specific area of the structure. Not only does the sensor array extract this information from the plate dynamics but because of the directional filtering ability, the location of the changed boundary is known also.

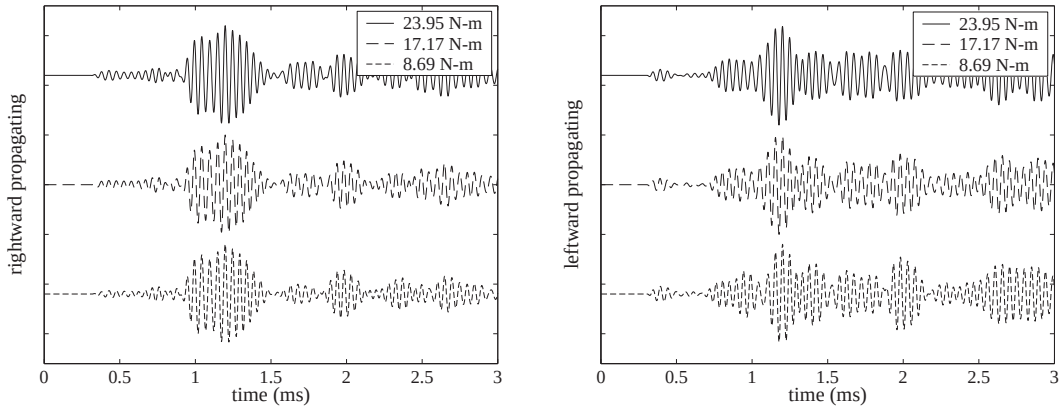

(a) Rightward propagating (b) Leftward propagating

Figure 4.33: Directionally filtered response for 20 kHz excitation

The change in the reflection from the boundary may be quantified using the same method of extracting reflection portions of the waveform and finding the energy

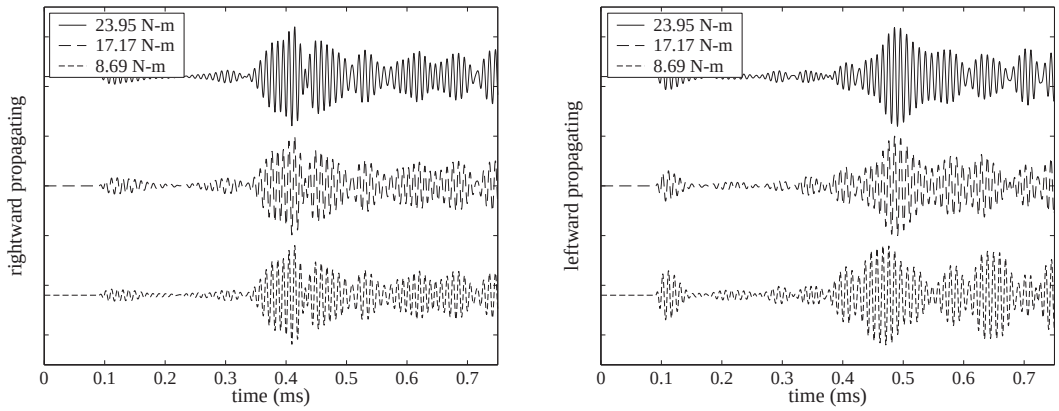

(a) Rightward propagating (b) Leftward propagating

Figure 4.34: Directionally filtered response for 100 kHz excitation

in the signal, as in Equation (4.2). The normalization is done using the excitation function. The incident wave can not be extracted from the sensor array signals because of electrical interference. The results are shown in Figure 4.35 for just the middle sensor response as well as the leftward and rightward components. The DI corresponding to the middle sensor response does not change as the torque load changes on the bolt. When examining the rightward and leftward components individually, the Damage Index does not change for the rightward components but does shift for the leftward components. There is then an indication of the region of the boundary which is altered as well as empirical information corresponding to a loss of torque load to the bolt.

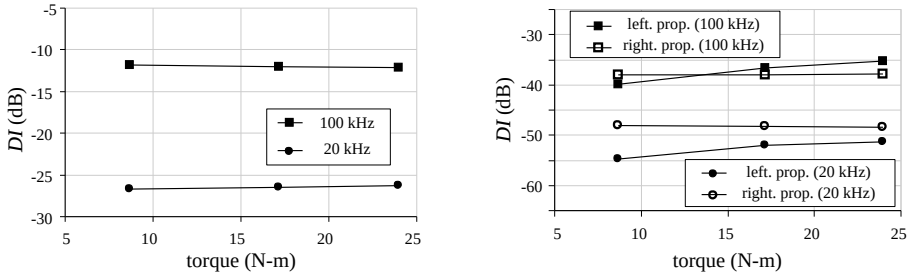

(a) Middle sensor (b) Left. and right. components

Figure 4.35: Damage Index for bolted joint case

4.7 Summary

The fundamental dispersion relations for an Aluminum plate were reconstructed experimentally using the sensor array. Both the A0 and S0 Lamb modes were extracted from the transient response of the plate. The array response using the transient signals showed the arrival of the incident transient Lamb wave as well as the reflections from the boundary edges of the plate. The effects of using a few sensor elements was shown to degrade the filtering capabilities. Additionally, various windowing functions were shown to affect the array response.

A damage detection application was explored where the sensor array and an actuation element actively interrogated an Aluminum plate for a hole damage in the structure. The sensor array and array processing showed the direction of the incoming reflection from the hole. As the size of the hole increased, the energy in the reflection increased, showing the ability to size damage. Both the A0 and S0 mode were used to locate damage in the structure. When multiple damage locations in the plate were present, the sensor array showed the ability to discern between the two and isolated each one to be analyzed separately.

A sizing study was performed where the interrogating frequency and size of the damage were compared. The energy in the incident and reflected waveforms were used to quantify the sensitivity of a Lamb mode of given frequency to a given damage. It was shown that the sensitivity increases with frequency up until a certain point where the sensitivity levels off. Similar trends were shown for the A0 and S0 modes.

A case was shown where the reflection of a Lamb wave from a bolted joint boundary changed when a bolt was loosened. When a single sensor is used, the change in the reflection from the bolted joint is not apparent. The sensor array is able to distinguish between waves arriving from different directions and isolate components arriving from each boundary separately. The reflection from the boundary corresponding to the loosened bolt was shown to change using the directionally filtered response.

Chapter 5

Damage Detection In Composite Plates

5.1 Introduction

An Acousto-Ultrasonic (AU) technique for composite plates becomes complicated due to the anisotropic nature of composite materials. While wave propagation in plates made of isotropic materials is well understood, wave propagation dynamics for composite laminates depends on the construction of the laminate. The dispersion relations for composite laminates need to be found before an attempt can be made for AU damage detection technique.

A finite element model is used to model the wave propagation dynamics of a composite laminate constructed of unidirectional plies. Two separate layups are examined and the dispersion relations are compared with experimental results using the sensor array.

With this understanding, an AU approach for delamination damage detection in a composite laminate is shown experimentally. The array is shown to be capable of directionally filtering the sensor signals with the goal of extracting the reflection from a delamination region. A single sensor used to monitor the plate would not be able to discern the presence of a delamination in the plate.

5.2 Wave Propagation in Composite Laminate

Wave propagation in composite laminates has been examined on both experimental as well as analytical levels. A common approach to understanding wave propagation is based on Classical Laminated Plate Theory to model the dynamics and is generally valid for low frequencies. For higher frequency applications, a more generalized finite

element scheme may be used to produce more accurate results.

Though different types of laminates may be examined, the construction of the laminates in the current study uses a carbon fiber prepreg made by Hexcel Composites. The IM7/8552 material consists of unidirectional carbon fibers (IM7) impregnated in an epoxy resin (8552) with a nominal fiber volume fraction of 57%. The properties of the material are presented in Table 5.1. The longitudinal modulus (E_L) indicates the modulus along the fiber direction and is much stiffer than the transverse modulus (E_T). The transverse modulus small because the stiffness in that direction is predominantly governed by the modulus of the epoxy resin and is relatively soft. The construction of a laminate is described by the stacking sequence of the plies where the rotation of each ply relative to the laminate axes is listed, shown in Figure 5.1. Through reciprocity relations, the complementary Poisson's ratios are related to each other by $\nu_{TL} = (E_T/E_L)\nu_{LT}$.

E_L (GPa)	E_T (GPa)	ν_{LT}	G_{LT} (GPa)	ρ (kg/m^3)	t_{ply} (mm)
170	11	.31	5.0	1430	.173

Table 5.1: IM7/8552 Material Properties

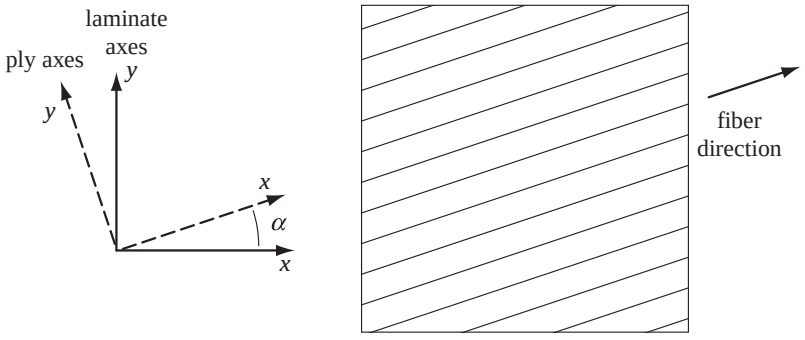

Figure 5.1: Rotation from ply to laminate axes

The material properties for the IM7/8552 material can be found in any right hand coordinate system by using the transformation shown in Equation (B.3) of Appendix B. From the general formulation of the stress-strain relations, the specific

cases of plane stress or plain strain are found by eliminating specific components of stress or strain vectors, respectively. This is useful for constructing the Classical Laminated Plate Theory model, which uses the plane stress representation, or the the more general Finite Element model to predict wave propagation behavior, which uses the plain strain representation.

5.2.1 Classical Laminated Plate Theory

The Classical Laminated Plate Theory (CLPT) approach has been used with success in determining the stiffness properties of a laminate. Though applicable to isotropic materials, CLPT is most useful for laminates constructed of plies with different material properties. The forces and moments on the edge of a plate are expressed by integrating the stresses through the thickness:

$$\mathbf{N} = \begin{bmatrix} N_x \\ N_y \\ N_{xy} \end{bmatrix} = \begin{bmatrix} \int \sigma_{xx}\, dz \\ \int \sigma_{yy}\, dz \\ \int \tau_{xy}\, dz \end{bmatrix} \qquad \mathbf{M} = \begin{bmatrix} M_y \\ M_x \\ M_{xy} \end{bmatrix} = \begin{bmatrix} \int \sigma_{xx}\, z\, dz \\ \int \sigma_{yy}\, z\, dz \\ \int \tau_{xy}\, z\, dz \end{bmatrix} \tag{5.1}$$

Coupled with the strain-displacement relations and the stress-strain relations, the in-plane loadings, N, and moments, M, are expressed in terms of displacement components. The CLPT model assumes a linear in-plane displacement distribution through the thickness of the laminate:

$$u(z) = u_0 - z w_{,x} \qquad\qquad v(z) = v_0 - z w_{,y} \tag{5.2}$$

u_0 and v_0 are constant in-plane displacements in the x and y directions respectively and the derivative of the transverse displacement $w_{,x}$ and $w_{,y}$ are used to describe the variation of the in-plane displacements. The strain-displacement relationships for the in-plane strains contains terms from both the in-plane and transverse displacements:

$$\varepsilon_{xx} = u_{0,x} - z w_{,xx} \qquad \varepsilon_{yy} = v_{0,y} - z w_{,yy} \qquad \gamma_{xy} = u_{0,y} + v_{0,x} - 2 z w_{,xy} \tag{5.3}$$

The strain vector may be separated into two components corresponding to pure

in-plane strain and curvatures:

$$\boldsymbol{\varepsilon} = \begin{bmatrix} \varepsilon_{xx} \\ \varepsilon_{yy} \\ \gamma_{xy} \end{bmatrix} = \begin{bmatrix} u_{0,x} \\ v_{0,y} \\ u_{0,y} + v_{0,x} \end{bmatrix} + z \begin{bmatrix} \kappa_x \\ \kappa_y \\ \kappa_{xy} \end{bmatrix} \tag{5.4}$$

The curvatures are: $\kappa_x = -w_{,xx}$, $\kappa_y = -w_{,yy}$, and $\kappa_{xy} = -2w_{,xy}$. Strain can be split into two components, a constant in-plane strain and the curvature effects, $\boldsymbol{\varepsilon} = \boldsymbol{\varepsilon}_0 + z\boldsymbol{\kappa}$.

A stress-strain expression for the nth ply is expressed using $\mathbf{E}_n$. For the CLPT formulation, plane stress is used because of the assumption of a thin laminate. The in-plane forces and moments are rewritten in terms of in-plane strain and curvature:

$$\mathbf{N} = \sum_{n=1}^{N_{plies}} \int_{z_n}^{z_{n+1}} \mathbf{E}_n \left(\boldsymbol{\varepsilon}_0 + z\boldsymbol{\kappa}\right) dz \qquad \mathbf{M} = \sum_{n=1}^{N_{plies}} \int_{z_n}^{z_{n+1}} \mathbf{E}_n \left(\boldsymbol{\varepsilon}_0 + z\boldsymbol{\kappa}\right) z\, dz \tag{5.5}$$

A matrix expression results which includes the in-plane forces and moments with the in-plane strains and curvatures:

$$\begin{bmatrix} \mathbf{N} \\ \mathbf{M} \end{bmatrix} = \begin{bmatrix} \mathbf{A} & \mathbf{B} \\ \mathbf{B} & \mathbf{D} \end{bmatrix} \begin{bmatrix} \boldsymbol{\varepsilon}_0 \\ \boldsymbol{\kappa} \end{bmatrix} \tag{5.6}$$

$$\mathbf{A} = \sum_{n=1}^{N_{plies}} \int_{z_n}^{z_{n+1}} \mathbf{E}_n \, dz \; ; \quad \mathbf{B} = \sum_{n=1}^{N_{plies}} \int_{z_n}^{z_{n+1}} \mathbf{E}_n \, z \, dz \; ; \quad \mathbf{D} = \sum_{n=1}^{N_{plies}} \int_{z_n}^{z_{n+1}} \mathbf{E}_n \, z^2 \, dz \tag{5.7}$$

The position of each ply is shown in Figure 5.2. The $\mathbf{B}$ matrix couples the in-plane and transverse components. This component is nonexistent when the layup of the laminate is symmetric with respect to the mid-plane.

For a laminate, the $\mathbf{A}$, $\mathbf{B}$, and $\mathbf{D}$ matrices are dependent on the stacking sequence of the plies. Because a single ply generally exhibits anisotropic behavior, the contribution of each ply to the system matrices depends on the orientation of the ply in the laminate frame of reference. Thus, laminates with different properties may be constructed using the same ply material with different stacking sequences.

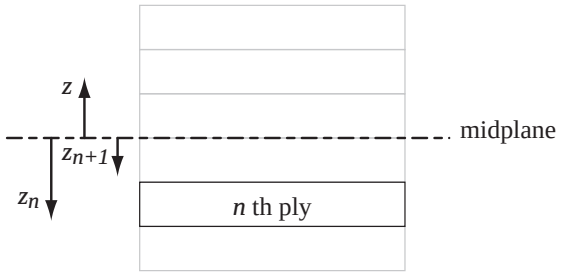

Figure 5.2: Position of ply relative to the mid-plane

Constructing $\mathbf{E}_n$ for each ply in the laminate may be accomplished by taking the tensor representation of the stress-strain relationship and performing a rotation using the coordinate axes and then eliminating the stresses in the transverse direction to obtain the plane stress case. Commonly though, the plane stress properties for a ply are already known in the principle directions, parallel and normal to the fiber direction. In this case, the properties of the ply in the laminate axes involves a rotation of the material from the ply axes. One way of performing this rotation is to use the invariants of the stress-strain relationship. Another method is the use of a rotation matrix which transforms the material properties from the ply axes into the laminate axes:

$$\mathbf{E}_{lam} = \mathbf{T}^{-1}(\alpha)\mathbf{E}_{ply}\mathbf{F}^{-1}\mathbf{T}(\alpha)\mathbf{F} \tag{5.8}$$

$\mathbf{T}$ is the rotation from the laminate axes to the ply axes and $\mathbf{F}$ is the transformation matrix from the engineering definition of strain to the mathematical definition of strain:

$$\mathbf{T}(\alpha) = \begin{bmatrix} \cos^2(\alpha) & \sin^2(\alpha) & 2\sin(\alpha)\cos(\alpha) \\ \sin^2(\alpha) & \cos^2(\alpha) & -2\sin(\alpha)\cos(\alpha) \\ -\sin(\alpha)\cos(\alpha) & \sin(\alpha)\cos(\alpha) & \cos^2(\alpha) - \sin^2(\alpha) \end{bmatrix} \tag{5.9}$$

$$\mathbf{F} = \begin{bmatrix} 1 & 0 & 0 \\ 0 & 1 & 0 \\ 0 & 0 & 2 \end{bmatrix} \tag{5.10}$$

For vibration problems involving a laminate, the dynamic equations of mo-

tion are found using the generalized expressions in Equation (C.27) for in-plane vibrations and Equation (C.14) for transverse vibrations. The development of these equations are shown in Appendix C:

$$\text{in-plane :} \qquad \begin{bmatrix} \frac{\partial}{\partial x} & 0 & \frac{\partial}{\partial y} \\ 0 & \frac{\partial}{\partial y} & \frac{\partial}{\partial x} \end{bmatrix} \begin{bmatrix} N_x \\ N_y \\ N_{xy} \end{bmatrix} = m \begin{bmatrix} \ddot{u} \\ \ddot{v} \end{bmatrix} \tag{5.11}$$

$$\text{transverse :} \qquad \begin{bmatrix} \frac{\partial^2}{\partial x^2} & \frac{\partial^2}{\partial y^2} & 2\frac{\partial^2}{\partial x\,\partial y} \end{bmatrix} \begin{bmatrix} M_y \\ M_x \\ M_{xy} \end{bmatrix} = m\ddot{w} \tag{5.12}$$

m is the mass per unit area of the laminate.

The governing equations of motion are found after substituting in the derived expressions for the forces and moments in Equation (5.6):

$$\text{in-plane :} \qquad \begin{bmatrix} \frac{\partial}{\partial x} & 0 & \frac{\partial}{\partial y} \\ 0 & \frac{\partial}{\partial y} & \frac{\partial}{\partial x} \end{bmatrix} \begin{bmatrix} \mathbf{A} & \mathbf{B} \end{bmatrix} \begin{bmatrix} \boldsymbol{\varepsilon}_0 \\ \boldsymbol{\kappa} \end{bmatrix} = m \begin{bmatrix} \ddot{u} \\ \ddot{v} \end{bmatrix} \tag{5.13}$$

$$\text{transverse :} \qquad \begin{bmatrix} \frac{\partial^2}{\partial x^2} & \frac{\partial^2}{\partial y^2} & 2\frac{\partial^2}{\partial x\,\partial y} \end{bmatrix} \begin{bmatrix} \mathbf{B} & \mathbf{D} \end{bmatrix} \begin{bmatrix} \boldsymbol{\varepsilon}_0 \\ \boldsymbol{\kappa} \end{bmatrix} = m\ddot{w} \tag{5.14}$$

If the layup is symmetric, the coupling matrix between in-plane and transverse vibrations is eliminated. In this case, the in-plane vibrations are solely a function of $\boldsymbol{\varepsilon}_0$ and the transverse vibrations are solely a function of $\boldsymbol{\kappa}$. For a laminate constructed of orthotropic plies where the normal strains are decoupled from the shear strain the, in-plane matrix, $\mathbf{A}$, and bending matrix, $\mathbf{D}$, take a simpler form:

$$\mathbf{A} = \begin{bmatrix} \mathsf{A}_{11} & \mathsf{A}_{12} & 0 \\ \mathsf{A}_{12} & \mathsf{A}_{22} & 0 \\ 0 & 0 & \mathsf{A}_{66} \end{bmatrix} \qquad \mathbf{D} = \begin{bmatrix} \mathsf{D}_{11} & \mathsf{D}_{12} & 0 \\ \mathsf{D}_{12} & \mathsf{D}_{22} & 0 \\ 0 & 0 & \mathsf{D}_{66} \end{bmatrix} \tag{5.15}$$

For transverse wave propagation, the governing equation from Equation (5.14) is simplified:

$$\mathsf{D}_{11}w_{,xxxx} + \mathsf{D}_{22}w_{,yyyy} + 2\left(\mathsf{D}_{12} + 2\mathsf{D}_{66}\right)w_{,xxyy} + m\ddot{w} = 0 \tag{5.16}$$

Assuming a plane wave traveling in the x and y directions, a wavenumber-frequency relationship similar to the isotropic case in Equation (2.20) can be found:

$$\begin{aligned} x\text{-dir.:} \quad & \left(w(x,y) = w_0 e^{i(\omega t - kx)}\right) \quad \rightarrow \quad k = \sqrt{\omega}\sqrt[4]{\frac{m}{\mathsf{D}_{11}}} \\ y\text{-dir.:} \quad & \left(w(x,y) = w_0 e^{i(\omega t - ky)}\right) \quad \rightarrow \quad k = \sqrt{\omega}\sqrt[4]{\frac{m}{\mathsf{D}_{22}}} \end{aligned} \tag{5.17}$$

The same type of behavior can be found for in-plane wave propagation, where the governing equations from Equation (5.13) describing the in-plane dynamics take the form:

$$\begin{aligned} \mathsf{A}_{11}u_{,xx} + \mathsf{A}_{12}v_{,xy} + \mathsf{A}_{66}(u_{,yy} + v_{,xy}) - m\ddot{u} = 0 \\ \mathsf{A}_{12}u_{,xy} + \mathsf{A}_{22}v_{,yy} + \mathsf{A}_{66}(u_{,xy} + v_{,xx}) - m\ddot{v} = 0 \end{aligned} \tag{5.18}$$

Assuming a plane wave traveling in the x and y directions separately, the familiar form of the wavenumber-frequency relationship seen in the isotropic case in Equation (2.29) is found:

$$\begin{aligned} x\text{-dir.:} \quad & \begin{pmatrix} u(x,y) = u_0 e^{i(\omega t - kx)} \\ \text{and} \quad v(x,y) = 0 \end{pmatrix} \quad \rightarrow \quad k = \omega\sqrt{\frac{m}{\mathsf{A}_{11}}} \\ y\text{-dir.:} \quad & \begin{pmatrix} u(x,y) = 0 \quad \text{and} \\ v(x,y) = v_0 e^{i(\omega t - ky)} \end{pmatrix} \quad \rightarrow \quad k = \omega\sqrt{\frac{m}{\mathsf{A}_{22}}} \end{aligned} \tag{5.19}$$

The wavenumber-frequency relationships for both transverse and in-plane wave propagation look very similar to the isotropic cases. For the orthotropic material given, though, the behavior depends on the direction of travel.

The CLPT model enables the properties the plies to be smeared together to construct representative stiffness matrices. This representation is useful for static and low frequency dynamic analysis of laminates. The limitations of the CLPT model are the same as for the Kirchoff plate case. Shear deformation, which was important in predicting Lamb wave propagation properties at higher frequencies, is eliminated in the CLPT formulation. Additionally, the plies are assumed to be perfectly bonded and the bond line between the plies have no thickness.

5.2.2 Finite Element Formulation

The finite element model constructed in Section 2.6 is used to produce a higher order model for the wave propagation dynamics in a composite laminate made up of unidirectional plies. The plate is discretized through the thickness with two node elements with two degrees of freedom per node. Since the model includes shear deformations in the construction of the finite element, high frequency dynamics Lamb wave propagation is more accurately predicted than the simplified model. The finite element method was shown to be able to reproduce the wavenumber-frequency plots for an isotropic plate and is comparable to the exact solutions. In the isotropic plate, each element essentially had the same material properties. For a laminate, the plain strain material properties of each element will depend on the ply orientation. Multiple elements may also be used to discretize each ply.

Using the diagram in Figure 5.3 for the principle material directions, the full 6×6 stress-strain matrix can be approximated using the relations in Table 5.2. The material properties in the directions normal to the fiber directions are assumed to be dominated by the matrix properties, which are isotropic. The stress-strain tensor, C_{jklm}, used in Appendix B can be constructed for the IM7/8552 material. The non-zero components of the tensor relations are shown in Table 5.3 where the material is assumed to be generally orthotropic. Construction of the stiffness matrix in Equation (2.62) for each individual ply in the finite element formulation is dependent on the material properties of the rotated ply, $\mathbf{E}_n$. This term is found using the general tensor relation described which is then rotated through the ply angle, α, into the laminate coordinate system. Since the finite element model uses the plane strain assumptions, the construction of the reduced stress-strain relations is found by eliminating the appropriate strain variables to reduce the expression to a 3×3 matrix.

$E_1 = E_L$, $E_2 = E_T$, $E_3 = E_T$
$\nu_{12} = \nu_{LT}$, $\nu_{21} = \nu_{TL}$, $\nu_{13} = \nu_{LT}$, $\nu_{31} = \nu_{TL}$, $\nu_{23} = .3$, $\nu_{32} = .3$
$G_{12} = G_{LT}$, $G_{13} = G_{LT}$, $G_{23} = E_T/(2(1+\nu_{23}))$

Table 5.2: Material Properties in Principle Axes

$\mathsf{C}_{1111} = E_1(1-\nu_{23}\nu_{32})/D$, $\mathsf{C}_{2222} = E_2(1-\nu_{13}\nu_{31})/D$, $\mathsf{C}_{3333} = E_3(1-\nu_{12}\nu_{21})/D$
$\mathsf{C}_{1122} = E_1(\nu_{21}+\nu_{23}\nu_{31})/D$, $\mathsf{C}_{1133} = E_1(\nu_{31}+\nu_{21}\nu_{32})/D$
$\mathsf{C}_{2211} = E_2(\nu_{12}+\nu_{13}\nu_{32})/D$, $\mathsf{C}_{2233} = E_2(\nu_{32}+\nu_{12}\nu_{31})/D$
$\mathsf{C}_{3311} = E_3(\nu_{13}+\nu_{12}\nu_{23})/D$, $\mathsf{C}_{3322} = E_3(\nu_{23}+\nu_{13}\nu_{21})/D$
$\mathsf{C}_{1212} = G_{12}/2$, $\mathsf{C}_{2121} = G_{12}/2$
$\mathsf{C}_{1313} = G_{13}/2$, $\mathsf{C}_{3131} = G_{13}/2$
$\mathsf{C}_{2323} = G_{23}/2$, $\mathsf{C}_{3232} = G_{23}/2$
where $D = 1-\nu_{12}\nu_{21}-\nu_{13}\nu_{31}-\nu_{23}\nu_{32}-\nu_{12}\nu_{23}\nu_{31}-\nu_{13}\nu_{21}\nu_{32}$

Table 5.3: Non-Zero Tensor Components of Stress-Strain Relations

5.3 Wavenumber-Frequency Relationship for Composite Laminates

The CLPT and FE method were used to predict the wavenumber-frequency relationships for composite laminates. A laminate composed of six plies of unidirectional fibers was constructed, denoted as $[0]_6$. Additionally, a laminated constructed of cross plies was constructed, denoted as $[90/0_2/90]_{\mathrm{s}}$. The subscript, s, refers to a symmetric layup with respect to the mid-plane. Both layups are decoupled between the in-plane and transverse degrees of freedom.

5.3.1 Dependence on Direction of Travel

The CLPT model can be used to predict the wave propagation properties of a plane wave traveling along any direction. For transverse plate motion, a plane wave traveling in the θ direction relative to the laminate axes is described using a displacement field described by $w(x,y) = w_0 e^{i(\omega t - k(ax+by))}$ where $a = \cos(\theta)$ and

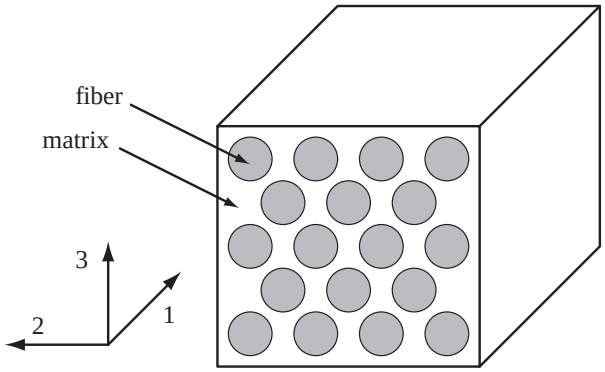

Figure 5.3: Principle axes for unidirectional fiber material

$b = \sin(\theta)$. The expression resulting from substitution in Equation (5.16) contains multiple stiffness terms:

$$k = \sqrt{\omega}\sqrt[4]{\frac{m}{a^4\mathsf{D}_{11} + b^4\mathsf{D}_{22} + 2\left(\mathsf{D}_{12} + 2\mathsf{D}_{66}\right)a^2b^2}} \tag{5.20}$$

The phase speed, ω/k, is shown for the $[0]_6$ and $[90/0_2/90]_\mathrm{s}$ laminates in Figure 5.4. For the unidirectional laminate, the stiffness of the laminate in the fiber direction is much higher than the stiffness perpendicular to the fiber direction, hence the larger phase speed when the wave is traveling along the fiber direction, 0°. For the cross-ply laminate, the difference in stiffness is not as drastic and the difference between the 0° and 90° directions is not as large. The stiffness in the 90° direction is slightly larger because the 90° plies in the layup are on the top and bottom surfaces and contribute more to the bending stiffness than the plies closer to the mid-plane.

For in-plane dynamics, displacements are assumed to be $u = u_0 e^{i(\omega t - k(ax+by))}$ and $v = v_0 e^{i(\omega t - k(ax+by))}$. Due to the coupled equations in Equation (5.18), an eigenvalue problem needs to be solved:

$$\left(m\omega^2\begin{bmatrix}1 & 0\\ 0 & 1\end{bmatrix} - k^2\begin{bmatrix}a^2\mathsf{A}_{11} + b^2\mathsf{A}_{66} & ab\left(\mathsf{A}_{12} + \mathsf{A}_{66}\right)\\ ab\left(\mathsf{A}_{12} + \mathsf{A}_{66}\right) & b^2\mathsf{A}_{22} + a^2\mathsf{A}_{66}\end{bmatrix}\right)\begin{bmatrix}u_0\\ v_0\end{bmatrix} = \begin{bmatrix}0\\ 0\end{bmatrix} \tag{5.21}$$

The two solutions to the eigenvalue problem describe the in-plane mode where the displacement of the material follows the movement of the plane wave and the shear horizontal mode of the plate. The phase speed is shown in Figure 5.5 for the S0

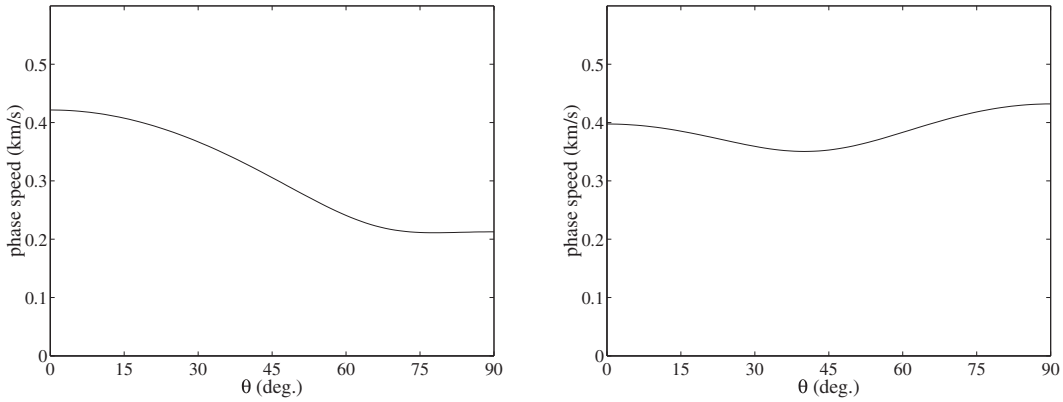

(a) 6[0] laminate (b) $[90/0_2/90]_s$ laminate

Figure 5.4: Phase speed for transverse waves at 10 kHz

mode in unidirectional and cross-ply laminates. For the unidirectional laminate, there is a large difference between the longitudinal and transverse directions. For the cross-ply laminate, the phase speed in the 0° and 90° directions is the same because the CLPT model assumes a constant deflection through the thickness for the in-plane displacement. The position of the plies relative to the mid-plane do not matter in the construction of the **A** matrix. Additionally, as with the isotropic case where the S0 mode travels much faster than the A0 mode, the phase speed of the in-plane waves in the composite laminate is faster than the transverse mode.

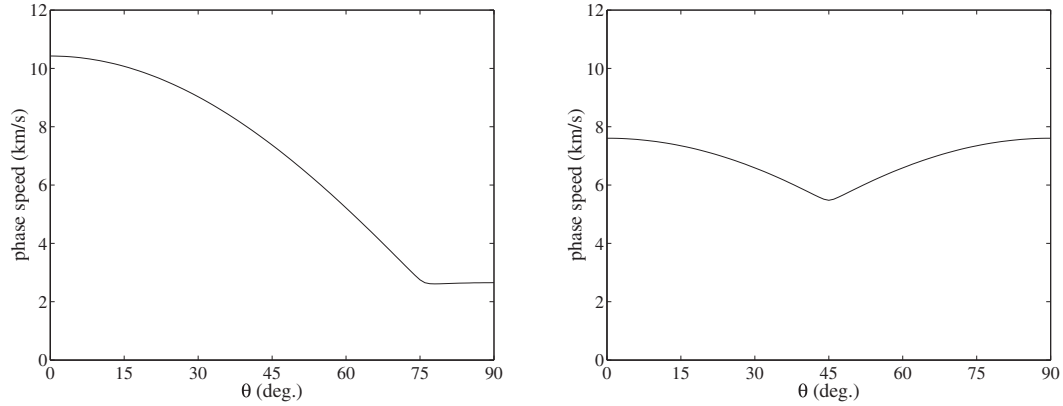

(a) 6[0] laminate (b) $[90/0_2/90]_s$ laminate

Figure 5.5: Phase speed for in-plane waves at 10 kHz

To illustrate the directional dependence on wave propagation, a 6.35 mm ×

6.35 mm (1/4 in. $\times$ 1/4 in.) PZT-5H patch was used to excite the $[0]_6$ laminate and a laser vibrometer was used to monitor several locations around the actuator, shown in Figure 5.6. The actuator was excited with a chirp signal which ranged from 5 kHz to 20 kHz. Since the laser vibrometer, as it is set up, is only able to measure transverse vibrations, only the A0 mode is able to be monitored. The bandwidth limit of the laser vibrometer system is 50 kHz. The vibrometer was used to scan a set of points located at constant radial distance from the actuator. Three sets of points were monitored, 2.54 cm (1 in.), 5 cm (2 in.), and 7.5 cm (3 in.) from the actuator. Figure 5.7 shows the response of the plate and the three radial locations. As expected, the wave propagating along the fiber direction, 0°, travels faster than in the transverse direction, 90°. As the A0 mode travels through the plate, the waveform spreads out due to dispersion. A wave returning from the boundary edges are seen later on in the time domain.

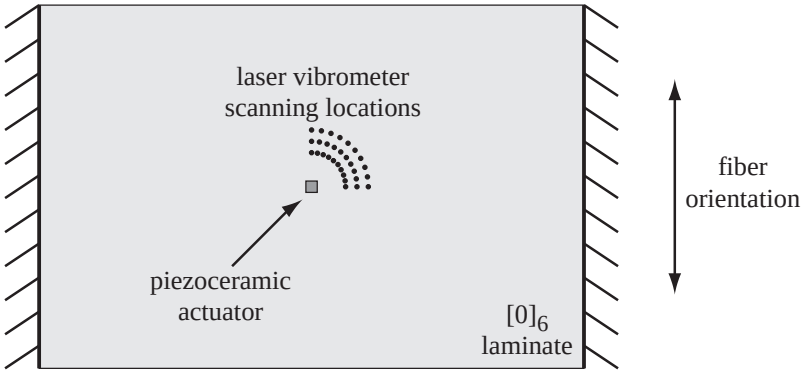

Figure 5.6: $[0]_6$ laminate setup for laser vibrometer

For the $[90/0_2/90]_s$ laminate, the response of the plate 10 cm (4 in.) from the actuation piezoceramic was monitored using the laser vibrometer along the 0° and 90° directions, shown in Figure 5.8. The response at the two positions are shown in Figure 5.9 for an excitation of 10 kHz and 20 kHz. In both cases, the transient reaches the sensing location in the 90° direction earlier than the 0° sensing location. The plate is slightly stiffer in the 90° direction and the waves travel faster.

In order to use the sensor array and signal processing effectively, the disper-

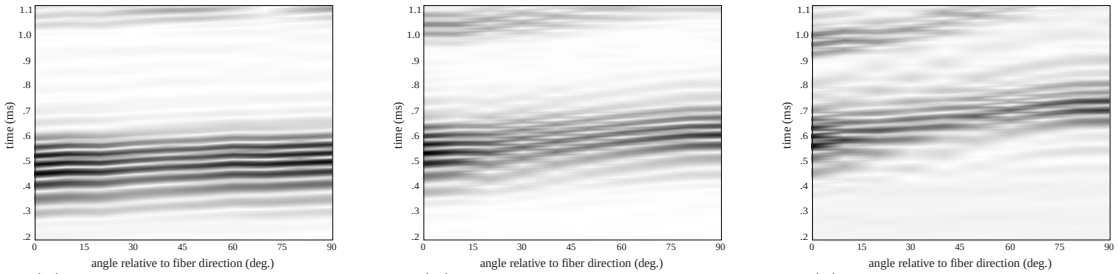

(a) 1 in. radial location (b) 3 in. radial location (c) 5 in. radial location

Figure 5.7: Wave propagation in $[0]_6$ laminate

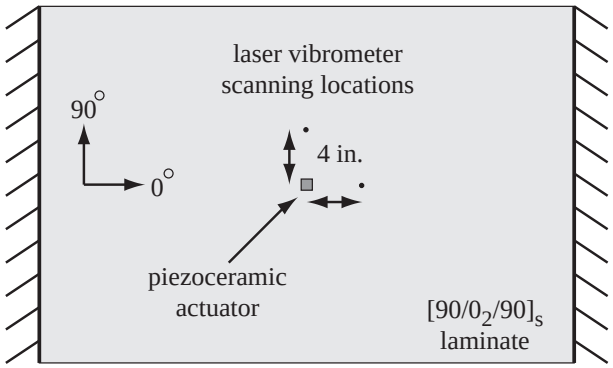

Figure 5.8: $[90/0_2/90]_s$ laminate setup for laser vibrometer

sion relations for composite laminate, and in particular, the wavenumber-frequency relationship, needs to be understood.

5.3.2 Experimental Setup and Results

The wavenumber-frequency relationships for the A0 and S0 modes are found experimentally for the $[0]_6$ and $[90/0_2/90]_s$ laminates and compared with the CLPT and FE models. Both the CLPT and FE models assume a plane wave where the wavefront is normal to the direction of propagation. This condition is only satisfied when the waves are traveling in the 0° and 90° directions for the given laminates. The wavenumber-frequency relationship is determined in only these two directions. Figure 5.10 shows a diagram of the experimental setup to determine the wavenumber-frequency relationship for the two different composite laminates. The processing

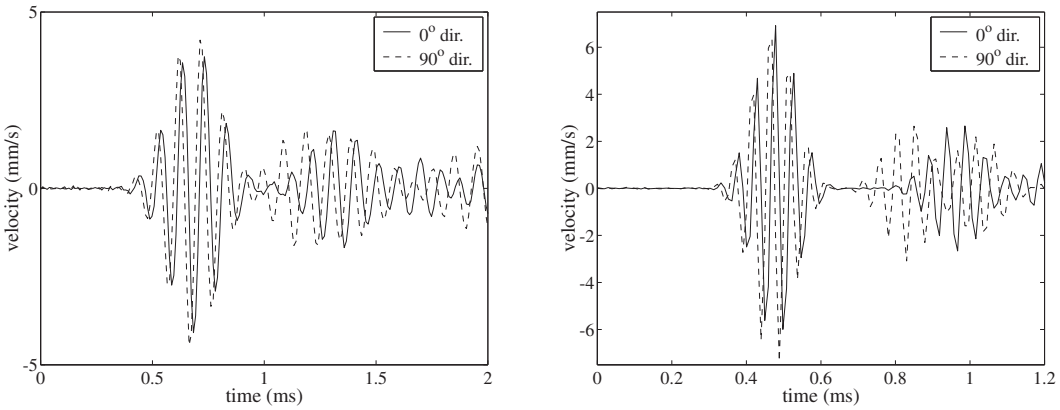

(a) 10 kHz excitation (b) 20 kHz excitation

Figure 5.9: Laser vibrometer response for $[90/0_2/90]_s$ laminate

of the sensor signals into the array response is similar to that performed on the signals from the Aluminum plate case in Section 4.3. The sensor array was used to deconstruct the transient waveforms at each excitation frequency into the wavenumber components. The maximum in the wavenumber spectrum corresponded to the wavenumber for the corresponding excitation frequency.

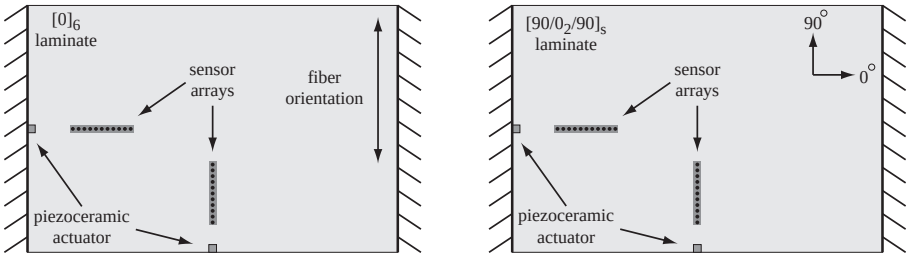

(a) $[0]_6$ laminate (b) $[90/0_2/90]_s$ laminate

Figure 5.10: Experimental setup to determine the relationship frequency-wavenumber for composite laminates

The results for the $[0]_6$ laminate is shown in Figure 5.11 for the A0 mode and Figure 5.12 for the S0 mode. The CLPT model is shown to under-predict the wavenumber for a given frequency in the A0 response. This is expected because the shear deformation is not allowed in the CLPT model and the A0 mode is affected by shear deformations at higher frequencies. There is not much difference between

the CLPT, FE, and experimental results for the S0 mode. At these low frequencies, there is no shear deformation in the S0 modes, thus the CLPT model does an accurate job of predicting in-plane wave propagation dynamics. There is no difference between results provided by the FE model when one or two elements were used per ply. The results for the cross-ply laminate, with a layup of $[90/0_2/90]_s$, are shown in Figures 5.13 and 5.14 for the A0 and S0 modes, respectively. As with the unidirectional case, there is significant difference between the CLPT and actual results for the A0 mode. The FE model does a satisfactory job in predicting the wave propagation behavior though it under-predicts the wavenumber curve. The experimental results suggest that the cross-ply laminate is more compliant than predicted.

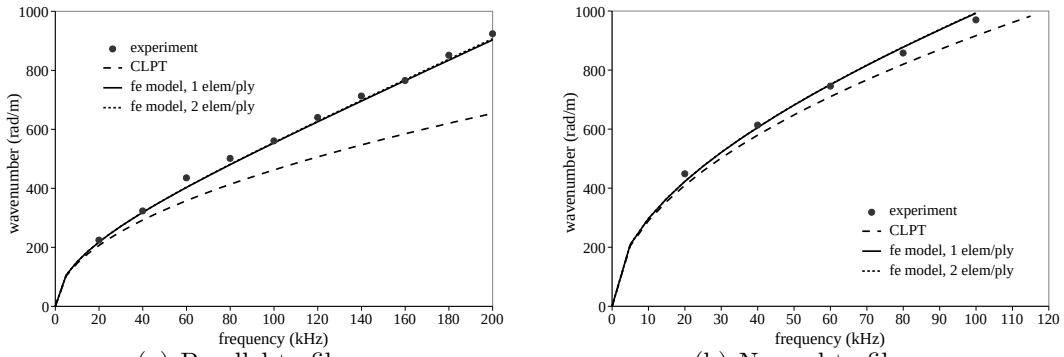

(a) Parallel to fibers (b) Normal to fibers

Figure 5.11: Wavenumber-Frequency relationship of A0 mode in $[0]_6$ laminate

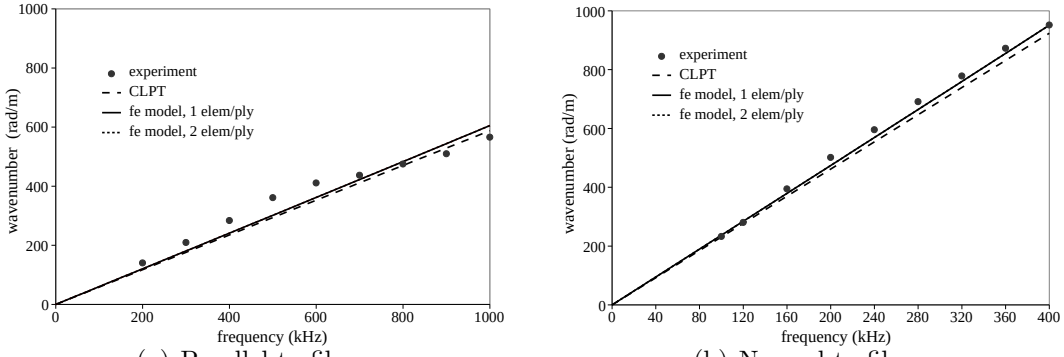

(a) Parallel to fibers (b) Normal to fibers

Figure 5.12: Wavenumber-Frequency relationship of S0 mode in $[0]_6$ laminate

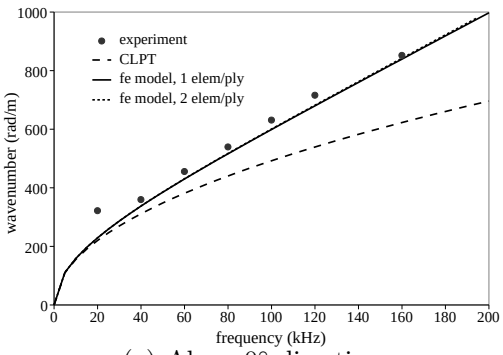

(a) Along 0° direction

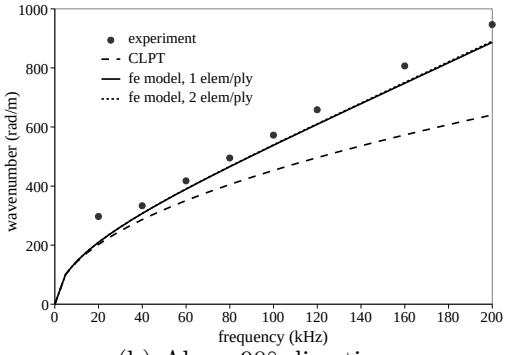

(b) Along 90° direction

Figure 5.13: Wavenumber-Frequency relationship of A0 mode in $[90/0_2/90]_s$ laminate

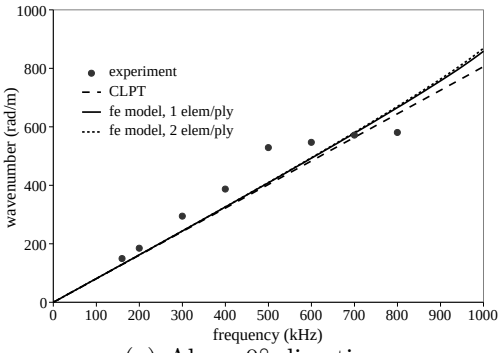

(a) Along 0° direction

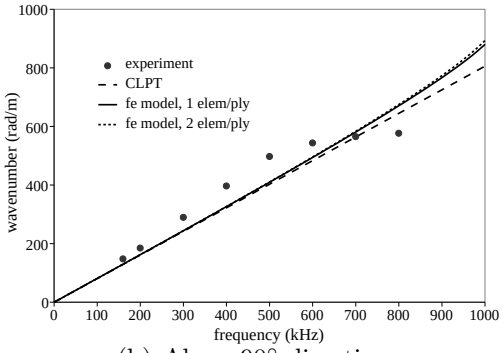

(b) Along 90° direction

Figure 5.14: Wavenumber-Frequency relationship of S0 mode in $[90/0_2/90]_s$ laminate

The group speeds, based on the CLPT and FE model, are determined from the wavenumber-frequency curves. For the unidirectional laminate, the group speed for the principle directions are shown in Figure 5.15. As observed using the laser vibrometer results, the waves moving along the fiber direction move faster than waves normal to the fiber orientation. The CLPT model over-predicts the group speed and the difference is substantial since the slope of the wavenumber-frequency curve is used to determine the group speed. For the cross-ply laminate, the group speed of the S0 mode in the 0° and 90° directions are the same in the CLPT formulation because the total number of 0° plies and 90° plies are the same. The stacking sequence does make a difference in the FE model. Group speeds for the cross-ply

laminate principle directions are presented in Figure 5.16.

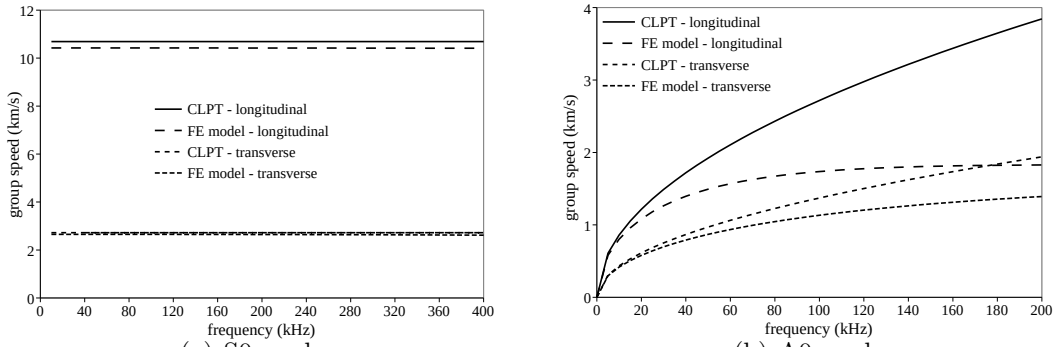

(a) S0 mode (b) A0 mode

Figure 5.15: Group speed of unidirectional laminate

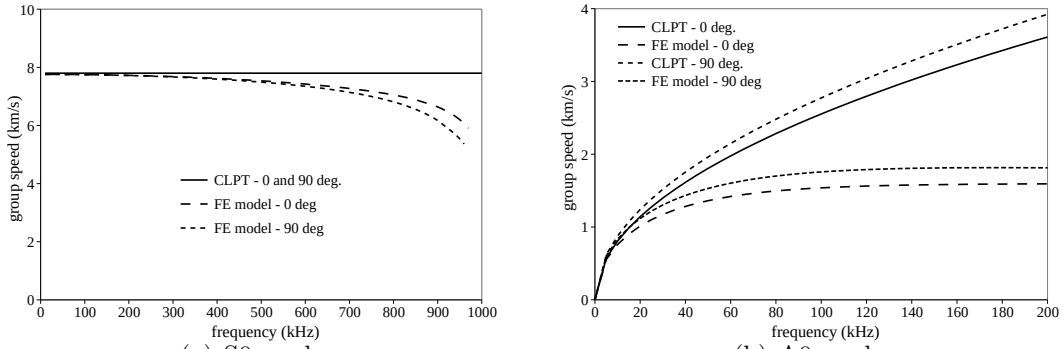

(a) S0 mode (b) A0 mode

Figure 5.16: Group speed of cross-ply laminate

5.4 Damage Detection in Composite Laminates

Damage in thin composite laminates typically form due to the large difference in the in-plane Poisson's ratio, ν_{LT} and ν_{TL}, for a unidirectional ply. When an in-plane load is applied to a cross ply laminate the region between the two dissimilar plies experiences high interlaminar shear stresses. The matrix in a composite typically carries the shear load and is relatively weak. Under cyclic loading the matrix cracks and the damaged region propagates through the interlaminar region to produce a delamination.

Most of the work dealing in damage detection in composite laminates focus on delamination damage. The Acousto-Ultrasonics (AU) approach for delamination damage detection looks for changes in the wave propagation characteristics based on the delamination. Mujumdar [134] developed a representative stiffness model of the delamination region by ensuring that the displacement, slope, moments, and shears at the delamination edge was equal to the undamaged region. The impedance change between the undamaged section of a laminate and a delamination portion causes waves to be reflected back though the reflections are relatively weak. These weak reflections are commonly drowned out by the dynamics of the plate associated with reflections from the boundary conditions. A sensor array is able to extract these reflections.

Previous work on delamination damage detection using an Acousto-Ultrasonics approach relied heavily on ultrasonic transducers and the use of the S0 mode for interrogation. Birt [85] used ultrasonic transducers to excite high frequency S0 modes to examine delaminations of various sizes and positions through the thickness. Guo [82] indicated that a modes shear stress distribution through the thickness is important in determining the sensitivity of the mode to a delamination. A delamination eliminates interlaminar shear stresses. Since all high frequency modes exhibit shear stresses, either the S0 or A0 mode may be used. In the low frequency region, only the A0 mode produces a shear stress distribution. In this study, the low frequency A0 mode is used in the composite laminate to determine the presence of a delamination. The sensor array is used to extract weak reflections from the delamination in the presence of much stronger signals corresponding to waves reflecting off of boundaries.

An experimental setup to examine delamination damage detection is shown in Figure 5.17. A piezoceramic actuator is used to excite the structure with interrogating waves. The sensor array is positioned in the middle of the plate and is used to observe the incoming rightward structural wave and any subsequent reflections from the right edge in the form of leftward waves. Along with the undamaged composite laminate, laminates with delaminations were constructed. Delamination

damage was created by introducing a circular layer of Teflon between a 90° in the middle of the plate and the adjacent 0° ply, shown in Figure 5.18. Laminates with a delamination sizes of 2.54 cm (1 in.) and 5.08 cm (2 in.) diameter were examined. Sensor arrays were made and bonded onto each laminate and were used in the damage detection setup.

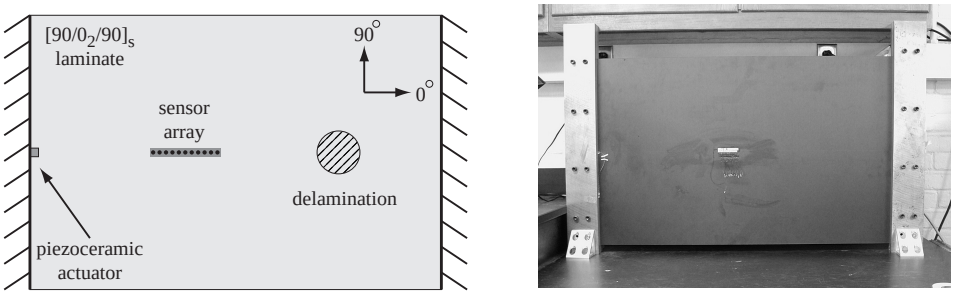

(a) Delamination detection setup (b) Picture of setup

Figure 5.17: Delamination detection in composite laminate

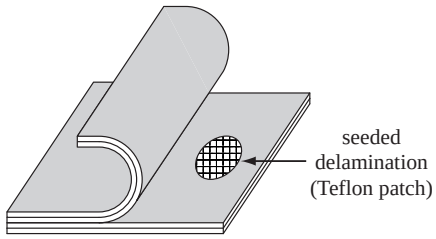

Figure 5.18: Teflon patch used to seed delamination

By using the piezoceramic patch to excite the structure and the sensor array to gather the responses, the same experimental wavenumber-frequency curve that is shown in Figure 5.13 can be produced using the initial portion of the transient data for the 2.54 cm and 5.08 cm delamination cases. This data can be used to characterize the laminate because there is no information regarding any damage in the initial burst from the actuator. Any information regarding damage in the structure would occur later on in time. For the delamination cases, only frequencies between 40 and 100 kHz were examined, and the wavenumbers corresponding to

those frequencies are shown in Figure 5.19. The direction of propagation is along the 0° direction using the A0 mode. The results from the laminates with the 2.54 cm and 5.04 cm delamination are very close to the results from the undamaged plate, indicating that the plates have similar wave propagation properties.

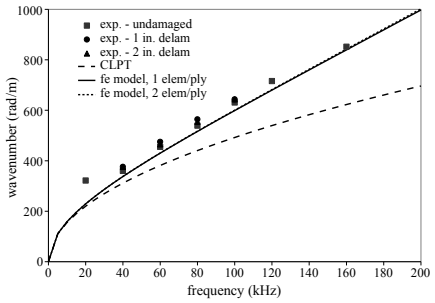

Figure 5.19: Wavenumber-Frequency relationship of A0 mode in $[90/0_2/90]_s$ laminate including delaminated plate data

Figure 5.20(a) shows the response of the middle sensor of the array for a 7 cycle tone burst of 40 kHz. The middle sensor response shows no significant qualitative difference between the responses of the undamaged and delaminated plates. The initial transient in the signals at ∼.45 ms corresponds to the incident wave from the actuation element. This initial wavefront is followed by reflections from the top and bottom edges which arrive coincidentally at ∼.7 ms and ∼1.1 ms. Whatever slight differences that are present do not necessarily point to the presence of damage in the structure. Any information regarding a reflection from the delamination in the damaged plates are drowned out by the reflections from the boundary edges. The sensor signals for the array are processed such that only the rightward and leftward propagating waves are present. The rightward and leftward propagating components are shown in Figures 5.20(b) and 5.20(c). The rightward propagating waves show no discernible difference. The incident wave from the actuator is seen at ∼.45 ms with a following transient at ∼.7 ms. This second transient is due to the reflections from the top and bottom edges leaking into the filtered array response. The leftward propagating waves show the presence of a reflection in the delaminated plate cases at ∼.8 ms. This reflection corresponds to the reflection

from the delaminated region. The reflection from the right edge of the plate is captured at ∼1.4 ms. There appears to be additional transient information in the leftward propagating signals which should not be there. Since the magnitude of the reflections from the delamination and right edge are relatively weak, noise in the signals and imperfections in the array spacing and element size become more pronounced. A different sensor array was used with each laminate and the leakage pattern is different for each array. Regardless of these hindrances, the array is still able to extract the reflections from the delamination region.

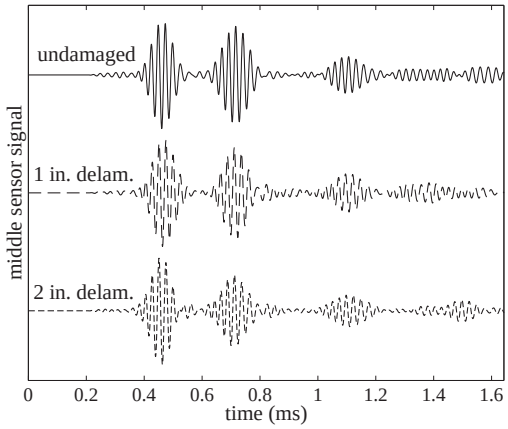

(a) Middle sensor response

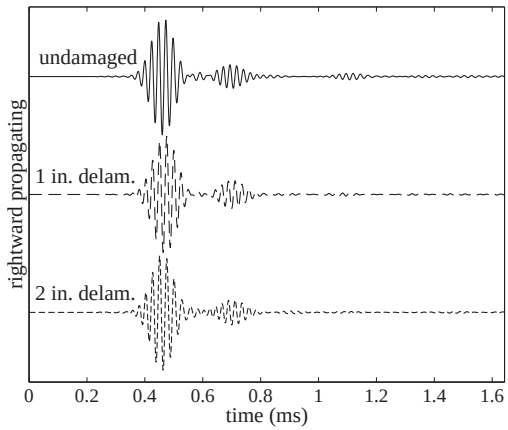

(b) Rightward propagating

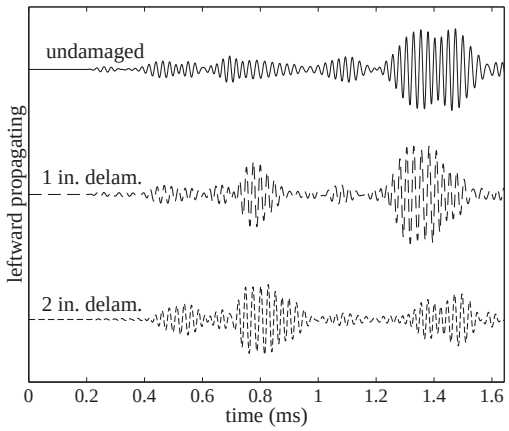

(c) Leftward propagating

Figure 5.20: Delamination damage detection - 40 kHz

Figure 5.21 shows the middle sensor signals as well as the rightward propagating and leftward propagating array responses corresponding to a seven cycle tone burst at 60 kHz. As with the 40 kHz case, the middle sensor response in Fig-

ure 5.21(a) shows no difference which would indicate the presence of delamination. The rightward propagating waves in Figure 5.21(b) shows clearly the incident wave from the actuation element. The leftward propagating waves from the delamination region shows the reflection from the delamination arrive earlier than the 40 kHz case at $\sim$.7 ms, which is expected. There is still the problem of spurious information interfering with the relatively weak reflections from the delamination.

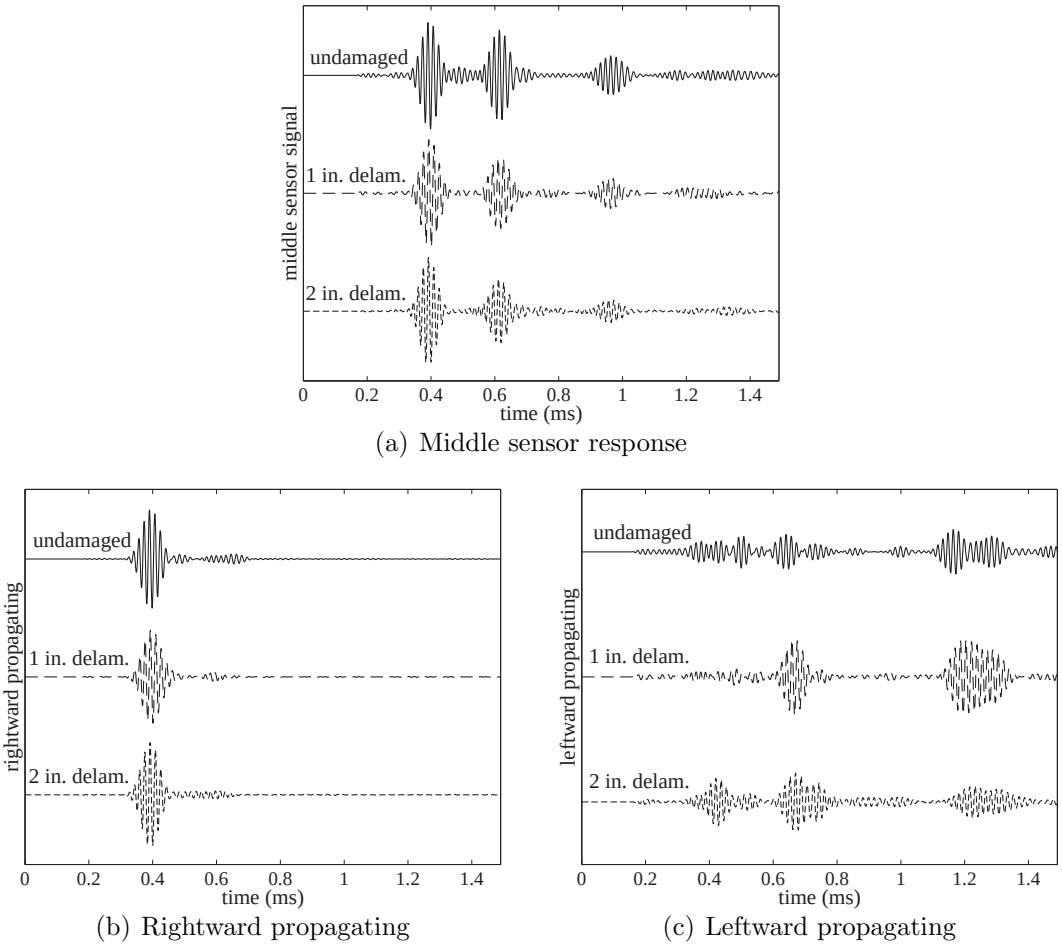

(a) Middle sensor response

(b) Rightward propagating

(c) Leftward propagating

Figure 5.21: Delamination damage detection - 60 kHz

Figures 5.22 and 5.23 show results for the cases of 5 cycle tone bursts of 80 kHz and 100 kHz, respectively. The results are similar to the previous results in that the array is able to extract the weak reflections from the delamination region. Leakage as well as small differences in the array spacing and element sizes corrupt the filtered array response.

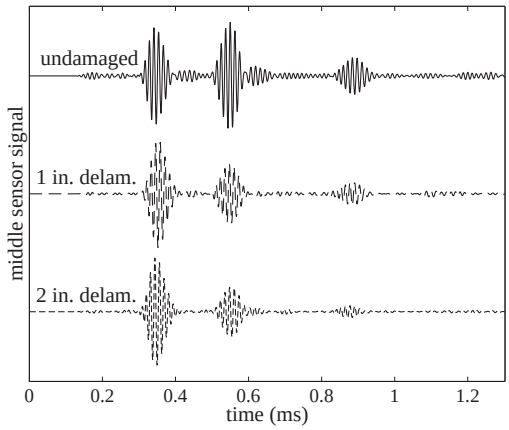

(a) Middle sensor response

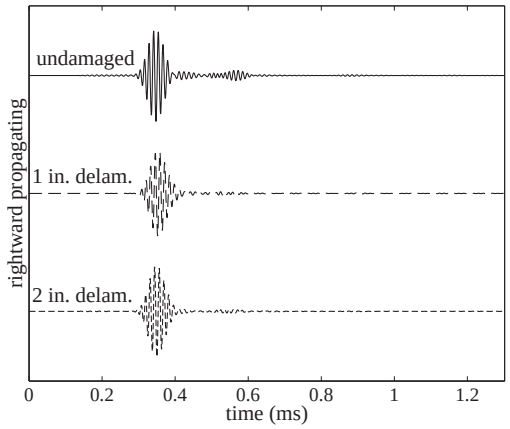

(b) Rightward propagating

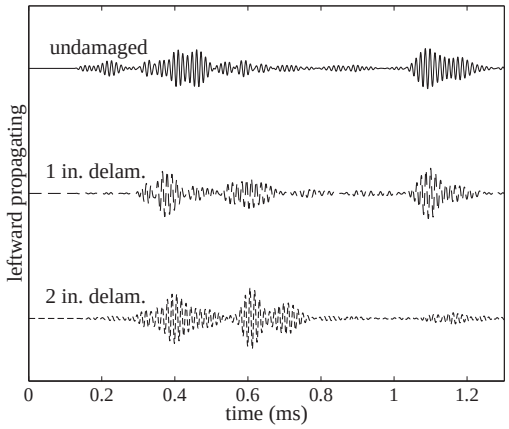

(c) Leftward popagating

Figure 5.22: Delamination damage detection - 80 kHz

Assuming that the identified portions of the time domain signals correspond to reflections from the delamination, a damage index, DI, can be constructed in a similar manner as the isotropic plate case. Figure 5.24 displays the results for the given sets of data. The simple damage index metric provides inconclusive results for the use of the energy in the transient signal as method of delamination size determination. The distance between the array and the delamination location and the array can also be determined based on the time interval between the incident rightward propagating waves and the identified reflected leftward propagating waves from the delamination. Since the group velocity of the tone burst at the different excitation frequencies are known, an estimate of the approximate location of the delamination can be determined. A summary of the results are shown in Table 5.4

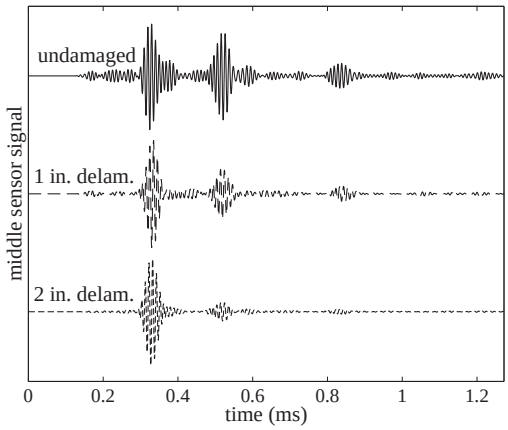

(a) Middle sensor response

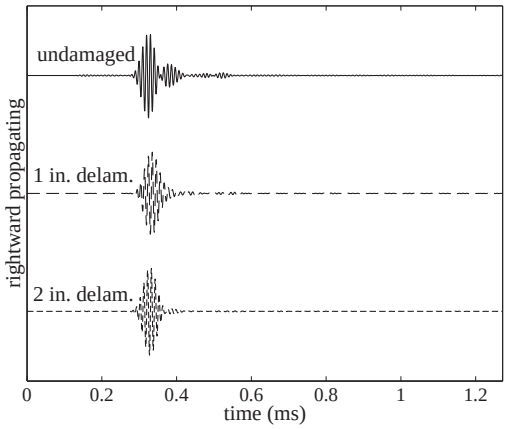

(b) Rightward propagating

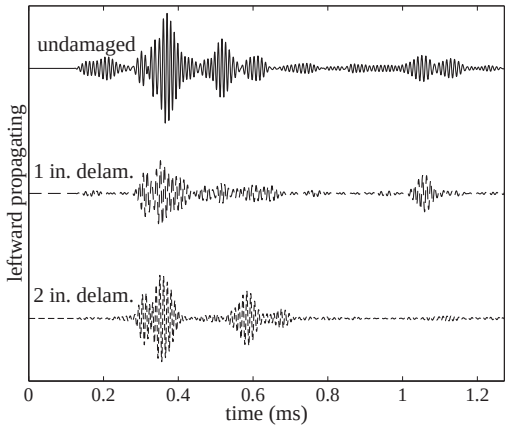

(c) Leftward propagating

Figure 5.23: Delamination damage detection - 100 kHz

where the location of the delamination can be placed accurately for the 5 cm (2 in.) delamination.

There are a number factors which affected the damage detection efforts:

1. Noise in sensor signals due to electromagnetic interference was on the order of the sensor signals. This was somewhat mitigated using signal averaging.

2. Different sensor arrays were bonded on each composite laminate. Thus each array had slightly different array spacing and element sizes, resulting in different filtering capabilities.

3. Small delaminations produce relatively small changes in the local impedance of the composite laminate. As a result, the reflections are much weaker than

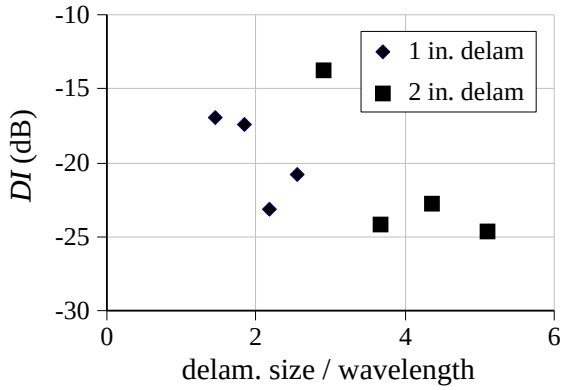

Figure 5.24: Damage Index (DI) for delamination damage

frequency (kHz)	inc. arrival (ms)	ref. arrival (ms)	time of flight (ms)	c_g (km/s)	distance (m) (in.)
40	.46	.79	.33	1.28	.208 (8.2)
60	.39	.67	.28	1.42	.195 (7.7)
80	.35	.61	.26	1.50	.193 (7.6)
100	.33	.58	.25	1.54	.197 (7.8)

Table 5.4: Delamination Location Relative to Array

the incident waves.

4. Different piezoceramic actuators were bonded to each laminate. The size of the actuator and the bonding conditions are slightly different among the plates resulting in actuation differences among the setups.

All of these factors limited the efficacy of the damage detection approach using directional filtering. Additionally, the effects of each of these factors is a function of frequency, producing varying results at the different excitation frequencies. Each of the factors can be improved upon in future efforts.

5.5 Summary

A Classical Laminated Plate (CLPT) theory is presented to model the dynamics of the composite laminate. From the CLPT formulation, the dynamics of both the in-plane and transverse modes of vibration may be determined. As in the simple Kirchoff plate theory, CLPT eliminates shear strain through the thickness, which reduces its applicability for high frequency wave propagation dynamics. A higher order model using finite elements presented in Section 2.6 is adapted for use in composite laminates.

Composite laminates of two different layups were constructed, a six ply unidirectional laminate and a cross-ply laminate with a layup of $[90/0_2/90]_s$. A laser vibrometer is used to show the variation in the wave propagation properties for both the unidirectional and the cross-ply laminate. In both cases, the transverse wave propagation properties are dependent on direction of travel.

A sensor array was used to determine the wavenumber-frequency relationship for both laminates in the two principle directions of each laminate. The experimental results were compared to results from the CLPT and FE models. The experimental results show good agreement with the FE model whereas the CLPT model results were lacking, especially for the A0 modes. The CLPT model predicted much stiffer behavior, which was expected.

A damage detection application was then presented. Cross-ply laminates were constructed with seeded delaminations of 2.54 cm (1 in.) and 5 cm (2 in.). The sensor array and associated signal processing is shown to extract the weak reflections from a delamination in the cross-ply laminate. In the results, spurious information is also included in the spatially filtered signals. This spurious information is due to number of factors. Further addressing of these factors, such as improving upon the manufacture of the sensor array as well as improved signal conditioning circuitry, would improve the quality of the results.

Chapter 6

Comparison Between Modal and Wave Propagation Methods

6.1 Introduction

In the previous chapters, wave propagation is seen to be useful for damage detection applications. Other techniques have been proposed for wide area damage detection. One relatively mature approach is the use of modal dynamics to identify changes in a structure. This chapter explores a comparison between typical modal methods and a wave propagation approach on a simple beam structure.

A description of the modal dynamics approach toward damage detection is presented with emphasis on three particular approaches, Modal Residual Method, Element-By-Element Sensitivity Method, and the Eigenstructure Assignment Method. These algorithms are used to detect damage in a beam structure with a loss in stiffness where the modal parameters are predicted numerically and passed to each algorithm.

A wave propagation approach is also presented where the transient dynamics of the beam is modeled and a simple sensor array is used to identify changes in the transient response. The changes in the transient response are compared to analytical formulations of the effect of a stiffness loss on wave propagation in a beam. A scattering relationship is developed to identify the amount of damage. The scattering from the damaged region of the structure is then used to predict the amount of damage.

6.2 Modal Dynamics

A modal dynamics approach to damage detection uses the changes in natural frequencies and modeshapes to locate and quantify damage in a structure. Typically, the damaged modal information, such as natural frequencies and/or modeshapes, are compared to the undamaged modal information. Algorithms predict the location and attempt to quantify the amount of damage in the structure.

The equation of motion for the structure is the starting point:

$$\mathbf{M}\ddot{\mathbf{x}} + \mathbf{K}\mathbf{x} = \mathbf{0} \tag{6.1}$$

$\mathbf{M}$ and $\mathbf{K}$ are the mass and stiffness matrices of the structure, respectively, and $\mathbf{x}$ is the vector of nodal degrees of freedom. The natural frequencies and modeshapes of the system are found from the eigenvalue problem:

$$\left(\mathbf{K} - \omega_n^2 \mathbf{M}\right) \mathbf{x}_n = \mathbf{0} \tag{6.2}$$

ω_n is one of the natural frequencies and the corresponding eigenvector, $\mathbf{x}_n$, is the modeshape.

In the presence of damage, the natural frequencies and modeshapes shift from the nominal values. The basic premise of damage detection using modal methods is to determine the location and extent of damage based on the nominal model of the structure, $\mathbf{M}$ and $\mathbf{K}$, and a set of natural frequencies and modeshapes of the damaged structure, $\omega_{d,n}$ and $\mathbf{x}_{d,n}$.

A simple schematic for damage detection using a modal dynamics approach involves several steps [13], shown in Figure 6.1. A baseline model of the structure is generated using an analytical model of the structure which is adjusted with experimental testing of the nominal structure. This baseline model of the nominal structure is used as the undamaged case. When the structure is tested again, the experimental modal properties are compared to the baseline model. For an undamaged case, Equation (6.2) is satisfied using the experimental natural frequencies and modeshapes along with the model of the structure. In the case of damage, the expression is not satisfied, indicating the presence of damage.

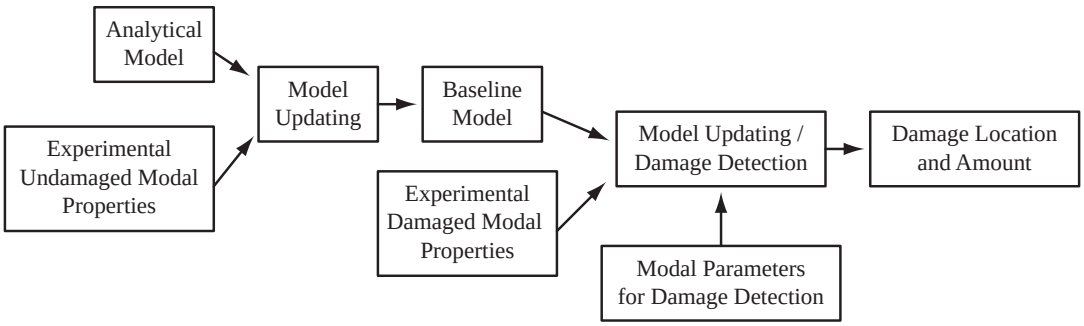

Figure 6.1: Damage detection using modal dynamics

Since the number of sensors used experimentally may not match the number of degrees of freedom in the model, either model reduction or modal expansion is used to maintain consistency. The degrees of freedom of the model are split into known degrees of freedom, $\mathbf{x}_k$, and unknown degrees of freedom, $\mathbf{x}_u$. For example, in the static case, the stiffness matrix, can be partitioned into four components:

$$\begin{bmatrix} \mathbf{K}_{kk} & \mathbf{K}_{ku} \\ \mathbf{K}_{ku}^T & \mathbf{K}_{uu} \end{bmatrix} \begin{bmatrix} \mathbf{x}_k \\ \mathbf{x}_u \end{bmatrix} \tag{6.3}$$

A reduced order model of the system matching the known degrees of freedom can be generated based on the work by Guyan [135] and Kidder [136]. In the formulation by Kidder, the reduced mass and stiffness matrices are formed from the submatrices:

$$\mathbf{K}_R = \mathbf{K}_{kk} - \mathbf{K}_{ku}^{-1}\mathbf{K}_{uu}\mathbf{K}_{ku}^T \tag{6.4}$$
$$\mathbf{M}_R = \mathbf{M}_{kk} - \mathbf{K}_{ku}\mathbf{K}_{uu}^{-1}\mathbf{M}_{ku}^T - \mathbf{M}_{ku}\mathbf{K}_{uu}^{-1}\mathbf{K}_{ku}^T + \mathbf{K}_{ku}\mathbf{K}_{uu}^{-1}\mathbf{M}_{uu}\mathbf{K}_{uu}^{-1}\mathbf{K}_{ku}^T$$

The subscript R refers to the new, reduced, model of the structure. In modal expansion, the opposite tactic is used to match the known variables with the order of the system. Rather than reducing the model of the system to match the known degrees of freedom, the known degrees of freedom can be expanded to match the order of the original system. The unknown degrees of freedom for a specific mode, n, are found based on the natural frequency and known degrees of freedom:

$$\mathbf{x}_{u,n} = -\left(\mathbf{K}_{uu}^{-1} + \omega_n^2\mathbf{K}_{uu}^{-1}\mathbf{M}_{uu}\mathbf{K}_{uu}\right)\left(-\omega_n^2\mathbf{M}_{ku}^T + \mathbf{K}_{ku}^T\right)\mathbf{x}_{k,n} \tag{6.5}$$

Damage detection in a structure using modal dynamics typically use either model reduction or modal expansion to match the number of sensor inputs with the order of the model.

6.2.1 Damage Detection Using Optimal Matrix Updating

The Minimum Rank Perturbation Theory (MRPT) algorithm [28, 29] uses a damage vector based on the modal residual. When the natural frequencies and modeshapes of the damaged structure are used in Equation (6.2) with the undamaged model of the structure, a modal residual results:

$$\left(\mathbf{K}_p - \omega_{d,n}^2 \mathbf{M}_p\right) \mathbf{x}_{d,n} = \mathbf{R}_n \tag{6.6}$$

The subscript p refers to the pristine, or undamaged, model of the structure. $\mathbf{R}_n$ is the residual for the nth mode with damaged modeshape, $\mathbf{x}_{d,n}$, and natural frequency, $\omega_{d,n}$. Each element of the modal residual can be normalized to construct an angle vector:

$$\beta_n^m = \cos^{-1}\left(\frac{\mathbf{R}_n^m}{\left|\left(\mathbf{K}_p - \omega_{d,n}^2 \mathbf{M}_p\right)^m\right|\left|\mathbf{x}_{d,n}\right|}\right)\left(\frac{180}{\pi}\right) - 90 \tag{6.7}$$

The superscript m refers to the mth element of a vector or the mth row of a matrix. The summation of the angle indicator vector for each mode, β_n, yields an overall indicator for damage in each element of the structure:

$$\beta = \sum_{n=1}^{N_{modes}} \beta_n \tag{6.8}$$

An estimate of the change in the structure can be found using the modal residual as well as the damaged modeshape:

$$\Delta\mathbf{K} = \mathbf{R}_n \left(\mathbf{R}_n^T \mathbf{x}_{d,n}\right)^{-1} \mathbf{R}_n^T \tag{6.9}$$

6.2.2 Damage Detection Using Sensitivity Methods

The Sensitivity Based Element-by-Element (SBEBE) method attempts to locate damage based on an a change in a local property of the structure. The local changes

in the structure affect the natural frequencies and modeshapes of the global dynamics. This change is quantified by an objective function. Typically, an optimization algorithm is used to minimize the objective function which determines the location and extent of damage simultaneously. A simple objective function is used based on the modal residual:

$$J_n = \mathbf{x}_{d,n}^T \left(-\omega_{d,n}^2 \mathbf{M}_d + \mathbf{K}_d\right)^T \left(-\omega_{d,n}^2 \mathbf{M}_d + \mathbf{K}_d\right) \mathbf{x}_{d,n} \tag{6.10}$$

The $\mathbf{M}_d$ and $\mathbf{K}_d$ matrices refer to the proposed damaged mass and stiffness matrices respectively. The damaged mass and stiffness matrices are constructed from elemental mass and stiffness matrix where the the properties of the element are deviated from the nominal value by a damage amount:

$$\mathbf{M}_d = \sum_{e=1}^{N_{elem}} \left(\mathbf{M}_e + d\alpha_e \frac{\partial \mathbf{M}_e}{\partial \alpha_e}\right) \qquad \mathbf{K}_d = \sum_{e=1}^{N_{elem}} \left(\mathbf{K}_e + d\beta_e \frac{\partial \mathbf{K}_e}{\partial \beta_e}\right) \tag{6.11}$$

α_e is a property of the elemental mass matrix and β_e is a property of the elemental stiffness matrix which may be altered by damage. The cost function for the particular mode, J_n, is then a function of these elemental parameters. Ideally, the cost function is minimized when the correct structural parameter is chosen and adjusted such that the eigenvalue problem for the damaged structure is solved for the given damaged natural frequency and modeshape. A total cost function for all of the modes of consideration may be constructed by summing them together:

$$J = \sum_{n=1}^{N_{modes}} J_n \tag{6.12}$$

6.2.3 Damage Detection Using Eigenstructure Assignment Methods

The Eigenstructure Assignment Damage Location (EADL) uses a first order approximation to change the elemental structure:

$$\mathbf{M}_d = \mathbf{M}_p + \sum_{e=1}^{N_{elem}} b_e \mathbf{M}_e \qquad \mathbf{K}_d = \mathbf{K}_p + \sum_{e=1}^{N_{elem}} a_e \mathbf{K}_e \tag{6.13}$$

The subscripts d and p refer to the damaged and pristine, or undamaged, global system matrices. The changes to the global system matrices are a function of small

changes to each individual elemental matrices. The damaged eigenvalue problem is used as a starting point:

$$\left(\mathbf{K}_d - \omega_{d,n}^2 \mathbf{M}_d\right) \mathbf{x}_{d,n} = \mathbf{0} \tag{6.14}$$

The representation of the damaged matrices in Equation (6.13) are substituted into the eigenvalue problem:

$$\left(-\mathbf{K}_p + \omega_{d,n}^2 \mathbf{M}_p\right) \mathbf{x}_{d,n} = \sum_{e=1}^{N_{elem}} \left(a_e \mathbf{K}_e - b_e \omega_{d,n}^2 \mathbf{M}_e\right) \mathbf{x}_{d,n} \tag{6.15}$$

By defining $\boldsymbol{\mathcal{R}}_n = \left(-\mathbf{K}_p + \omega_{d,n}^2 \mathbf{M}_p\right)^{-1}$, the structural stiffness influence matrix and mass influence matrix are defined:

$$\boldsymbol{\mathcal{A}}_{en} = \boldsymbol{\mathcal{R}}_n \mathbf{K}_e \qquad\qquad \boldsymbol{\mathcal{B}}_{en} = \omega_{d,n}^2 \boldsymbol{\mathcal{R}}_n \mathbf{M}_e \tag{6.16}$$

If only one element is considered to be damaged, Equation (6.15) can rewritten:

$$\mathbf{x}_{d,n} = \boldsymbol{\mathcal{A}}_{en} a_e \mathbf{x}_{d,n} + \boldsymbol{\mathcal{B}}_{en} b_e \mathbf{x}_{d,n} \tag{6.17}$$

The subscript e refers to the damaged element. Using this formulation, the location and extent of damage may be located simultaneously. The best achievable modeshape, $\mathbf{x}_{a,n}$, is defined using the influence matrices:

$$\mathbf{x}_{a,n} = \boldsymbol{\mathcal{L}}_{en}^{+} \boldsymbol{\mathcal{L}}_{en} \mathbf{x}_{d,n} \qquad\qquad \boldsymbol{\mathcal{L}}_{en} = \begin{bmatrix} \boldsymbol{\mathcal{A}}_{en} & \boldsymbol{\mathcal{B}}_{en} \end{bmatrix} \tag{6.18}$$

The superscript, $+$, refers to the pseudo-inverse of the given matrix. Ideally, the best achievable modeshape vector, $\mathbf{x}_{a,n}$, should lie along the damaged modeshape vector, $\mathbf{x}_{d,n}$. The angle between the two vectors may used to quantify this relationship:

$$\alpha(e) = \cos^{-1}\left(\frac{\mathbf{x}_{a,n} \cdot \mathbf{x}_{d,n}}{|\mathbf{x}_{a,n}||\mathbf{x}_{d,n}|}\right) \tag{6.19}$$

The angle between the damaged modeshape and the best achievable modeshape is found for each element. The element corresponding to the smallest angle, $\alpha(e)$, points to the element where the damage is located. The amount of damage may be determined from Equation (6.17) where the change in mass and stiffness for the given element may be determined simultaneously:

$$\begin{bmatrix} a_e \\ b_e \end{bmatrix} = \begin{bmatrix} \boldsymbol{\mathcal{A}}_{en} \mathbf{x}_{d,n} & \boldsymbol{\mathcal{B}}_{en} \mathbf{x}_{d,n} \end{bmatrix}^{+} \mathbf{x}_{d,n} \tag{6.20}$$

6.3 Simulation - Damage Detection in Beam

A finite element model of a beam is used to predict the modal properties of a beam for damage detection purposes. The model is based on the Bernoulli-Euler two node element, shown in Figure 6.2, where the degrees of freedom at each node are displacement and slope. The common form of the elemental mass and stiffness matrices are used:

$$\mathbf{M}_e = \frac{\rho A l_e}{420}\begin{bmatrix} 156 & 22l_e & 54 & -13l_e \\ 22l_e & 4l_e^2 & 13l_e & -3l_e^2 \\ 54 & 13l_e & 156 & -22l_e \\ -13l_e & -3l_e^2 & -22l_e & 4l_e^2 \end{bmatrix} \quad \mathbf{K}_e = \frac{EI}{l_e^3}\begin{bmatrix} 12 & 6l_e & -12 & 6l_e \\ 6l_e & 4l_e^2 & -6l_e & 2l_e^2 \\ -12 & -6l_e & 12 & -6l_e \\ 6l_e & 2l_e^2 & -6l_e & 4l_e^2 \end{bmatrix} \tag{6.21}$$

l_e is the length of the element. Each element is added into the global mass and stiffness matrices and cantilever boundary conditions are applied where the displacement and slope at the root of the beam are eliminated. A diagram of the beam model is shown in Figure 6.3. The beam to be examined has a length of .6096 m. (2 ft.), a thickness of 3.2 mm (1/8 in.), and is made of Aluminum. The finite element model is constructed of Bernoulli-Euler two node elements with an element length of 3.2 mm (1/8 in.). A section of the beam is damaged, in the form of stiffness loss, and the resulting mass and stiffness matrix are used to compute the natural frequencies and modeshapes of the damaged structure. The natural frequencies based on the damaged structure are passed to the modal based damage detection algorithms.

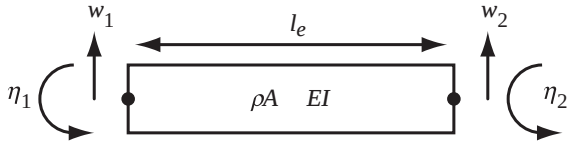

Figure 6.2: Beam element and degrees of freedom

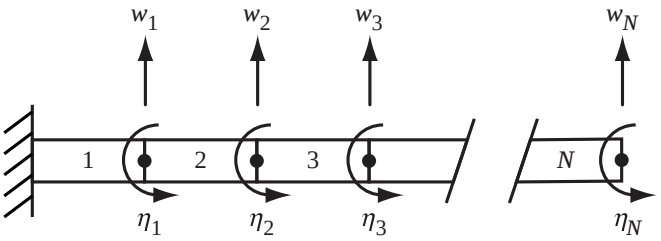

Figure 6.3: Global model of beam

6.4 Modal Response of Damaged Beam

The finite element model of the beam is reduced to a model with only the displacement degrees of freedom. Damage is introduced by reducing the stiffness in one of the elements of the finite element model. Figure 6.4 shows the change in the 1st and 2nd natural frequency based on a loss of stiffness of an element located at different locations on the structure. The natural frequencies do not change significantly regardless of where the damage is located or how much stiffness the element has lost.

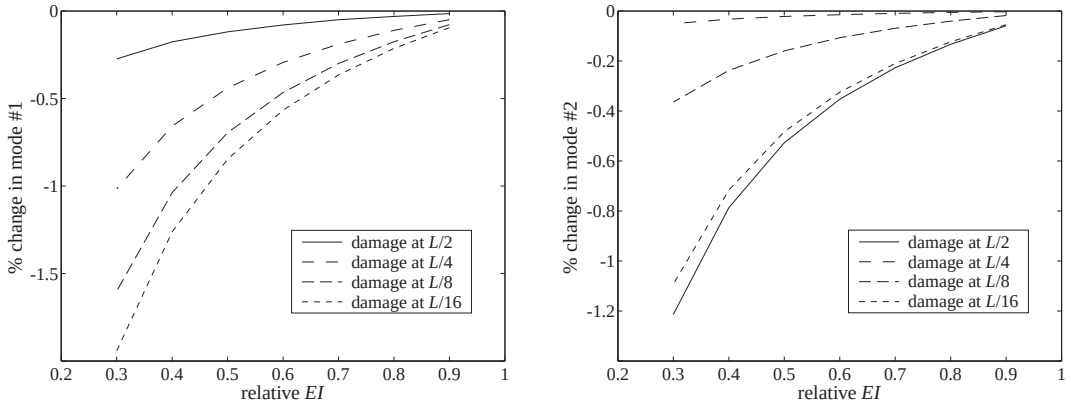

(a) Change in 1st Mode. (b) Change in 2nd Mode.

Figure 6.4: Change in natural frequency due to damage

The change in modeshapes due to damage may also be observed for damage at quarter span in Figure 6.5 and at half span in Figure 6.6 where the element at the damaged location had a relative EI of .4 compared to the undamaged elements.

While the actual modeshapes do not appear to change much, the difference between the modeshapes show large curvatures at the location of the damaged region.

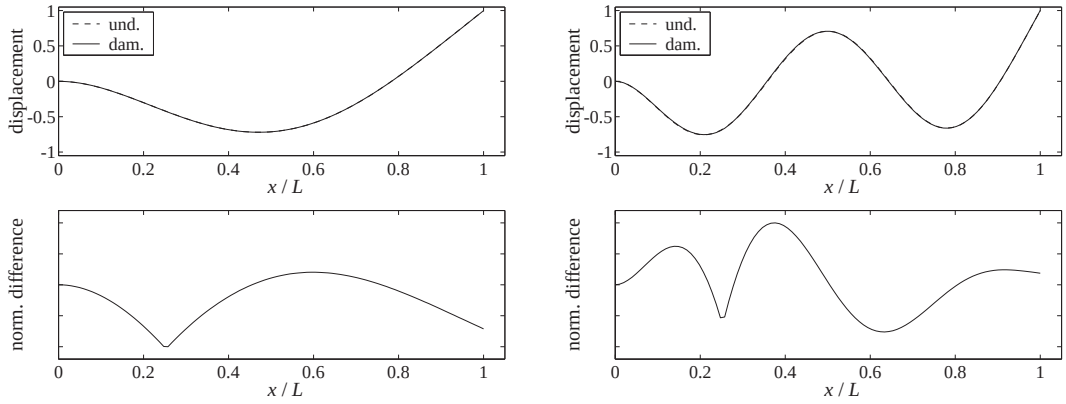

(a) 2nd modeshape (b) 4th modeshape

Figure 6.5: Damage at $L/4$

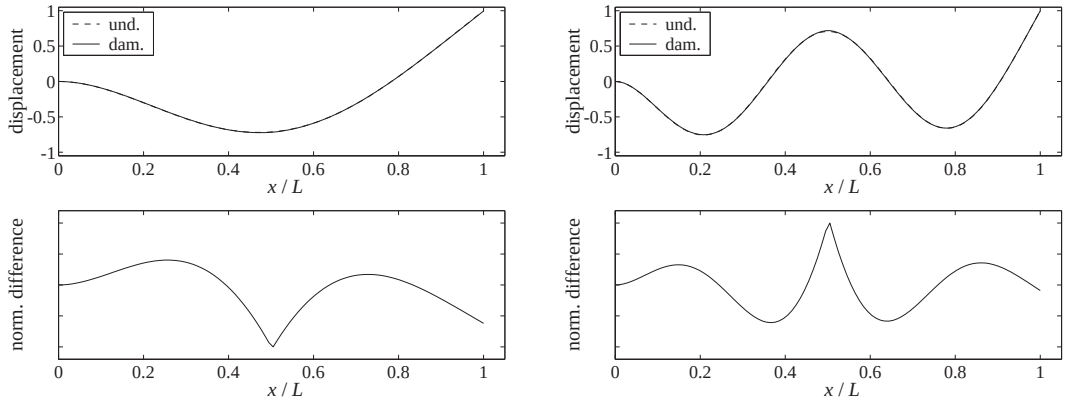

(a) 2nd modeshape (b) 4th modeshape

Figure 6.6: Damage at $L/2$

The modeshape information along with the shifts in natural frequencies are used in the modal based damage detection techniques. It is assumed that displacement at each nodal location is known and is used for modal damage detection. The first 25 modes of the beam are used in the damage detection algorithm where the 25th mode vibrates at a frequency of $\sim$12 kHz.

6.4.1 Damage Detection Using Minimum Rank Perturbation Theory

The Minimum Rank Perturbation Theory is used to identify the location of damage on the structure using the natural frequencies and modeshapes of the damaged structure and the model of the undamaged structure. The modal residual, $\mathbf{R}$, was determined for each mode and the damage vector for each mode, β_n, was found for various damaged cases. The damage vector for different modes are shown for damage located at $L/2$ and $L/4$ in Figure 6.7. The maximum value of the damage vector, β_n, points to the location of damage. The damage vector points to the location of damage accurately for higher modes but has difficulty at the lower modes. This is seen in the case of the damage vector for the first mode, where multiple significant peaks exist. Figure 6.8 summarizes the ability of the MRPT technique to identify the location of the damage for different modes of the beam. It can be seen that the lower modes are not as effective as the higher modes for locating damage, particularly when the amount of damage is small. The interpretation of extent of damage in the structure based on the MRPT method has inconclusive results.

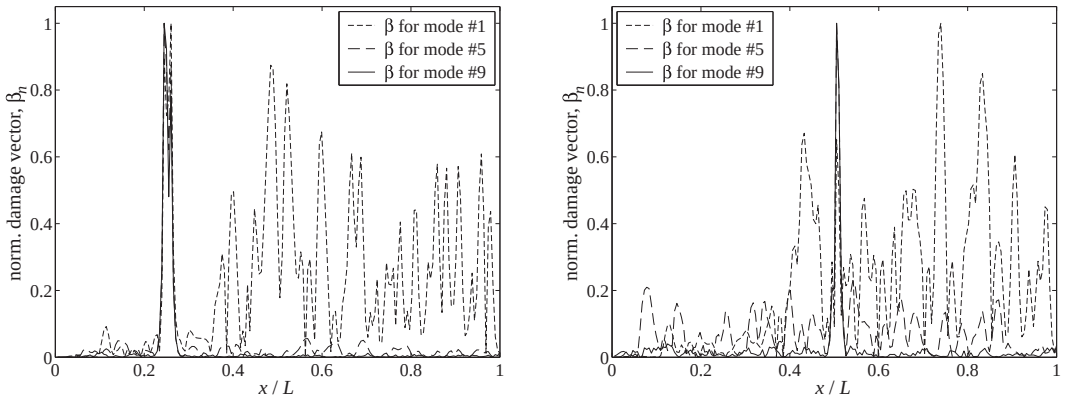

(a) Damage at $L/4$ (b) Damage at $L/2$

Figure 6.7: Damage vector, β_n for individual modes (rel. $EI = 0.7$)

MRPT Predictions with Noise

When noise is present in the data, there is significant degradation of the results. The natural frequencies and modeshapes used in the MRPT method were shifted by a

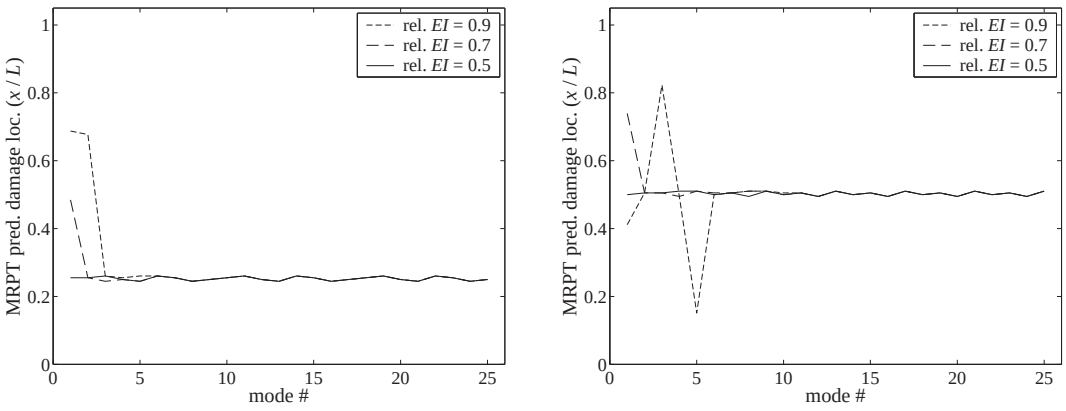

(a) Damage at $L/4$ (b) Damage at $L/2$

Figure 6.8: Predicted location of damage using MRPT

maximum of .1% and the MRPT method was used to locate the position of damage. The predicted location of damage is shown in Figure 6.9. The relatively small amount of noise significantly degrades the damage locating ability of the MRPT algorithm.

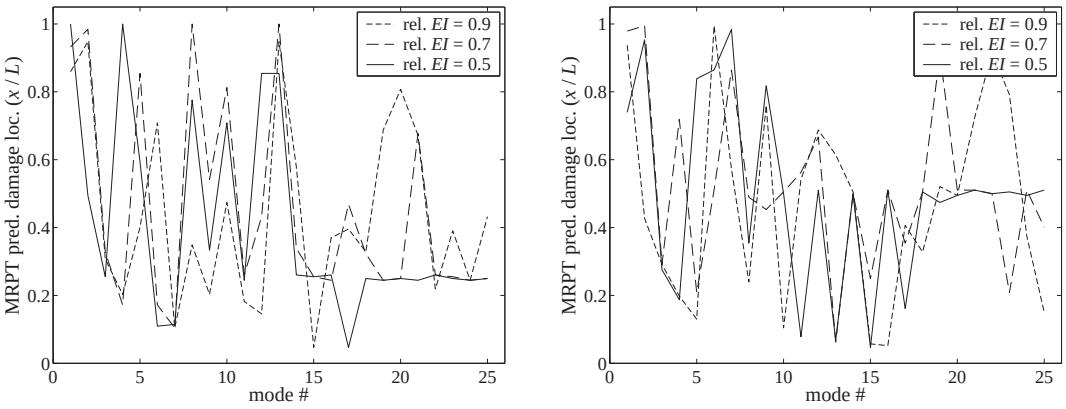

(a) Damage at $L/4$ (b) Damage at $L/2$

Figure 6.9: Predicted location of damage using MRPT (.1% noise)

6.4.2 Damage Detection Using Sensitivity Based - Element by Element

The Sensitivity Based Element-by-Element (SBEBE) method is used to identify both the position of the damaged element and amount of stiffness loss simultaneously using an optimization approach. The algorithm is computationally expensive but

is able correctly identify the damage location and amount. Only the change in the elemental stiffness matrix is used in the optimization algorithm. The cost function for each mode, J_n, is computed and the minimum of the function points to the damaged element and loss in stiffness. Figure 6.10 shows the damaged element and loss in stiffness of the element for for each mode. Though the lower modes were not useful, the predicted location and damage amount was correctly predicted overall. The modal cost functions can be combined into the total cost function which allows for one single metric to be used. Figure 6.11 shows the total cost function, J, as a function of element number and relative EI of the element. In both cases, the minimum of the cost function occurs at the appropriate locations. Table 6.1 shows the actual and predicted locations of damage for various cases.

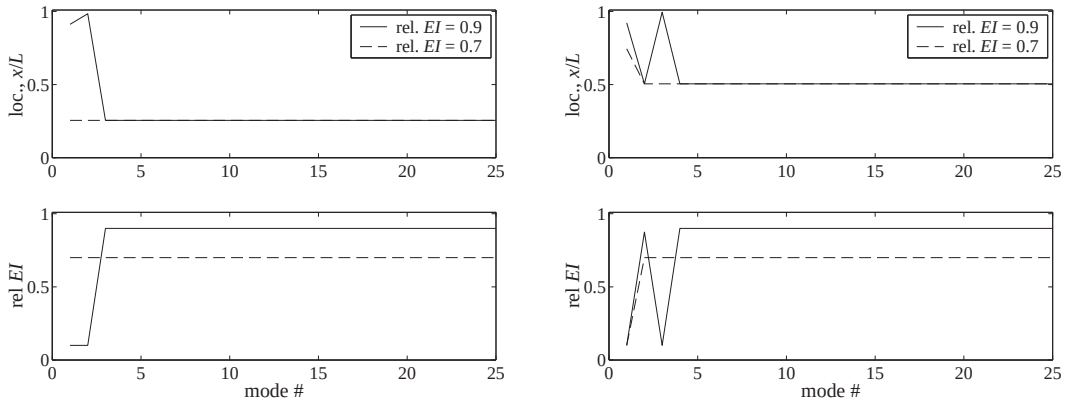

(a) Damage at $L/4$ (b) Damage at $L/2$

Figure 6.10: Damaged element and rel. EI for each mode

SBEBE Predictions with Noise

The presence of noise in the natural frequencies and modeshapes also affects the calculated cost function. The effect of .1% and 1% noise in the natural frequencies and modeshapes are shown in Figure 6.12 where the minimum of the cost function is not as apparent as with the noise-free case. The predicted damage location and amount for the different damage levels are shown in Table 6.2 for .1% noise and Table 6.3 for 1% noise.

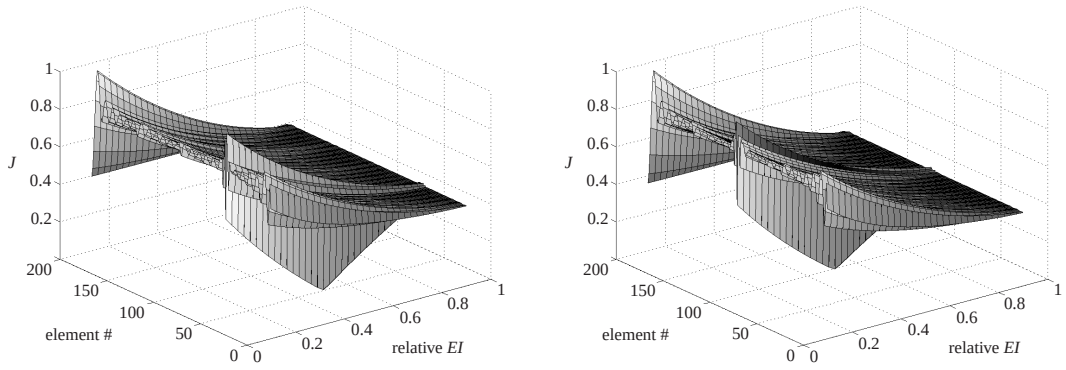

(a) Damage at $L/4$ (b) Damage at $L/2$

Figure 6.11: Cost function for SBEBE (rel. $EI = 0.5$)

rel. EI	dam. location ($L/4$)		dam. location ($L/2$)	
	pred. loc. (x/L)	pred. rel. EI	pred. loc. (x/L)	pred. rel. EI
.9	.25	.9	.50	.9
.7	.25	.7	.50	.7
.5	.25	.5	.50	.5
.3	.25	.3	.50	.3

Table 6.1: Predicted damage location and amount using SBEBE

6.4.3 Damage Detection Using Eigenstructure Assignment Damage Location

The Eigenstructure Assignment Damage Location method is also used to place damage using shifts in natural frequencies and modeshapes. As with the SBEBE method, there is significant computational cost. The predicted damage location is shown in Figure 6.13 for each mode. There is wide variation in ability of the EADL method for determining the damage location. While the EADL method seems to predict the location of damage accurately when the damage is placed at $L/2$, for the case where the actual damage is located at $L/4$, the EADL algorithm predicts the damage is $L/2$ also. Thus the EADL algorithm is unreliable for the current application. This is due to the large mass and stiffness matrices which are used in the algorithm. Since the EADL method applied to this system relies on the pseudo-inverse of a sparse

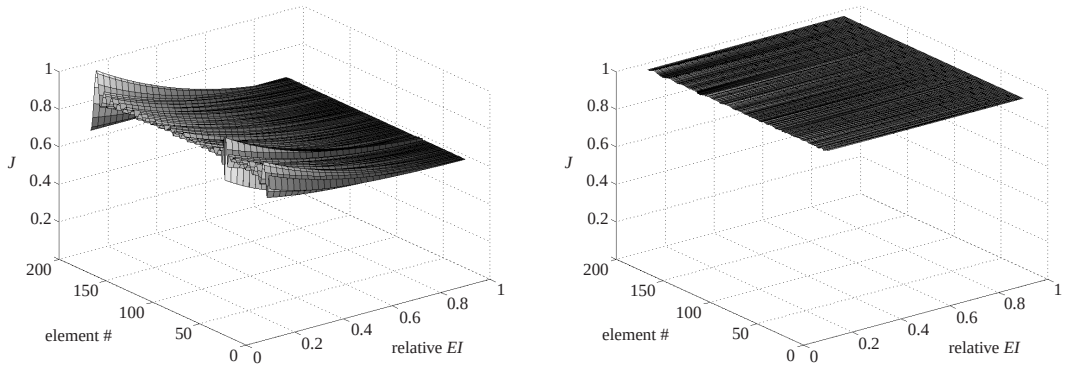

(a) .1% noise (b) 1% noise

Figure 6.12: Cost function for SBEBE (damage at $L/4$, rel. $EI = 0.5$)

rel. EI	dam. location ($L/4$)		dam. location ($L/2$)	
	pred. loc. (x/L)	pred. rel. EI	pred. loc. (x/L)	pred. rel. EI
.9	.25	.9	.50	.875
.7	.25	.725	.50	.7
.5	.25	.525	.50	.5
.3	.25	.275	.50	.3

Table 6.2: Damage location and amount using SBEBE (.1% noise)

matrix, numerical issues degrade the damage location and amount predictions.

6.4.4 Summary of Modal Damage Detection Techniques

The three modal damage detection techniques were used to determine the location of damage in a beam given the damaged natural frequencies and modeshapes. The undamaged model of the beam has 192 elements and it is assumed that the displacements are known at the node points over the whole beam. The MRPT method, based on the modal residual, had difficulty in predicting the location of damage at the lower modes. The higher modes were more effective in determining the location of damage. When a small amount of noise was added to the damaged modal information, the MRPT method had difficulty in locating the damage.

rel. EI	dam. location ($L/4$)		dam. location ($L/2$)	
	pred. loc. (x/L)	pred. rel. EI	pred. loc. (x/L)	pred. rel. EI
.9	.99	.1	.70	.1
.7	.54	.1	.99	.1
.5	.72	.1	.29	.1
.3	.25	.15	.50	.15

Table 6.3: Damage location and amount using SBEBE (1% noise)

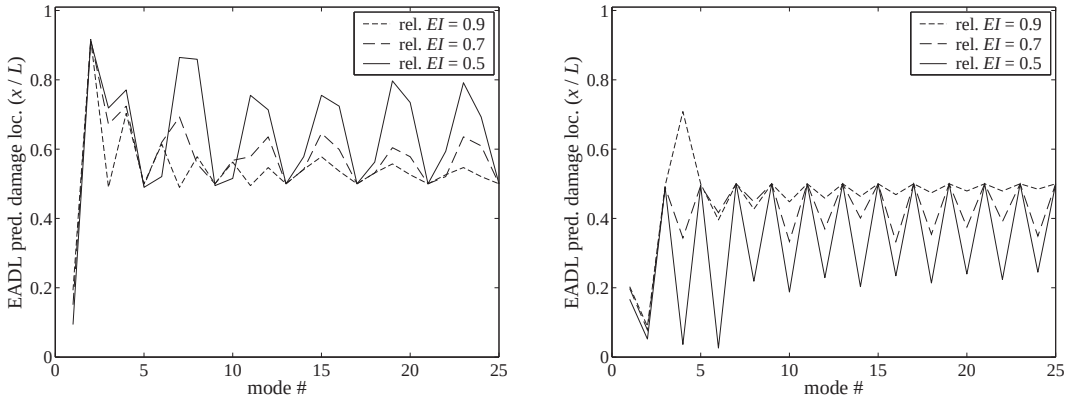

(a) Damage at $L/4$ (b) Damage at $L/2$

Figure 6.13: Predicted location of damage using EADL

The SBEBE method was effective in locating and estimating the amount of damage in the structure simultaneously. Though computationally expensive, the SBEBE method provided the best results. This was true even when noise was added to the modal information. For noise amounts of .1%, which significantly reduced the MRPT method's capability, the SBEBE method was able to accurately locate and size the damage accurately. When the amount of noise was increased to 1%, the SBEBE method became inaccurate. The EADL method is also computationally expensive but was unable to perform in the same manner as the SBEBE method. The predicted location of the damaged region was inaccurate. Thus, though computationally expensive, the SBEBE method performed the best out of the three modal damage detection algorithms used. There was significant degradation in the SBEBE

method when the modal data of the damaged system was slightly altered with noise to simulate uncertainty.

6.4.5 Limited Number of Sensors

In discrete structures the number of modes which may be used is finite and a sensor is typically used at each degree of freedom. For continuous structures the number of modes is theoretically infinite so only a limited number of modes may be used. The techniques used to match the order of the model of the structure to the number of sensor locations places a limitation on modal damage detection techniques. The number of sensors used on the continuous structure determines the highest mode which may be used for damage detection. Using known modeshapes for the uniform structure, the displacement at 11 evenly distributed locations along the span of the beam are used along with the finite element model used earlier in an attempt to reconstruct the full modeshape based on the modal expansion relation in Equation (6.5). The reconstructed modeshapes are shown in Figure 6.14 for the 8th and 12th modes. The 8th mode is reconstructed relatively well but the 12th mode differs significantly from the known modeshape. The number of sensors on the continuous structure limits the highest order mode which may be used. For damage detection, a limit of the highest mode which may be used restricts spatial resolution. The location of damage inside the element is unknown as well as its overall effect on the properties of the element.

Given the natural frequencies and modeshapes of the damaged beam, the SBEBE algorithm was applied to a nominal 11 element structure. The displacement at each of the nodal locations was interpolated based on the full damaged modeshape. The predicted location of damage based on the SBEBE method is shown in Figure 6.15 for the case where damage is at $L/4$ and $L/2$. The algorithm has difficultly establishing the location of the damaged element even for the higher modes. For an effective modal damage detection algorithm, the full displacement modeshape needs to be used with a fine spatial resolution.

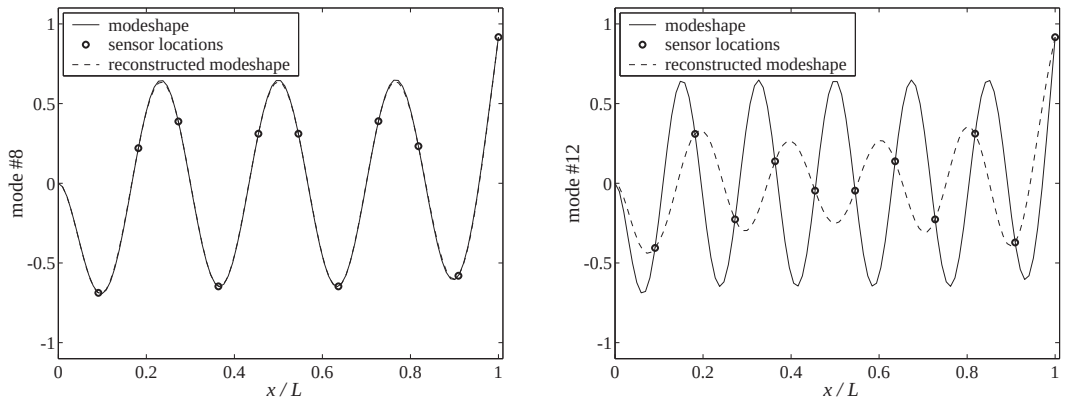

(a) Mode #8 (b) Mode #12

Figure 6.14: Modal expansion using 11 sensors

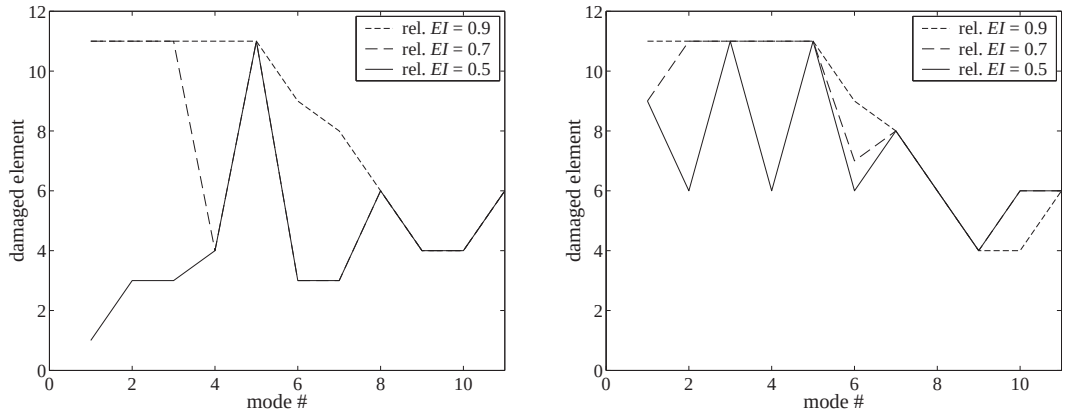

(a) Damage at $L/4$ (b) Damage at $L/2$

Figure 6.15: SBEBE method using 11 sensors

6.5 Wave Propagation in Beams

The governing differential equation which describes the transverse dynamics for the Bernoulli-Euler beam is used as a starting point:

$$EI\frac{\partial^4 w}{\partial x^4} + \rho A\frac{\partial^2 w}{\partial t^2} = 0 \tag{6.22}$$

EI is the bending stiffness and ρA is the mass per length of a beam section. This model for the beam assumes no rotational inertia as well as no shear deformation, making it equivalent to the Kirchoff plate model. As with wave propagation in thin plates, the displacement field is assumed of the form $w = w_o e^{i(\omega t - kx)}$. The resulting

wavenumber-frequency relationship for the beam is similar to that for the thin plate in Equation 2.20:

$$k = \sqrt{\omega}\sqrt[4]{\frac{\rho A}{EI}} \tag{6.23}$$

The governing differential equation for the Bernoulli-Euler beam in Equation 6.22 has four solutions, two propagating solutions and two evanescent, or near field, solutions:

$$w = \left(w_{rp}e^{-ikx} + w_{lp}e^{ikx} + w_{re}e^{-kx} + w_{le}e^{kx}\right)e^{i\omega t} \tag{6.24}$$

The propagating solutions, with subscripts rp and lp, travel through the length of the beam while the evanescent components, with subscripts re and le, die out with distance, shown in Figure 6.16. At high frequencies, the dynamics of a beam are largely influenced by the propagating solutions. The frequency response of the beam can be constructed based on the four solutions to the beam equation using the concepts of phase closure.

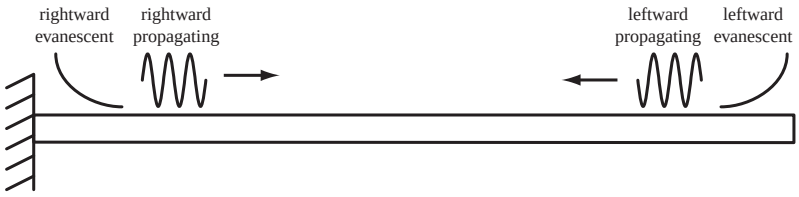

Figure 6.16: Wave modes on beam

For the propagating solutions, the concepts of phase and group speeds still apply and are based on the wavenumber-frequency relationship. The phase and group speeds are frequency dependent, indicating dispersive wave propagation:

$$c_p = \sqrt{\omega}\sqrt[4]{\frac{EI}{\rho A}} \qquad\qquad c_g = 2\sqrt{\omega}\sqrt[4]{\frac{EI}{\rho A}} \tag{6.25}$$

Besides displacement, other relevant quantities at a cross section of the beam, such as slope, moment, and shear force, can be described based on the assumption

of a wave like motion:

$$\begin{aligned} \text{slope}: &\quad w' = \partial w/\partial x \\ \text{moment}: &\quad M = -EI\partial^2 w/\partial x^2 \\ \text{shear}: &\quad V = -EI\partial^3 w/\partial x^3 \end{aligned} \tag{6.26}$$

Using the solution in Equation 6.24, the state of the beam at a particular cross-section can be described in terms of the four components:

$$\begin{bmatrix} w \\ w' \\ M \\ V \end{bmatrix} = \begin{bmatrix} 1 & 1 & 1 & 1 \\ -ik & -k & ik & k \\ -EIk^2 & EIk^2 & -EIk^2 & EIk^2 \\ iEIk^3 & -EIk^3 & -iEIk^3 & EIk^3 \end{bmatrix} \begin{bmatrix} w_{rp} \\ w_{re} \\ w_{lp} \\ w_{le} \end{bmatrix} \tag{6.27}$$

The beam states are used to define scattering matrices which describe the interaction of the different wave modes at a boundary condition or discontinuity. The scattering matrix, $\mathbf{S}$, is an input-output relationship where incident waves to a discontinuity produces reflected or transmitted wave modes moving outward. A general form of the scattering related incoming and outgoing components:

$$\boldsymbol{w}_{ref} = \mathbf{S}\boldsymbol{w}_{inc} \quad \text{where} \quad \boldsymbol{w} = \begin{bmatrix} w_{prop} & w_{evan} \end{bmatrix}^T \tag{6.28}$$

The subscripts ref and inc refer to reflected and incident components, respectively. A diagram of the incident and reflected waves are shown in Figure 6.17. The boundary conditions in Figure 6.16 are a fixed and free end. At the fixed end, the displacement and slope are nonexistent and at the free end, the moment and shear terms are nonexistent. For a pinned end, the displacement and moment are eliminated. Scattering matrices for each of these boundary conditions can be determined based on the beam states:

$$\mathbf{S}_{fixed} = \begin{bmatrix} -i & -1-i \\ -1+i & i \end{bmatrix} \qquad \mathbf{S}_{free} = \begin{bmatrix} -i & -1-i \\ -1+i & i \end{bmatrix}$$

$$\mathbf{S}_{pinned} = \begin{bmatrix} -1 & 0 \\ 0 & -1 \end{bmatrix} \tag{6.29}$$

The scattering relationship at a boundary conditions is only concerned with reflections due to incident wave modes. Each element of the scattering matrix describes the properties of the reflected wave mode given an incident wave mode. Since the pinned scattering matrix, $\mathbf{S}_{pinned}$, is diagonal, there is no coupling between the evanescent and propagating wave modes. For the fixed and free boundary conditions, the scattering matrix is fully populated so a propagating incident wave produces both outward propagating and evanescent components. Since the elements are complex, the scattering also describes a phase shift between in the incident and outward propagating modes. The terms in each of the scattering matrices are constant, making the scattering at a boundary frequency independent.

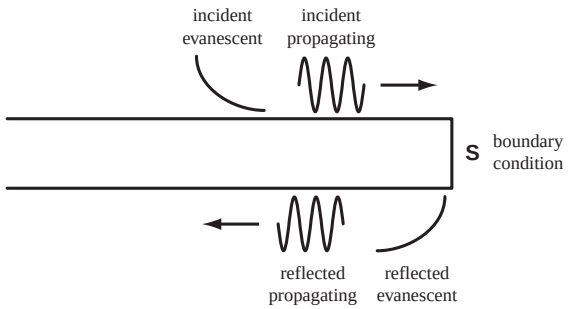

Figure 6.17: Scattering at a boundary

For a more complex situation where structural waves interact with a discontinuity, waves may also travel through the discontinuity and produce transmitted waves, resulting in a more general form of the scattering:

$$\boldsymbol{w}_{ref} = \mathbf{S}_{ref}\boldsymbol{w}_{inc} \qquad\qquad \boldsymbol{w}_{trans} = \mathbf{S}_{trans}\boldsymbol{w}_{inc} \tag{6.30}$$

The subscripts ref and $trans$ refer to reflected and transmitted components, respectively. The general diagram for this relationship is shown in Figure 6.18. At a boundary, two states are used to define the scattering relationship while at a discontinuity, all four states are needed to form the scattering relationships. The state matrix in Equation (6.27) is expressed in terms of the bending stiffness, EI, and wavenumber, k, in the beam. Before and after the discontinuity, the displacement,

slope, moment, and shear of the beam are the same, while the bending stiffness and wavenumber in the two sections are different.

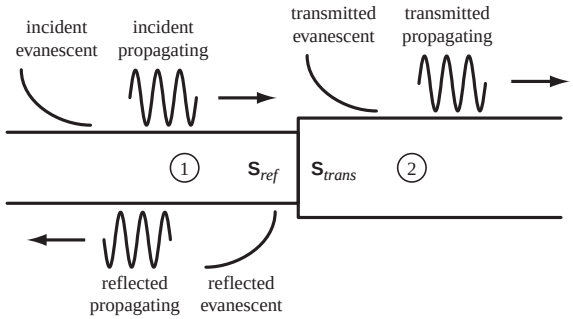

Figure 6.18: Scattering at a discontinuity

The state matrix can be reformulated:

$$\begin{bmatrix} w \\ M \\ w' \\ V \end{bmatrix} = \mathbf{P} \begin{bmatrix} w_{rp} \\ w_{re} \\ w_{lp} \\ w_{le} \end{bmatrix} \quad ; \quad \mathbf{P} = \begin{bmatrix} 1 & 1 & 1 & 1 \\ -EIk^2 & EIk^2 & -EIk^2 & EIk^2 \\ -ik & -k & ik & k \\ iEIk^3 & -EIk^3 & -iEIk^3 & EIk^3 \end{bmatrix} \tag{6.31}$$

The state matrix, $\mathbf{P}$, can be rewritten in a more concise form:

$$\mathbf{P} = \begin{bmatrix} \mathbf{L} & \mathbf{L} \\ -k\mathbf{L}\mathbf{V} & k\mathbf{L}\mathbf{V} \end{bmatrix} \text{ where } \mathbf{L} = \begin{bmatrix} 1 & 1 \\ -EIk^2 & EIk^2 \end{bmatrix} ; \mathbf{V} = \begin{bmatrix} i & 0 \\ 0 & 1 \end{bmatrix} \tag{6.32}$$

The matrix, $\mathbf{L}$, is dependent on frequency and the bending stiffness of the region. Using the subscripts 1 and 2 to distinguish between the properties on either side of the discontinuity, the states in both regions are matched:

$$\mathbf{P}_1 \begin{bmatrix} \boldsymbol{w}_{1,in} \\ \boldsymbol{w}_{1,out} \end{bmatrix} = \mathbf{P}_2 \begin{bmatrix} \boldsymbol{w}_{2,out} \\ \boldsymbol{w}_{2,in} \end{bmatrix} \tag{6.33}$$

A set of matrix equations is produced based on the incoming and outgoing wave components in each region:

$$\mathbf{L}_1 \boldsymbol{w}_{1,in} + \mathbf{L}_1 \boldsymbol{w}_{1,out} = \mathbf{L}_2 \boldsymbol{w}_{2,in} + \mathbf{L}_2 \boldsymbol{w}_{2,out} \tag{6.34}$$

$$-k_1 \mathbf{L}_1 \mathbf{V} \boldsymbol{w}_{1,in} + k_1 \mathbf{L}_1 \mathbf{V} \boldsymbol{w}_{1,out} = k_2 \mathbf{L}_2 \mathbf{V} \boldsymbol{w}_{2,in} - k_2 \mathbf{L}_2 \mathbf{V} \boldsymbol{w}_{2,out}$$

In the transient case, only one set of incident waves are examined. The set of incoming waves in the second region are eliminated, resulting in a simpler set of equations:

$$\begin{aligned} \mathbf{L}_1 \boldsymbol{w}_{1,in} + \mathbf{L}_1 \boldsymbol{w}_{1,out} &= \mathbf{L}_2 \boldsymbol{w}_{2,out} \\ -k_1 \mathbf{L}_1 \mathbf{V} \boldsymbol{w}_{1,in} + k_1 \mathbf{L}_1 \mathbf{V} \boldsymbol{w}_{1,out} &= -k_2 \mathbf{L}_2 \mathbf{V} \boldsymbol{w}_{2,out} \end{aligned} \tag{6.35}$$

The relationship between $\boldsymbol{w}_{1,in}$ and $\boldsymbol{w}_{1,out}$ defines the reflection scattering matrix, $\mathbf{S}_{ref}$, in the first region. Similarly, the relationship between $\boldsymbol{w}_{1,in}$ and $\boldsymbol{w}_{2,out}$ defines the transmission scattering matrix, $\mathbf{S}_{trans}$, from the first to second region of the beam.

The reflection scattering matrix at the discontinuity is found by eliminating $\boldsymbol{w}_{2,out}$ in the set of equations in Equation 6.35:

$$\left(\boldsymbol{I} - \frac{k_1}{k_2} \left(\mathbf{V} \mathbf{L}_{21} \right)^{-1} \mathbf{L}_{21} \mathbf{V} \right) \boldsymbol{w}_{1,in} = - \left(\boldsymbol{I} + \frac{k_1}{k_2} \left(\mathbf{V} \mathbf{L}_{21} \right)^{-1} \mathbf{L}_{21} \mathbf{V} \right) \boldsymbol{w}_{1,out} \tag{6.36}$$

$\boldsymbol{I}$ is the 2×2 identity matrix and $\mathbf{L}_{21}$ relates the properties in the two regions:

$$\mathbf{L}_{21} = \mathbf{L}_2^{-1} \mathbf{L}_1 = \frac{1}{2} \begin{bmatrix} 1 + \dfrac{EI_1 k_1^2}{EI_2 k_2^2} & 1 - \dfrac{EI_1 k_1^2}{EI_2 k_2^2} \\ 1 - \dfrac{EI_1 k_1^2}{EI_2 k_2^2} & 1 + \dfrac{EI_1 k_1^2}{EI_2 k_2^2} \end{bmatrix} \tag{6.37}$$

Intermediate matrices, $\mathbf{S}_a$ and $\mathbf{S}_b$, are used to simplify the expressions:

$$\mathbf{S}_a = \left(\boldsymbol{I} + \frac{k_1}{k_2} \left(\mathbf{V} \mathbf{L}_{21} \right)^{-1} \mathbf{L}_{21} \mathbf{V} \right) \qquad \mathbf{S}_b = \left(\boldsymbol{I} - \frac{k_1}{k_2} \left(\mathbf{V} \mathbf{L}_{21} \right)^{-1} \mathbf{L}_{21} \mathbf{V} \right) \tag{6.38}$$

The reflection scattering matrix takes on a simple form:

$$\mathbf{S}_{ref} = -\mathbf{S}_a^{-1} \mathbf{S}_b \tag{6.39}$$

The transmission scattering matrix is found in a similar manner:

$$\mathbf{S}_{trans} = \frac{1}{2} \mathbf{L}_{21} \left(\mathbf{S}_a - \mathbf{S}_b \mathbf{S}_a^{-1} \mathbf{S}_b \right) \tag{6.40}$$

Since the expressions for transmission and reflection from a discontinuity use $\mathbf{L}_{21}$ which uses the ratio of the wavenumbers in the different regions, the scattering matrices are frequency independent.

A simple model of a damaged region can constructed using the scattering at a discontinuity as a building block [137]. A diagram of the damaged region and the reflection scattering is shown in Figure 6.19. The reflection scattering can be used in a damage detection scenario where reflections from the damaged region can point to the location as well as the amount of damage. As with the previous case, the intermediate matrices $\mathbf{S}_a$ and $\mathbf{S}_b$ are used:

$$\mathbf{S}_a = \left(\boldsymbol{I} + \frac{k_p}{k_d} \left(\mathbf{V} \mathbf{L}_{dp} \right)^{-1} \mathbf{L}_{dp} \mathbf{V} \right) \qquad \mathbf{S}_b = \left(\boldsymbol{I} - \frac{k_p}{k_d} \left(\mathbf{V} \mathbf{L}_{dp} \right)^{-1} \mathbf{L}_{dp} \mathbf{V} \right) \tag{6.41}$$

The subscripts p and d describing the properties in the undamaged and damaged regions, respectively. The reflection scattering matrix is found using phase closure at all of the junctions:

$$\begin{aligned} \mathbf{S}_{ref,dam} = - \left(\mathbf{S}_a^{-1} \mathbf{L}_{pd} \boldsymbol{\xi} \mathbf{L}_{dp} \mathbf{S}_b - \mathbf{S}_b^{-1} \mathbf{L}_{pd} \boldsymbol{\xi}^{-1} \mathbf{L}_{dp} \mathbf{S}_a \right)^{-1} \times \\ \left(\mathbf{S}_a^{-1} \mathbf{L}_{pd} \boldsymbol{\xi} \mathbf{L}_{dp} \mathbf{S}_a - \mathbf{S}_b^{-1} \mathbf{L}_{pd} \boldsymbol{\xi}^{-1} \mathbf{L}_{dp} \mathbf{S}_b \right) \end{aligned} \tag{6.42}$$

$\boldsymbol{\xi}$ is the spatial transition of the propagating and evanescent wave modes:

$$\boldsymbol{\xi} = \begin{bmatrix} e^{-ik_d l_d} & 0 \\ 0 & e^{-k_d l_d} \end{bmatrix} \tag{6.43}$$

l_d is the length of the damaged region. This is a general formulation where the damaged region could be modeled as a loss in stiffness or a change in thickness, as in the case of a crack region. The spatial transition term is the only frequency dependent term in the scattering from a damaged region in Equation (6.42). The spatial transition term does make a significant contribution to the overall scattering from the crack. In a similar manner, the transmission scattering through the damaged region may be found:

$$\mathbf{S}_{trans,dam} = \left(\mathbf{S}_a \mathbf{S}_b^{-1} \mathbf{L}_{pd} \boldsymbol{\xi}^{-1} \mathbf{L}_{dp} \mathbf{S}_a - \mathbf{L}_{pd} \boldsymbol{\xi} \mathbf{L}_{dp} \mathbf{S}_b \right)^{-1} \left(\mathbf{S}_a \mathbf{S}_b^{-1} \mathbf{S}_a - \mathbf{S}_b \right) \tag{6.44}$$

An example of the scattering based on Equations (6.42) and (6.44) is shown in Figure 6.20 where the damaged section is 3.2 mm (1/8 in.) long and the only

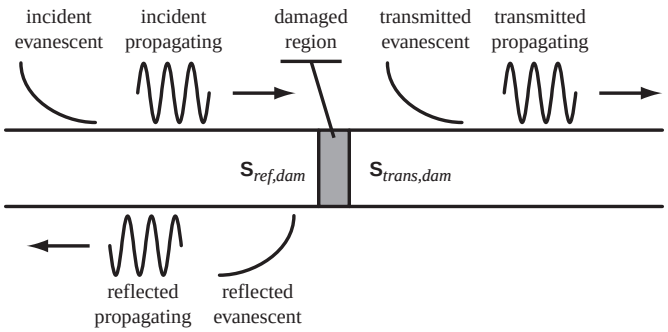

Figure 6.19: Scattering at a damaged region

difference between the undamaged and damaged sections is a thickness change. The resulting reflected propagating wave from an incident propagating wave is shown in Figure 6.20(a). When the thickness is the same as the undamaged region, there is no reflected component in the scattering. As the thickness of the damaged region decreases, the magnitude of the reflection from the damaged region increases. The transmitted propagating wave for an incident propagating wave is shown in Figure 6.20(b). In this case, the magnitude of the transmitted waves is large while the thickness in the damaged region is close to the undamaged region. When the thickness of the damaged region decreases, eventually the magnitude of the transmitted component drops. The greatest change in the scattering occurs at the higher wavenumbers. For damage detection purposes, it is best to work at higher wavenumbers and the corresponding higher frequencies for better damage resolution. A first order model of crack damage can be approximated using the above approach where the appropriate bending stiffness and wavenumber in the crack region is used.

For a damage detection applications, an interrogating signal can be used to excite a propagating wave and the resulting reflection from damage, if present, can be used to determine damage presence and location. An example setup is shown in Figure 6.21. The location of damage is determined based on the position of the reflection from the damage in the time domain. An estimate of the size or amount can be estimated based on the incident and reflected wave components in the sensor signals. The scattering relationship based on Equation (6.42) for a

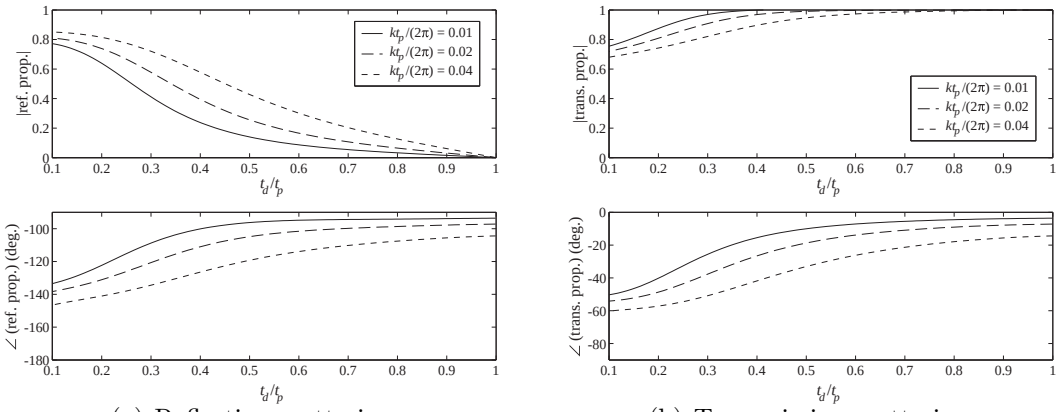

(a) Reflection scattering (b) Transmission scattering

Figure 6.20: Scattering at damaged region

reflected propagating wave from the incident propagating wave indicates the amount of damage to the region.

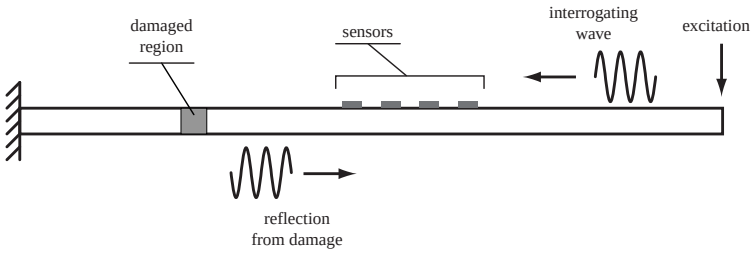

Figure 6.21: Wave propagation damage detection for beam

6.5.1 Timoshenko Theory

Timoshenko beam theory includes rotational inertia as well as shear strains in the beam model. The derivation of the governing equations is similar to the higher order Mindlin plate theory approach in Appendix C. The governing differential equations are coupled and include terms for rotational inertia and shear deformation:

$$\begin{aligned} GA\kappa\left(\frac{\partial\eta}{\partial x} - \frac{\partial^2 w}{\partial x^2}\right) + \rho A\frac{\partial^2 w}{\partial t^2} &= 0 \\ GA\kappa\left(\frac{\partial w}{\partial x} - \eta\right) + EI\frac{\partial^2\eta}{\partial x^2} &= \rho I\frac{\partial^2\eta}{\partial t^2} \end{aligned} \tag{6.45}$$

w is the transverse displacement and η is the rotation of the section. G is the shear modulus of the material and κ is the Timoshenko shear correction factor which is used to ensure the proper determination of the shear force and is dependent on the cross-section of the beam. Typically, for rectangular cross sections, κ=.833. A propagating wave solution is assumed for both the displacement and rotation:

$$w = w_0 e^{i(\omega t - kx)} \qquad \eta = \eta_0 e^{i(\omega t - kx)} \tag{6.46}$$

A coupled system of equations results where the solution to the characteristic equation produces the wavenumber-frequency relationship for the Timoshenko beam model:

$$\begin{bmatrix} k^2 GA\kappa - \omega^2 \rho A & -ikGA\kappa \\ -ikGA\kappa & \omega^2 \rho I - GA\kappa - k^2 EI \end{bmatrix} \begin{bmatrix} w_0 \\ \eta_0 \end{bmatrix} = \begin{bmatrix} 0 \\ 0 \end{bmatrix} \tag{6.47}$$

At low frequencies, the real solution to the characteristic equation matches the Bernoulli-Euler beam model. As the frequency of interest increases, the Timoshenko and Bernoulli-Euler models diverge due to the addition of the extra effects of rotary inertia and shear deformation. While the Bernoulli-Euler beam model predicts infinite wave velocities, the results from the Timoshenko model approach the shear wave velocity, c_t, found in solid elasticity. A comparison between the Timoshenko beam model and Bernoulli-Euler theory are shown in Figure 6.22. The Bernoulli-Euler beam model matches the Timoshenko model relatively well for wavenumber-thickness products up to $\sim$.05 rad. for both the wavenumber-frequency relationship as well as group velocities.

6.6 Transient Response of Beam

For the wave propagation damage detection technique, the transient response of the beam is predicted using a time integration method. The algorithm for time integration used is the Newmark method which is discussed further in Appendix D. A transient forcing is applied at the free end of the beam. A set of sensors are grouped at $\frac{3}{4}L$ with a sensor spacing of 6.3 mm (1/4 in.). A schematic is shown

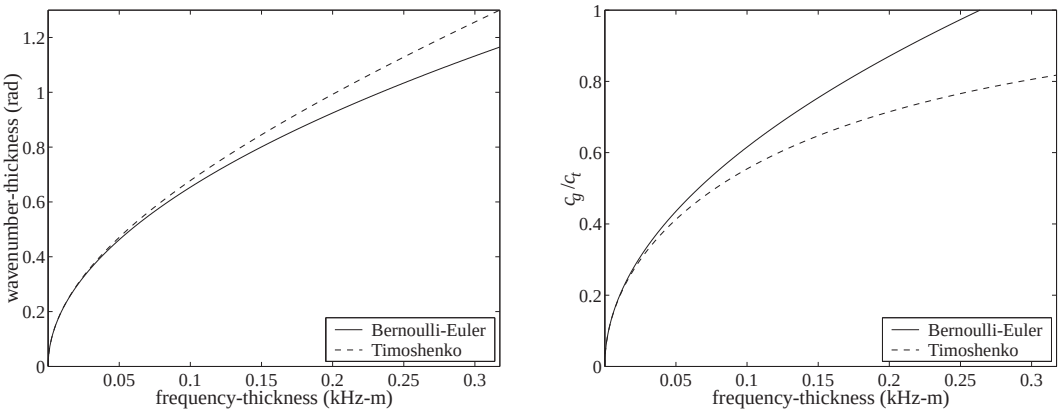

(a) Wavenumber-Frequency relationship (b) Group velocity

Figure 6.22: Comparison between Bernoulli-Euler and Timoshenko models

in Figure 6.21. A 3 cycle tone burst of 15 kHz is used to excite the beam at its tip. This frequency range roughly corresponds to the natural frequency of the highest mode used in the modal damage detection routines. In the modal damage detection cases, it was shown that the higher frequency modes were more sensitive to small amounts of damage. This frequency range also corresponds to the limit of the Bernoulli-Euler assumption for beam dynamics. In practice, much higher frequency waves are used for interrogation, with the expense that the wavenumber-frequency relationship becomes more complicated. The benefit of going to higher frequencies is the increase in the spatial resolution of the beam as well as greater damage sensitivity. Since the wavelengths are much smaller, the propagating waves traveling through the structure are more compact.

The transient response of the undamaged and damaged beam is gathered and used with the directional filtering algorithm to extract reflections from the damaged region, if present. Figure 6.23 shows the response of the middle sensor of the 11 sensor array for a damage located at $L/2$. The incident transient from the forcing location is seen first as well as the reflection from the fixed edge later on in time. There does not appear to be a significant difference between the undamaged and damaged response. When the wavenumber filtering algorithm is use to separate leftward and rightward waves, slight differences in the transient responses are apparent, as shown

in Figure 6.24. The incident waveform due to the forcing is apparent at ∼.28 ms in the undamaged and damaged cases. A reflection from the damaged region is seen as a reflection at ∼.51 ms while the undamaged case transient response does not exhibit this behavior. A reflection from the fixed edges is seen at ∼1 ms. The differential response between the damaged cases and undamaged case is presented in Figure 6.25(a) which brings out the reflection from the damaged region. There is a also difference in the waveform corresponding to the reflection from the fixed edge. This occurs because the incident waveform is split into both transmitted and reflected waves at the damage location. The location of the damaged region is found by estimating the time between arrival of the incident wave from the forcing and the reflection from the damaged region. Along with the group speed of the beam, 1.3 km/s for a forcing frequency of 15 kHz, the location of the damaged region is estimated as .153 m (6 in.). The scattering coefficient can be found by windowing the time domain response around the incident wave and the reflection from damage and determining the amplitude of the appropriate frequency component inside the window. The reflection scattering is shown in Figure 6.25(b) for various damaged cases. The scattering is shown to match well with the trend line from the reflection scattering analysis presented earlier. By using the wave propagation methodology, the location and an estimate of the amount of damage may be inferred based on the transient response of the beam.

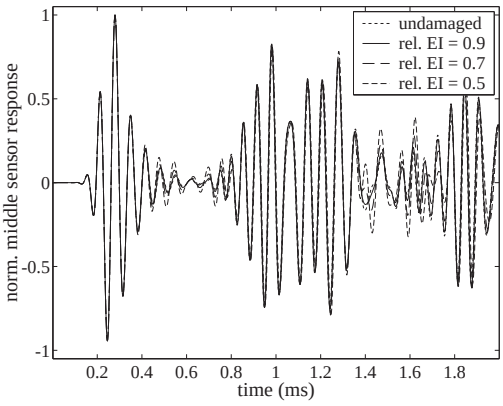

Figure 6.23: Response at middle sensor of array

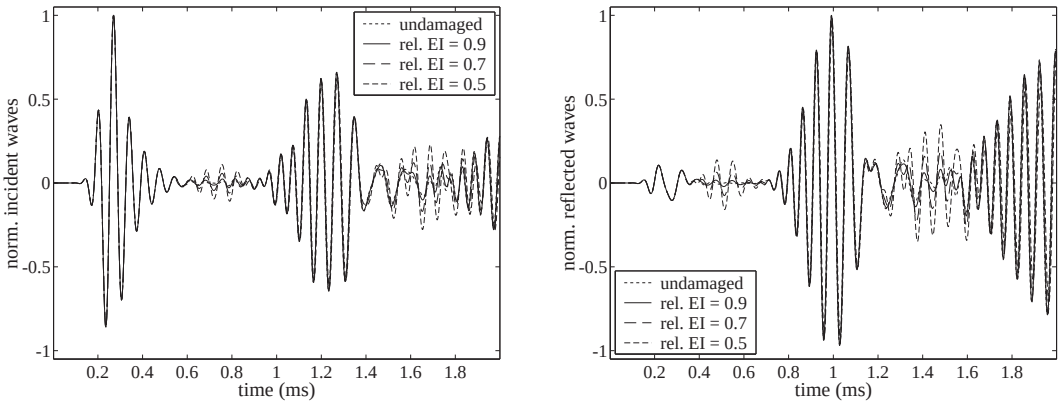

(a) Incident waves from forcing location (b) Reflections from damage and boundary

Figure 6.24: Incident and reflected waves on beam

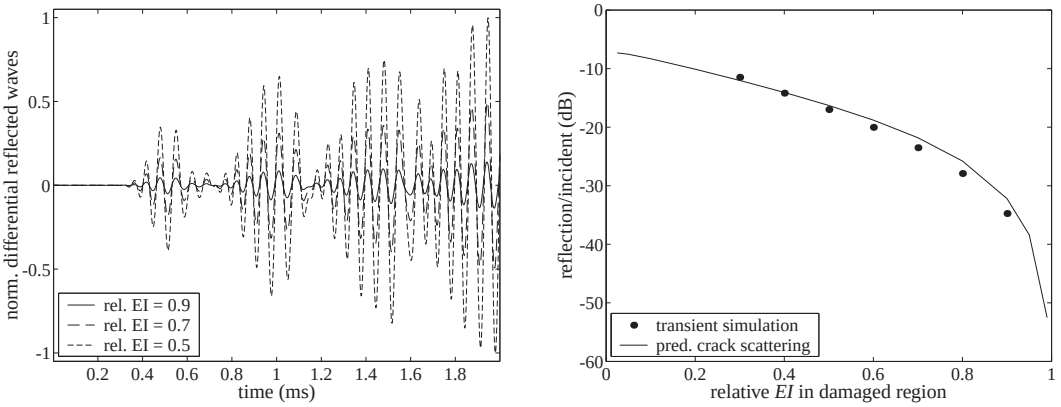

(a) Diff. between undamaged and damaged (b) Scattering from simulation

Figure 6.25: Scattering from damage

The transient response of the beam changes when the damage is placed at $L/4$. Figure 6.26(a) shows the transient response of the beam and Figure 6.26(b) shows the reflection components. There is a small change in the transient response due to damage at $\sim$.72 ms. The reflection from the fixed edges dwarfs the response. This displays one of the issues central to damage detection using wave propagation methods. If the damage is located near the boundary, the weak reflection from the damaged region may be corrupted by the reflection from the boundary. This can be alleviated by using higher frequency interrogating waves to gain better spatial resolution. Nevertheless, the transient response does show a difference compared

to the undamaged transient response, indicating the presence of damage. The differential response in Figure 6.27(a) is used to determine the scattering, shown in Figure 6.27(b).

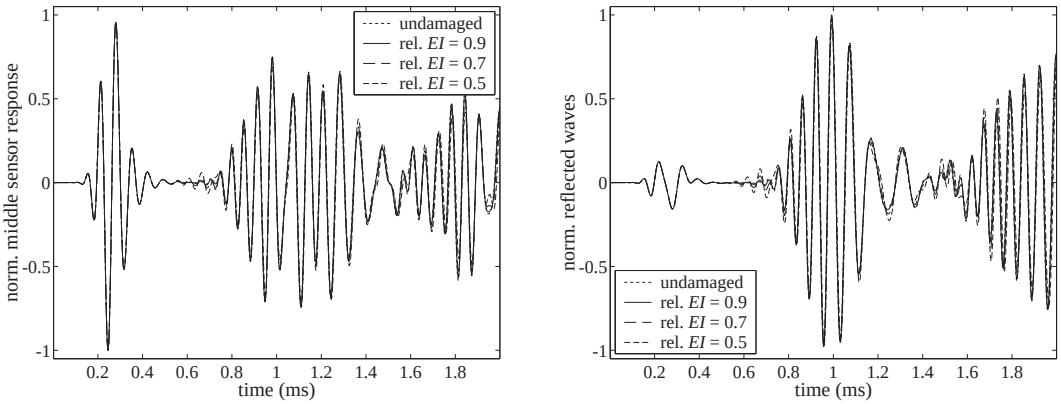

(a) Transient response (b) Reflections

Figure 6.26: Damage at $L/4$

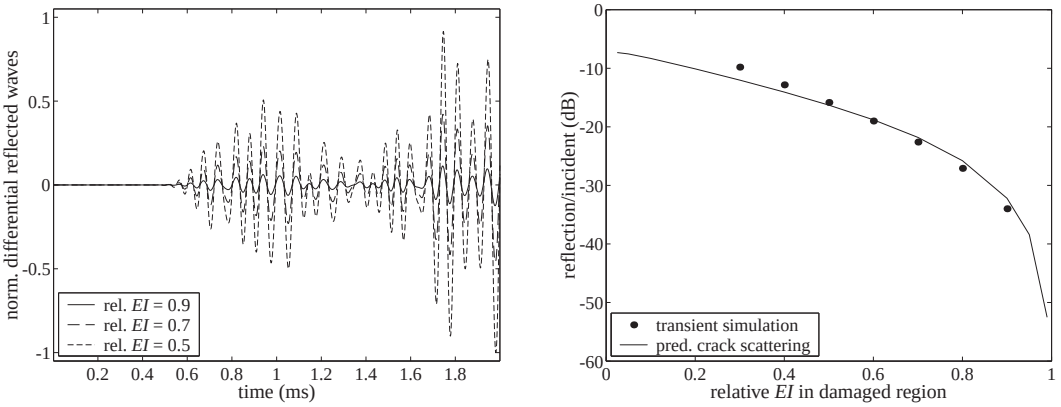

(a) Differential reflection (b) Scattering

Figure 6.27: Scattering for damage at $L/4$

Transient Predictions with Noise

The transient response of the beam is altered by adding noise with a magnitude of 1% of the maximum amplitude of the signal. The case where the damage located at $L/4$ is used. An example of the resulting transient response with noise is shown

in Figure 6.28(a). The difference between the reflected damaged signals and the reference undamaged signal is shown in Figure 6.28(b). The reflections due to small amounts of damage still stand out and can be distinguished. The scattering due to 10 cases where the noise level was about 1% was determined. The average of the scattering for 10 samples is shown in Figure 6.29. The results are shown to the match the noise free case relatively well, even for small amounts of damage. Thus, the sensitivity of the wave propagation method remains even in the presence of damage. This is partly due to the nature of the directional filtering algorithm. The sensor signals are summed together which helps cancel out the effect of noise present in the sensor signals.

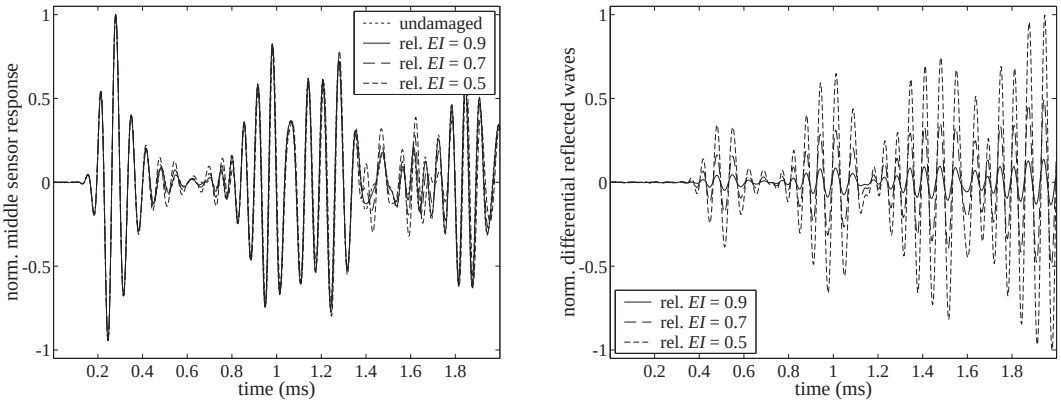

(a) Middle sensor responses (b) Differential response

Figure 6.28: Transients with 1% noise

6.7 Summary

For the case where there is small amounts of damage in a beam, both the modal and wave propagation damage detection techniques are used to identify the location and quantify the amount of damage. The MRPT technique was able to identify the location of damage based on the modal residual. The Sensitivity Based Element-By-Element method is shown to work the best even though it is computational expensive. For small amounts of damage, the SBEBE method is shown to be able to place the damage and estimate the amount relatively well. The EADL algorithm

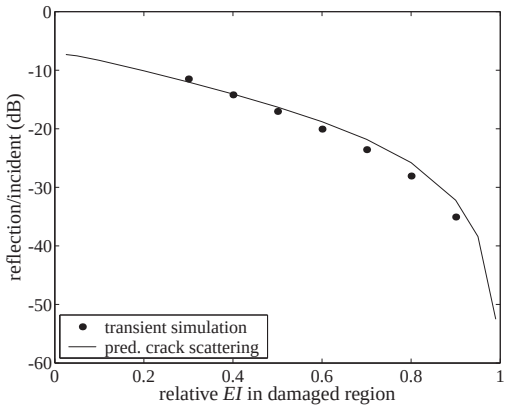

Figure 6.29: Scattering from simulation (1% Noise)

had difficulty predicting the location of damage.

Of the three modal techniques, the SBEBE method worked the best in terms of location and damage amount prediction. Even when small amounts of noise is introduced in the modal properties of the damaged beam, where the natural frequencies were shifted by up to .1% and the modeshapes where given a maximum .1% change in the nodal amplitudes, the SBEBE method is useful. The MRPT technique has difficulty when small amounts of noise is present in the information. When the uncertainty level reached 1%, the SBEBE method faltered in its ability for damage detection.

It is assumed that the natural frequencies and modeshapes of the damaged structure are precisely known. In practice, these quantities need to be found experimentally and are typically found using transfer function information. In actual structures, damping becomes an issue where the peaks in the transfer functions corresponding to a natural frequency are not as clearly defined, adding a level of uncertainty in the modal information.

An approach based on wave propagation and the transient response of the damaged and undamaged beam is used for damage detection purposes also. The wave propagation technique is shown to be able to isolate the reflection from the damaged region, placing the damage relative to the sensor locations. The amount of damage is found based on the scattering from the damage and is shown to correlate

with a simple scattering model relatively well. As the damage location approaches the fixed boundary, the reflection from the damage gets drowned out by the reflection from the fixed boundary. There is still useful information since the transient response still varies relative to the undamaged transient response of the beam. When noise is introduced to the transient signals, the wave propagation approach is still able to predict the location and determine the amount of damage. Damping in wave propagation methods is not as critical as with the modal damage detection cases since only initial portion of the transient response is typically used.

Chapter 7

Concluding Remarks

7.1 Contributions

Structural Health Monitoring (SHM) has benefits useful for a variety of aerospace structures. A building block of a successful SHM system is a damage detection technique. Though a variety of techniques are available, wave propagation methods can potentially provide the benefit of wide area damage detection for incipient forms of damage. This thesis presents a damage detection approach using wave propagation methods in thin plates. The high frequency dynamics of a structure may be described in terms of structural waves. For thin plates, wave propagation is described in terms of Lamb waves. The two fundamental wave modes is the S0, or in-plane wave, and the A0, or transverse wave. The in-plane wave behaves like acoustic waves and the transverse waves have displacements normal to the surface of the plate. The characteristics of wave propagation is described by the dispersion relations which relate the phase speed, group speed, and spatial wavenumber as a function of temporal frequency. Using this information, a damage detection methodology is developed using a sensor array which looks for the interactions of Lamb waves with damage in a thin plate. The damage detection technique is applied for plates made from an isotropic material as well as laminates constructed of unidirectional fiber plies. The major contributions resulting from this work are highlighted:

1. In order to successfully use a wave propagation technique for damage detection, the dispersion relations for the structure needs to be understood. For a thin plate made from an isotropic material, the dispersion relations are well known;

however, for laminates constructed of anisotropic plies, the wave propagation properties are not as well known. A finite element model is used to predict the wave propagation properties of a thin laminate. The displacement distribution through the width and breadth of the laminate is assumed to be of the form of a plane wave. The laminate is discretized through the thickness and simple linear finite elements are used to model the in-plane and transverse displacements at each node. Mass and stiffness matrices are constructed which depend on the material properties of the plies. These material properties take into account the anisotropic nature of each ply. The solution to an eigenvalue problem predicts the wavenumber-frequency relationship for the laminate. The model can predict both the in-plane and transverse modes of the laminate. This model is validated using the known Lamb wave modes for an isotropic thin plate. Besides the fundamental S0 and A0 modes, the wavenumber-frequency relationship of higher order modes may also be predicted.

2. A sensor array examined for use in analyzing the transient response of a thin plate. Concepts from acoustics and antenna theory are used to process the transient signals gathered from each element of the sensor array. It is shown that the linear sensor array acts as a filter in the wavenumber domain along the array distribution. The dynamics of the thin plate can then be deconstructed into the component wavenumbers. Two issues associated with the sensor array affect its capabilities. The maximum wavenumber which may be used depends on the spacing of the discrete sensors in the array. The beamwidth of the sensor array limits its ability to discern wavenumber close to each other. The beamwidth is dependent on the number of sensors in the array. The sensor array under consideration is made of a piezoelectric polymer material.

3. The sensor array is used to deconstruct the transient response of an Aluminum plate. The wavenumber-frequency relationship for both the A0 and S0 modes is reconstructed experimentally and shown to match analytical predictions.

4. For an isotropic structure, where the wave propagation characteristics are

independent of the direction of travel, the sensor array may also act as a directional filter using a simple transformation. This is shown for an Aluminum plate where the direction of the incoming waves to the sensor array can be determined.

5. In a pulse-echo damage detection application, the sensor array and associated signal processing is used along with a piezoceramic actuator to actively interrogate a thin plate with damage in the form of a hole. The actuator sends out a transient interrogating signal which is reflected from the damage region, if present. The sensor array is shown to be able to accurately deconstruct the response and identify the incoming direction of the reflection. Along with a knowledge of the wave propagation velocities, the location of the damaged region can be placed. The magnitude of the reflection from the damaged region is shown to indicate the size of the hole.

6. The sensor array is also shown to be able to identify two separate damaged areas on a plate. Due to the directional filtering capabilities of the sensor array, reflections from multiple different directions can be identified and separated.

7. A sensitivity study is performed where the reflection from a given size hole is examined for various excitation frequencies. It is shown that as the wavenumber of the excited wave approaches the size of the damage, the magnitude of the reflection increases. After a point, the magnitude of the reflection levels off. This is important for damage detection purposes so that the excitation frequency can be chosen to be sensitive to certain size damage. Additionally, it is noted that after a point, there is no need to increase the excitation frequency as the magnitude of the reflection does not increase.

8. The interaction of Lamb waves with a bolted joint boundary conditions is shown to be sensitive to the torque loading of the mounting bolts. In an experimental setup, the torque level on a single bolt of a bolted joint is changed and the reflection from the boundary is shown to be altered. The sensor array

is able to distinguish which boundary is affected and a simple metric shows the change in the reflection characteristics.

9. Composite laminates of two different layups are constructed for an exploration into the wave propagation properties of an anisotropic structure. It is shown that the group speed, and as a result, the wavenumber-frequency relationship, depends on the direction of travel. The sensor array is used to experimentally determine the wavenumber-frequency relationship for the composite laminates. The finite element model developed previously is used to predict the dispersion relations and is shown to match up relatively well with experimental results for both the A0 and S0 modes.

10. The sensor array is used in a delamination detection exercise on the composite laminate. It is shown experimentally that the sensor array is able to separate the response of the laminate into various propagating components. Damage detection for delamination worked well for lower frequency tests. The results at higher frequencies were inconclusive. Various factors were identified which degraded the damage detection efforts.

11. A comparison is made between commonly used modal damage detection methods and a wave propagation approach. For small amounts of damage, it is shown that modal damage detection methods have difficulty identifying the location of damage. When noise is added to the damage structures modal information, the modal damage detection results degrade even further. In the wave propagation approach, small damage amounts may be identified through the scattering relationship. Using a transient simulation of the beam, the scattering from a damage area is shown to match the analytical results.

7.2 Limitations of Current Method

Though the wave propagation approach has many potential benefits, there are issues which need to be addressed that could extend its use. A few of the limitations of

the current methodology are illustrated:

1. The number of elements in the array and the sensor spacing limits wavenumber filtering capability. There is a limit to the wavenumber resolution of the array which hinders the signal processing and data extraction from the signals. Additionally, since there is maximum wavenumber which may be used, there is a limit on the size of the damage examined. Damage detection techniques need to be able to scan for incipient forms of damage which are generally very small in size.

2. The wave propagation characteristics for a wave traveling in the principle directions of an orthotropic laminate are modeled and experimentally verified. The wave propagation behavior for the non-principle directions is more difficult to ascertain because the fundamental assumptions used in the model are not satisfied. For this reason, the sensor array can not be used as a directional filter in an orthotropic laminate. A more thorough understanding of the nature of wave propagation in the non-principle directions is needed in order to treat an orthotropic composite laminate in the same manner as an isotropic plate. The same issues are present for a general anisotropic set up also.

3. Though the sensor array is able to extract the reflection from the delamination, the quality of the signal is poor. Because the reflections are weak, there is difficulty in ascertaining properties of the delamination such as position through the thickness of the laminate or the size of the delamination. An improved signal will bring out features of the delamination useful for damage sizing. This can be accomplished by using better signal conditioning electronics and improving the manufacturing process for the sensor array.

7.3 Recommendations for Future Work

In order to extend the idea of wave propagation techniques for practical implementation into an SHM system, there are several advancements in the current state of the art which need to take place. The most immediate are discussed as follows:

1. Improved wave propagation modeling of an anisotropic composite laminate. This enables the sensor array to be used as a directional filter on an arbitrary laminate in much the same way as it was used for the isotropic plate.

2. Improved understanding of the interaction of the fundamental plate modes with a delamination. This may be performed either numerically, using finite element software, or experimentally. Properties of either the reflection or transmission characteristics can be used in a damage detection scenario.

3. Extension of wave propagation damage detection technique for use in thick laminates or sandwich panels. The wave propagation characteristics are different for these type of structures and needs to be understood in order to use structural waves for damage detection.

4. Use of improved time domain signal processing techniques for analyzing the response of the structure. While the signal processing in this work relies heavily on the Fourier transform and its application, newer signal processing techniques such as the Wavelet Transform or the Empirical Mode Decomposition may be useful in extracting additional information from the signals.

5. Modeling and testing of plates with non-uniform thickness or composite laminates with ply drops. Most analysis dealing with wave propagation in plates or laminates concentrate on cases with uniform thickness. A more general understanding of wave propagation in non-uniform plates expands the reach of a wave propagation technique for damage detection.

Appendix A

Derivation of 3-D Equilibrium Equations

The three dimensional equilibrium equations describe the dynamic motions of a particle. Figure A.1 shows the stresses acting in the x direction on an element. Force equilibrium in the x-direction results in a differential equation:

$$\sum F_x = \rho\, dx\, dy\, dz\, \ddot{u} = \left(\left(\sigma_{xx} + \frac{\partial \sigma_{xx}}{\partial x} dx\right) - \sigma_{xx}\right) dy\, dz + \left(\left(\sigma_{zx} + \frac{\partial \sigma_{zx}}{\partial z} dz\right) - \sigma_{zx}\right) dx\, dy + \left(\left(\sigma_{yx} + \frac{\partial \sigma_{yx}}{\partial y} dy\right) - \sigma_{yx}\right) dx\, dz \quad \text{(A.1)}$$

The force equilibrium in the y and z directions are similar:

$$\begin{aligned} \left(\frac{\partial \sigma_{xx}}{\partial x} + \frac{\partial \sigma_{zx}}{\partial z} + \frac{\partial \sigma_{yx}}{\partial y}\right) &= \rho \ddot{u} \\ \left(\frac{\partial \sigma_{yy}}{\partial y} + \frac{\partial \sigma_{zy}}{\partial z} + \frac{\partial \sigma_{xy}}{\partial x}\right) &= \rho \ddot{v} \\ \left(\frac{\partial \sigma_{zz}}{\partial z} + \frac{\partial \sigma_{yz}}{\partial y} + \frac{\partial \sigma_{xz}}{\partial x}\right) &= \rho \ddot{w} \end{aligned} \quad \text{(A.2)}$$

All three equations can be expressed in a more simplified form using tensorial notation:

$$\frac{\partial \sigma_{ij}}{\partial x_i} = \rho \ddot{u}_j \quad \text{(A.3)}$$

The stress-strain relationship for an isotropic material using the Lamé constants, λ and μ, is used:

$$\sigma_{ij} = \lambda \varepsilon_{kk} \delta_{ij} + 2\mu \varepsilon_{ij} \quad \text{(A.4)}$$

and the common form of strain-displacement relationship is applied:

$$\varepsilon_{ij} = \frac{1}{2}\left(u_{i,j} + u_{j,i}\right) \quad \text{(A.5)}$$

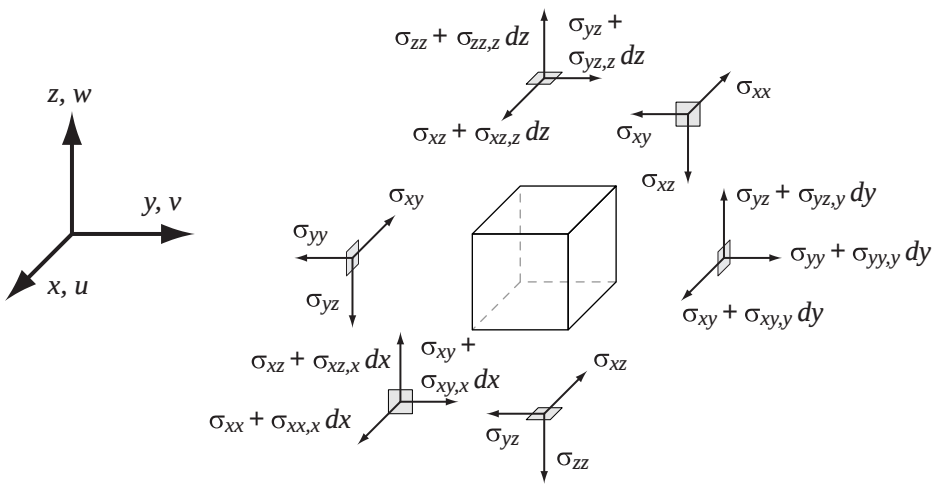

Figure A.1: Stresses on element

The resulting governing differential equations can be expressed in tensorial notation:

$$(\lambda + \mu)\, u_{i,ji} + \mu u_{j,ii} = \rho \ddot{u}_j \tag{A.6}$$

The dynamic behavior of a particle is expressed in terms of three differential equations. The above expression can also be written in vector notation:

$$(\lambda + \mu)\, \nabla\, (\nabla \cdot \mathbf{u}) + \mu \nabla^2 \mathbf{u} = \rho \ddot{\mathbf{u}} \tag{A.7}$$

At this point, the displacement field, $\mathbf{u}$ is decomposed into a distortional and dilatational component:

$$\mathbf{u} = \nabla\phi + \nabla \times \mathbf{H} \qquad \text{such that} \quad \nabla \cdot \mathbf{H} = 0 \tag{A.8}$$

ϕ corresponds to a dilatational, or volumetric, component and $\mathbf{H}$ corresponds to a distortional, or rotational, component of the displacement field, $\mathbf{u}$. This expression is substituted into the vectorial equation:

$$\nabla \left((\lambda + 2\mu)\, \nabla^2 \phi - \rho \ddot{\phi} \right) + \nabla \times \left(\mu \nabla^2 \mathbf{H} - \rho \ddot{\mathbf{H}} \right) = 0 \tag{A.9}$$

Two separate differential equations are produced

$$\underbrace{(\lambda + 2\mu)\, \nabla^2 \phi = \rho \ddot{\phi}}_{\text{dilatation}} \qquad \text{and} \qquad \underbrace{\mu \nabla^2 \mathbf{H} = \rho \ddot{\mathbf{H}}}_{\text{distortion}} \tag{A.10}$$

A.1 Dilatational Waves

The divergence of Equation A.7 is taken:

$$(\lambda + \mu) \nabla \cdot (\nabla (\nabla \cdot \mathbf{u})) + \mu \nabla \cdot \left(\nabla^2 \mathbf{u}\right) = \rho \nabla \cdot \ddot{\mathbf{u}} \tag{A.11}$$

The above expression can be rewritten:

$$\begin{aligned} (\lambda + \mu) \nabla^2 (\nabla \cdot \mathbf{u}) + \mu \nabla^2 (\nabla \cdot \mathbf{u}) &= \rho (\nabla \cdot \ddot{\mathbf{u}}) \\ (\lambda + 2\mu) \nabla^2 \Delta &= \rho \ddot{\Delta} \end{aligned} \tag{A.12}$$

Δ is $\nabla \cdot \mathbf{u} = \varepsilon_x + \varepsilon_y + \varepsilon_z$ and is regarded as the deviatoric strain in the element. The above expression for the dynamics associated with deviatoric strain is the same as the dilatation component of Equation A.10. This equation is the wave equation with a given propagation velocity:

$$c = \sqrt{\frac{\lambda + 2\mu}{\rho}} \tag{A.13}$$

A.2 Distortional Waves

The curl of Equation A.7 is taken:

$$(\lambda + \mu) \nabla \times (\nabla (\nabla \cdot \mathbf{u})) + \mu \nabla \times \left(\nabla^2 \mathbf{u}\right) = \rho \nabla \times \ddot{\mathbf{u}} \tag{A.14}$$

The above expression can be reduced to:

$$\mu \nabla^2 (\nabla \times \mathbf{u}) = \rho (\nabla \times \ddot{\mathbf{u}}) \tag{A.15}$$

Again, this is the wave equation with a propagation velocity:

$$c = \sqrt{\frac{\mu}{\rho}} \tag{A.16}$$

Appendix B

Stress-Strain Relations

In tensor notation, the mathematical definition of strain is used:

$$\varepsilon_{jk} = \frac{1}{2}\left(u_{j,k} + u_{k,j}\right) \quad \text{for} \quad j,k = 1,2,3 \tag{B.1}$$

The generalized Hooke's Law for a material can be expressed in tensor notation:

$$\sigma_{jk} = \mathsf{C}_{jklm}\varepsilon_{lm} \quad \text{for} \quad j,k,l,m = 1,2,3 \tag{B.2}$$

C_{jklm} is the set of elastic coefficients for the material. Using symmetry, the set of 81 coefficients can be reduced to a set of 21 constants that describe the material properties of a general anisotropic material. A rotation from one set of coordinates to another is performed using direction cosines:

$$\mathsf{C}^{\text{new}}_{nopq} = \mathsf{C}^{\text{old}}_{jklm} a_{nj} a_{ok} a_{pl} a_{qm} \quad \text{for} \quad j,k,l,m,n,o,p,q = 1,2,3 \tag{B.3}$$

a_{nj} is the set of direction cosines corresponding to the projection of the axes of the new coordinate system onto the axes of the old coordinate system.

For an orthotropic material, the stress-strain relationship in the principal material directions can be reduced and presented in matrix form:

$$\begin{bmatrix} \sigma_{11} \\ \sigma_{22} \\ \sigma_{33} \\ \sigma_{23} \\ \sigma_{13} \\ \sigma_{12} \end{bmatrix} = \begin{bmatrix} \frac{E_1(1-\nu_{23}\nu_{32})}{D} & \frac{E_1(\nu_{21}+\nu_{23}\nu_{31})}{D} & \frac{E_1(\nu_{31}+\nu_{21}\nu_{32})}{D} & 0 & 0 & 0 \\ \frac{E_2(\nu_{12}+\nu_{13}\nu_{32})}{D} & \frac{E_2(1-\nu_{13}\nu_{31})}{D} & \frac{E_2(\nu_{32}+\nu_{12}\nu_{31})}{D} & 0 & 0 & 0 \\ \frac{E_3(\nu_{13}+\nu_{12}\nu_{23})}{D} & \frac{E_3(\nu_{23}+\nu_{13}\nu_{21})}{D} & \frac{E_3(1-\nu_{12}\nu_{21})}{D} & 0 & 0 & 0 \\ 0 & 0 & 0 & 2G_{23} & 0 & 0 \\ 0 & 0 & 0 & 0 & 2G_{13} & 0 \\ 0 & 0 & 0 & 0 & 0 & 2G_{12} \end{bmatrix} \begin{bmatrix} \varepsilon_{11} \\ \varepsilon_{22} \\ \varepsilon_{33} \\ \varepsilon_{23} \\ \varepsilon_{13} \\ \varepsilon_{12} \end{bmatrix}$$

$$\text{where} \quad D = 1 - \nu_{12}\nu_{21} - \nu_{13}\nu_{31} - \nu_{23}\nu_{32} - \nu_{12}\nu_{23}\nu_{31} - \nu_{13}\nu_{21}\nu_{32} \tag{B.4}$$

For an isotropic material, a single modulus, Poisson's ratio, and shear modulus can be used instead of the directional ones present in the orthotropic material. Plane stress material properties are determined from Equation (B.4) by setting the stress components for a desired direction equal to zero. For example, if σ_1, σ_{13}, and σ_{23} are forced to be nonexistent, the strain in the 3 direction becomes a function of the strain in the 1 and 2 directions:

$$\varepsilon_{33} = -\frac{\nu_{13} + \nu_{12}\nu_{23}}{1 - \nu_{12}\nu_{21}}\varepsilon_{11} - \frac{\nu_{23} + \nu_{13}\nu_{21}}{1 - \nu_{12}\nu_{21}}\varepsilon_{22} \tag{B.5}$$

When substituted back into the remaining equations, the stress-strain relationship for the material is reduced:

$$\text{plane stress :} \quad \begin{bmatrix} \sigma_{11} \\ \sigma_{22} \\ \sigma_{12} \end{bmatrix} = \begin{bmatrix} \frac{E_1}{1-\nu_{12}\nu_{21}} & \frac{\nu_{21}E_1}{1-\nu_{12}\nu_{21}} & 0 \\ \frac{\nu_{12}E_2}{1-\nu_{12}\nu_{21}} & \frac{E_2}{1-\nu_{12}\nu_{21}} & 0 \\ 0 & 0 & 2G_{12} \end{bmatrix} \begin{bmatrix} \varepsilon_{11} \\ \varepsilon_{22} \\ \varepsilon_{12} \end{bmatrix} \tag{B.6}$$

The plane stress case using engineering strain and an isotropic material, the stress-strain relationship takes on a simpler form:

$$\begin{bmatrix} \sigma_{xx} \\ \sigma_{yy} \\ \tau_{xy} \end{bmatrix} = \mathbf{E} \begin{bmatrix} \varepsilon_{xx} \\ \varepsilon_{yy} \\ \gamma_{xy} \end{bmatrix} \qquad \text{where} \qquad \mathbf{E} = \frac{E}{1-\nu^2} \begin{bmatrix} 1 & \nu & 0 \\ \nu & 1 & 0 \\ 0 & 0 & \frac{1-\nu}{2} \end{bmatrix} \tag{B.7}$$

E and ν are the modulus of elasticity and Poisson's ratio of the of the material.

Similarly, a plain strain condition can be met by eliminating the strain components from a desired direction in Equation (B.4). The strains in the vertical direction, ε_{11}, ε_{12}, and ε_{13}, are set to zero. The vertical stress still exists:

$$\sigma_{33} = E_3 \left(\frac{\nu_{13} + \nu_{12}\nu_{23}}{D}\varepsilon_{11} + \frac{\nu_{23} + \nu_{13}\nu_{21}}{D}\varepsilon_{22} \right) \tag{B.8}$$

The stress-strain relation for the plane strain case is a reduced set of the original expression

$$\begin{bmatrix} \sigma_{11} \\ \sigma_{22} \\ \sigma_{12} \end{bmatrix} = \begin{bmatrix} \frac{E_1(1-\nu_{23}\nu_{32})}{D} & \frac{E_1(\nu_{21}+\nu_{23}\nu_{31})}{D} & 0 \\ \frac{E_2(\nu_{12}+\nu_{13}\nu_{32})}{D} & \frac{E_2(1-\nu_{13}\nu_{31})}{D} & 0 \\ 0 & 0 & 2G_{12} \end{bmatrix} \begin{bmatrix} \varepsilon_{11} \\ \varepsilon_{22} \\ \varepsilon_{12} \end{bmatrix} \tag{B.9}$$

For an isotropic material, the plane strain material properties can be simplified:

$$\mathbf{E} = \frac{E}{(1+\nu)(1-2\nu)} \begin{bmatrix} 1-\nu & \nu & 0 \\ \nu & 1-\nu & 0 \\ 0 & 0 & \frac{1-2\nu}{2} \end{bmatrix} \tag{B.10}$$

Appendix C

Derivation of Governing Differential Equation for Plate Dynamics

C.1 Transverse Vibrations

The governing equations of a thin plate are based on a plane stress state for the material. The full stress-strain relationship for the plate is reduced by assuming that the stresses associated with the vertical direction, σ_{zz}, σ_{yz}, and σ_{xz} are eliminated resulting in the stress-strain relationship in Equation (B.7).

A diagram of the loads on a plate element in shown in Figure C.1. Equilibrium of the forces in the z direction and the moments along the x and y axes yield three coupled equations:

$$\begin{aligned} \sum \text{forces}_{\,z-\text{axis}} \rightarrow \quad & \frac{\partial V_{xz}}{\partial x} + \frac{\partial V_{yz}}{\partial y} = \rho t_p \ddot{w} \\ \sum \text{moments}_{\,x-\text{axis}} \rightarrow \quad & \frac{\partial M_x}{\partial y} + \frac{\partial M_{xy}}{\partial x} - V_{yz} = \rho I \ddot{\eta}_x \\ \sum \text{moments}_{\,y-\text{axis}} \rightarrow \quad & \frac{\partial M_y}{\partial x} + \frac{\partial M_{yx}}{\partial y} - V_{xz} = \rho I \ddot{\eta}_y \end{aligned} \tag{C.1}$$

V_{xz} and V_{yz} refers to the vertical shear forces on the x and y faces of the element respectively, M_x and M_y are the moments with respect to the x and y axes, M_{xy} and M_{yx} are the twist moments and equal to each other, η_x and η_y are the rotations about the x and y axes, respectively, and I is the moment of inertia with respect to the mid-plane. The same set of equations can be found from Equation (A.2) by

multiplying the first and second equations with z and integrating while the third equation can just be integrated:

$$\int_{-t_p/2}^{t_p/2} z\left(\frac{\partial \sigma_{xx}}{\partial x}+\frac{\partial \sigma_{zx}}{\partial z}+\frac{\partial \sigma_{yx}}{\partial y}\right) dz = \int_{-t_p/2}^{t_p/2} \rho\, \ddot{u}\, z\, dz$$
$$\int_{-t_p/2}^{t_p/2} z\left(\frac{\partial \sigma_{yy}}{\partial y}+\frac{\partial \sigma_{zy}}{\partial z}+\frac{\partial \sigma_{xy}}{\partial x}\right) dz = \int_{-t_p/2}^{t_p/2} \rho\, \ddot{v}\, z\, dz$$
$$\int_{-t_p/2}^{t_p/2} \left(\frac{\partial \sigma_{zz}}{\partial z}+\frac{\partial \sigma_{yz}}{\partial y}+\frac{\partial \sigma_{xz}}{\partial x}\right) dz = \int_{-t_p/2}^{t_p/2} \rho\, \ddot{w}\, dz$$

The moments are defined by integrating over the thickness:

$$M_y = \int_{-t_p/2}^{t_p/2} \sigma_{xx}\, z\, dz \qquad M_x = \int_{-t_p/2}^{t_p/2} \sigma_{yy}\, z\, dz \qquad M_{xy} = \int_{-t_p/2}^{t_p/2} \sigma_{xy}\, z\, dz \tag{C.2}$$

Shear loads are found from integrating the vertical shear stresses and using integration by parts:

$$\begin{aligned}
\int_{-t_p/2}^{t_p/2} z\frac{\partial \sigma_{xz}}{\partial z} dz &= z\sigma_{xz}\big|_{-t_p/2}^{t_p/2} - V_{xz} \quad \text{where} \quad V_{xz} = \int_{-t_p/2}^{t_p/2} \sigma_{xz}\, dz \\
\int_{-t_p/2}^{t_p/2} z\frac{\partial \sigma_{yz}}{\partial z} dz &= z\sigma_{yz}\big|_{-t_p/2}^{t_p/2} - V_{yz} \quad \text{where} \quad V_{yz} = \int_{-t_p/2}^{t_p/2} \sigma_{yz}\, dz
\end{aligned} \tag{C.3}$$

Due to equilibrium conditions, the shear stresses at the top and bottom of the plate are non-existent. The integration of the vertical stresses becomes the external vertical loading:

$$\int_{-t_p/2}^{t_p/2} \frac{\partial \sigma_{zz}}{\partial z} dz = \sigma_{zz}|_{t_p/2} - \sigma_{zz}|_{-t_p/2} = q \tag{C.4}$$

Thus the governing equations for a particle from Equation (A.2) can be used to produce the force balance terms for a thin plate, in Equation (C.1).

The kinematic relations take on a general form:

$$u(z)(x,y) = z\eta_y(x,y) \qquad v(z)(x,y) = z\eta_x(x,y) \qquad w(x,y,z) = w(x,y) \tag{C.5}$$

There is no dependence on the vertical direction, z, for any of the displacement components. The kinematic relations in Equation (C.5) states that all of the information regarding the displacement field in the plate is solely a function of the displacements and rotations at the mid-plane. The assumption for the in-plane displacements, u and v, prescribes a linear displacement through the thickness which

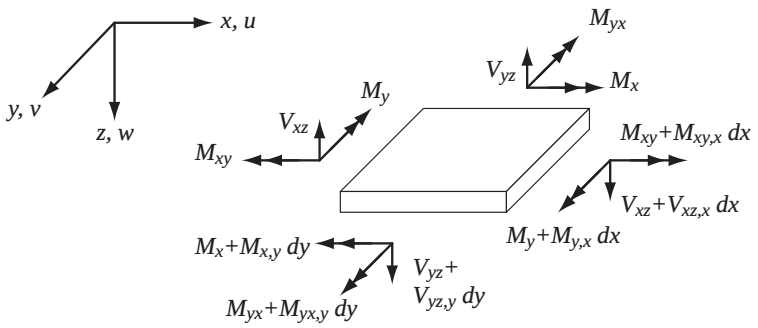

Figure C.1: Loads on plate element

is dependent on the rotations, η_y and η_x, respectively. The rotational inertia terms can be found:

$$\int_{-t_p/2}^{t_p/2} \rho\ddot{u}\, z\, dz = \rho\, I\, \ddot{\eta}_y \qquad \int_{-t_p/2}^{t_p/2} \rho\ddot{v}\, z\, dz = \rho\, I\, \ddot{\eta}_x \qquad \text{where} \quad I = t_p^3/12 \tag{C.6}$$

Using the isotropic stress-strain relationship and the given kinematic relations, the moment relations are expressed in terms of the rotations:

$$M_y = D\left(\eta_{y,x} + \nu\eta_{x,y}\right) \quad M_x = D\left(\eta_{x,y} + \nu\eta_{y,x}\right) \quad M_{xy} = D\frac{1-\nu}{2}\left(\eta_{y,y} + \eta_{x,x}\right) \tag{C.7}$$

where $D = Et_p^3/12(1-\nu^2)$ is the plate rigidity The two shear strains in the vertical directions are function of both the rotations as well as transverse displacement:

$$\varepsilon_{xz} = \frac{\partial u}{\partial z} + \frac{\partial w}{\partial x} = \eta_y + \frac{\partial w}{\partial x} \qquad \varepsilon_{yz} = \frac{\partial v}{\partial z} + \frac{\partial w}{\partial y} = \eta_x + \frac{\partial w}{\partial y} \tag{C.8}$$

The expressions for the shear loads, V_{xz} and V_{yz}, in Equation (C.3) involve an integration of the shear stresses through the thickness which requires an understanding of the shear stress distribution. A simplification can be made where the mid-plane shear stresses (and resulting mid-plane shear strains) are used:

$$V_{xz} = \int_{-t_p/2}^{t_p/2} \sigma_{xz} dz \approx G\frac{t_p}{2}\kappa^2\left(\eta_y + w_{,x}\right) \quad V_{yz} = \int_{-t_p/2}^{t_p/2} \sigma_{yz} dz \approx G\frac{t_p}{2}\kappa^2\left(\eta_x + w_{,y}\right) \tag{C.9}$$

κ^2 is a correction factor. Using the expressions for the moments in Equation (C.7) and shears in Equation (C.9) with the governing equations in Equation (C.1) yields

the coupled governing equations of motion:

$$\begin{gathered} G\frac{t_p}{2}\kappa^2\left(\eta_{y,x}+\eta_{x,y}+\nabla^2 w\right)=\rho t_p\ddot{w} \\ D(\eta_{x,yy}+\nu\eta_{y,xy})-D\frac{1-\nu}{2}(\eta_{y,yx}+\eta_{x,xx})-G\frac{t_p}{2}\kappa^2(\eta_y+w_{,x})=\rho I\ddot{\eta}_x \\ D(\eta_{y,xx}+\nu\eta_{x,yx})-D\frac{1-\nu}{2}(\eta_{y,yy}+\eta_{x,xy})-G\frac{t_p}{2}\kappa^2(\eta_x+w_{,y})=\rho I\ddot{\eta}_y \end{gathered} \tag{C.10}$$

The above equations represent the plate dynamics including rotary inertia as well as first order shear deformation, known as Mindlin plate theory.

A simplification can be made where the shear strains, ε_{xz} and ε_{yz}, are constrained to be non-existent. As a result, the relationship between the rotation terms and transverse displacement of the plate is defined:

$$(\varepsilon_{xz}=0)\rightarrow\eta_y=-w_{,x} \qquad (\varepsilon_{yz}=0)\rightarrow\eta_x=-w_{,y} \tag{C.11}$$

The moment relationships in Equation (C.7) are reduced to simpler expressions using just transverse displacement:

$$M_y=-D\left(w_{,xx}+\nu w_{,yy}\right) \quad M_x=-D\left(w_{,yy}+\nu w_{,xx}\right) \quad M_{xy}=-D\frac{1-\nu}{2}\left(2w_{,xy}\right) \tag{C.12}$$

The shear stresses in Equation (C.9) then become nonexistent due to the lack of a shear strain. The cross section shear forces are determined from the moment equilibrium equations in Equation (C.2) neglecting the rotary inertia terms:

$$V_{yz}=\frac{\partial M_x}{\partial y}+\frac{\partial M_{xy}}{\partial x} \qquad V_{xz}=\frac{\partial M_y}{\partial x}+\frac{\partial M_{xy}}{\partial y} \tag{C.13}$$

Using the relations for the shear terms and moments in the vertical force balance equation in Equation (C.2), the governing differential equation for the simplified model can be found:

$$\begin{gathered} \frac{\partial^2 M_x}{\partial y^2}+\frac{\partial^2 M_y}{\partial x^2}+2\frac{\partial^2 M_{xy}}{\partial x\partial y}=\rho t_p\ddot{w} \\ -D\left(\frac{\partial^4 w}{\partial x^4}+2\frac{\partial^4 w}{\partial x^2\partial y^2}+\frac{\partial^4 w}{\partial y^4}+\right)=\rho t_p\ddot{w} \end{gathered} \tag{C.14}$$

The Kirchoff model assumes no rotary inertia and eliminates shear deformations while still keeping shear loads. Although the model is restricted, the formulation

tends to be easier to work with and provides accurate results for the lower modes of vibration.

The above expressions are valid for an isotropic medium. The same type of development may be done with the orthotropic material properties and the resulting moment and shear terms depend on orientation.

The same expression for the simplified governing equation for a thin plate can be found using variational mechanics. Both the kinetic and potential energies for a plate element are found as a function of the vertical displacement, w. The expression for the kinetic energy involves a square of the velocity, $\dot{w}$. The expression for the potential energy is more complicated and uses the stress-strain relation in Equation (B.7) as well as the strain-displacement relationships with the constraint of no shear stress and strain. This potential energy expression consists the spatial derivatives of w. Using variational mechanics, the governing differential equation arises along with the expressions for the boundary conditions:

$$\begin{aligned} &\text{along edge parallel to } x\text{-axis}: \quad wM_x = 0 \quad \text{and} \quad w_{,y}\left(M_{xy,y} + V_{yz}\right) = 0 \\ &\text{along edge parallel to } y\text{-axis}: \quad wM_y = 0 \quad \text{and} \quad w_{,x}\left(M_{xy,x} + V_{xz}\right) = 0 \end{aligned} \tag{C.15}$$

C.2 In-Plane Vibrations

A description of in-plane vibrations may be found using variational mechanics where the governing differential equations of motion are determined with the boundary conditions found as a by-product. The kinetic and potential energies for a solid body are used:

$$\begin{aligned} \text{kinetic energy}: \; T &= \frac{1}{2}\int\int_V \rho\, \dot{\boldsymbol{u}}^T\, \dot{\boldsymbol{u}}\, dV\, dt \\ \text{potential energy}: \; U &= \frac{1}{2}\int\int_V \boldsymbol{\varepsilon}^T\, \mathbf{E}\, \boldsymbol{\varepsilon}\, dV\, dt \end{aligned} \tag{C.16}$$

For first order approximation to the in-plane dynamics, only u and v displacement components, shown in Figure C.2, are used and are constant through the thickness:

$$u(x,y,z,t) = u(x,y,t) \qquad\qquad v(x,y,z,t) = v(x,y,t) \tag{C.17}$$

Only the in-plane strain components are used:

$$\varepsilon_{xx} = u_{,x} \qquad \varepsilon_{yy} = v_{,y} \qquad \varepsilon_{xy} = u_{,y} + v_{,x} \tag{C.18}$$

The kinetic and potential energies for the plate element become simpler expressions:

$$T = \frac{1}{2} t_p \rho \int \int_{-b}^{b} \int_{-a}^{a} \left(\dot{u}^2 + \dot{v}^2 \right) \, dx \, dy \, dt \tag{C.19}$$

$$U = \frac{1}{2} t_p \int \int_{-b}^{b} \int_{-a}^{a} \begin{bmatrix} u_{,x} & v_{,y} & u_{,y} + v_{,x} \end{bmatrix} \mathbf{E} \begin{bmatrix} u_{,x} \\ v_{,y} \\ u_{,y} + v_{,x} \end{bmatrix} dx \, dy \, dt \tag{C.20}$$

E is the plane stress material properties of the material.

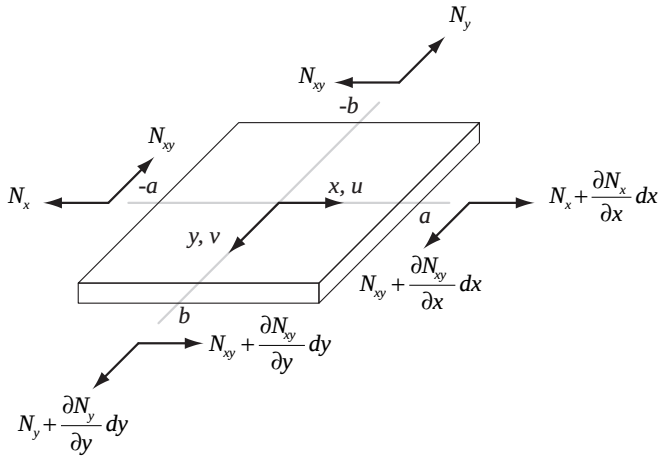

Figure C.2: In-plane diagram

The variation of the difference between the potential and kinetic energies is used to derive the governing equations of motion as well as the boundary conditions:

$$\delta(U - T) = 0 \quad \text{where} \quad \delta = \text{ variational operator} \tag{C.21}$$

Withholding the integration along the x and y axis, the variation of the kinetic energy is taken:

$$\begin{aligned} \delta T &= \frac{1}{2} t_p \rho \int \delta \left(\dot{u}^2 + \dot{v}^2 \right) dt \\ &= t_p \frac{1}{2} \rho \int \left(2 \, \dot{u} \, \delta \dot{u} + 2 \, \dot{v} \, \delta \dot{v} dt \right) \end{aligned} \tag{C.22}$$

Integration by parts is used to evaluate the integral with time such that only the variations of the displacements are present, δu and δv:

$$\delta T = t_p \rho \left((\dot{u}\,\delta u + \dot{v}\,\delta v)\Big|_{t_0}^{t_{end}} - \int (\ddot{u}\,\delta u + \ddot{v}\,\delta v)\,dt \right) \tag{C.23}$$

The first term in the variation is used used to specify the initial conditions in the time domain response. The second term of the variation is used in conjunction with the variation of the potential energy to find the equations of motion. The integration along the x and y axes are brought back when incorporating into the governing equations.

For the potential energy term, the plane stress material properties for an isotropic material is used in Equation (B.7). The variation of the potential equation is found neglecting the integration with time:

$$\delta U = t_p \int_{-b}^{b}\int_{-a}^{a} \frac{E}{1-\nu^2} \left(u_{,x}\delta u_{,x} + v_{,y}\delta v_{,y} + \nu\left(v_{,y}\delta u_{,x} + u_{,x}\delta v_{,y}\right) + \frac{1-\nu}{2}\left(u_{,y}+v_{,x}\right)\left(\delta u_{,y}+\delta v_{,x}\right)\right) dy\,dx \tag{C.24}$$

Each term in the integrand can be taken separately and evaluated using integration by parts such that only variational term, δu and δv remain and not their derivatives. Gathering the terms with $\delta u_{,x}$, $\delta u_{,y}$, $\delta v_{,x}$, and $\delta v_{,y}$ together yields four integrals:

$$\int_{-b}^{b}\int_{-a}^{a} \left(u_{,x}+\nu v_{,y}\right)\,\delta u_{,x}\,dx\,dy = \int_{-b}^{b}\left(\left(u_{,x}+\nu v_{,y}\right)\delta u\Big|_{-a}^{a} - \int_{-a}^{a}\left(u_{,xx}+\nu v_{,xy}\right)\delta u\,dx \right) dy$$

$$\int_{-b}^{b}\int_{-a}^{a} \left(v_{,y}+\nu u_{,x}\right)\,\delta v_{,y}\,dx\,dy = \int_{-a}^{a}\left(\left(v_{,y}+\nu u_{,x}\right)\delta v\Big|_{-b}^{b} - \int_{-b}^{b}\left(v_{,yy}+\nu u_{,xy}\right)\delta v\,dy \right) dx$$

$$\int_{-b}^{b}\int_{-a}^{a} \left(u_{,y}+v_{,x}\right)\,\delta u_{,y}\,dx\,dy = \int_{-a}^{a}\left(\left(u_{,y}+v_{,x}\right)\delta u\Big|_{-b}^{b} - \int_{-b}^{b}\left(u_{,yy}+v_{,xy}\right)\delta u\,dy \right) dx$$

$$\int_{-b}^{b}\int_{-a}^{a}\left(u_{,y}+v_{,x}\right)\,\delta v_{,x}\,dx\,dy = \int_{-b}^{b}\left(\left(u_{,y}+v_{,x}\right)\delta v\Big|_{-a}^{a}-\int_{-a}^{a}\left(u_{,xy}+v_{,xx}\right)\delta v\,dx\right)dy$$

The first term in the integrations is the boundary condition along the specified edge. The second term in the integrations is the contribution to the governing differential equation. Thus the variation of both the kinetic and potential energies can be split into boundary conditions and contributions to the governing differential equation.

The governing equations for the in-plane dynamics are found by including the potential and kinetic energy terms and gathering terms corresponding to δu and δv:

$$\delta(U-T) = -\int_{-b}^{b}\int_{-a}^{a}\left[\left(t_p\frac{E}{1-\nu^2}\left(u_{,xx}+\nu v_{,xy}+\frac{1-\nu}{2}\left(u_{,yy}+v_{,xy}\right)\right)-\rho t_p\ddot{u}\right)\delta u+ \left(t_p\frac{E}{1-\nu^2}\left(v_{,yy}+\nu u_{,xy}+\frac{1-\nu}{2}\left(u_{,xy}+v_{,xx}\right)\right)-\rho t_p\ddot{v}\right)\delta v\right]dy\,dx \quad \text{(C.25)}$$

From the above expression, two governing equations emerge describing the in-plane dynamics of the plate:

$$\begin{aligned}\frac{Et_p}{1-\nu^2}\left(u_{,xx}+\nu v_{,xy}+\frac{1-\nu}{2}\left(u_{,yy}+v_{,xy}\right)\right)-\rho t_p\ddot{u}=0\\ \frac{Et_p}{1-\nu^2}\left(v_{,yy}+\nu u_{,xy}+\frac{1-\nu}{2}\left(u_{,xy}+v_{,xx}\right)\right)-\rho t_p\ddot{v}=0\end{aligned} \quad \text{(C.26)}$$

The boundary conditions are of the form:

$$\begin{array}{lll}\text{along}\quad x=-a\,,a & \left(u_{,x}+\nu v_{,y}\right)\delta u=0 & \left(u_{,y}+v_{,x}\right)\delta v=0\\ \text{along}\quad y=-b\,,b & \left(v_{,y}+\nu u_{,x}\right)\delta v=0 & \left(u_{,y}+v_{,x}\right)\delta u=0\end{array}$$

The boundary conditions describe the state of the plate at each face of the element. There are two boundary conditions for each face. One of the boundary conditions state that either the normal stress must be non-existent or the normal displacement must be prescribed. Similarly, the other boundary condition for each face states that the shear stress must be non-existent or the tangential displacement must be prescribed.

In terms of the forces on the element, the governing equations of motion may

also be described by balancing the in-plane forces in Figure C.2:

$$\frac{\partial N_x}{\partial x} + \frac{\partial N_{xy}}{\partial y} = \rho t_p \ddot{u} \qquad \frac{\partial N_y}{\partial y} + \frac{\partial N_{xy}}{\partial x} = \rho t_p \ddot{v} \tag{C.27}$$

N_x, N_y, and N_{xy} are found by integrating each of the stresses in Equation (B.7) through the thickness:

$$N_x = \frac{E\, t_p}{1-\nu^2}\left(u_{,x} + \nu v_{,y}\right) \qquad N_y = \frac{E\, t_p}{1-\nu^2}\left(v_{,y} + \nu u_{,x}\right)$$
$$N_{xy} = \frac{E\, t_p}{1-\nu^2}\left(\left(\frac{1-\nu}{2}\right)\left(u_{,y} + v_{,x}\right)\right) \tag{C.28}$$

Appendix D

Newmark Time Integration

The Newmark method is an implicit algorithm for predicting the time domain response of a second order system [138]. In the case of structural dynamics, the system of equations is used:

$$\mathbf{M}\ddot{\mathbf{x}} + \mathbf{C}\dot{\mathbf{x}} + \mathbf{K}\ddot{\mathbf{x}} = \mathbf{F}(t) \tag{D.1}$$

$\mathbf{M}$, $\mathbf{C}$, and $\mathbf{K}$ are the mass, damping, and stiffness matrices, respectively, of the system, and $\mathbf{x}$ is the vector of degrees of freedom. The term, $\mathbf{F}$, is the vector describing the forcing and may be time varying. The Newmark method for time integration is based on the assumption of linear acceleration between two points in time. The velocities at two adjacent time steps are related:

$$\frac{\dot{\mathbf{x}}^{t+\Delta t} - \dot{\mathbf{x}}^{t}}{\Delta t} = (1-\delta)\ddot{\mathbf{x}}^{t} + \delta\ddot{\mathbf{x}}^{t+\Delta t} \tag{D.2}$$

The superscripts, t and $t+\Delta t$, refer to adjacent moments in time and δ specifies where along the time axis the acceleration is approximated as. Similarly, the displacement at two adjacent moments is set:

$$\frac{\mathbf{x}^{t+\Delta t} - \mathbf{x}^{t}}{\Delta t} = \dot{\mathbf{x}}^{t} + \left(\left(\frac{1}{2} - \alpha\right)\ddot{\mathbf{x}}^{t} + \alpha\ddot{\mathbf{x}}^{t+\Delta t}\right)\Delta t \tag{D.3}$$

The expressions for $\ddot{\mathbf{x}}^{t+\Delta t}$ and $\dot{\mathbf{x}}^{t+\Delta t}$ from the above equations can be found in terms of $\mathbf{x}^{t+\Delta t}$ and the displacement, velocity, and acceleration at time t:

$$\ddot{\mathbf{x}}^{t+\Delta t} = \frac{1}{\alpha\,\Delta t^2}\left(\mathbf{x}^{t+\Delta t} - \mathbf{x}^{t}\right) - \frac{1}{\alpha\,\Delta t}\dot{\mathbf{x}}^{t} - \left(\frac{1}{2\alpha} - 1\right)\ddot{\mathbf{x}}^{t} \tag{D.4}$$

$$\dot{\mathbf{x}}^{t+\Delta t} = \frac{\delta}{\alpha\,\Delta t}\left(\mathbf{x}^{t+\Delta t} - \mathbf{x}^{t}\right) + \left(1 - \frac{\delta}{\alpha}\right)\dot{\mathbf{x}}^{t} + \Delta t\left(1 - \frac{\delta}{2\alpha}\right)\ddot{\mathbf{x}}^{t}$$

These expressions are substituted into the governing equations of motion at time $t + \Delta t$:

$$\mathbf{M}\ddot{\mathbf{x}}^{t+\Delta t} + \mathbf{C}\dot{\mathbf{x}}^{t+\Delta t} + \mathbf{K}\mathbf{x}^{t+\Delta t} = \mathbf{F}^{t+\Delta t} \tag{D.5}$$

A matrix equation results which can be solved for to determine $\mathbf{x}$ at time $t + \Delta t$:

$$\boldsymbol{\mathcal{K}}\mathbf{x}^{t+\Delta t} = \boldsymbol{\mathcal{F}} \tag{D.6}$$

$$\boldsymbol{\mathcal{K}} = \frac{1}{\alpha\,\Delta t^2}\mathbf{M} + \frac{\delta}{\alpha\,\Delta t}\mathbf{C} + \mathbf{K} \tag{D.7}$$

$$\boldsymbol{\mathcal{F}} = \mathbf{F}^{t+\Delta t} + \mathbf{M}\left(\frac{1}{\alpha\,\Delta t^2}\mathbf{x}^{t} + \frac{1}{\alpha\,\Delta t}\dot{\mathbf{x}}^{t} + \left(\frac{1}{2\alpha} - 1\right)\ddot{\mathbf{x}}^{t}\right) + \mathbf{C}\left(\frac{\delta}{\alpha\,\Delta t}\mathbf{x}^{t} + \left(\frac{\delta}{\alpha} - 1\right)\dot{\mathbf{x}}^{t} + \Delta t\left(\frac{\delta}{2\alpha} - 1\right)\ddot{\mathbf{x}}^{t}\right) \tag{D.8}$$

At each time step, the solution to the linear equation in Equation (D.6) is found based on the displacement, velocity, and acceleration from the previous time step. For the current time step, the velocity and acceleration can be found by using the expression in Equation (D.4). The values for for α and δ typically follow a general rule:

$$\delta \geq .50 \qquad\qquad \alpha \geq .25\,(.50 + \delta)^2 \tag{D.9}$$

Appendix E

Dolph-Chebyshev Windowing Functions

For a discrete set of points, a spatial weighting function which is symmetric with respect to the center element is used:

$$h(x) = \sum_{-(N-1)/2}^{(N-1)/2} h_n \delta(x - n\Delta x) \tag{E.1}$$

h_n is the spatial weight at location $x_n = n\Delta x$ relative to the center element and $h_{-n} = h_n$ due to symmetry. The wavenumber response of this discrete set of weights is found by taking the Fourier transform and simplifying:

$$H(k) = \int h(x) e^{-ikx} dx = h_0 + \sum_{n=1}^{(N-1)/2} h_n 2 \cos\left(2n \frac{k\Delta x}{2}\right) \tag{E.2}$$

Chebyshev polynomials can be used to express each of the terms in the summation:

$$T_n\left(\cos(\theta)\right) = \cos\left(n\theta\right) \tag{E.3}$$

The wavenumber response then takes an alternate form:

$$H(k) = h_0 T_0 + \sum_{n=1}^{(N-1)/2} 2h_n T_{2n}\left(\cos\left(\frac{k\Delta x}{2}\right)\right) \tag{E.4}$$

The general expression for a Chebyshev polynomial of the first kind is used:

$$T_n(y) = \begin{cases} \cos\left(n \cos^{-1}(y)\right) & \text{if} \quad |y| \leq 1 \\ \cosh\left(n \cosh^{-1}(y)\right) & \text{if} \quad |y| > 1 \end{cases} \tag{E.5}$$

Note that the Chebyshev polynomials are bounded for $|y| \leq 1$ but grow exponentially outside of that region, shown in Figure E.1 for the first four even order

functions. A recurrence relation may be applied to express a Chebyshev polynomial in terms of lower order polynomials:

$$T_n(y) = 2yT_{n-1}(y) - T_{n-2}(y) \qquad \begin{aligned} T_0(y) &= 1 \\ T_1(y) &= y \\ T_2(y) &= 2y^2 - 1 \end{aligned} \tag{E.6}$$

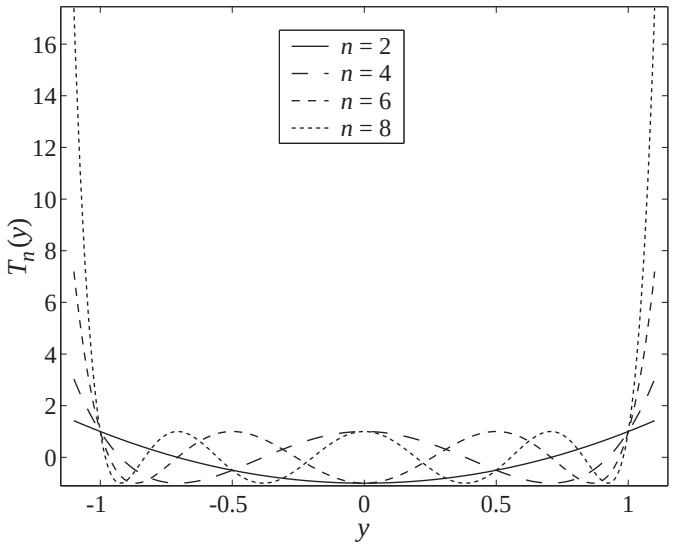

Figure E.1: Chebyshev Polynomials

The wavenumber response in Equation (E.4) is then composed of the even ordered Chebyshev polynomials up to order $(N-1)$ weighted with the appropriate h_n. The resulting polynomial is also a Chebyshev polynomial of order $N-1$. The wavenumber response for various N are shown in Figure E.2(a). There is a main lobe present at the $k\Delta x/2 = 0$ and additional side lobes of equal magnitude. The main lobe should be taller than the corresponding side lobes for useful wavenumber filtering. In order to accomplish this, the argument of the Chebyshev polynomial can be scaled by y_m:

$$y_m = \cosh\left(\frac{1}{N-1}\cosh^{-1}\left(\frac{1}{r}\right)\right) \quad \text{where} \quad r = \frac{\text{height of side lobes}}{\text{height of main lobe}} \tag{E.7}$$

The final wavenumber response of the Dolph-Chebyshev window can be found:

$$H(k) = T_{N-1}\left(y_m \cos\left(\frac{k\Delta x}{2}\right)\right) \tag{E.8}$$

The resulting wavenumber response is shown in Figure E.2(b) for N=19 sensor elements. The size of the side lobes are specified relative to the main lobe. The side lobes can be effectively removed from the wavenumber response at the expense of a lager beamwidth.

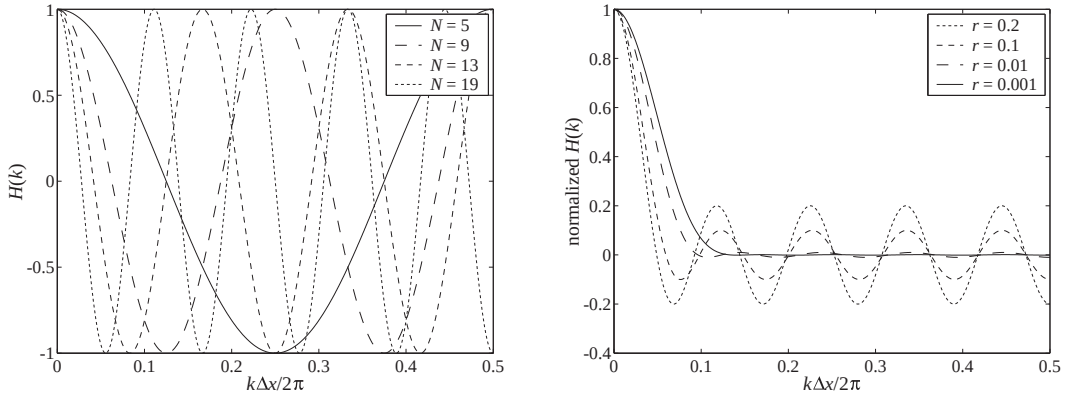

(a) Wavenumber response for various N (b) Reducing side lobe heights (N=19)

Figure E.2: Dolph-Chebyshev wavenumber responses

The weights, h_n, which produce the wavenumber response in Equation (E.8) are found by a series summation of polynomials using the recurrence relation in Equation (E.6):

$$h_0 T_0 + \sum_{n=1}^{(N-1)/2} 2h_n T_{2n}\left(\cos\left(\frac{k\Delta x}{2}\right)\right) = T_{N-1}\left(y_m \cos\left(\frac{k\Delta x}{2}\right)\right) \tag{E.9}$$

Both sides of Equation (E.9) is a polynomial of order $N-1$ of the quantity $\cos(k\Delta x/2)$. The coefficients of both polynomials are set equal to each other resulting in a matrix equation. The solution of the matrix equation is the spatial weights, h_n.

BIBLIOGRAPHY

[1] J. E. Land, "HUMS - the benefits – past, present, and future," in *Proceedings of 2001 IEEE Aerospace Conference*, vol. 6, pp. 3083–3094, 2001.

[2] "Columbia accident investigation report," Tech. Rep. Volume 1, Columbia Accident Investigation Board, 2003.

[3] Y. C. Tong, "Literature review on aircraft structural risk and reliability analysis," Tech. Rep. DSTO-TR-1110, DSTO Aeronautical and Maritime Research Laboratory, 2001.

[4] S. C. Forth, R. A. Everett, and J. A. Newman, "A novel approach to rotorcraft damage tolerance," 6th Joint FAA/DoD/NASA Aging Aircraft Conference, 2002.

[5] U. D. Kumar, "New trends in aircraft reliability and maintenance measures," *Journal of Quality in Maintenance Engineering* **5**(4), pp. 287–295, 1999.

[6] F. W. Spencer, "Visual inspection reliability of transport aircraft," in *Proceedings of SPIE*, vol. 2945, pp. 161–171, 1996.

[7] R. M. Knotts, "Civil aircraft maintenance and supprt : Fault diagnosis from a business perspective," *Journal of Quality in Maintenance Engineering* **5**(4), pp. 335–347, 1999.

[8] C. Boller, "Ways and options for aircraft structural health management," *Smart Materials and Structures* **10**, pp. 432–440, 2001.

[9] C. B. V. Way, J. N. Kudva, J. N. Schoess, M. L. Zeigler, and J. M. Alper, "Aircraft structural health monitoring system development - overview of the Air Force/Navy smart metallic structures program," in *Proceedings of SPIE*, vol. 2443, pp. 277–285, 1995.

[10] E. Lindgren, D. Judd, J. Mandeville, T. MacInnis, M. Concordia, B. Drennen, R. Grills, J. Aldrin, E. Pratt, and R. Waldbusser, "Enhanced nondestructive

evaluation techniques for the C-130 center wing," 6th Joint FAA/DoD/NASA Aging Aircraft Conference, 2002.

[11] S. R. Hunt and I. G. Hebden, "Validation of the Eurofighter Typhoon structural health and usage monitoring system," *Smart Materials and Structures* **10**, pp. 497–503, 2001.

[12] J. J. Gill, "Lessons learned from rotary- and fixed-wing HUMS applications," in *Proceedings of 2001 IEEE Aerospace Conference*, vol. 6, pp. 423–431, 2000.

[13] J. Kiddy, *A Modal-Based Damage Detection Technique for Helicopter Rotor Blades*. PhD thesis, University of Maryland, College Park, Department of Aerospace Engineering, 1999.

[14] P. F. Lichtenwalner, J. P. Dunne, R. S. Becker, and E. W. Baumann, "Active damage interrogation system for structural health monitoring," in *Proceedings of SPIE*, vol. 3044, pp. 186–194, 1997.

[15] P. F. Lichtenwalner and D. A. Sofge, "Local area damage detection in composite structures using piezoelectric transducers," in *Proceedings of SPIE*, vol. 3326, pp. 509–515, 1998.

[16] W. S. Chan, L. W. Rehfield, and T. K. O'Brien, "Analysis, prediction, and prevention of edge delamination in rotor system structures," in *43th Annual AHS Forum Proceedings*, pp. 587–596, 1987.

[17] G. B. Murri, T. K. O'Brien, and C. Q. Rousseau, "Fatigue life methodology for tapered composite flexbeam laminates," *Journal of the American Helicopter Society* **43**, pp. 146–155, April 1998.

[18] D. L. Hunt, S. P. Weiss, W. M. West, T. A. Dunlap, and S. R. Freesmeyer, "Development and implementation of a Shuttle modal inspection system," *Sound and Vibration* **24**(6), pp. 34–42, 1990.

[19] L. Emery and E. J. Zisk, "Health monitoring of reusable composite cryogenic tanks," in *Proceedings of the 36rd AIAA/ASME/AHS/ASC Structures, Structural Dynamics, and Materials Conference*, pp. 2237–2242, 1995.

[20] C. Wilkerson, "Acoustic emission monitoring of the DC-XA composite liquid hydrogen tank during structural testing," Technical Memorandum NASA TM-108520, National Aeronautics and Space Administration, 1996.

[21] R. Graue, M. Krisson, M. Erdmann, and A. Reutlinger, "Integrated health monitoring approach for resusable cryogenic tank structures," *Journal of Spacecraft and Rockets* **37**(5), pp. 580–585, 2000.

[22] T. A.-L. Kashangaki, "On-orbit damage detection and health monitoring of large space trusses - status and critical issues," in *Proceedings of the 32rd AIAA/ASME/AHS/ASC Structures, Structural Dynamics, and Materials Conference*, pp. 2947–2958, 1991.

[23] T. A.-L. Kashangaki, S. W. Smith, and T. W. Lim, "Underlying modal data issues for detecting damage in truss structures," in *Proceedings of the 33rd AIAA/ASME/AHS/ASC Structures, Structural Dynamics, and Materials Conference*, pp. 1437–1446, 1992.

[24] E. Baroth, W. T. Powers, J. Fox, B. Prosser, J. Pallix, K. Schweikard, and J. Zakrajsek, "IVHM (Integrated Vehicle Health Management) techniques for future space vehicles," in *Proceedings of the 37th Joint Propulsion Conference & Exhibit*, 1995. AIAA 2001-3523.

[25] P. J. Shull, ed., *Nondestructive Evaluation : Theory, Techniques, and Applications*, Marcel Dekker, 2002.

[26] S. W. Doebling, C. R. Farrar, M. B. Prime, and D. W. Shevitz, "Damage identification and health monitoring of structural and mechanical systems from changes in their vibration characteristics : A literature review," Technical Memorandum LA-13070-MS, Los Alamos National Laboratory, 1996.

[27] H. Sohn, C. R. Farrar, F. M. Hemez, D. D. Shunk, D. W. Stinemates, and B. R. Nadler, "A review of structural health monitoring literature : 1996-2001," Technical Memorandum LA-13976-MS, Los Alamos National Laboratory, 2003.

[28] D. C. Zimmerman and M. Kaouk, "Structural damage detection using a subspace rotation algorithm," in *Proceedings of the 33rd AIAA/ASME/AHS/ASC Structures, Structural Dynamics, and Materials Conference*, pp. 2341–2350, 1992.

[29] D. C. Zimmerman and M. Kaouk, "Structural damage detection using a minimum rank update theory," *Journal of Vibration and Acoustics* **116**(2), pp. 222–231, 1994.

[30] C. Farhat and F. Hemez, "Updating finite element dynamic models using an element-by-element sensitivity metholodgy," *AIAA Journal* **31**(9), pp. 1702–1711, 1993.

[31] S. W. Smith and P. E. McGowan, "Locating damaged members in a truss structure using modal test data : A demonstration experiment," in *Proceedings of 36th AIAA/ASME/ASCE/AHS/ASC Structures, Structural Dynamics and Materials Conference*, No. AIAA-89-1291-CP, 1989.

[32] A. Rytter and P. Kirkegaard, "Vibration based inspection using neural networks," in *Proceedings of DAMAS 1997, Structral Damage Assessment Using Advanced Signal Processing Procedures*, pp. 97–108, 1997.

[33] J. M. B. Peeters and D. D. Roeck, "Damage identification of the z24-bridge using vibration monitoring," in *Proceedings of European COST F3 Conference on System Identification and Structural Health Monitoring*, pp. 233–242, 2000.

[34] O. Loland and J. C. Dodds, "Experience in developing and operating integrity monitoring systems in north sea," in *Proceedings of the 8th Annual Offshore Technology Conference*, pp. 313–319, 1976.

[35] A. Kabe, "Stiffness matrix adjustment using mode data," *AIAA Journal* **23**, pp. 1431–1436, 1985.

[36] S. S. Kessler, *Piezoelectric-Based In-Situ Damage Detection of Composite Materials for Structural Health Monitoring Systems.* PhD thesis, Massachusetts Institute of Technology, Department of Aeronautics and Astronautics, 2002.

[37] J. J. Tracy and G. C. Pardoen, "Effect of delamination on the natural frequencies of composite laminates," *Journal of Composite Materials* **23**, pp. 1200–1215, 1989.

[38] S. V. Kulkarni and D. Frederick, "Frequency as a parameter in delamination problems - a preliminary investigation," *Journal of Composite Materials* **5**, pp. 112–117, 1971.

[39] C. Liang, F. Sun, and C. A. Rogers, "Electro-mechanical impedance modeling of active material systems," *Smart Materials and Structures* **5**, pp. 171–186, 1996.

[40] J. W. Ayres, F. Lalande, Z. Chaudhry, and C. A. Rogers, "Qualitative impedance-based health monitoring of civil infrastructures," *Smart Materials and Structures* **7**, pp. 599–605, 1998.

[41] Z. Chaudhry, T. Joseph, F. Sun, and C. A. Rogers, "Local-area health monitoring of aircraft via piezoelectric sensor/actuator patches," in *Proceedings of SPIE*, vol. 2443, pp. 268–276, 1995.

[42] G. Park, H. H. Cudney, and D. J. Inman, "An integrated health monitoring technique using structural impedance sensors," *Journal of Intelligent Material Systems and Structures* **11**, pp. 448–455, 2000.

[43] A. N. Zagrai and V. Giurgiutiu, "Electro-mechanical impedance method for crack detection in thin plates," *Journal of Intelligent Material Systems and Structures* **12**, pp. 709–718, 2001.

[44] R. D. Finlayson, M. Friesel, M. Carlos, P. Cole, and J. C. Lenain, "Health monitoring of aerospace structures with acoustic emission and acousto-ultrasonics," *Insight* **43**(3), 2001.

[45] M. Huang, L. Jiang, P. K. Liaw, C. R. Brooks, R. Seeley, and D. L. Klarstrom, "Using acoustic emission in fatigue and fracture materials research," *JOM: The Member Journal of The Minerals, Metals & Materials Society* **50**(11), 1998. available online at http://www.tms.org/pubs/journals/JOM/9811/Huang/Huang-9811.html.

[46] C. Marantidis, C. B. V. Way, and J. N. Kudva, "Acoustic-emission sensing in an on-board smart structural health monitoring system for military aircraft," in *Proceedings of SPIE*, vol. 2191, pp. 258–264, 1994.

[47] K. F. Graff, *Wave Motion in Elastic Solids*, Dover Publications, Inc., 1975.

[48] H. Lamb, "On waves in an elastic plate," in *Proceedings of the Royal Society of London. Series A*, vol. 93, pp. 114–128, 1917.

[49] I. A. Viktorov, *Rayleigh and Lamb Waves: Physical Theory and Applications*, Plenum Press, 1967.

[50] D. C. Worlton, "Ultrasonic testing with Lamb waves," *Nondestructive Testing* **15**, pp. 218–222, 1957.

[51] J. L. Rose, "A baseline and vision of ultrasonic guided wave inspection potential," *Journal of Pressure Vessel Technology* **124**, pp. 273–282, 2002.

[52] R. P. Dalton, *The Propagation of Lamb Waves Through Metallic Aircraft Fuselage Structure*. PhD thesis, University of London, Department of Mechanical Engineering, 2000.

[53] R. P. Dalton, P. Cawley, and M. J. S. Lowe, "The potential of guided waves for monitoring large areas of metallic aircraft fuselage structure," *Journal of Nondestructive Evaluation* **20**(1), pp. 29–46, 2001.

[54] P. Cawley and D. Alleyne, "The use of Lamb waves for the long range inspection of large structures," *Ultrasonics* **34**, pp. 287–290, 1996.

[55] P. D. Wilcox, M. J. S. Lowe, and P. Cawley, "Mode and transducer selection for long range Lamb wave inspection," *Journal of Intelligent Material Systems and Structures* **12**, pp. 553–565, 2001.

[56] E. A. Kraut, "Review of theories of scattering of elastic waves by cracks," *IEEE Transactions on Sonic and Ultrasonics* **SU-23**(3), pp. 162–167, 1976.

[57] J. E. Gubernatis, E. Domany, and J. A. Krumhansi, "Formal aspects of the theory of the scattering of ultrasound by flaws in elastic materials," *Journal of Applied Physics* **48**(7), pp. 2804–2811, 1977.

[58] J. E. Gubernatis, E. Domany, J. A. Krumhansi, and M. Huberman, "The Born approximation in the theory of the scattering of elastic waves by flaws," *Journal of Applied Physics* **48**(7), pp. 2812–2819, 1977.

[59] P. Agrawal, "Health monitoring of smart structures by method of wave scattering techniques," Master's thesis, The University of Texas at Arlington, Department of Aerospace Engineering, 1996.

[60] A. Boström, "Review of hypersingular integral equation method for crack scattering and application to modeling of ultrasonic nondestructive evaluation," *Appl. Mech. Rev.* **56**(4), pp. 383–405, 2003.

[61] D. N. Alleyne and P. Cawley, "The interaction of Lamb waves with defects," *IEEE Transactions on Ultrasonics, Ferroelectrics, and Frequency Control* **39**(3), pp. 381–397, 1992.

[62] M. J. S. Lowe and O. Diligent, "Low-frequency reflection characteristics of the S0 Lamb wave from a rectangular notch in a plate," *Journal of Acoustical Society of America* **111**(1), pp. 64–74, 2002.

[63] R. P. Dalton, *Interaction Between Fundamental Lamb Modes and Defects in Plates*. PhD thesis, University of London, Department of Mechanical Engineering, 2003.

[64] B. C. Lee and W. J. Staszewski, "Modelling of Lamb waves for damage detection in metallic structures: Part i. wave propagation," *Smart Materials and Structures* **12**, pp. 804–814, 2003.

[65] B. C. Lee and W. J. Staszewski, "Modelling of Lamb waves for damage detection in metallic structures: Part ii. wave interactions with damage," *Smart Materials and Structures* **12**, pp. 815–824, 2003.

[66] V. Giurgiutiu, J. Bao, and W. Zhao, "Piezoelectric wafer active sensor embedded ultrasonics in beams and plates," *Experimental Mechanics* **43**(4), pp. 428–449, 2003.

[67] M. Kehlenbach, B. Köler, X. Cao, and H. Hanselka, "Numerical and experimental investigation of Lamb wave interaction with discontinuities," in *4th International Workshop on Structural Health Monitoring*, pp. 421–428, 2003.

[68] J.-B. Ihn and F.-K. Chang, "Detection and monitoring of hidden fatigue crack growth using a built-in piezoelectric sensor/actuator network: I. diagnostics," *Smart Materials and Structures* **13**, pp. 609–620, 2004.

[69] S. B. Dong and R. B. Nelson, "On natural vibrations and waves in laminated orthotropic plates," *Journal of Applied Mechanics* **39**, pp. 739–745, 1972.

[70] M. Yamada and S. Nemat-Nasser, "Harmonic waves with arbitrary propagation direction in layered orthotropic elastic composites," *Journal of Composite Materials* **15**, pp. 531–542, 1981.

[71] W. M. Karunasena, R. L. Bratton, S. K. Datta, and A. H. Shah, "Elastic wave propagation in laminated composite plates," *Journal of Engineering Materials and Technology* **113**, pp. 411–418, 1991.

[72] H. Murakami, "A mixture theory for wave propagation in angle-ply laminates, part 1: Theory," *Journal of Applied Mechanics* **52**, pp. 331–337, 1985.

[73] H. Murakami, "A mixture theory for wave propagation in angle-ply laminates, part 1: Application," *Journal of Applied Mechanics* **52**, pp. 338–344, 1985.

[74] J. M. Galán and R. Abascal, "Numerical simulation of Lamb wave scattering in semi-infinite plates," *International Journal for Numerical Methods in Engineering* **53**, pp. 1145–1173, 2002.

[75] C. T. Sun and T. M. Tan, "Wave propagation in a Graphite/Epoxy laminate," *The Journal of the Astronautical Sciences* **32**(3), pp. 269–284, 1984.

[76] N. H. Clark and S. Thwaites, "Local phase velocity measurements in plates," *Journal of Sound and Vibration* **187**(2), pp. 241–252, 1995.

[77] V. S. K. M. A. Jaleel, N. N. Kishore, "Finite-Element simluation of elastic wave propagation in orthotropic composite materials," *Materials Evaluation* **51**, pp. 830–838, 1993.

[78] S.-S. Lih and A. K. Mal, "On the accuracy of approximate plate theories for wave field calculations in composite laminates," *Wave Motion* **21**, pp. 17–34, 1995.

[79] S. Banarjee, A. K. Mal, , and W. H. Prosser, "Analysis of transient Lamb waves generated by dynamic surface sources in thin composite plates," *Journal of Acoustical Society of America* **115**(5), pp. 1905–1911, 2004.

[80] K.-E. Fällström, "A nondestructive method to detect delaminations and defects in plates," *NDT International* **24**(2), pp. 67–76, 1991.

[81] F. Taillade, J.-C. Krapez, F. Lepoutre, and D. Balageas, "Shearographic visualization of Lamb waves in carbon epoxy plates interaction with delaminations," *European Physical Journal: Applied Physics* **9**, pp. 69–73, 2000.

[82] N. Guo and P. Cawley, "The interaction of Lamb waves with delaminations in composite laminates," *Journal of the Acoustical Society of America* **94**(4), pp. 2240–2246, 1993.

[83] N. Guo and P. Cawley, "Lamb wave propagation in composite laminates and its relationship with acousto-ultrasonics," *NDT & E International* **26**(2), pp. 75–84, 1993.

[84] K. S. Tan, N. Guo, B. S. Wong, and C. G. Tui, "Experimental evaluation of delaminations in composite plates by the use of Lamb waves," *Composite Science and Technology* **53**, pp. 77–84, 1995.

[85] E. A. Birt, "Damage detection in carbon-fibre composites using ultrasonic Lamb waves," *Insight* **40**(5), pp. 335–339, 1998.

[86] S. H. D. Valdés and C. Soutis, "Real-time nondestructive evaluation of fiber composite laminates using low-frequency Lamb waves," *Journal of the Acoustical Society of America* **111**, pp. 2026–2033, 2002.

[87] E. F. Crawley and J. de Luis, "Use of piezoelectric actuators as elements of intelligent structures," *AIAA Journal* **25**(10), pp. 1373–1385, 1987.

[88] V. R. Sonti, S. J. Kim, and J. D. Jones, "Equivalent forces and wavenumber spectra of shaped piezoelectric actuators," *Journal of Sound and Vibration* **187**(1), pp. 111–131, 1995.

[89] S. Grondel, C. Paget, C. Delebarre, J. Assad, and K. Levin, "Design of optimal configuration for generating A_0 Lamb mode in a composite plate using piezoceramic transducers," *Journal of the Acoustical Society of America* **112**(1), pp. 84–90, 2002.

[90] V. Giurgiutiu, "Tuned Lamb wave excitation and detection with piezoelectric wafer active sensors for structural health monitoring," *Journal of Intelligent Material Systems and Structures* **16**, pp. 291–305, 2005.

[91] M. Veidt, T. Liu, and S. Kitipornchai, "Flexural waves transmitted by rectangular piezoceramic transducers," *Smart Materials and Structures* **10**, pp. 681–588, 2001.

[92] A. Raghavan and C. Cesnik, "Piezoelectric-actuator excited-wave field solutions for guided-wave structural health monitoring," in *Proceedings of SPIE*, vol. 5765, pp. 313–323, 2005.

[93] M. A. Moetakef, S. P. Joshi, and K. L. Lawrence, "Elastic wave generation by piezoceramic patches," *AIAA Journal* **34**(10), pp. 2110–2117, 1996.

[94] S. P. Joshi, "Feasibility study on phased array of interdigital mesoscale transducers for health monitoring of smart structures," in *Proceedings of SPIE*, vol. 2443, pp. 248–257, 1995.

[95] P. D. Wilcox, *Lamb Wave Inspection of Large Structures Using Permanently Attached Transducers*. PhD thesis, University of London, Department of Mechanical Engineering, 1998.

[96] W. J. Staszewski, "Structural and mechanical damage detection using wavelets," *Shock and Vibration Digest* **30**(6), pp. 457–472, 1998.

[97] A. Abbate, J. Koay, J. Frankel, S. C. Schroeder, and P. Das, "Application of wavelet transform signal processor to ultrasound," in *Proceedings of the IEEE Ultrasonics Symposium*, vol. 2, pp. 1147–1152, 1994.

[98] W. H. Prosser, M. D. Seale, and B. T. Smith, "Time-frequency analysis of the dispersion of Lamb modes," *Journal of the Acoustical Society of America* **105**(5), pp. 2669–2676, 1999.

[99] S. T. Quek, Q. Wang, L. Zhang, and K. H. Ong, "Practical issues in the detection of damage in beams using wavelets," *Smart Materials and Structures* **10**, pp. 1009–1017, 2001.

[100] M. Z. Silva, R. Gouyon, and F. Lepoutre, "Hidden corrosion detection in aircraft aluminum structures using laser ultrasonics and wavelet transform signal analysis," *Ultrasonics* **41**, pp. 301–305, 2003.

[101] Z. Su and L. Ye, "Lamb wave propagation-based damage identification for quasi-isotropic CF/EP composite laminates using artificial neural algorithm: Part I - methodology and database development," *Journal of Intelligent Material Systems and Structures* **16**, pp. 97–111, 2005.

[102] Z. Su and L. Ye, "Lamb wave propagation-based damage identification for quasi-isotropic CF/EP composite laminates using artificial neural algorithm: Part II - implementation and validation," *Journal of Intelligent Material Systems and Structures* **16**, pp. 113–125, 2005.

[103] N. E. Huang, Z. Shen, S. R. Long, M. C. Wu, H. H. Shih, Q. Zheng, N.-C. Yen, C. C. Tung, and H. H. Liu, "The empirical mode decomposition and the Hilbert spectrum for nonlinear and non-stationary time series analysis," *Proceedings of R. Soc. Lond. A* **454**, pp. 903–995, 1998.

[104] S. T. Quek, P. S. Tua, and Q. Wang, "Detecting anomalies in beams and plate based on the Hilbert-Huang transform of real signals," *Smart Materials and Structures* **12**, pp. 447–460, 2003.

[105] L. W. Salvino and D. J. Pines, "Structural damage detection using empirical mode decomposition and HHT," in *Proceedings of 6th World Conference on Systemic, Cybernetics, and Informatics*, pp. 3171–3184, 2002.

[106] D. J. Pines, "Damage detection using wave element by element sensitivity analysis on 1-dimensional structures," in *Proceedings of the AIAA/ASME Adaptive Structures Forum*, 1997. AIAA-1997-1347.

[107] D. J. Pines, "Structural damage detection in civil structures using wave propagation modesl," in *Proceedings of the Second World Conference on Structural Control*, 1998.

[108] J. Ma, *Structural Health Monitoring and Damage Detection Using Dereverberated Transfer Function Wave Mechanics*. PhD thesis, University of Maryland, College Park, Department of Aerospace Engineering, 2002.

[109] J. F. Doyle, "An experimental method for determining the location and time of initiation of an unknown dispersing pulse," *Experimental Mechanics* **27**, pp. 229–233, 1987.

[110] T. N. Farris and J. F. Doyle, "Wave propagation in split timoshenko beam," *Journal of Sound and Vibration* **130**, pp. 137–147, 1989.

[111] J. F. Doyle, "Determining the size and location of transverse cracks in beams," *Experimental Mechanics* **35**, pp. 272–280, 1995.

[112] K. A. Lakshmanan and D. J. Pines, "Local damage detection in structures using wave models," in *Proceedings from the AIAA/ASME/AHS Adaptive Structures Forum*, pp. 381–386, 1996.

[113] K. A. Lakshmanan and D. J. Pines, "Modeling damage in rotorcraft flexbeams using wave mechanics," *Smart Materials and Structures* **6**, pp. 383–392, 1997.

[114] K. A. Lakshmanan and D. J. Pines, "Damage identification of chordwise crack size and location in uncoupled composite rotorcraft flexbeams," *Journal of Intelligent Materials Systems and Structures* **9**, pp. 146–155, 1998.

[115] R. Dugnani and M. Malkin, "Damage detection on a large composite structure," in *4th International Workshop on Structural Health Monitoring*, pp. 301–309, 2003.

[116] H. Sohn, G. Park, J. R. Wait, N. P. Limback, and C. R. Farrar, "Wavelet-based active sensing for delamination detection in composite structures," *Smart Materials and Structures* **13**, pp. 153–160, 2004.

[117] D. Berlincourt, H. H. A. Krueger, and C. Near, "Properties of piezoelectricity ceramics," Tech. Rep. TP-226, Morgan Electro Ceramics.

[118] Measurement Specialities, Inc., Sensor Products Division, 960 Forge Avenue, Norristown, PA 19403, *Piezo Film Sensors Technical Manual*.

[119] J. Sirohi and I. Chopra, "Fundamental understanding of piezoelectric strain sensors," *Journal of Intelligent Material Systems and Structures* **11**(4), pp. 246–257, 2000.

[120] L. J. Ziomek, *Fundamentals of Acoustic Field Theory and Space-Time Signal Processing*, CRC Press, 1995.

[121] S. E. Burke and J. E. H. Jr., "Spatial filtering concepts in distributed parameter control," *Journal of Dynamic Systems, Measurement, and Control* **112**, pp. 565–573, 1990.

[122] D. W. Miller, S. A. Collins, and S. P. Peltzman, "Development of spatially convolving sensors for structural control applications," in *AIAA/ASME/ASCE/AHS/ASC Structures, Structural Dynamics, and Materials Conference*, pp. 2283–2297, 1990.

[123] D. J. Pines, D. W. Miller, and A. H. von Flotow, "Directional filters for sensing 1-D structural dynamics," in *AIAA/ASME/ASCE/AHS/ASC Structures, Structural Dynamics, and Materials Conference*, pp. 1687–1699, 1992. AIAA-1992-2333.

[124] S. A. Collins, D. W. Miller, and A. H. von Flotow, "Distributed sensors as spatial filters in active structural control," *Journal of Sound and Vibration* **173**(4), pp. 471–501, 1994.

[125] D. J. Pines and A. H. von Flotow, "Spatially convolving wave propagation sensors for structural control - part 1: Analytical development for one-dimensional structures," *Journal of Intelligent Material Systems and Structures* **8**, pp. 929–952, 1997.

[126] D. J. Pines and A. H. von Flotow, "Spatially convolving wave sensors for structural control - part 2: Experimental verification using pvdf sensors," *Journal of Intelligent Material Systems and Structures* **8**, pp. 1059–1072, 1997.

[127] A. Yousefi-Koma and G. Vukovich, "Vibration suppression of flexible beams with bonded piezotransducers using wave-absorbing controllers," *Journal of Guidance, Control, and Dynamics* **23**(2), pp. 347–354, 2000.

[128] S.-C. Wooh and Y. Shi, "A simulation study of the beam steering characteristics for linear phased arrays," *Journal of Nondestructive Evaluation* **18**(2), pp. 39–57, 1999.

[129] S.-C. Wooh and Y. Shi, "Three-dimensional beam directivity of phase-steered ultrasound," *Journal of Acoustical Society of America* **105**(6), pp. 3275–3282, 1999.

[130] A. S. Purekar and D. J. Pines, "Interrogation of plate structures using phased array concepts," in *Proceedings of 12th International Conference on Adaptive Structures and Technologies*, pp. 275–288, 2001. University of Maryland, College Park, MD.

[131] V. Giurgiutiu and J. Bao, "Embedded-ultrasonics structural radar for in-situ structural health monitoring of thin-wall structures," *Structural Health Monitoring - An International Journal* **3**(2), pp. 121–140, 2004.

[132] S. Sundararaman, D. E. Adams, and E. J. Rigas, "Structural damage characterization through beamforming with phased arrays," in *4th International Workshop on Structural Health Monitoring*, pp. 634–641, 2003.

[133] K.-P. Kress, H. J. Baderschneider, and G. Guse, "Imaging ultrasonic sensor system SWISS completed 60.00 simulated flight hours to check structural integrety of aircraft subcomponent," in *Proceedings of SPIE*, vol. 5046, pp. 284–290, 2003.

[134] P. M. Mujumdar and S. Suryanarayan, "Flexural vibrations of beams with delaminations," *Journal of Sound and Vibration* **125**, pp. 441–461, 1988.

[135] R. J. Guyan, "Reduction of stiffness and mass matrices," *AIAA Journal* **3**, p. 380, 1965.

[136] R. L. Kidder, "Reduction of structural frequency equations," *AIAA Journal* **11**, p. 892, 1973.

[137] A. S. Purekar and D. J. Pines, "Near field effects of damage," in *Proceedings of SPIE*, vol. 4327, pp. 732–742, 2001.

[138] K.-J. Bathe and E. L. Wilson, *Numerical Methods in Finite Element Analysis*, Prentice-Hall, Inc., 1976.